Re-scanning in scanned ion beam therapy in the presence of organ motion

Mehrfachbestrahlung in der Ionentherapie in der Gegenwart von Organbewegung
Zur Erlangung des Grades eines Doktors der Naturwissenschaften (Dr. rer. nat.)
genehmigte Dissertation von Dipl.-Phys. Dirk Müssig aus Miltenberg
Februar 2014 — Darmstadt — D 17

TECHNISCHE
UNIVERSITÄT
DARMSTADT

GSI

Re-scanning in scanned ion beam therapy in the presence of organ motion

Mehrfachbestrahlung in der Ionentherapie in der Gegenwart von Organbewegung

Vom Fachbereich Physik
der Technischen Universität Darmstadt
zur Erlangung des Grades
eines Doktors der Naturwissenschaften
(Dr. rer. nat.)

genehmigte Dissertation von

Dipl.-Phys. Dirk Müssig
aus Miltenberg

Referent: Prof. Marco Durante, Ph. D.
Korreferent: Prof. Dr. Christoph Bert

Tag der Einreichung: 17. Dezember 2013
Tag der mündlichen Prüfung: 15. Januar 2014

Darmstadt 2014

D17

Abstract

Therapeutic dose application by highly tumor-conformal scanned ion beam radiation therapy is currently in most cases not possible for indications which exhibit tumor motion. Due to interference effects, the dose application is likely to be distorted so that treatment is not safely possible. Distorted dose profiles can be improved by means of statistical averaging - the corresponding technique is known as *re-scanning* and was investigated in this work.

Carbon ion treatment planning studies for five lung cancer cases and six different *re-scanning* flavors were performed. The data show that at least the techniques *breath-sampled* and *random-time-delay re-scanning* should be able to compensate dose inhomogeneities sufficiently as to enable patient treatment.

Re-scanning was technically implemented in a research version. Experiments were performed to test the implementation, to verify the dose application and to investigate the motion mitigation efficiency. The corresponding dose levels showed only small deviations compared to the therapy delivery mode for stationary targets. The experimental data for motion mitigation strengthened the findings of the simulations. Over- and underdosage can be efficiently reduced using *re-scanning*.

Zusammenfassung

Tumorkonforme Bestrahlung mit einem gescannten Ionenstrahl ist meistens nicht möglich, wenn sich der Tumor während der Bestrahlung bewegt. Die Interferenz von Bewegung und Bestrahlung verfälscht die Dosisapplikation oft in einem klinisch nicht vertretbaren Maß. Eine Methode, die als *Mehrfachbestrahlung* (*MB*) bekannt ist und im Rahmen dieser Arbeit untersucht wurde, kann diese Interferenzeffekte durch statistische Mittelung reduzieren.

Mittels Bestrahlungsplanungsstudien auf Basis von fünf Lungentumordatensätzen wurden sechs verschiedene *MB*-Varianten bewertet. Mindestens zwei Varianten, die *Atemperiode-angepasste* und die *Zufalls-Pausen MB*, konnten die Dosisinhomogenitäten so weit reduzieren, dass eine klinische Anwendung möglich sein sollte.

Die MB wurde als Forschungsmodalität auch technisch implementiert. Durch Experimente konnten die Implementierung, die Dosisapplikation und die Effizienz der Bewegungskompensation validiert werden. Im statischen Fall zeigen die Ergebnisse zeigen nur geringe Abweichungen im Vergleich zum Therapiemodus. Die Experimente zur Reduzierung der Interferenzeffekte stützen die Ergebnisse der Simulationen. Über- und Unterdosierungen können effizient durch die MB reduziert werden.

Contents

List of Abbreviations

4DCT	time resolved computed tomography
ADC	analog-to-digital converter
ACCvirtual	virtual-accelerator
AP	anterior-posterior
BT	*beam tracking*
BEV	beam's eye view
BED	biological effective dose
BreThoPho	breathing-thorax-phantom-with-6D-target-motion
BS	breath-sampled (*re-scanning*)
CT	computed tomography
CTV	clinical target volume
DNA	deoxyribonucleic acid
DVH	dose volume histogram
DAH	dose area histogram
DeVarPho	density-variation-phantom
FWHM	full width at half maximum
GSI	GSI Helmholtzzentrum für Schwerionenforschung GmbH
GTV	gross tumor volume
HIMAC	Heavy-Ion Medical Accelerator in Chiba
HIT	Heidelberg Ion-Beam Therapy Centre
HU	Hounsfield unit
IC	ionisation chamber
IES	iso-energy slice
IMPT	intensity modulated particle therapy
IMRT	intensity modulated radiotherapy
ITV	internal target volume
LR	left-right
LEM	local effect model
LET	linear energy transfer
MBP	machine beam plan
MBR	machine beam record
MDACC	MD Anderson Cancer Center
MGH	Massachusetts General Hospital
MRI	magnetic resonance imaging
MWPC	multiwire proportional chamber
MU	monitor units
NIRS	National Institute of Radiological Sciences
NSCLC	non-small cell lung cancer
OD	optical density
PET	positron emission tomography
PBP	physical-beam-plan
PBR	physical-beam-record
PBRSimEnv	physical-beam-record simulation environment
PCR	*phase-controlled re-scanning*
PDF	probability density function
PMMA	polymethyl methacrylate
PPIC1	parallel-plate ionization chamber 1
PPIC3	parallel-plate ionization chamber 3
PSI	Paul Scherer Institut
PTV	planning target volume
RBE	relative biological effectiveness
RDBT	*real-time dose compensation combined with beam tracking*
RKI	Robert Koch Institute
ROI	region of interest
RPTC	Rinecker Proton Therapy Centre
SI	superior-inferior
Slice	*slice-by-slice re-scanning*
SOBP	spread out Bragg peak
TCU	therapy control unit
OAR	organ at risk

TRiP	TReatment planning for Particles
TKR	therapy control room
VOI	volume of interest
WEPL	water-equivalent path length

1 Motivation

Cancer is one of the most leading causes of pain and death to patients worldwide. The Robert Koch-Institut (RKI, 2012) lists about 470.000 new cases and 216.000 deaths per year in Germany. Up to 40% of all cancer deaths could be avoided by reducing tobacco use, improving diets and physical activity, lowering alcohol consumption, eliminating workplace carcinogens and immunizing against hepatitis B virus and the human papillomavirus (WHO, 2007). The most effective treatment options include surgery, chemotherapy, radiotherapy and combinations of these. In about 50% of the incidences radiation is used in the treatment course (Schardt et al., 2010). In principle, every tumor can be controlled if a sufficient level of radiation can be applied to it (Durante and Loeffler, 2010, 2013). However, this is not always possible because it cannot be avoided in radiotherapy that healthy tissue receives a certain level of dose, too. If an organ at risk (OAR) (e.g kidneys, liver, heart, spinal cord or brain stem) is too close to the tumor it might not be possible to irradiate the tumor with a high dose level without causing severe side effects. Therefore the development of radiotherapy techniques is driven by the aim to deliver a dose distribution as conformal as possible to the tumor.

A method called active beam scanning with heavy ions, which is used at GSI Helmholtzzentrum für Schwerionenforschung GmbH (GSI) and Heidelberg Ion-Beam Therapy Centre (HIT), is the latest development in that direction and clinical studies have shown the physical and biological advantages of ion beams in dose conformity and tumor control rates (Schulz-Ertner and Tsujii, 2007). Up to date, heavy ion beams are mainly used for stationary tumor types because the conformal irradiation of moving tumors is a big challenge. Especially lung tumors are subjected to a rather large motion trajectory and, unfortunately, this type is the most frequent cause of cancer death worldwide (and in Germany) with approximately 20% of the total cancer mortalities with an absolute number of 1.4 million humans (IARC, 2013). A moving tumor causes several problems for radiotherapy: When determining the position of the tumor with a computed tomography (CT) its movement leads to a blurred image, the same movement then disturbs the dose application because the medical physicist is only able to apply a certain dose to a specific position inside the tumor when its position is known.

The main effect of organ motion on conformal radiotherapy can easily be understood through an analogy with photography. When a photo is taken of an object that moves significantly during the exposure, the image will be blurred like displayed in figure 1.1. It can further be seen that the area of the moving picture has been enlarged. The same is true if one tries to paint a picture with a pencil on a moving canvas. The analogies represent e.g. making a 3D CT or irradiating a dose distribution to the tumor, respectively. Some strategies have been proposed to treat moving

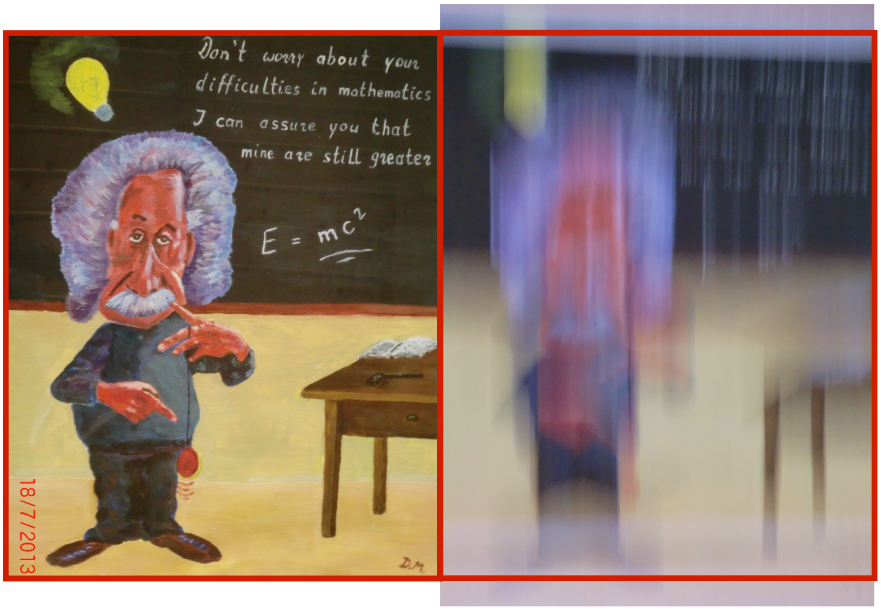

Figure 1.1.: Left picture: *Brilliant* Einstein. Right picture: Motion effects can ruin taking or painting a clear picture as well as therapy success in heavy ion irradiation.

tumors using ions (Bert and Durante, 2011). One of these strategies, namely *re-scanning*, will be addressed in this thesis. The beneficial outcome of a treatment course is very likely to fail if dose inhomgeneities, which are due to the motion, cannot be efficiently reduced. In contrast to standard heavy ion irradiation, the beam crosses the tumor volume in *re-scanning* mode many times to reduce those dose inhomgeneities. It shall be shown in this work if *re-scanning* could be a sensible option to treat patients with moving tumor in the near future at clinics like the HIT.

The scope of this thesis can be grouped as follows:

- Chapter 2 gives an overview of the physical and biological fundamentals of ion beam therapy and introduces the *re-scanning* technique.
- Chapter 3 presents treatment planning studies of five patients with lung tumors on a basis of simulated beam applications in the *re-scan* mode. The effectiveness of *re-scanning* with respect to reducing dose inhomogeneities will be addressed and discussed.
- Chapter 4 address the technical feasibility of *re-scanning* and presents experimental results performed at GSI and HIT. Simulations which complement and confirm the experimental results are presented and discussed.
- Chapter 5 contains a discussion and a summary.
- Chapter 6 will conclude the thesis.

2 Introduction - research background and fundamentals

2.1 Development of heavy ion therapy

The discovery of the X-rays as a "new kind of radiation" in 1895 by W. C. Röntgen marked a quantum jump in the field of physics. In the following years radiation became an important tool in various academic fields like nuclear physics or medicine. The first medical use of the X-rays was reported in the *Lancet* in 1896 - only one month after Röntgen's discovery (Hall and Giaccia, 2006). In the historical development of radiotherapy two general tendencies are visible: The clinical results of therapies are improved by a greater conformity of the applied radiation to the target volume and by an increased biological effectiveness of the radiation (Kraft, 2000). In 1946 R. Wilson (Wilson, 1946) first wrote that ions will meet these requirements much better than photons. The first patient was treated with protons in 1954 at Lawrence Berkeley Laboratory (Tobias et al., 1958). Due to the technically very challenging tasks involved it took many years until the full physical and biological benefit of the heavy ions could be exploited in a therapy pilot project at GSI Helmholtzzentrum für Schwerionenforschung GmbH (GSI) which started patient treatment in the year 1998 (Kraft, 2000). Until today, both photon and ion therapy are constantly improved in terms of dose application by the development of new techniques and advantages in the understanding of the interaction of radiation with human cells.

Figure 2.1 compares an optimized dose distribution for two state of the art techniques, namely intensity modulated radiotherapy (IMRT) and intensity modulated particle therapy (IMPT). While both methods show a homogeneous target coverage, the integral dose delivered to the patient is much smaller when using IMPT and, especially, the dosage to an organ at risk (OAR) can be greatly reduced. Furthermore, the reduced dose low dose region in case of IMPT (Kaderka, 2011) is believed to reduce the risk of secondary cancer or side effects after modern radiotherapy (Newhauser and Durante, 2011), so that even a pregnant 27-year-old woman (diagnosed for a skull-base chordoma) was irradiated and no abnormalities have been observed in a follow-up study of the child (Münter et al., 2010).

Since this work is focused on heavy ion therapy, information about new developments in photon therapy can be found elsewhere (Kilby et al., 2010). In the following physical, technical, medical and biological details will be introduced concerning heavy ion therapy.

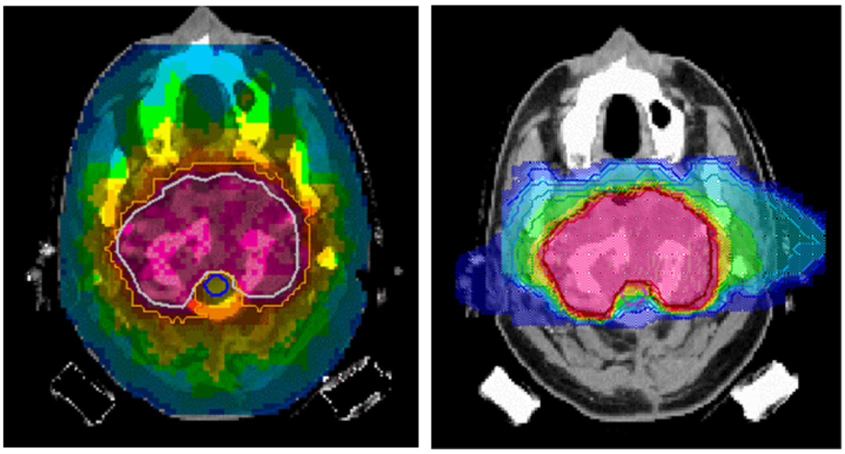

Figure 2.1.: Comparison of treatment plans with 9 fields of X-rays (IMRT – left picture) and with 2 fields of carbon ion (IMPT – right picture). In both cases the dose coverage of the target volume is good but for carbon ions the dose to the normal tissue is much smaller. Figure from (Amaldi and Kraft, 2008).

2.1.1 Physical properties of heavy ion interaction with matter

Figure 2.1 already showed that a tumor can be irradiated more conformal and with less integral dose to the whole body by using carbon ions instead of photons. Both types of radiation mainly interact with the tissue by the means of so called secondary electrons which have been produced by the elementary interaction processes. However, these elementary interaction processes are diverse for both heavy ion and photon irradiation which results in a different distribution of the secondary electrons which then leads to different biological damage (Alpen, 1998; Hall and Giaccia, 2006). After a small maximum in the entrance region, the dose of the photons drops exponentially with the penetration depth. The depth dose curve of heavy ions on the other side features a distinct narrow peak with a sharp dose fall off. This maximum is commonly known as the *Bragg-Peak*. The basic physic interactions of these different properties are briefly introduced in the following sections. An overview of the different depth dose distribution for various kinds of radiation is illustrated in figure 2.2.

The dose, D, deposited in the tissue as a physical quantity is defined by the ratio of the absorbed energy dE per mass element dm (Alpen, 1998)

$$D = \frac{dE}{dm} \quad [1\ \mathrm{Gy} = 1\ \mathrm{J/kg}]. \tag{2.1}$$

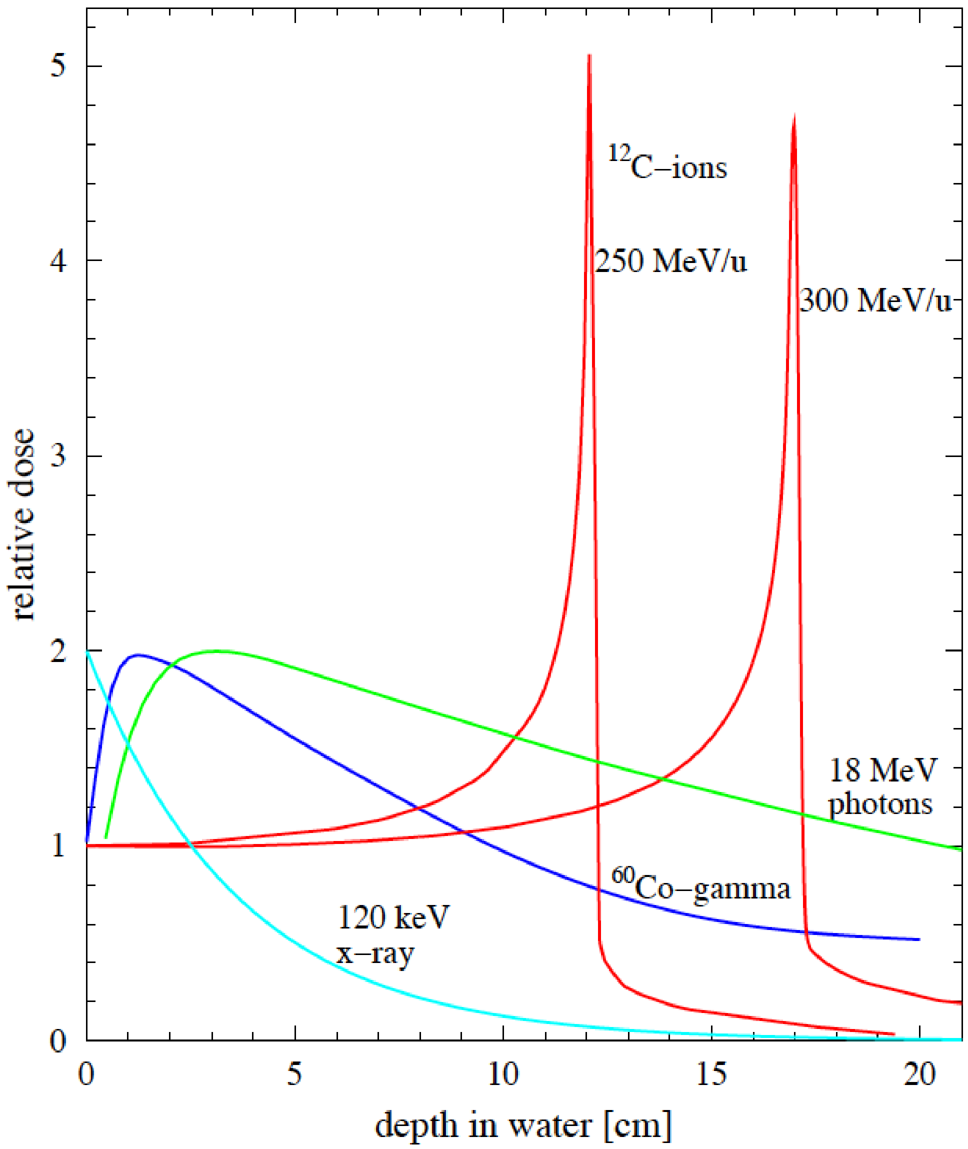

Figure 2.2.: Depth dose profiles with different energies compared to carbon ions at two different energies. The photon curves drop exponentially after reaching a maximum (build-up effect) shortly after entering the medium. The maximum of the dose deposition of the carbon ions is a well defined function of the initial energy of the particles. This maximum of the dose deposition is the so called Bragg-Peak which is located around the end of the particle track. The distinct Bragg-Peak can be used to deposit the dose in case of heavy ion irradiation more conformal to the target than by using photons. Figure from (Lüchtenborg, 2012).

Interactions of photons and matter

An overview of the interaction process of photons with matter are given e.g. in (Alpen, 1998). To summarize the most important facts:

While passing through matter, photons in the energy regime (approximately 18 MeV) of radiotherapy are mainly scattered by the photoelectric effect (cross section τ_{photo}), by Compton scattering (cross section $\sigma_{Compton}$) and pair production (cross section κ_{pair}). The cross sections depend on photon energy and material. Due to the nature of these interactions it follows that the intensity I of a monoenergetic beam of photons with initial energy of I_0 passing through an absorber material of the thickness x is described by an exponential function:

$$I(x) = I_0 \cdot e^{-(\tau_{photo}+\sigma_{Compton}+\kappa_{pair})x}. \tag{2.2}$$

This function determines the depth dose distribution of photon in tissue (see figure 2.2).

Interactions of ions and matter

The absorbed dose of a parallel ion beam with the fluence F transversing a thin layer of material with the mass density ρ can be calculated as (Schardt et al., 2010):

$$D\ [\mathrm{Gy}] = 1.6 \cdot 10^{-9} \cdot \frac{dE}{dx}\left[\frac{\mathrm{keV}}{\mu\mathrm{m}}\right] \cdot F\left[\mathrm{cm}^{-2}\right] \cdot \frac{1}{\rho}\left[\frac{\mathrm{cm}^3}{\mathrm{g}}\right], \tag{2.3}$$

with dE/dx being the specific energy loss per unit length. Within the therapeutic energy range of carbon ions, $\beta = v/c \approx 0.7$ ($c =$ speed of light,$v =$ particle's velocity), dE/dx is dominated by inelastic collisions of the incident particles with the target electrons and can be well described with the Bethe-Bloch (Bethe, 1930; Bloch, 1933a,b) formula (Schardt et al., 2010; Nakamaru, 2010) including the shell correction C/Z_t (which takes orbital velocities of the target molecules into account) and a density correction term $\delta/2$ (Fano, 1963):

$$\frac{dE}{dx} = \frac{4\pi e^4 Z_t Z_p^2}{m_e v^2}\left[\ln\frac{2m_e v^2}{\langle I\rangle} - \ln(1-\beta^2) - \beta^2 - \frac{C}{Z_t} - \frac{\delta}{2}\right]. \tag{2.4}$$

Z_p and Z_t tag the nuclear charges of the projectile and target, m_e and e are the mass ind the charge of an electron and $\langle I\rangle$ denotes the mean ionization energy of the target medium. At high velocities the electrons of the projectile carbon ion are complete stripped off. At lower velocities the mean charge decreases due to recombination processes and Z_p needs to be replaced by the empirical *effective charge* formula (Barkas, 1963):

$$Z_{eff} = Z_p \left[1 - \exp(-125\,\beta\, Z_p^{-2/3}) \right] . \tag{2.5}$$

Stopping power curves can be seen in figure 2.3.

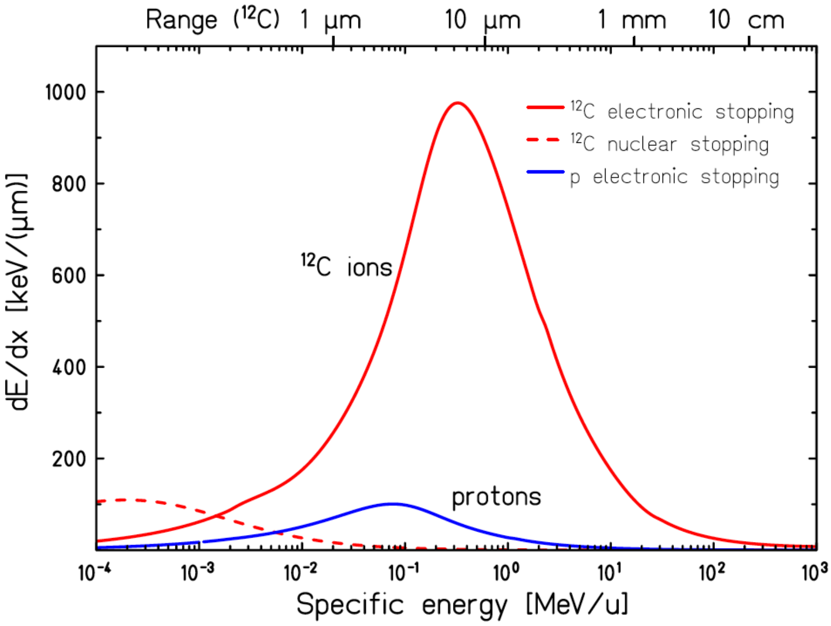

Figure 2.3.: Specific energy loss of carbon ions and protons in water. Equation 2.4 describes the electronic energy loss. Figure from (Schardt et al., 2010)

Equations 2.4 illustrates that the distinct Bragg-Peak at low projectile energies of the heavy ions is mainly caused by the $1/v^2$ dependence. This increase of the specific energy loss at low velocities is caused by the fact that the projectile ion spends more time in the Coulomb field of the interacting atom. When the velocity gets gradually lower, the *effective charge* of the projectile (see equation 2.5) is reduced so that the energy loss decreases again until the particle finally stops.

The presented concepts illustrate the most important physical properties of heavy ion irradiation concerning this thesis. Further information like range straggling, lateral scattering, nuclear fragmentation or online in-vivo PET imaging can be found elsewhere (Kraft, 2000; Schardt et al., 2010).

It was already mentioned that the main biological effect is caused by the secondary electrons, which primarily transfer their energy via bremsstrahlung. Their distribution and energy spectra is therefore crucial to understand the difference between different types of radiation. Figure 2.4 shows as an example the microscopic track structure of protons and carbon ions. Why different physical properties result in diverse implications for therapeutic beam application can only be understood by including related concepts and ideas of *radiobiology*, which will be introduced in the next section.

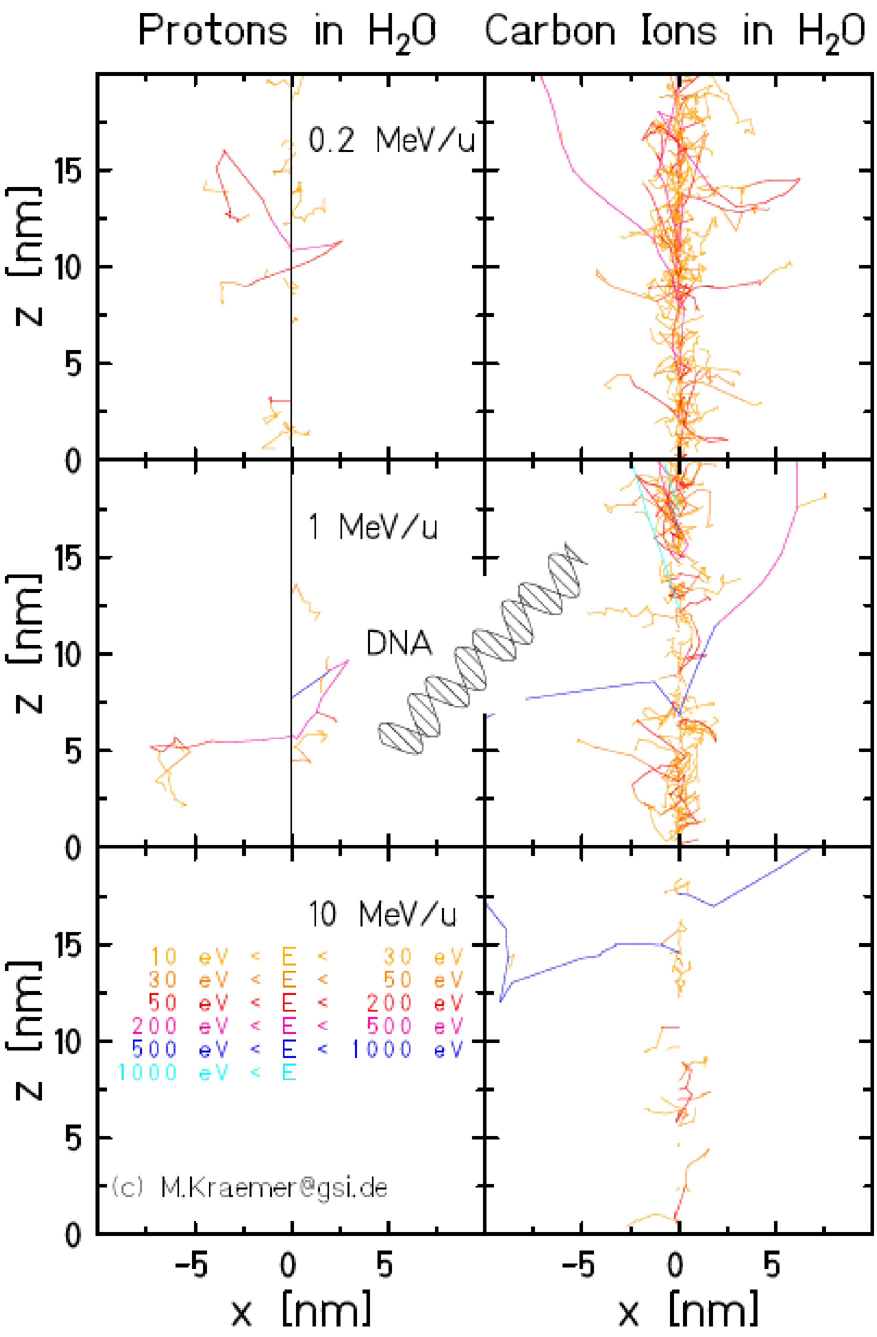

Figure 2.4.: Simulated paths of and energy distribution of secondary electrons produced by protons and carbon ions at different energies. Figure courtesy of M. Krämer.

To summarize:

- X-rays and ions interact fundamentally different with matter. Nevertheless, both types of radiation generate secondary electrons which then transmit the energy to the tissue.
- X-rays have an exponentially decreasing depth-dose profile wheres heavy ions show a sharp peak (Bragg-peak) shortly before they stop. The depth of this peak is a function of the particle's energy.
- Carbon ions are especially well suited to apply a very conformal dose distribution to the target.

2.1.2 Radiobiology of heavy ion irradiation

The effects of radiation on humans do not only depend on the total amount of energy which is absorbed by the body but also to a great amount on how the energy is deposited. A total body dose of 4 Gy of X-rays given to a human is lethal in about half of the individuals exposed (Hall and Giaccia, 2006). In case of a body mass of 70 kg this corresponds to 67 calories which is the energy necessary to heat 3 ml of coffee from a temperature of 37°C to 60°C. Drinking a sip of the 60°C does not cause damage to humans. It follows that the evenly absorbed energy of heat is obviously less harmful than the energy of X-rays which is delivered in small individual energy packets - the photons.

DNA - the primary target of radiation

The biological effect caused by photons and heavy ions is due to the potential of both irradiation types to ionize the molecules of a cell. These ionizations damage parts of the cell which can result in cell death, malfunctioning or genetic mutations. Since the deoxyribonucleic acid (DNA) is the carrier of the genetic information and associated with the just mentioned process, it is believed that the DNA is the main critical target in radiotherapy. Many experiments demonstrating that the chromosomal asymmetric exchange aberrations (dicentric, ring) are proportional to cell killing (Hall and Giaccia, 2006), support this thesis.

As schematically illustrated in figure 2.5, the DNA consist of a backbone made of sugar-phosphate groups. Attached to this backbone are four different bases adenine (A), cytosine (C), guanine (G) and thymine (T) which code the genetic information via their sequence. Figure 2.5 a) shows that damage to the DNA can be caused by direct and indirect action which may result in b) either single-strand or double-strand breaks. Double-strand breaks can be very complex so that the different repair mechanism of a cell can fail when trying to restore the original DNA coding sequence. The goal of radiotherapy is to induce severe damage to the tumor cells so that these repair mechanisms fail and the cell takes the controlled pathways of apoptosis or mitotic cell death[1].

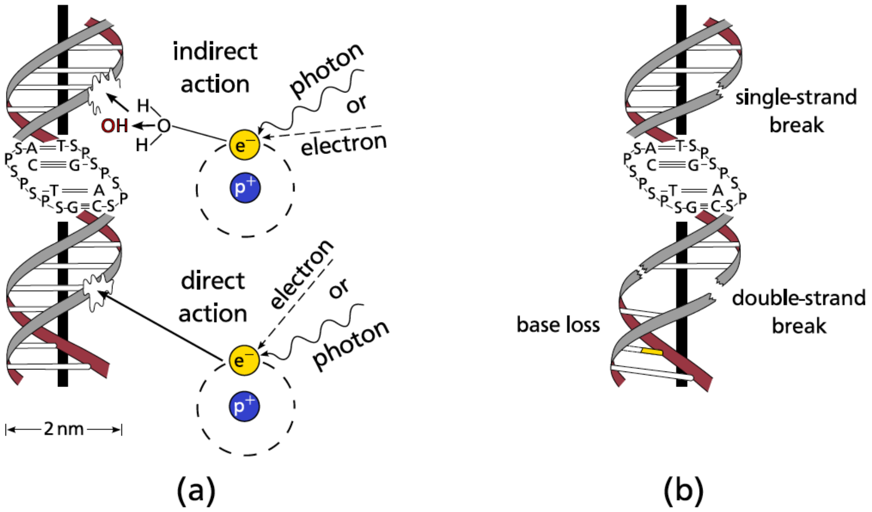

Figure 2.5.: (a) Direct and indirect radiation damage to the DNA. Direct damage is caused by energy deposition in direct hits from electrons liberated in ionization processes. Free hydroxyl radicals (OH), formed by ionization in the hydrolysis of water, can cause indirect damage to the DNA in chemical reactions. (b) Schematic illustration of selected types of radiation damage to the DNA. The effectiveness of the repair mechanisms of cells depends on the complexity of the damage (Richter, 2012).

The probability to induce complex lesions to the DNA increases with increasing local energy deposition. The associated measured quantity is the so called linear energy transfer (LET). It is defined as the energy locally deposited per length and typically given in keV/μm. Figure 2.6 shows the LET values for X-ray and carbon ion radiation. The LET of carbon ions is amongst others a function of the energy of the carbon ions. The greatest value is reached in the region around the Bragg-peak. It follows that carbon ions are much more efficient in causing complex lesions to the cell. The rational behind this is that a uniform dose distribution, as caused by the X-rays, can cause many simple lesions, as single-strand breaks, at different sites of the DNA (or the cell) but these are repaired very efficiently. For example, if the DNA is in a non replicative state, the repair of single-strand breaks lesions is in the order of one error per $10^7 - 10^{11}$ depending on the source of data (Alpen, 1998).

---

[1] Necrosis is another pathway of cell death. It is marked by an uncontrolled destruction of the cell which can cause unwanted reaction of the immune system like inflammation.

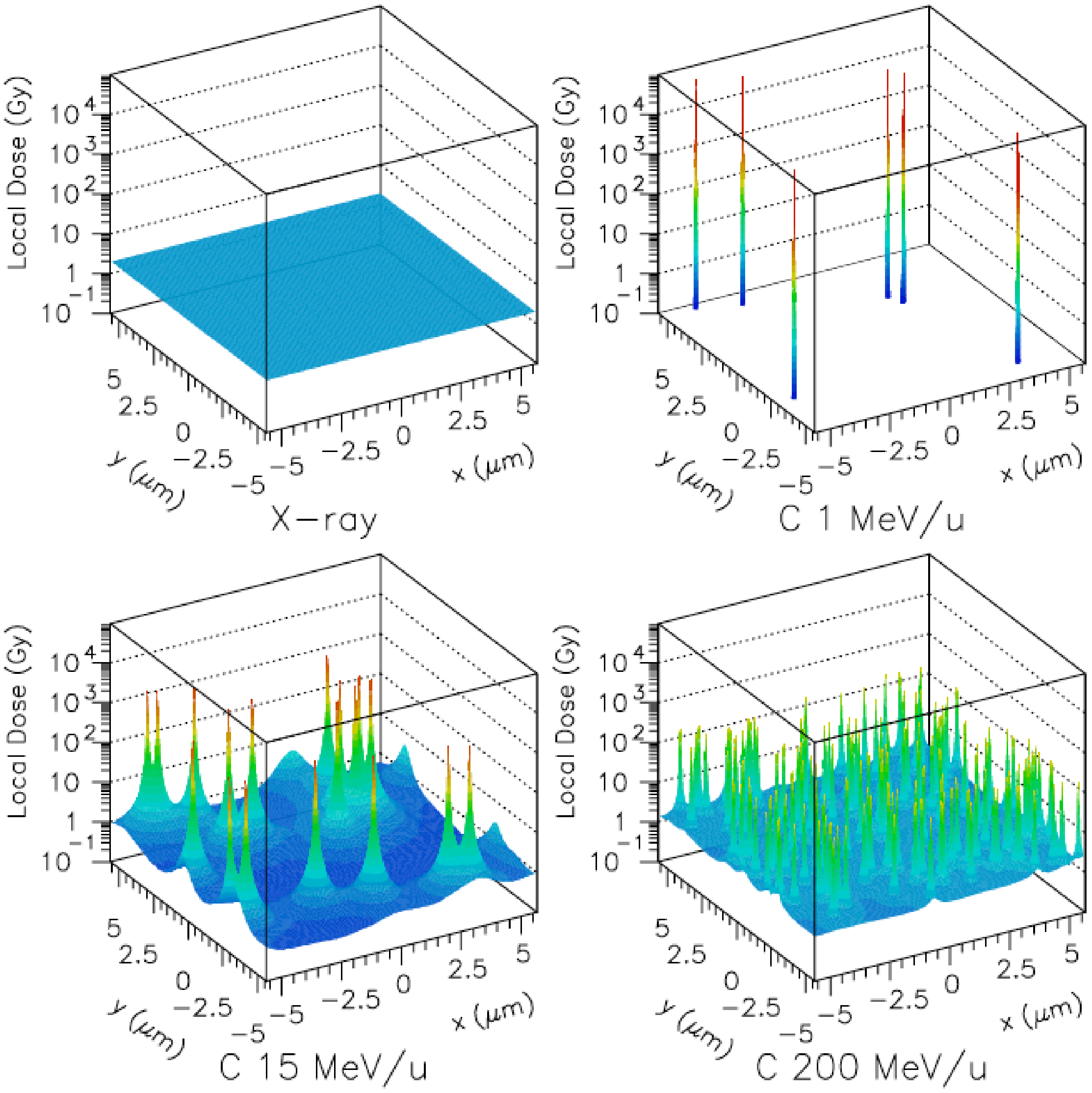

Figure 2.6.: Microscopic dose distribution for photons and carbon ions with different specific energies (Scholz, 2003). The local dose deposition of the X-rays is rather uniform. When the energy of a carbon ion decreases the local dose position is increased until the energy which corresponds to the Bragg-peak is reached.

The repair of complex double-strand lesions on the other hand is very error-prone. Therefore heavy ions are more efficient in causing cell death. This is accounted by the relative biological effectiveness (RBE):

$$\mathrm{RBE} = \left.\frac{D_{\gamma}^{\mathrm{ref}}}{D_{\mathrm{ion}}}\right|_{\text{iso-effect}} . \tag{2.6}$$

The RBE is defined as the ratio of a reference dose of X-rays $D_{\gamma}^{\mathrm{ref}}$ divided by the dose D_{ion} of ion irradiation that results in the same biological effect. It depends on many different parameters such as the biological end point, dose, particle type, and energy as well as the tissue under consideration. As a result, the RBE is different for every location in the treatment field. For particle therapy the RBE-weighted[2] dose is defined as the product of the RBE and the absorbed physical dose. It takes the higher efficacy of ions into account and is reported in units of Gy(RBE). It follows, that if a tissue is irradiated with a certain level of RBE-weighted dose than the same biological effect can be expected - independent of the used radiation type.

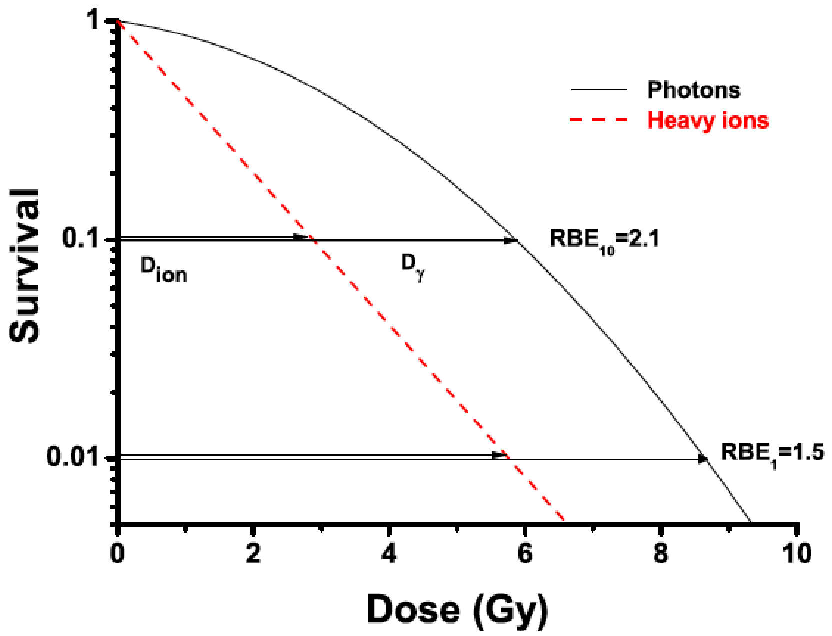

Figure 2.7.: Exemplary survival curve that compares heavy ion and photon radiation as a function of dose. Depending on the endpoint the RBE value changes. Figure from (Schardt et al., 2010).

---

[2] sometimes also called photon-equivalent or biological dose

Linear-quadratic and local effect model (LEM)

The cell survival curves S as a function of the dose D like shown in figure 2.7 are usually described by a linear quadratic model:

$$S(D) = \exp(-\alpha D - \beta D^2). \tag{2.7}$$

α and β are the linear-quadratic parameters which describe the model (Alpen, 1998). The ratio α/β is characteristic of the tissue type and the kind of radiation and is related to the repair capacities of the cells. A large α/β indicates a high radiation sensitivity. The linear part (αD) corresponds to cell damage caused by the traverse of a single event (e.g. one ion) and the quadric term (βD^2) caused by two independent events (e.g. two ions). For ion radiation the linear term is more dominant than in the case of photon irradiation. It follows that single events are the main cause of radiation damage when using heavy ions. The large variations of the RBE with respect to many parameters like the mixed radiation field, the energy, the kind of radiation or the tissue type facilitate the need for a biological model which predicts the RBE values across the treatment field in the dose optimization process (see section 2.2.2). The local effect model (LEM) was developed at GSI by Scholz et al. (Scholz and Kraft, 1994) to meet these demands. The basic assumptions are: 1) On the local level the radiation damage by sparsely ionizing photon radiation is the same as for ion radiation because both damages are transmitted via secondary electrons. 2) The cell nucleus is the sensitive target. 3) The effect of the heavy ion irradiation for a specific tissue can be predicted by knowing the X-ray cell inactivation dose-response curve along with the radial dose distribution of the heavy ions. It follows that the different biological response originates from the characteristic dose deposition pattern like displayed in figure 2.6. The quality of the LEM has increased over the years (Elsässer and Scholz, 2007) and validated in cell experiments (Elsässer et al., 2010; Gemmel et al., 2011) and is still extensively investigated at GSI (Friedrich et al., 2012). The LEM was used in clinical routine in the GSI pilot project (Krämer and Scholz, 2000) as well as it used currently at Heidelberg Ion-Beam Therapy Centre (HIT) since 2009.

Fractionation

Fractionation basically means splitting the planned dose of the tumor in n-parts and to irradiate the patient in each fraction with a dose of $d = D/n$ (Hall and Giaccia, 2006). Fractionation schemes can take as long as several weeks and its effects are commonly known as *the four Rs of radiobiology*: 1) Repair of sublethal damage. 2) Reassortment of cells within the cell cycle. 3) Repopulation. 4) Reoxygenation. The rational of fractionation is that e.g. tumors and healthy tissue have a different α/β ratio. Applying the dose in many fractions harms the tumor more severely than the healthy tissue. The biological effective dose (BED)

$$\frac{E}{\alpha} = (n\,d)\left(1 + \frac{d}{\alpha/\beta}\right), \tag{2.8}$$

with $E = \exp(-\alpha D - \beta D^2)$ being the biologic effect, is the quantity by which different fractionation regimes are intercompared. It follows that tissues with a different α/β ratio exhibit different sensitivity to various fractionation schemes. These can therefore be chosen as to stress the healthy volume less while almost having the same damage to the tumor. Since the α/β ratio of the affected healthy tissue and tumor can be different it follows that there is no ideal fractionation procedure that fits for all patients. In general the effect is much smaller in case of heavy ions compared to X-ray irradiation because the α/β ratio does not show the characteristic shoulder in the linear-quadric model - as can be seen in figure 2.7. But the additional sparing of the normal tissue is not so important in heavy ion therapy since the integral dose to the healthy tissue is anyway much smaller as by using X-rays like displayed in figure 2.1.

To summarize:

- The DNA is the primary target for radiation damage.
- The local dose deposition determines how efficiently the DNA is damaged. High local doses lead to more complex lesions which may not be repaired readily and can lead to cell death.
- Carbon ion irradiation causes more complex lesions to the DNA then X-rays.
- The effectiveness of the carbon ion radiation compared to X-rays can be described by the RBE which is complex function of tissue, projectile particle, biological endpoint, energy and the particle field.

2.1.3 Generation and application of ion beams

The required maximum penetration depth of about 30 cm in the human body corresponds to kinetic energies of protons and carbon ions of 200 and 430 MeV/u, respectively. Therefore, a broad range of energy has to be accessible[3]. Particle acceleration is typically realized using either cyclotron (Pedroni et al., 1995) or synchrotron (Haberer et al., 1993) (figure 2.8) accelerators.

Cyclotrons are smaller, less expensive and technically not so challenging as synchrotrons but the beam leaves the cyclotron with only one well defined energy so that passive beam shaping elements (see below) are necessary to receive the required energy range to irradiate the whole

---

[3] At GSI the energy spectrum is from 88.83 to 430.10 MeV/u for carbon ions.

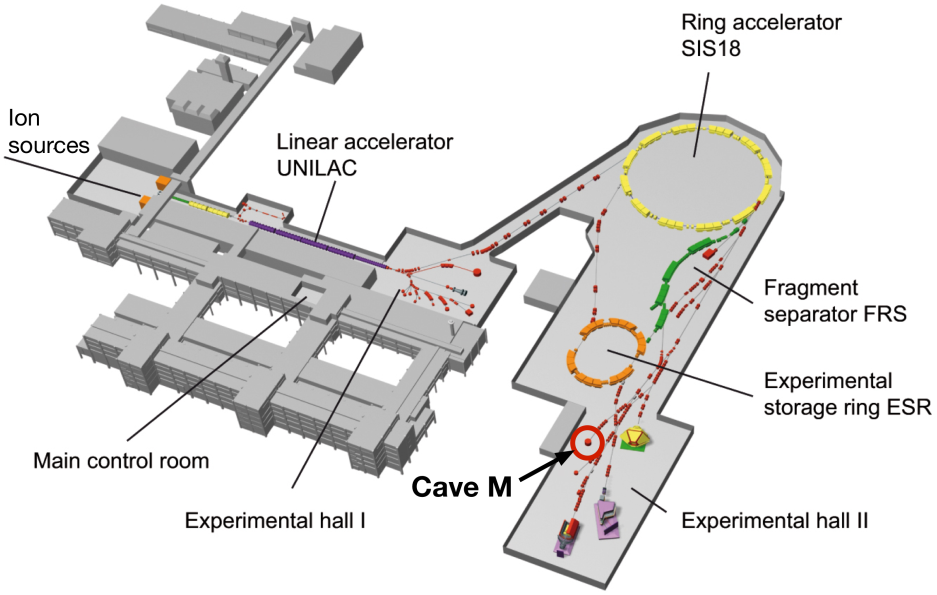

Figure 2.8.: Heavy ion acceleration at GSI. Starting from the ion sources, the beam is accelerated in the UNILAC and than injected into the ring accelerator SIS 18. If the beam has reached the desired energy it is extracted be electromagnetic impulses and enters the beam line which leads to Cave M, where the patient treatment was realized (figure from (GSI, 2013)).

tumor volume. Synchrotrons provide a very flexible pulse-to-pulse energy variation which allows using active beam shaping delivery (see below) allowing a better dose conformity to the target volume. The dynamics of the pulse delivery is in general different for each synchrotron. This includes the spill profile, the particle extraction time, the intensity levels and the time to accelerate the particles. The sophisticated synchrotron system is very expensive so that strong efforts are done to reduce the costs. New and promising accelerator techniques especially in the field of the particle acceleration via interaction of thin foils with high power lasers (Kraft et al., 2010; Weichsel et al., 2008) are currently investigated but it will certainly take some years until they can be implemented in a therapy system.

Passive beam delivery

In the early years of patient treatment with ions passive beam delivery was used (Koehler et al., 1975, 1977) because its technical demands are much less than using active beam scanning (see 2.1.3). Figure 2.9 gives an overview of this technique. A thin beam leaves the accelerator. Several beam shaping steps have to be done in order that the dose deposition of the beam matches the tumor. How the beam profile is influenced by these steps (in the middle row of the corresponding figure) can be seen in the upper and lower rows. 1) The beam is broadened using a scattering system. 2) Then the energy spectrum of the beam is broadened with a range modulator. 3) The maximum energy is adjusted using a range shifter. 4) Lateral and distal conformity are achieved by a collimator and a compensator. New compensator have to be designed and build in case of every patient treatment field.

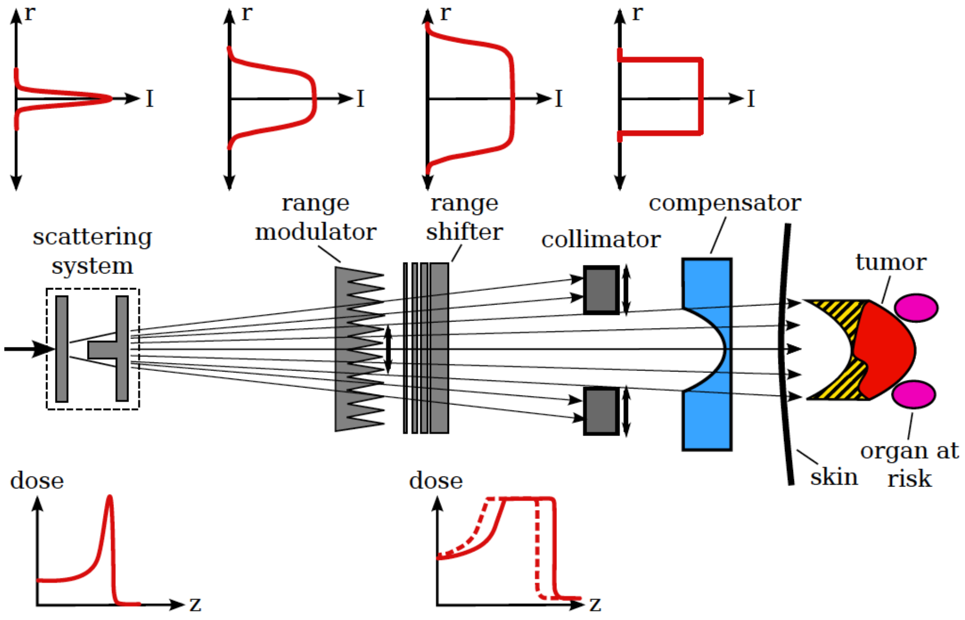

Figure 2.9.: Schematic overview of the passive beam delivery system. The beam size and the penetration depth is shaped by the devices in the middle row as to irradiate the target volume. The hatched area indicates the resulting inevitable irradiation of normal tissue. The degree of irradiation of normal tissue depends on the tumor shape. A target with a rectangle shape could be irradiated more conformal. Figure from (Richter, 2012).

It can be seen that the system has several drawbacks. Healthy tissue close to the proximal tumor regions inevitable receive the full treatment dose. The volume of healthy tissue that is irradiated largely depends on the tumor size. The interaction of the initial beam with the system leads to fragmentation and a greatly enhanced neutron dose, which leads to an irradiation of large parts of the patient's body, so that passive delivery beam systems are not the perfect solution when treating pediatric patients (Newhauser and Durante, 2011; Hall and Giaccia, 2006) whose sensitivity with respect to additional dose stress is higher than for adults. No active energy variation is needed for this technique so that cost-effective cyclotrons can be used.

Active beam delivery

The best conformity can be reached by using active beam scanning. The following introduction of active beam scanning describes the principle mechanisms used at GSI and HIT. The tumor is separated into iso-energy slices (IES) which essentially represent the water-equivalent path length (WEPL) of the particles having the same energy. The actual geometrical path length might be different in regions with different density (e.g. bone or normal tissue). Many slices are needed to cover the longitudinal dimension of the tumor. To reduce the number of these slices a 3 mm ripple filter is used at HIT and GSI (Weber and Kraft, 1999) which broadens the Bragg-peak. However, to obtain a homogenous dose distribution in the direction of the particles, the IESs need to be superimposed. This leads to the so called spread out Bragg peak (SOBP), which is depicted in figure 2.10.

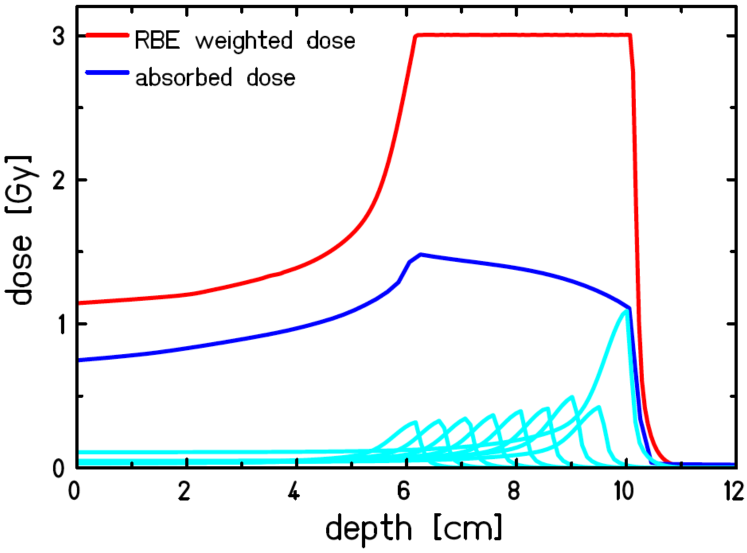

Figure 2.10.: shows the superposition of nine Bragg-Peaks which results in the SOBP. The most distal IES receives its dose essentially only from one IES whereas the most proximal IES is eight-times pre-irradiated until beam's particles have the energy that coresponds to its WEPL. Although the RBE weighted dose is very flat around the target, the corresponding absorbed (physical) dose is not flat. That is because the RBE is not constant throughout the SOBP but depends e.g. on the LET. Figure courtesy of Michael Scholz.

Each slice then contains of many so-called rasterpoints which represent the tumor's lateral dimension. The grid spacing of the rasterpoints is typically 2 mm and 3 mm, respectively. To ensure homogenous dose distribution the full width at half maximum (FWHM) of the beam is set to be at least three times larger than the grid spacing. The rasterpoints are being scanned according to a pre-optimized scan path (see figure 2.11). The beam's direction, intensity and energy are adjusted to irradiated each of these rasterpoints. The figure 2.12 provides an overview of the active beam scanning process. While the particle beam irradiates a certain rasterpoint, the beam monitor checks whether the actual measured values (e.g. position, intensity) correspond to the planned values. If the prescribed dose is reached a signal is sent which changes the current of the deflecting magnets so that the beam is directed to the next point. If on the other hand the therapy control unit (TCU) detects an deviation between the actual position of the pencil beam and the prescribed on then a signal is sent to the magnets in order to shift the beam the the prescribed position. In case of a failure or an error the extraction of the beam must be stopped by sending interlock signals within 1 ms at GSI. This is done by deactivating a fast quadrupol and a bending magnet in the beam line.

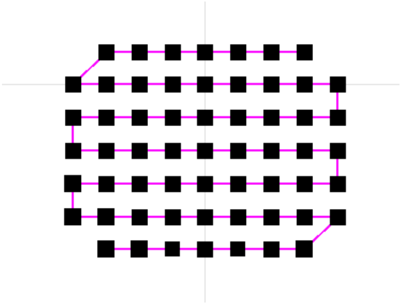

Figure 2.11.: IES from a real patient irradiated at GSI. The size of the black squares is equivalent to the prescribed number of particles to the rasterpoint. The typical grid spacing between the points is 2 mm and 3 mm, respectively. The purple line shows the scan path. If the irradiation of an IES is finished, the energy of the beam is changed and the same procedure starts again for the next IES.

The active scanning beam system at GSI and HIT is a little bit different from the technique used at Paul Scherer Institut (PSI). At PSI the spot scanning method is used (Pedroni et al., 1995). In this procedure the beam is switched of between two positions whereas the raster scanning at GSI and HIT works in continuous mode (Haberer et al., 1993), i.e., the beam is not switched off while the beam travels to the next position. Both approaches offer excellent sparing of healthy tissue when irradiating static tumors.

To summarize:

- Heavy ions are accelerated by linear accelerators, cyclotrons or synchrotrons.
- Active beam scanning systems provide the best tumor conformity.

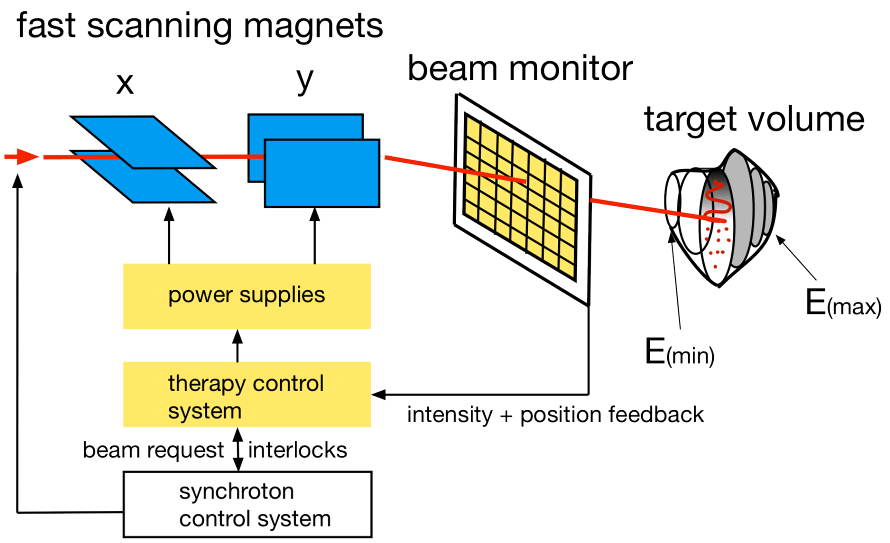

Figure 2.12.: Active beam delivery system. The therapy control system requests beams which correspond the IES of the tumor. Those energy levels generally differ for each patient. The treatment is performed slice-be-slice by moving the beam on a meander path. The heavy ion pencil beam is steered to each individual rasterpoint by changing the magnet field of the scanning magnets. The beam position and particle number is measured by a beam monitor system and fed back to the therapy control. Adapted from (Schardt et al., 2010).

2.2 Treatment of static tumors with heavy ions

Each patient needs a specific treatment. Treatment planning systems calculate these individual irradiation plans mainly according to the size and the location of the tumor. Other aspects which influence the calculation of these specific plans are e.g. the number of fractions or the position of OARs. All treatment planning systems, independent of irradiation with photons or heavy ions, aim to deliver an adequate dose to the tumor while sparing healthy tissue and especially OARs. According to recommendations of the ICRU, 100% of the target volume should receive between 95% and 107% of the prescribed dose (ICRU, 1993). Several steps are necessary to facilitate the optimization process which will be presented below.

2.2.1 Tumor imaging and delineation

"*If you can't see it, you can miss it*" (Schlegel, 2010) underlines the importance of precise imaging devices to delineate the tumor from its surroundings. In case of static tumors X-ray computed tomography (CT)s provide quantitative information about anatomical structures by recording photon attenuation images. This data is in the further planning process also used to determine the particle range and the deposited dose in the tissue. Typical pixel resolution is in the order of 1 mm. Magnetic resonance imaging (MRI) is often applied in combination with the CT to get a higher resolution of the anatomy (Schardt et al., 2010). This enhances the accuracy with which the physician is able to distinguish the subvolumes shown in figure 2.13 defined by the ICRU (ICRU, 1993) as

GTV "The Gross Tumor Volume (GTV) is the gross palpable or visible/demonstrable extent and location of the malignant growth."

CTV "The Clinical Target Volume (CTV) is a tissue volume that contains a GTV and/or subclinical microscopic malignant disease, which has to be eliminated. This volume thus has to be treated adequately in order to achieve the aim of therapy: cure or palliation." Concepts that deal with the size of the clinical target volume (CTV) can be found elsewhere (van Herk et al., 2000).

PTV "The Planning Target Volume (PTV) is a geometrical concept, and it is defined to select appropriate beam sizes and beam arrangements, taking into consideration the net effect of all the possible geometrical variations and inaccuracies in order to ensure that the prescribed dose is actually absorbed in the CTV."

OAR "Organs at risk (OAR) are normal tissue whose radiation sensitivity may significantly influence treatment planning and/or prescribed dose." (e.g. heart, brain stem, diaphragm)

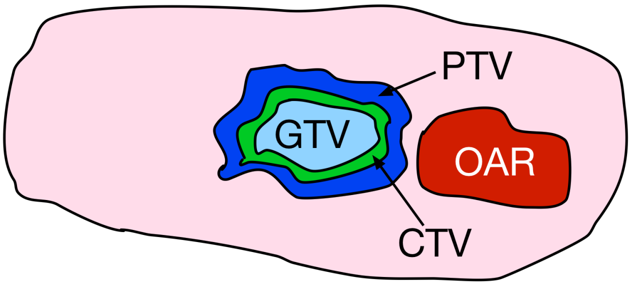

Figure 2.13.: Sub-volumes of a static tumor (e.g. in the head) described in 2.2.2 which are necessary to perform the treatment planning.

2.2.2 Treatment planning

After delineation, the dose treatment planning optimization calculation starts. Each of these processes must take the properties of the individual therapy system into account. At GSI the dedicated software tool TReatment planning for Particles (TRiP) was developed (Krämer and Scholz, 2000). First a grid is set up which covers the lateral (by creating planes with raster-points) and depth dimensions of the tumor (by selecting the energy range). The number of degrees of freedom in heavy ion therapy is much greater than in photon therapy, since each rasterpoint can be irradiated with a different particle number. A typical single treatment field may comprise as many as 50 000 individual beam spots. Then the optimization can be formulated as a least-squares minimization problem (in simplified form)

$$\begin{aligned} \chi^2 = \sum_{\mathbf{x}_{target}} (D_P(\mathbf{x}) - D_A(\mathbf{x}))^2 \\ + \sum_{\mathbf{x}_{OAR}} (D_P(\mathbf{x}) - D_A(\mathbf{x}))^2 \times \theta(D_A(\mathbf{x}) - D_{OAR}(\mathbf{x})) \\ = min \end{aligned}$$

with $D_P(\mathbf{x})$ as the planned dose at the point $\mathbf{x}$, $D_A(\mathbf{x})$ is the actual calculated dose distribution and $D_{OAR}(\mathbf{x})$ is the maximum allowed RBE-weighted dose in the OAR. θ denotes the Heaviside function. Its purpose is to impose a penalty if $D_{OAR}(\mathbf{x})$ is exceeded, but to do nothing if the actual dose is below that limit (Krämer and Durante, 2010). Biological effects due to the LEM are also incorporated in the optimization process according to

$$D_{bio}(\mathbf{x}) = D_A(\mathbf{x}) \times RBE(\mathbf{x}),$$

with $D_{bio}(\mathbf{x})$ being the RBE-weighted (or biological) dose. The RBE is a complex function of the LET and the mixed radiation field (Krämer et al., 2000). An example of the optimized dose distribution with TRiP was already shown in figure 2.1.

2.3 Treatment of moving tumors with heavy ions

2.3.1 Tumor motion

Tumors can change their position relative to the coordinate system of the treatment room in general due to the following reasons:

Patient motion: Motion of the patient itself by e.g. unintended movement of the head or other parts of the body or stress versus relaxation of muscles during the treatment[4]. These motions can usually be suppressed (e.g. by mechanical fixation of the patient's head like done in the pilot project at GSI).

Inter-fractional motion: Motion in-between two fractions. These kind of motion effect is negligible within one fraction. The time-scale of inter-fractional motion ranges between hours

---

[4] Sometimes patient are afraid when irradiations starts but relax after some time because they cannot feel any pain from the interaction of the ions.

and days. Internal anatomical position can change due to different filling of the bladder or rectum or because of regression of the tumor volume during the radiation course (Britton et al., 2007).

Intra-fractional motion: Motion within one fraction. The movement is mainly caused by respiration which affects tumors located in the thorax and the abdomen. The time-scale of the motion is therefore linked to the breathing period of the patient. Lung tumors and tumors close to the diaphragm are effected by this kind of motion. The motion traces of lung tumors have been observed by many researches. Liu et al. (Liu et al., 2007) report that lung tumor motion is most prominent in the superior-inferior (SI) direction. The proportions of tumors that moved more than 0.5 cm along the SI, lateral, and anterior-posterior (AP) axes during normal breathing were 39%, 2%, and 5%, respectively. Only 11% of the tumors moved more than 1 cm. Sonke et al. (Sonke and Belderbos, 2010) report that respiratory motion greater than 2 cm has been observed for tumors located close to the diaphragm and occasionally in other positions, but are generally smaller than 1 cm. Shirato et al. (Shirato et al., 2004) observed a hysteresis in the relationship between pressure and lung volume; the lung volume is different between inspiration and expiration at the same pressure. In the same individual, the tidal volume and frequency can change with the biochemical condition, body position, abdominal contents and emotional condition (anxiety). The medians of the mean amplitude in tidal respiration were 1.0 (range, 0.2 - 2.8) mm, 2.8 (0.2 - 24.6) mm, and 1.5 (0.2 - 8.2) mm for left-right (LR), cranial-caudal (CC), and anterior-posterior (AP) directions, respectively. No correlation has been reported between the amplitude of tumor respiratory movements and patient characteristics such as weight, height, age and pulmonary function in a small series of data acquisition from patients. At rest, a healthy person breathes 12 to 15 times per minute. Shirato et al. (Shirato et al., 2004) report that the average length of 1 breathing cycle was 3.6 ± 0.8 seconds. The breathing cycle fits well with equation

$$z(t) = z_0 - b\cos^{2n}(\frac{\pi t}{\tau} - \phi), \tag{2.9}$$

where z_0 is the position at exhale, b the extent of motion, τ the breathing period, ϕ the starting phase and n a general parameter which describes the shape of the model. 43 % of their patients yielded the best results of the fitting curve with $n = 1$ and for 38% with $n = 2$ of these lung tumors, respectively. Lujan et al. (Lujan et al., 1999) showed that equation 2.9 describes tumor motion much better than pure sinusoidal motion because it takes into account that the tumor generally stays longer in the exhale than in the inhale phase.

In the following, this work deals only with effects and challenges of **intra-fractional motion** since this type currently inhibits the treatment of e.g. lung tumors with heavy ions when using active scanning systems as will be described in more detail below.

2.3.2 A moving tumor - challenges in dose application, imaging, motion monitoring and delineation

The motion of the tumor introduces several difficulties as well in the planning and the beam application process which will be introduced in the following. The severity of these effects is so large that no satisfying homogenous dose distribution can be delivered to moving lung tumors so far.

Interplay effect

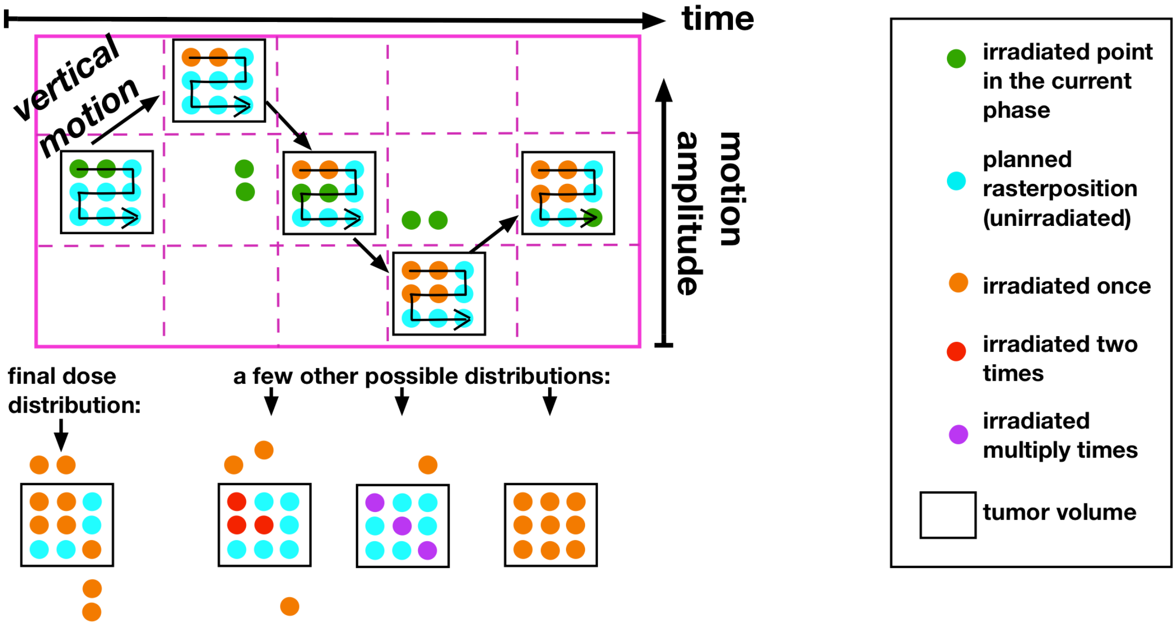

Figure 2.14.: Interference of dose application and tumor motion can cause severe dose distortion. This schematic shows a target which moves crosses in a vertical motion three different motion phases. The points symbolize the rasterpoints and the scanpath is indicated by the arrows. The middle phase is the planning and treatment phase. If the tumor rests in this phase the final dose distribution would agree with the planned one. Due to the tumor motion, the actual irradiated points do often not agree with the planned ones. Therefore, the interplay effect can cause inhomogeneities in the final dose distributions (cold and hot spots). In addition, it might happen that the normal tissue also receives radiation exposure.

Figure 2.14 shows the so called interplay effect which is especially severe when using active scanning systems. Due to the interaction of the tumor motion and the beam application interference patterns are likely to arise in the dose distribution which are so large that successful treatment of e.g. lung tumors is not possible by using the planning target volume (PTV) concept above which is clinically used, e.g. for treatments with photons or passive particle beam systems (Phillips et al., 1992; Jiang et al., 2003; Bert et al., 2008b). Intra-fractional motion is especially challenging when the dynamics of the beam delivery system is on the same time scale as the tumor motion.

Figure 2.14 displays that simply increasing the area of irradiation, so that it encompasses the whole motion contour, would not reduce the interplay effect, because the interference effects will still be present. Methods to eliminate these obstacles will be presented in the sections 2.3.5, 2.3.4 and 2.3.6.

Tumor imaging and delineation

In addition to the subvolumes gross tumor volume (GTV), CTV and PTV, which have been already introduced in section 2.2.1, the motion requires the definition of another sub volume which takes the motion into account. The so-called internal margin (IM) and internal target volume (ITV) are illustrated in figure 2.15 and defined as follows (ICRU, 1999):

IM "The Internal Margin, commonly asymmetric around the CTV, is intended to compensate for all movements and all variations in site, size and shape of the organs and tissues contained or adjacent to the CTV. They may result, e.g., from respiration, different fillings of the bladder, different fillings of the rectum, swallowing, heart beat, movements of the bowel."

ITV The term ITV is commonly used to describe the volume encompassing CTV and IM.

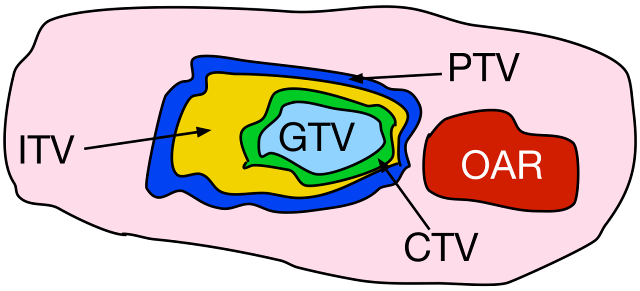

Figure 2.15.: Sub-volumes which are necessary to perform the treatment planning in case of a moving tumor. This example shows a snapshot of the position of the tumor. It is either in ex- or inhale position and will move to the left within the contour of the ITV.

The imaging process usually covers at least a whole motion period as to see the total size of the tumor movement. Dedicated time resolved computed tomography (4DCT) methods had to be developed (Ford et al., 2002; Rietzel et al., 2005). The CT is then subdivided into several phases and a CTV is contoured in each of these phases. The geometrical union of these individual CTVs compromises the ITV. Like shown in figure 2.15, the ITV is subsequently extended to the PTV which accounts for additional uncertainties. This geometrical union is sufficient in photon therapy to account for the motion extent when calculating the PTV. To clarify, this geometrical union does not reduce interplay effects either in IMRT (Bortfeld et al., 2002) and IMPT. In contrast to photons, heavy ions exhibit large variations in the particle range when transversing materials of different densities like shown in figure 2.16.

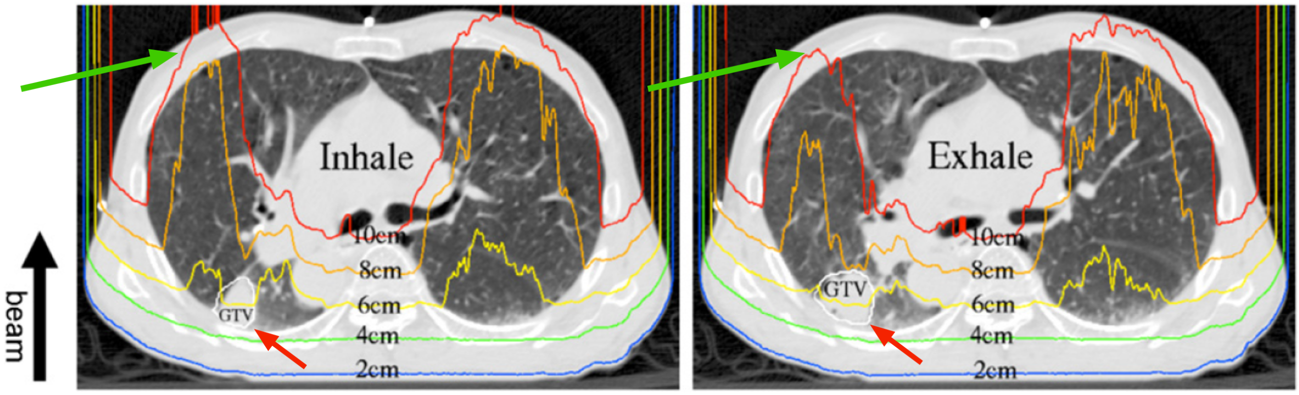

Figure 2.16.: Changes in the radiological path length induced by lung tumor motion are indicated by iso-range lines for posterior-anterior incidence of the ion beam. The motion changes the relative positions of the body's anatomy. The green arrow shows e.g. the change of the 10 cm iso-range line when the tumor moves from the exhale to the inhale position. The location of the tumor is indicated by the red arrows. The induced range changes can lead to underdosage of the tumor if e.g. a rib moves in and out the radiologic path or to additional dosage to the normal tissue. Adapted from Bert et al. (Bert and Durante, 2011).

A new way of creating an ITV which covers all the motion induced radiological path changes had to be found in order that the target always receives its prescribed dose independent of its motion phase. Graeff et al. (Graeff et al., 2012) implemented such a method at GSI which fulfills this criteria. The ITV is created as a union of all CT motion phases which take the changes of the WEPL into account (ICRU, 2007). Therefore it accounts for lateral and longitudinal motion related expansion of the radiated volume. If beam delivery is performed in the passive mode, the interplay effect does not occur and homogeneous dose delivery to the tumor volume is achievable by the irradiation of an ITV according to (Graeff et al., 2012). The term ITV is in the following always meant to be an ITV in the flavor of Graeff et al. (Graeff et al., 2012).

Motion monitoring

Some techniques which (sections 2.3.5 and 2.3.4) shall enable irradiation in the face of tumor motion require the information about its spatiotemporal position during treatment delivery. An overview of those imaging techniques is given by Evans et al. (Evans, 2008). Direct tumor positions can be obtained by e.g. fluoroscopy (Kilby et al., 2010) or electromagnetic transponders or markers (Mendenhall et al., 2012) implanted in or nearby the tumor. The implantation of markers and transponders is always a risk to the patient as well as the additional dose due to the imaging by the fluoroscopy. The amount of the additional dose exposure depends and the chosen sampling rate and on the system in use. The more images are taken during treatment the better is the knowledge of the tumor's spatiotemporal position and the higher is the unwanted radiation exposure to the patient. To reduce the additional dose, methods and models have been developed which describe and predict the position of the tumor relative to so-called surrogate signals. This includes camera systems (Riboldi et al., 2012) or pressure belts measuring the deformation of the thorax due to breathing (Steidl et al., 2012a; Korreman, 2012). The position of the tumor is then predicted by measuring the surrogate signals and inserting this information into a model which describes the external and internal motion correlation. Ionascu et al. (Ionascu et al., 2007) report good internal-external correlation along the superior-inferior direction with small or no internal external time shifts and amplitude mismatches. Along the anterior-posterior direction, they found relatively large time shifts and amplitude mismatches.

2.3.3 Treatment planning and dose calculation

The optimization of the beam plan parameters has already been described in case of a static tumor in section 2.2.2. In the scope of this thesis the treatment planning in case of a moving target basically includes the usage of the ITV according to Graeff et al. (Graeff et al., 2012) which accounts for the motion related extension of the PTV.

D. Richter (Richter, 2012) reports in detail on the implementation of a 4D functionality into TRiP in order to perform dose calculations. These methods have to temporally correlate the delivery of each single pencil beam position with the motion of the target as described by motion trajectory and 4DCT as shown in figure 2.17. Input data are the motion trace of the target and the so called physical-beam-record (PBR) file. A PBR[5] file can in principle be generated by a dedicated simulation tool (see chapter 3) or by measurement. The former case is used when doing forward dose simulations and the latter when doing dose reconstruction. A PBR contains the information which rasterpoint of the tumor was irradiated along with the measured particle number and the time stamp when irradiation was finished. Validation of the used models and

---

[5] The PBR files at HIT and GSI are slightly different. At HIT the time stamp can only be obtained by including the information of a so called machine beam record (MBR) file.

algorithms, with biological as well as physical measurements, have been performed in numerous experiments (Bert et al., 2010; Gemmel et al., 2011; Richter, 2012). After the successful implementation of 4D dose calculation in TRiP it was possible to tackle motion mitigation techniques as well in simulations and experiments.

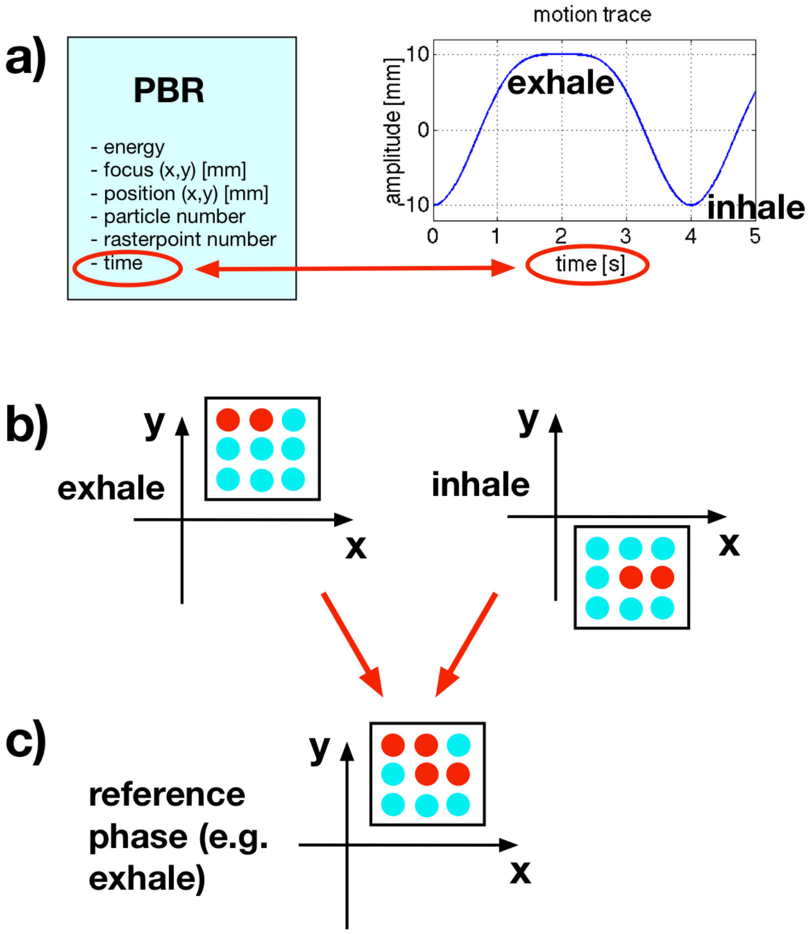

Figure 2.17.: a) PBR files contains the information when a certain rasterpoint has been irradiated. The mutual time stamp of the motion trace and the PBR file enables TRiP to know in which motion phase the point was irradiated, as seen in b). Those different sub-treatment plans are then merged into the reference phase as shown in c) so that the 4D dose calculation can be performed.

2.3.4 Motion mitigation by *gating*

Figure 2.18 illustrates the concepts of the *gating* techniques. Motion monitoring is mandatory to get spatiotemporal information of the tumor. The irradiation is only performed in a selected part of the breathing cycle. Usually this part is the more stable exhale position or it can be selected in order to irradiate the tumor at a great distance away from the OAR (see 2.15). If the tumor is within that amplitude region, which is named the *gating* window (see figure 2.18

a) and (Minohara et al., 2000)), a *gate signal* is sent which permits irradiation of the tumor (see figure 2.18 b)). If the beam is available in this period, the particles are extracted and the tumor is irradiated (see figure 2.18 b)-c)). The main reason for reducing the interplay effect is the reduction of the motion amplitude (the *gating* window) while irradiating the tumor. The drawback of this method is that the folding of the *gate signal* with the duty cycle of the synchrotron which results on prolongation of the treatment time (see figure 2.18 d)). The smaller the gating window the more homogeneous is the dose distribution but the longer the treatment time. Therefore the selection of the size of the *gating* window is always a compromise between clinical and economical factors. Nevertheless, some residual motion will still be present within the *gating* window which will still cause minor interplay effects, that can be further reduced by combining *gating* with the *re-scanning* (see (Furukawa et al., 2007) and section 2.3.6) technique. *Gating* can be used with active as well as with passive beam scanning systems and is already implemented at a few therapy centers (Iwata et al., 2010; Minohara et al., 2000). P. Steidl reports about the implementation of *gating* at HIT (Steidl, 2011).

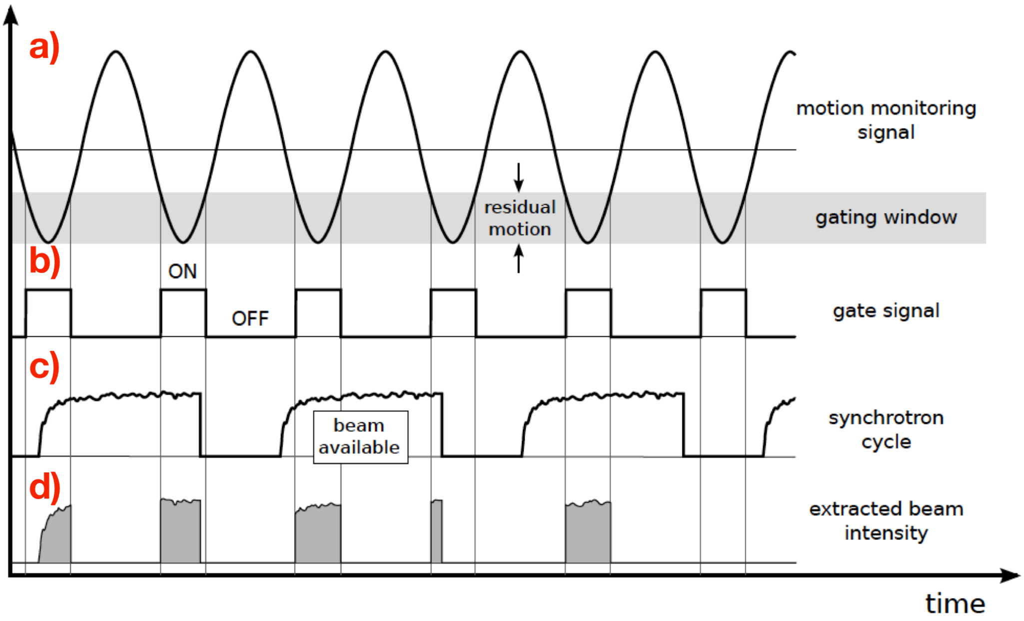

Figure 2.18.: illustrates the principles of the *gating* method. The scanning beam is only extracted if the tumor is within a well defined part of the breathing cycle. This reduces interplay effects but prolongates treatment time. Figure from (Richter, 2012).

2.3.5 Motion mitigation by *beam tracking*

Beam tracking was first proposed for photon IMRT (Keall et al., 2001) and is e.g. currently clinical used in X-ray surgery in the Cyberknife synchrony system (Kilby et al., 2010). The clinical usage of *beam tracking* in heavy ion therapy is likely to take a few more years since it is the technically most challenging motion mitigation technique.

The **ideal** *beam tracking* system *knows* the exact position of the target during the whole treatment course and adapts the beam application accordingly. Assuming the rasterpoint be irradiated next is named n_i. The system would adjust the energy and the magnets in a way that the pencil beam can follow n_i precisely as to irradiated it like the tumor was static. Healthy tissue could be spared to the same level as in the static irradiation.

The **real** *beam tracking* system however never *knows* the position of n_i exactly and cannot adapt the beam plan parameters instantly. Continuous fluoroscopy, to get the tumor's potion, would lead to unacceptable dose exposure of the patient and substitute internal-external correlation methods always introduce some uncertainties. By adapting the beam parameters to the motion, the system needs to estimate where the target will be a few moments later. If e.g. the patient starts coughing in between regular fluoroscopy checks (which are necessary to adapt and confirm the model) the internal-external correlation will be lost and the pencil beam will deposit its whole dose at the wrong place. The magnets cannot follow n_i without a small time shift and the adaption of energy also takes some time and includes the implementation of additional range shifters into the beam line (Saito et al., 2009). Experiments demonstrating the precision of an ion-*beam tracking* system have been performed at GSI (Bert et al., 2010) and shows that regular motion with a homogeneous phantom can be compensated. Due to rotation of the tumor or a beam which transfers the tumor with a different angle due to translational motion, the pre-irradiated dose distribution changes which has to be adapted online which is a very challenging task as described in (Luchtenborg et al., 2011).

Van de Water et a. (van de Water et al., 2009) simulated *beam tracking* with active proton scanning. For their most realistic case of a heterogenous target and positional error they found that *beam tracking* can even have negative influence on the dose homogeneity and that the *re-scanning* (see section 2.3.6) technique performed best. To reduce the impact of positional errors and uncertainties of other kinds *beam tracking* can be combined with *re-scanning* to the so-called *re-tracking* technique.

2.3.6 Motion mitigation by *re-scanning*

Re-scanning was first proposed by Phillips et al. (Phillips et al., 1992) to reduce interplay effects in active proton scanning in the presence of motion. The basic assumption is that interplay patterns (see figure 2.14) of the same IES very likely differ from each other due to a different starting phase, different intensity or different motion trace characteristics. If many of these interplay patterns are merged, it is very likely that the overdose a rasterpoint has received in one scan is compensated by underdosage of the very same rasterpoint in another scan so that the resulting dose distribution gets more homogeneous. Therefore, if a slice shall be *re-scanned* r-times, the dose per *re-scan* run is reduced to $D_r = {}^{D_0}/_{r}$, with D_0 being the original prescribed dose and r the number of *re-scans*.

Figure 2.19 displays how *re-scanning* can, in the **ideal** case, compensate motion effects.

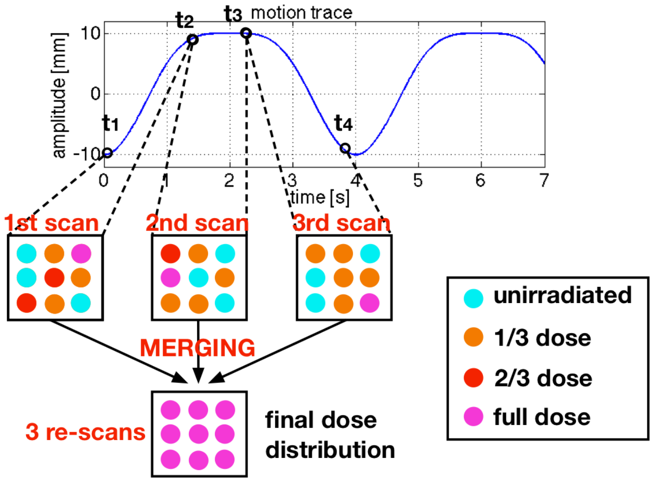

Figure 2.19.: The irradiation is planned to be performed with a *re-scan* number e.g. of $r = 3$. Therefore $D_r = 1/3 \cdot D_0$ which is symbolized by the orange circles. The 1st scan starts at t_1 and ends at t_2 - the interplay pattern emerges like sheen in figure 2.14. The 2nd scan starts at t_2 - the target is therefore in another motion phase, so that the interplay pattern looks different (the same is true for the 3rd scan). In the **ideal** case the merging of these three different interplay patterns results in a homogenous final dose distribution.

In reality it is a priori not known at which *re-scan* number the final dose distribution has converged close enough to the homogeneity values of the static irradiation as to treat patients. Dedicated measurements and simulations have to be performed with as realistic conditions as possible. The effectiveness of *re-scanning* to reduce interplay patterns can depend i.a. on the following multiple parameters (Zenklusen et al., 2010; Mori et al., 2013; Knopf et al., 2011; Furukawa et al., 2007; Bortfeld et al., 2002; Bert and Durante, 2011):

Patient specific parameters: Breathing period, amplitude of motion, target volume and target motion direction.

Beam application specific parameters: *Re-scanning* method and *re-scan* number, time to change the particle's energy, scanning speed and scanning direction, applied dosage, dose gradients in the treatment field, field direction and number of fields.

The averaging effect of *re-scanning* is addressed in Bortfeld et al. (Bortfeld et al., 2002). Under the condition that the beam application and the motion are not correlated they tackled the dose variance of a rasterpoint by statistical means. They report that the probability density function (PDF) of the dose variation of a voxel turns into a Gaussian shape centered around the expected value after approximately five *fractions* (see section 2.1.2) due to the central limit theorem. In terms of physical dose the effect of $f = n$ fractions is very similar to $r = n$ *re-scans*. The FWHM of the Gaussian shape PDF gets efficiently smaller due to the averaging effect by increasing the number of *fractions*, but the width depends strongly on the delivery technique and has to be investigated individually with the properties of the individual system. They also report, that additional *re-scanning* in each fraction which takes approximately as long as the breathing cycle is especially well suited to reduce the dose variance which also reported by Furukawa et al. (Furukawa et al., 2007).

The ITV generated for *re-scanning* irradiation is larger than the ITVs when using *beam tracking* or *gating* because it has to cover all motion phases. On the other hand, *re-scanning* does not need additional radiation exposure during the treatment to determine the trajectory of the tumor. It follows that *re-scanning* is best suited for small motion amplitudes of tumors which are not located too close to OAR. A great advantage of *re-scanning* is that it can also be combined with *gating* and with *beam tracking* as improve their outcome.

Re-scanning exists in different flavors with different demands on hardware and and treatment planning. The methods also differ with respect to their effectiveness to reduce interplay pattern. Some of the most prominent variations will be presented in the following. In principle many more types are imaginable and will be presented in chapter 3.

Slice-by-slice re-scanning

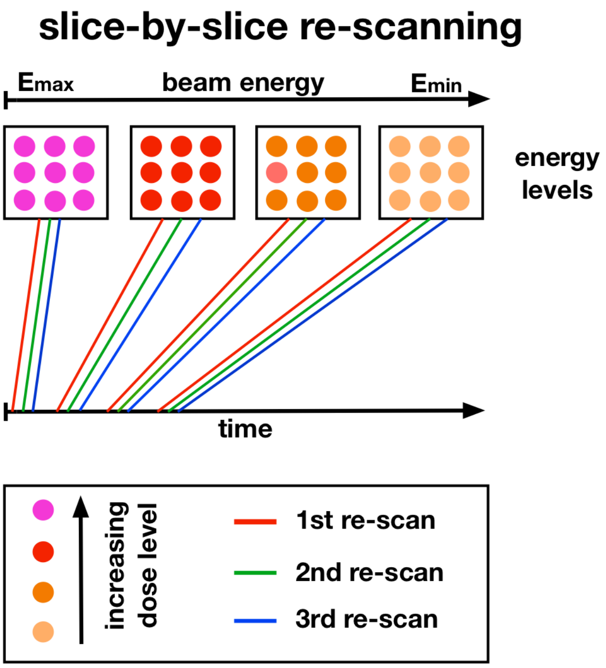

Figure 2.20.: Illustration of the *slice-by-slice re-scanning* mode. Figure adapted from (Seco et al., 2009).

The schematic drawing of the *slice-by-slice re-scanning* mode can be seen in figure 2.20. In the *slice-by-slice re-scanning* (in graphics often abbreviated as *slice*) mode, with $r = n$, the pencil beam sweeps in the first *re-scan* run in normal sequence over the rasterpoints. The second *re-scan* run starts when the pencil beam arrives at the last point of the IES, then the scanning direction is reversed and the beam travels back to the starting point. This procedure is repeated n-times so that the actual IES nominally receives its total prescribes dose. Subsequently the energy is decreased and the identical process starts with the next IES until the whole volume is irradiated. This method generates the fewest energy changes and often uses the maximal possible spill intensity. At GSI and at HIT treatment time in *slice-by-slice re-scanning* mode is in general as short as in the standard delivery mode used for patients.

Volumetric re-scanning

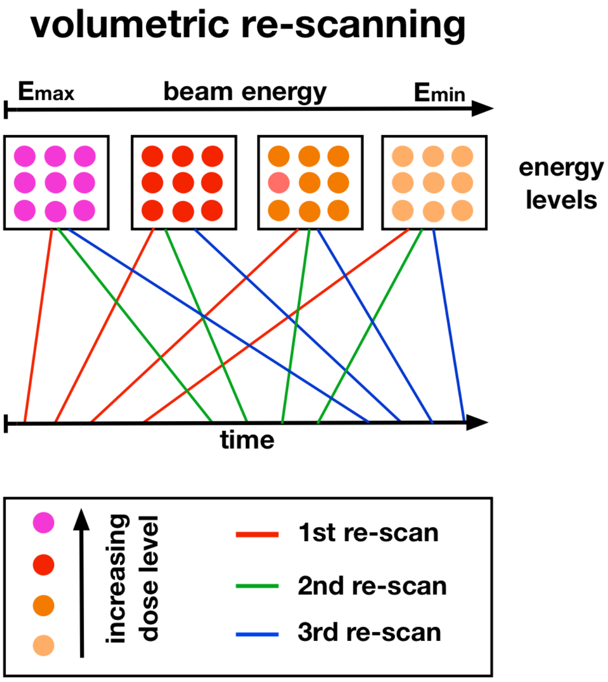

Figure 2.21.: Illustration of the *volumetric re-scanning* mode. Figure adapted from (Seco et al., 2009).

The schematic drawing of the *volumetric re-scanning* mode can be seen in figure 2.21. In the *volumetric re-scanning* (in graphics often abbreviated as *vol*) mode, with $r = n$, the pencil beam scans subsequently all IES with $1/n$ of their prescribed doses by decreasing the energy after each run. If the whole volume is scanned the precess is repeated $n - 1$ times until the the volume is nominally irradiated with its prescribed dose. In general this mode prolongs the treatment time compared to *slice-by-slice re-scanning* because the method creates the maximum number of energy chances. At GSI it takes 3.3 s to change the energy of the pencil beam.

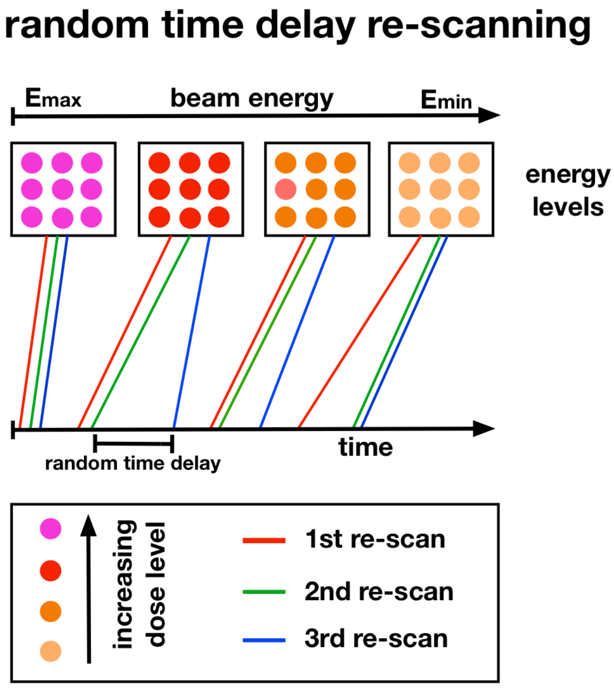

Figure 2.22.: Illustration of the *random-time-delay re-scanning* mode. Figure adapted from (Seco et al., 2009).

Random-time-delay re-scanning

The schematic drawing of the *random-time-delay re-scanning* (in graphics often abbreviated as *random*) mode can be seen in figure 2.22. The sequence of the *random-time-delay re-scanning* mode is identical to the one of the *slice-by-slice re-scanning* mode. The difference is that a random pause is added if a *re-scan* run is finished. The motivation is the reduce synchronity effects (Rietzel and Bert, 2010) between motion and beam application. Interplay patterns will look very similar if the tumor is almost in the same motion phase each time a *re-scan* run starts (which is called the synchronity effect). Therefore the averaging effect might be greatly reduced when a IES is merged after the irradiation like shown in figure 2.19. The likelihood that the irradiation always starts in the same phase decreases by adding the random pause after each *re-scan* run. As a consequence the treatment time is prolonged compared to *slice-by-slice re-scanning*.

Breath-sampled re-scanning

The schematic drawing of the *breath-sampled re-scanning* (in graphics often abbreviated as *BS*) mode can be seen in figure 2.23. The sequence of the *breath-sampled re-scanning* mode with $r = n$ *re-scans* is identical to the one of the *slice-by-slice re-scanning* mode. Prior to the treatment the breathing period of the patient is measured (e.g. with the help of VisionRT system (Vision

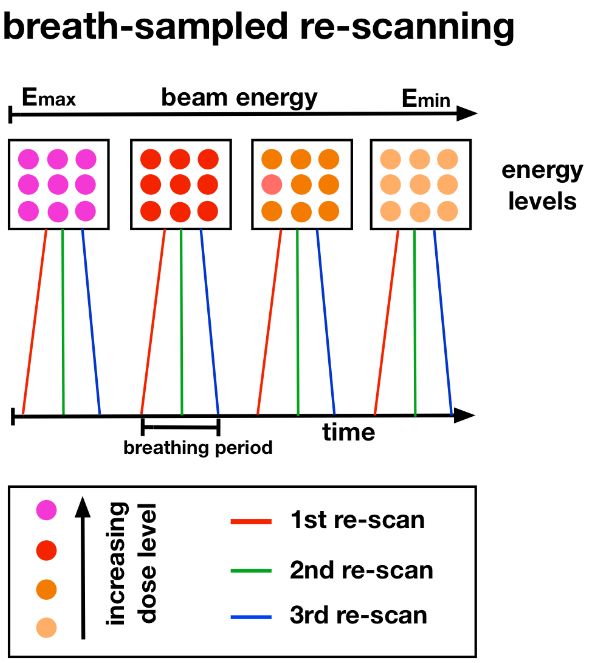

Figure 2.23.: Illustration of the *breath-sampled re-scanning* mode. Figure adapted from (Seco et al., 2009).

RT Ltd, London, UK) or the Anzai belt (Anzai Medical Co., Ltd, Tokyo, Japan)). For every IES, the intensity of the spill is adjusted in order to match the *n re-scans* as good as possible with the breathing period of the patient. *Slice-by-slice re-scanning* often finishes the beam application of a IES, with the currently existing systems, in a fraction of the breathing period[6]. It follows that very often not all motion states of the tumor receive dose application in the *slice-by-slice re-scanning* mode. In *breath-sampled re-scanning* mode however all motion states receive dose. *Breath-sampled re-scanning* is technically more challenging than the other methods presented above, since a reliable and precise intensity control of the beam is mandatory in addition to the dedicated treatment planning. The treatment time is generally a little bit longer than in the *slice-by-slice re-scanning* mode, because the pencil beam speed is greatly reduced in the proximal IESs. It will be shown in chapter 4 that this fact has positive influence with respect to dosimetry.

Furukawa et al. (Furukawa et al., 2007) also show that *breath-sampled re-scanning* strongly reduces synchronity effects between motion and beam application so that the averaging effect works more efficiently. Initial measurement and simulation show (Furukawa et al., 2007; Seco et al., 2009) that *breath-sampled re-scanning* seems to be one of the most promising *re-scanning* techniques.

---

[6] This depends not only on the systems's intensity, but also on the tumor volume and the location of the IES. Distal IES generally take longer to irradiate.

Iso-layered *re-scanning*

The schematic drawing of the *iso-layered re-scanning* mode can be seen in figure 2.24. *Iso-layered re-scanning* limits the dose application per rasterpoint by a maximal value for each *re-scan* run (Zenklusen et al., 2010). This means that points with higher prescribed dose is *re-scanned* more often which is a sensible choice because its weight to the overall total dose delivery is large. The pencil beam is forced to sweep much faster over the target area in *slice-by-slice re-scanning* mode so that *iso-layered re-scanning* is technically less challenging for the system. However, the beam path needs to be optimized many more times. Figure 2.24 b) illustrates that the rasterpoints in the middle of the IES are only *re-scanned* two times and are singled out in the third *re-scan* run. As a consequence, often scan paths will be created with too large distances from one rasterpoint to the next in case of the raster scanning approach used at GSI and HIT. On the other hand, the spot scanning system of PSI is well suited for this task.

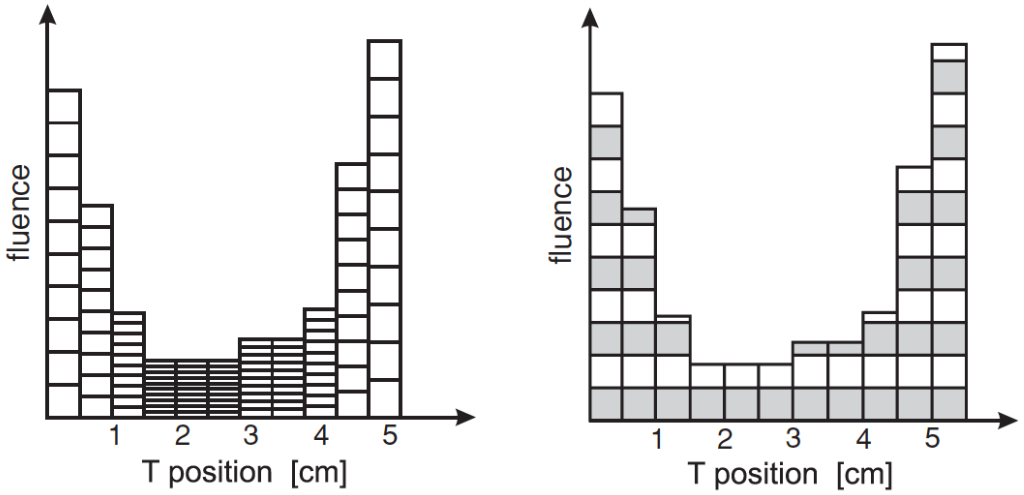

Figure 2.24.: Left picture: illustration of the *slice-by-slice re-scanning* mode when irradiating an inhomogeneous IES. Right picture: illustration of the *iso-layered re-scanning* mode when irradiating an inhomogeneous IES. Figure from (Zenklusen et al., 2010).

To summarize:

- Moving (lung) tumors are very likely to ruin the outcome of a treatment for a active beam scanning system because some parts of the tumor are likely to receive under- and over-dosage. This is the so-called interplay effect.

- In general the motion is distinguished in 1) patient motion, 2) inter-fractional motion and 3) intra-fractional motion. The intra-fractional motion, which is e.g. associated with breathing happens on a time scale of seconds, is the kind of motion which is addressed in this thesis.

- At GSI 3D treatment planning and dose calculation were extended to include temporal behavior of the target.
- Three techniques are proposed to mitigate motion effects in radiotherapy. *Beam tracking*, *gating* and *re-scanning*. The *re-scanning* method relies on statistical averaging of the dose distribution and exists in various flavors and its effects toward motion mitigation shall be addressed in this thesis.

2.4 Aim of this work

This work investigates the motion mitigation technique called *re-scanning*. Its tumor conformity is not as good as using the *beam tracking* or *gating* method but it is believed to compensate interplay patterns inside the tumor more robustly than *beam tracking* (van de Water et al., 2009) and in contrast to *gating* the treatment time is greatly reduced. Furthermore, *re-scanning* can be combined with both techniques in order to make *beam tracking* more robust or to decrease the treatment time in case of *gating*. In contrast to the other techniques, *re-scanning* is technically less challenging and therefore much easier to implement in a clinical environment. *Beam tracking* and *gating* rely on very precise motion detection during therapy and the reliability of patient data, e.g. 4DCT image registration which can introduce additional uncertainties. The different *re-scanning* flavors do not need the knowledge about the position of the tumor during treatment and are less sensitive to uncertainties in the patient data. Only one *re-scanning* techniques relies on information about the breathing period of the patient which can be obtained very easily. *Re-scanning* is based on statistical averaging of different interplay patterns in a way that the resulting dose distribution is homogeneous and can be used in patient treatment.

Chapter 3 explains how *re-scanning* is implemented in the existing treatment planning and dose calculation environment at GSI. Theses tools are then used to perform treatment planning studies for five lung cancer patients. The outcome of the motion mitigation efficiency of *re-scanning* depends on parameters like the motion amplitude, spill shape, spill intensity, motion period, target trajectory, starting phase and the *re-scanning* flavor. The different *re-scanning* methods are simulated over a broad range of these parameters as to cover almost all relevant clinical cases. The resulting dose distribution are investigated whether treatment of patients will be possible in the presence of motion.

Before a new technology is used to treat patient elaborate measurements have to be performed as to check whether safe and precise dose irradiation is possible. Those measurements are presented in chapter 4 for *re-scanning* irradiation performed at GSI and at HIT. An overview about the implementation at both facilities is given. Experiments are done *slice-by-slice re-scanning* and *breath-sampled re-scanning* in *re-scanning* modes with and without motion of detectors (which represent the tumor). Comparing the static measurements of *standard* and *re-scanning* irradiation mode reveals if the new method is compatible with the existing systems. In addition, simulations are done which mimic the experimental setup as to broaden the range of investigated parameters. It shall be shown if *re-scanning* irradiation is in principle possible to treat patients at HIT and at GSI.

3 Treatment planning studies

3.1 Introduction

Treatment planning studies are valuable for various reasons. It was shown in numerous studies that experimental dose measurement and simulation results obtained by TReatment planning for Particles (TRiP) in the presence of motion match very well and exhibit a good correlation (Richter, 2012; Gemmel et al., 2011; Lüchtenborg, 2012) so that TRiP can be used to predict the outcome of patient treatment if the used parameters are chosen appropriately. Due to limited experimental beam time new mitigation techniques are often tested in simulation studies before the implementation in the therapy control system is performed. In addition, the accessible parameter space is much greater when doing simulations compared to experiments. Both approaches, experiments and simulations, are necessary and stimulate each other.

The studies in this chapter make use of time resolved computed tomography (4DCT) datasets of five lung cancer patients treated at MD Anderson Cancer Center (MDACC) and investigate, via simulations, how efficiently the various *re-scanning* modes can reduce interplay effects in the presence of motion in case of parameter sets which should cover almost all clinical relevant cases for active scanning carbon ion therapy. A great benefit arises from the fact that at GSI Helmholtzzentrum für Schwerionenforschung GmbH (GSI) various motion mitigation techniques are investigated so that the results can easily be compared if they are optimized in a similar fashion. The present work and the treatment planning studies of J. Woelfelschneider (Woelfelschneider, 2011) use exactly the same optimization methods and patient data set to generate the internal target volume (ITV)-treatment fields so that *re-scanning* can be compared to the use of *fractionations* as motion mitigation technique. R. Luechtenborg (Lüchtenborg, 2012) also used the same patients data sets along with the corresponding α/β ratios to study the *beam tracking* motion mitigation approach. Trials at the National Institute of Radiological Sciences (NIRS) with passive beam shaping methods examined clinically different fractionation schemes and showed promising results even for one fraction (Tsujii and Kamada, 2012). With respect to motion mitigation in beam scanning, hypo-fractionation is contra-productive so that motion mitigation techniques like *re-scanning* become even more important. The more fractions are used the higher is the probability that the random interplay patterns of each fraction homogenize the dose distribution. Therefore, the *fractionation* effect is similar to *re-scanning* but happens on a different time scale.

Due to the fact that passive carbon beam delivery is less sensitive to interplay effects most patients with lung tumors have so far been irradiated at NIRS in Japan (Tsujii and Kamada, 2012). 5-year survival among those patients receiving a single fraction was 52.6% (Mori et al., 2013). Active proton beam scanning was recently used to treat patients with small motion amplitudes at MDACC patients have been treated under anesthesia at Rinecker Proton Therapy Centre (RPTC) (Eckermann et al., 2011) so that the intrafractional motion could be considered as being quasi-static.

3.2 Material & methods

3.2.1 4D treatment planning framework

Figure 3.1 gives an overview of the 4D treatment planning framework. The basic ideas shall be summarized at this point in order to clarify the meaning and functionality of the individual methods which will be described in more detail in the following sections.

1. The basic input is the 4DCT data set. Each data set contains specific information about the patient which is used by TRiP to generate the optimized treatment plan for each patient.

2. The treatment plan is written to a so-called physical-beam-plan (PBP). In patient irradiation mode this PBP can be uploaded to the therapy control system and then the treatment can start.

3. In the 4D treatment planning framework the PBP and data about the accelerator performance are basic input data for the physical-beam-record simulation environment (PBRSimEnv) tool which was written in the scope of this thesis. This tool calculates the irradiation sequence for different accelerator setting and irradiation modes (e.g., normal irradiation or the different *re-scanning* modes).

4. The PBRSimEnv writes the irradiation course into a simulated PBP. The $\mathrm{PBR}_{\mathrm{sim}}$ is in general different for each *re-scanning* method. In addition, the file $\mathrm{PBP}_{\mathrm{corrected}}$ is produced which accounts for the fact that the prescribed particle number deviates from the actual irradiated particle number because of systematic errors of the ionization chambers.

5. The 4DCT information (which contains the patient specific information) and the $\mathrm{PBR}_{\mathrm{sim}}$ and $\mathrm{PBP}_{\mathrm{corrected}}$ files (that describe which rasterpoint has been irradiated in which motion phase along with the actual dose level) are mandatory input data for TRiP.

6. TRiP calculates the 4D dose distribution which can then by analyzed by several means in order to judge the quality of the irradiation process.

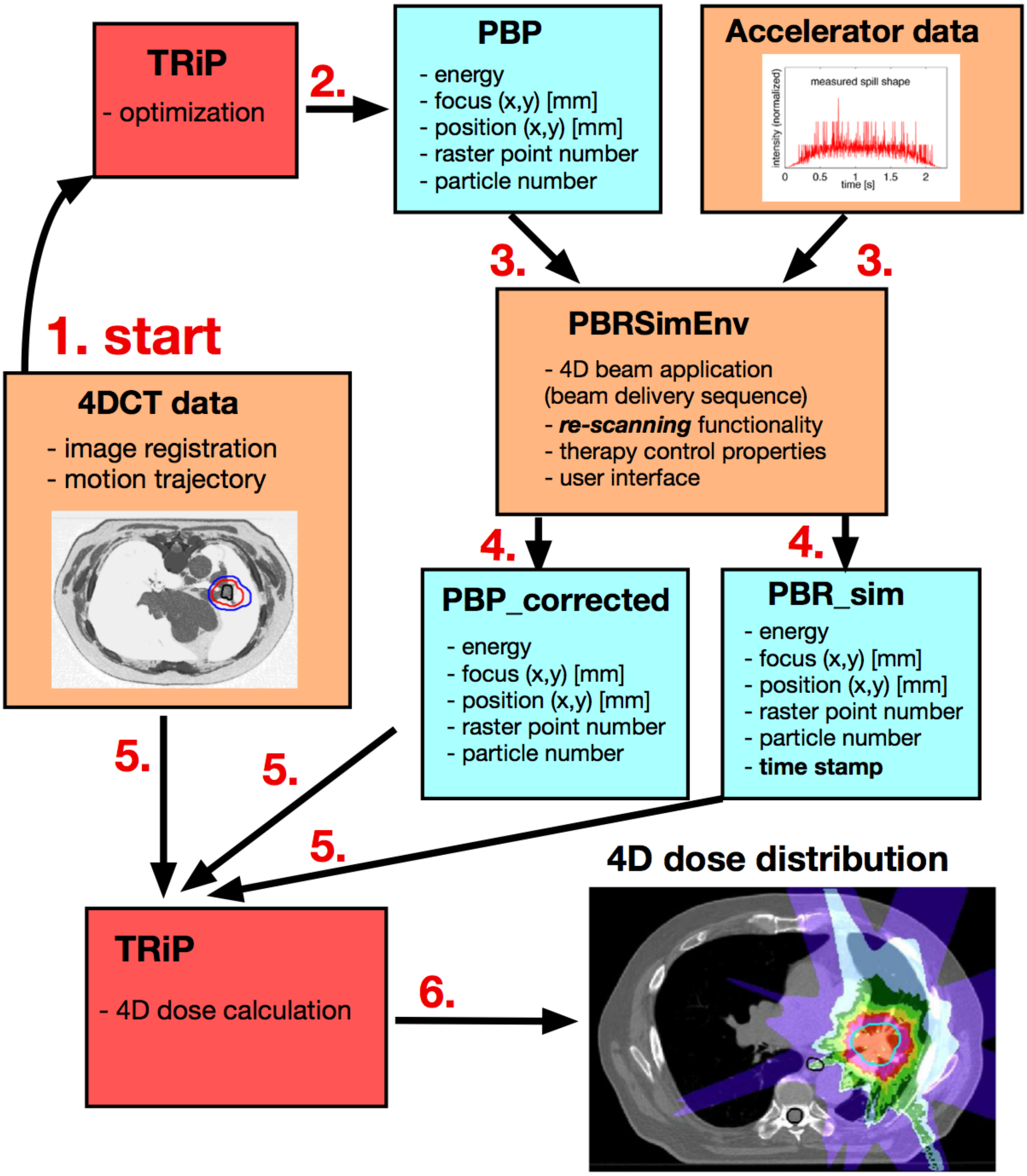

Figure 3.1.: Overview of the 4D treatment planning framework. The numbers represent the sequence in the 4D treatment planning framework. Details will be described in the following sections.

Time resolved computed tomography (4DCT) patient data

This section refers to figure 3.1 (1.):

Five lung tumor patients have been treated at the MDACC in Houston, Texas, USA. The associated 4DCT data sets have kindly been provided so that they could be used as data input for the patient treatment studies. The clinical target volume (CTV) range is from 45 cm^3 to 236 cm^3. The motion amplitude along the direction of the largest motion were from 1 mm to 25 mm. An overview about the data set is given in table 3.1. The patient numbering is sorted with respect to the magnitude of the motion which shall make it easier for the reader to catch the correlation between the severity of the interplay effect as function of the amplitude. The 4DCTs consist of ten motion states. All computed tomography (CT) states represent an equally long time span, this method is known as phase-based motion state definition. Contours of the gross tumor volume (GTV), the CTV and several organs at risk (OAR) were drawn on the reference motion state (end-exhale) CT image. Non-rigid registration has been performed to propagate the contours through the motion phases. Transformation fields, to establish the voxel correspondence between the respiratory phases, were determined by the open source software *Plastimatch* using a B-spline algorithm (Shackleford et al., 2010). Based on this registration, the motion of the tumor and the surrounding tissue are described by a set of 3D transformation fields. These fields are used to propagate the CTV from the reference phase to each motion phase forming the ITV.

For each patient an individual ITV (Graeff et al., 2012) had to be generated as to compensate for both target motion and range changes caused by motion. This method has already been described in section 2.3.2.

patient	pathology	volume [cm^3]	LR [mm]	AP [mm]	SI [mm]	3D motion [mm]
1	Adenocarinom	123	-1	< 0.3	-1	1.4
2	SCC	236	< 0.5	1	-5	5.1
3	NSCLC	45	-2	-3	-5	6.2
4	NSCLC	160	-5	2	-20	20.7
5	Adenocarinom	125	1	-3	-26	26.2

Table 3.1.: Patient data with tumor type (Non-small-cell lung carcinoma (NSCLC), Squamous cell carcinoma (SCC) and Adenocarinom), CTV size and maximal tumor motion in superior-inferior (SI), left-right (LR) and anterior-posterior (AP) direction. The 3D motion amplitude is calculated as being the Euclidean norm.

Treatment plan parameters

This section refers to figure 3.1 (1. and 2).:

The design of the treatment planning studies performed in this work are based on the method used for treatments with scattered carbon beams at the NIRS, taking four fields in the transversal plane with beam entrance angles of 20°, $-20°$, $-70°$ and $-110°$ with respect to the horizontal beam (Miyamoto et al., 2003, 2007; Woelfelschneider, 2011).

For each field the particle number to be delivered per grid position of the ITV was optimized individually using TRiP according to a single-field uniform dose approach. Iso-energy slices were spaced at 3 mm water-equivalent distance using a 3 mm ripple filter (Weber and Kraft, 1999). The lateral spacing of beam positions within an iso-energy slice (IES) was 2 mm. The carbon beam focus size, which is in general a function of the particles energy, was about 6 mm full width at half maximum (FWHM). No planning target volume (PTV) margins were used since only intra-fractional motion related uncertainties were studied.

The relative biological effectiveness (RBE) weighted dose has been calculated with TRiP using the local effect model (LEM) model (see section 2.1.2). The α and β values used in this thesis and in the reports of J. Woelfelschneider (Woelfelschneider, 2011) and R. Luechtenborg (Lüchtenborg, 2012) are identical as to facilitate the highest degree of comparability. As introduced in section 2.1.2, normal tissue and tumor cells generally have a different α/β ratio. For the CTV tissue, an $\alpha/\beta_{\text{CTV}} = 6$ Gy ($\alpha = 0.021$ Gy^{-1}, $\beta = 0.0035$ Gy^{-2}) was chosen. This value is close to the α/β ratio of 5.585Gy used by Kanai et al. for NSCLC (Kanai et al., 2006).

Normal tissue typically has a lower α/β ratio (see Section 1.2.2). In this work $\alpha/\beta_{\text{norm}} = 2$ Gy ($\alpha = 0.3$ Gy^{-1}, $\beta = 0.0015$ Gy^{-2}) has been assigned to all tissues but the CTV. This value has been based on results from carbon irradiation of the spinal cord of rats (Karger et al., 2006).

Fractionation scheme

This section refers to figure 3.1 (1. and 2.):

The RBE weighted dose, which was used to optimize each field, depends on the fractionation scheme. To separate the different influences on interplay reduction of many treatment fractions (Woelfelschneider, 2011) and *re-scanning* the chosen fraction number in this work was set to one. The treatment approach thus mimics the case that a patient is being irradiated with four different fields on a single day. The RBE weighted dose for one fraction was calculated to be 17.70 Gy(RBE). The dose per field is the fraction dose divided by the number of fields (Woelfelschneider, 2011; Lüchtenborg, 2012).

Re-scanning modes

This section refers to figure 3.1 (3. and 4.):

Six different *re-scanning* methods have been investigated in this thesis. *Breath-sampled re-scanning*, *slice-by-slice re-scanning*, *volumetric re-scanning* and *random-time-delay re-scanning* were already introduced in 2.3.6 as they have been already proposed elsewhere (Seco et al., 2009). *Local-parameter re-scanning* and *mixed-scanpath re-scanning* have been created in the scope of this work and will be introduced briefly in this section. The implementation of *random-time-delay re-scanning* was different than proposed in the literature, details are listed below.

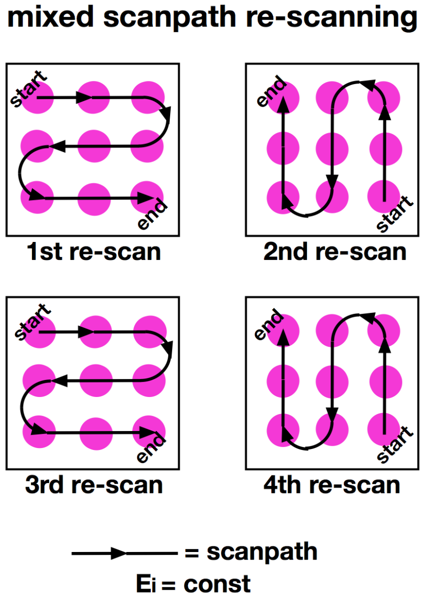

Figure 3.2.: Illustration of the *mixed-scanpath re-scanning* mode. The four squares represent a single IES which is irradiated with a *re-scan* number of $r = 4$. The main direction of the scan-path is changed for every new *re-scan* run from horizontal to vertical and vice versa.

Mixed-scanpath re-scanning is carried out in the same order as *slice-by-slice re-scanning* with the only difference that the scan-path is changed for each subsequent *re-scan* run like illustrated in figure 3.2. This is motivated by results of initial *re-scanning* experiments (see section 4.3.3) and simulations at GSI and other researchers (e.g., (Knopf et al., 2011)) which showed that the interplay effect is more severe (less severe) if the motion direction and the main scanpath direction are perpendicular (parallel) to each other. The rational is, that *mixed-scanpath re-scanning* makes the irradiation more robust and predictable because switching of the main scan-paths shall prohibit the worst case scenario of a scan-path which is perpendicular to the target motion.

Local-parameter re-scanning: Figure 2.10 shows that the spread out Bragg peak (SOBP) composed of many Bragg-peaks. If, e.g., the most distal IES is irradiated with a *re-scan* number of r all of the more proximal IESs get some pre-irradiation dose. If the energy is decreased as to irradiated the next IES, parts of the IES have de facto already received r *re-scans* due to the pre-irradiation. Therefore it is a rational assumption that the number of *re-scans* can be decreased in case of the more proximal IESs which is illustrated in figure 3.3. The *re-scan* number is then no longer a global but rather a local parameter. The calculation workflow is illustrated in figure 3.4. The rational of this method is: 1) the therapy systems at Heidelberg Ion-Beam Therapy Centre (HIT) and GSI need a minimum particle number of each rasterpoint. In case of high *re-scan* numbers when irradiating proximal IES the particle number can fall below this threshold which is typical between 5000 and 10000 particles. 2) By using a constant *re-scan* number and intensity, the pencil beam needs to sweep faster the more proximal the IES is. Eventually, the scanning speed might be too high for the magnets. The *local-parameter re-scanning* approach will slow down the lateral scanning speed.

Random-time-delay re-scanning: To allow for a more flexible number of *random-pauses* and to make this number independent of the number of *re-scans* the factor μ_{random} is used to calculate the number of *random-pauses* $N_{\text{random}}(i)$ of each IES i as follows

$$N_{\text{random}}(i) = \mu_{\text{random}} \cdot N_{\text{rasterpoints}}(i), \tag{3.1}$$

with $N_{\text{rasterpoints}}(i)$ being the number of rasterpoints of the the corresponding IES. For instance, taking $\mu_{\text{random}} = 0.1$ an IES with 1000 points is halted for a random pause after every 100 points. The number of random pauses does not increase with the *re-scan* number. In contrast to the *random-time-delay re-scanning* flavor proposed in the literature, even small *re-scan* numbers can be irradiated with a high number of *random-pauses*. Throughout this thesis a random number generator automatically selects for each *random-pause* a time length in the range of $0\,\text{s} < T_{\text{random pause}} \leq T_{\text{random, max}}$, with $T_{\text{random, max}} = 1\,\text{s}$.

The abbreviations listed in table 3.2 are commonly used when naming the different *re-scanning* modes in figures.

full *re-scan* mode name	abbreviation used in figures or legends
breath-sampled re-scanning	BS
slice-by-slice re-scanning	slice
volumetric re-scanning	vol
random-time-delay re-scanning	random
local-parameter re-scanning	local
mixed-scanpath re-scanning	mixed

Table 3.2.: Table of the commonly used abbreviations of the different *re-scan* modes in the figures.

The physical-beam-record simulation environment

This section refers to figure 3.1 (3. and 4.):

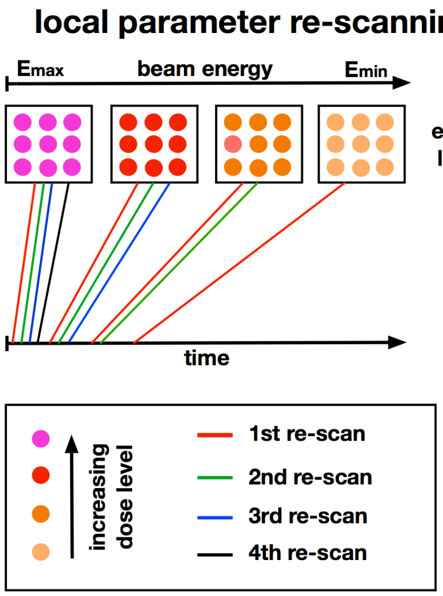

Figure 3.3.: Illustration of the *local-parameter re-scanning* mode. The *re-scan* number r is no longer a constant parameter throughout all IESs but generally decreases in case of lower beam energies. Each IES is assigned with a *local re-scan* number $r(i)$.

The PBRSimEnv, which was written in the scope of this thesis, is a beam delivery sequence generation software which is needed in order that TRiP can calculate 4D dose distribution. Mandatory input data are the PBP and parameters about the performance of the used accelerator. In order to mimic the accelerator at GSI spill profiles were measured and normalized to one particle per spill. In advance of each irradiation the therapy control system suggests an appropriate intensity level for each IES of the PBP which can be multiplied with the normalized spill profile. This results in a realistic scanning speed of the pencil beam in the simulation of the beam delivery sequence. A sample spill profile measured at GSI with a resolution of 10 μs and an artificially created square spill profile[1] can be seen in figure 3.5. The accelerator data also include other properties like spill length or spill pauses with and without energy variation which are listed in table 3.3. In addition to the accelerator properties of the system at GSI, a virtual-accelerator (ACCvirtual) was introduced. The accelerator properties of the ACCvirtual were only used for simulating *breath-sampled re-scanning* mode. The spill length of GSI's accelerator in therapy mode is too short to match typical breathing periods.

	spill length [s]	spill pause with energy variation [s]	spill pause without energy variation [s]
GSI	2.2	3.3	2.3
ACCvirtual	10	3.3	2.3

Table 3.3.: Table of the spill on and spill pause times of the accelerators at GSI and the the virtual-accelerator (ACCvirtual).

---

[1] The spill profiles at HIT are quite close to an artificial square spill profile.

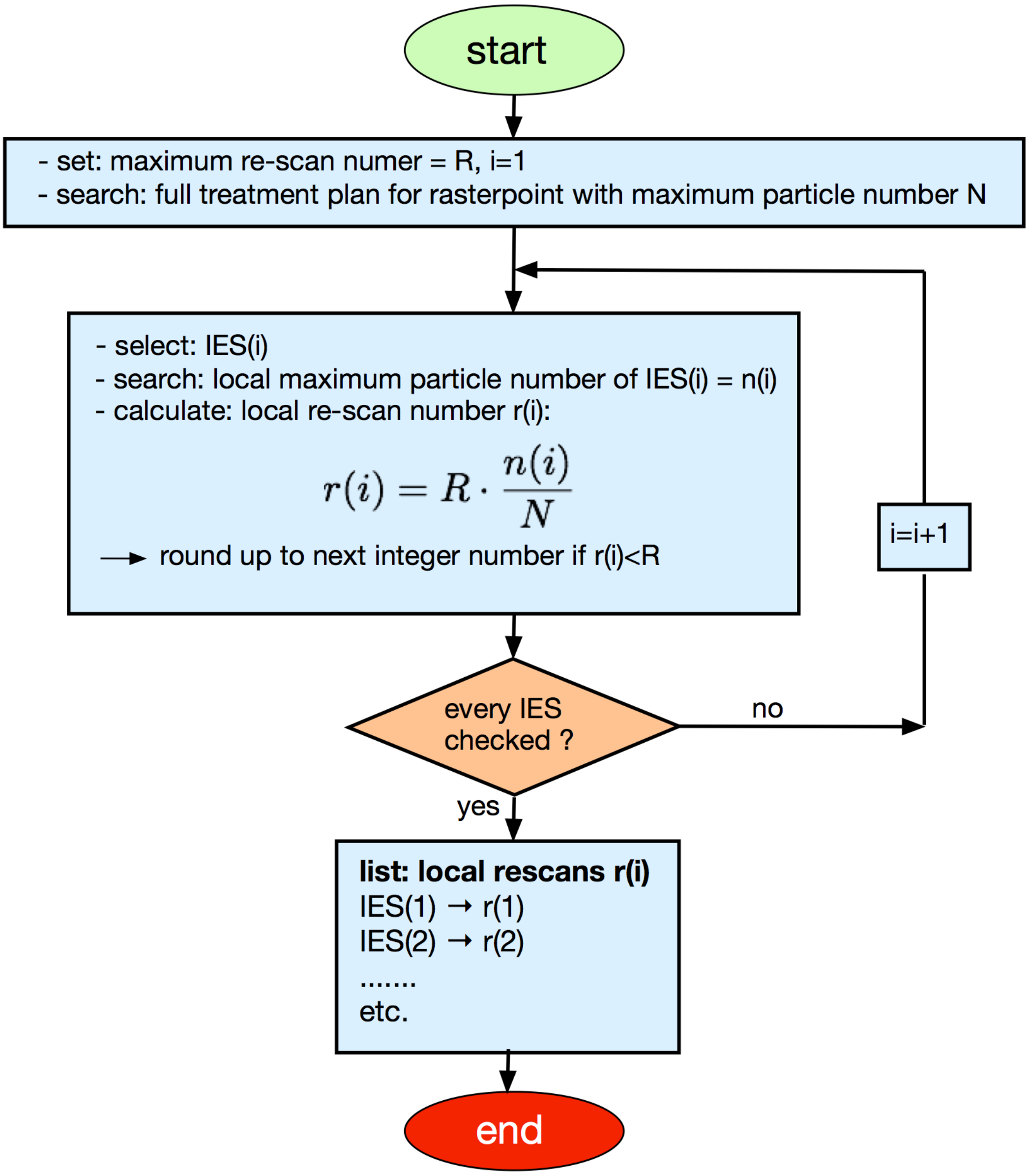

Figure 3.4.: This flowchart shows how the *local-parameter re-scanning* numbers $r(i)$ are calculated.

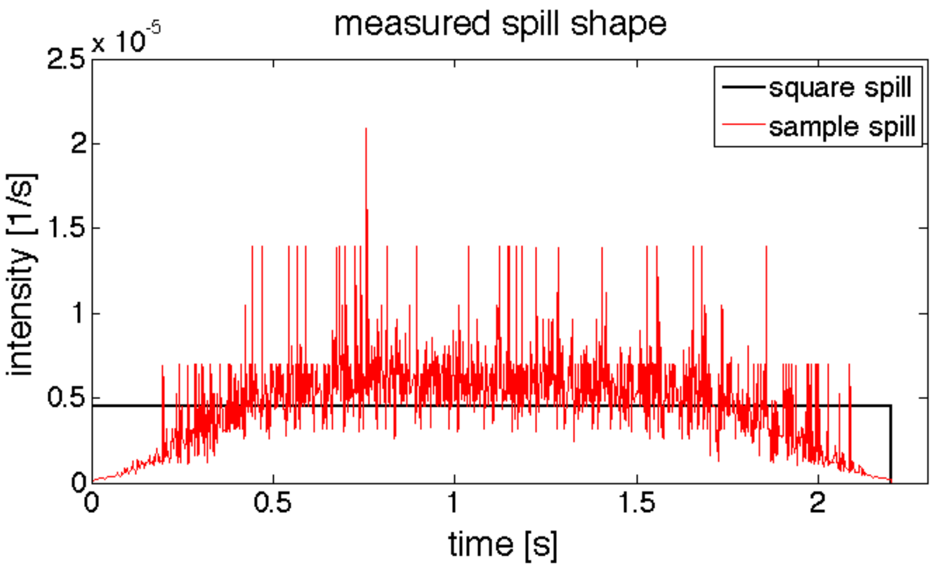

Figure 3.5.: shows a measured spill profile at GSI (red line) and an artificially created square spill (black line). Both spill are normalized to one particle per spill and can be used in the simulation environment to represent spill extraction behavior of accelerators.

The *breath-sampled re-scanning* mode needs an accelerator with a spill extraction time that is as long as the breathing period. Therefore a square spill profile with a spill length of 10 s was created and used in those cases. All other *re-scanning* modes used randomly selected spill files measured at GSI with the appropriate spill pauses.

At GSI, the therapy control system checks every 12.5 μs (Haberer et al., 1993) if the prescribed particle number is reached for each rasterpoint (see figure 3.6) of the PBP. Due to the fact that these checks have finite spacing in time the signal to step over to the next rasterpoint is sent for an actual particle value that always exceeds the prescribed value. This overdose is inversely proportional to the total treatment time of this point. As *re-scanning* decreases the treatment time of each rasterpoint roughly by the factor of the *re-scans* this overdose effect is expected to get more severe. The therapy control unit at GSI subtracts the overdose of the previous rasterpoint from the nominal dose of the next one within the same IES because due to the lateral Gaussian beam width, each rasterpoint contributes to a major part to the dose of the next rasterpoint.

At HIT, the system checks every 2 μs (Naumann, 2011) if the prescribed particle number is reached for each rasterpoint but does not correct overdose (see 3.7).

To quantify the effect of *re-scanning* on the finite dose sampling rate, this feature was implemented, as shown in the figures 3.6 and 3.7, in the simulation environment. Using the PBP$_{planned}$ as input data a corrected PBP$_{corr}$ with the actual applied particle numbers is generated by the PBRSimEnv. This plan is then used to calculate the dose distribution.

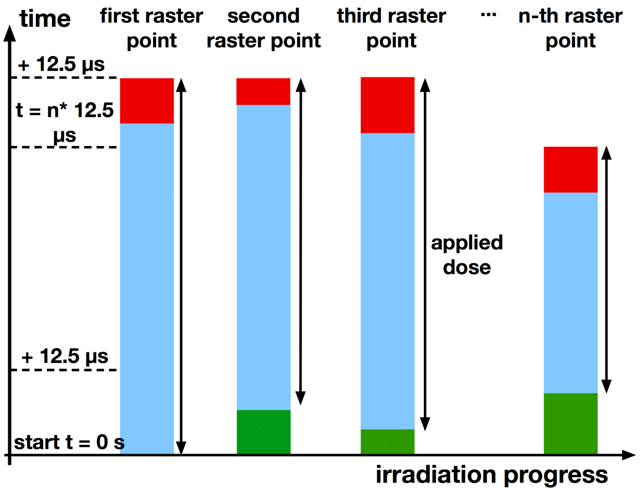

Figure 3.6.: Treatment control at GSI. The sum of the blue and green segment represents the prescribed particle number for each raster point in the PBP$_{planned}$. The red area pictures the overdose that occurs because of the finite time increment of the control system. The green segment is subtracted from the prescribed particle number due to the overdose of the foregoing rasterpoint. Therefore the sum of the blue and red parts equals the applied dose.

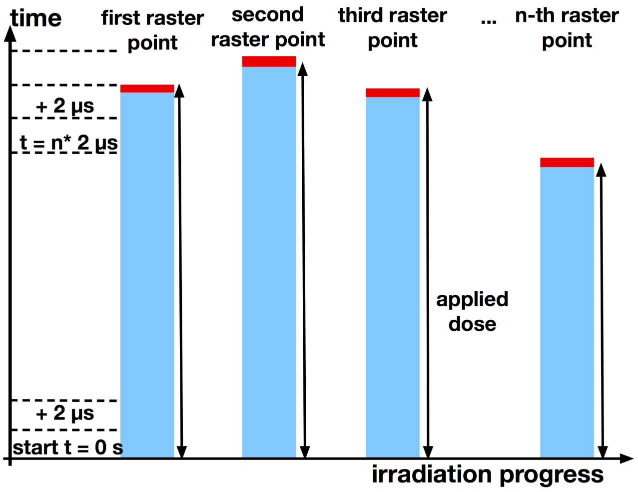

Figure 3.7.: Treatment control at HIT. Analog to figure 3.6.

An elaborate analysis of the differences between PBP$_{planned}$ and PBP$_{corr}$ was done. For this purpose the PBP$_{planned}$ of patient 2 (see table 3.1) was chosen because of its big CTV so that the largest effects can be expected.

The highest intensities at GSI ($2 \cdot 10^8 \frac{particles}{spill}$) and at HIT ($8 \cdot 10^7 \frac{particles}{s}$), a *re-scan* number of 25, a measured and an artificial square spill profile (see figure 3.5) and *slice-by-slice re-scanning* mode were taken as input parameters to calculate the simulated physical-beam-record (PBR) data along with the PBP$_{corr}$ files. The measured spill profile was used to calculate the effects at GSI and the square spill profile the corresponding effects at HIT, respectively.

In general, the intensity decreases for proximal slices. It follows that this parameter selection can be expected to have a larger impact on the PBP$_{corr}$ than in real cases. Therefore, if this worst case scenario will result in negligible changes of the applied compared to the planned particle numbers it shall also be expected in case of lower intensities and smaller *re-scan* numbers. The analysis includes several steps. First, the relative deviation of each rasterpoint i was calculated

$$\xi(i) = \frac{\left(N(i)_{corr} - N(i)_{planned}\right)}{N(i)_{planned}}, \tag{3.2}$$

with N being the particle number of the corrected and the planned PBP, respectively. Second, rasterpoints closer to the proximal slices receive in general less dose because they have already been pre-irradiated when applying the dose to the more distal slices. Therefore the deviation of each point according to formula (3.2) shall be weighted to account for the pre-irradiation. In the optimization the dose level was set to be constant across the whole tumor tissue. Therefore, if a rasterpoint shall be irradiated with the maximum particle number of N_{max} this correspond to the prescribed dose. The weighted deviation for each rasterpoint can then be expressed as:

$$\xi(i)_{weighted} = \frac{\left(N(i)_{corr} - N(i)_{planned}\right) \cdot \frac{N(i)_{planned}}{N_{max}}}{N(i)_{planned}}. \tag{3.3}$$

Considering that the beam sweeps n-times over the area in *slice-by-slice re-scanning* mode, the particle numbers $N(i)_{corr}$ and $N(i)_{planned}$, having the same x and y positions along with the same energy, can be summed according to

$$N_{summed}(j) = \sum_{\substack{i=1 \\ \text{for x,y and E} \\ \text{being identical}}}^{\text{all points}} N(i) \tag{3.4}$$

before calculating (3.2) and (3.3).

This section refers to figure 3.1 (3. and 4.):

Figure 3.8 shows the beam delivery sequence calculated by the PBRSimEnv in case of patient 5 for *slice-by-slice re-scanning* with $r = 3$. The spill status is represented by a logical signal and the total number of rasterpoints is normalized to one. In case of *slice-by-slice re-scanning*, *volumetric re-scanning*, *local-parameter re-scanning* and *mixed-scanpath re-scanning* the spill characteristics of the GSI system were used (see table 3.3) along with randomly selected measured spill files recorded at GSI.

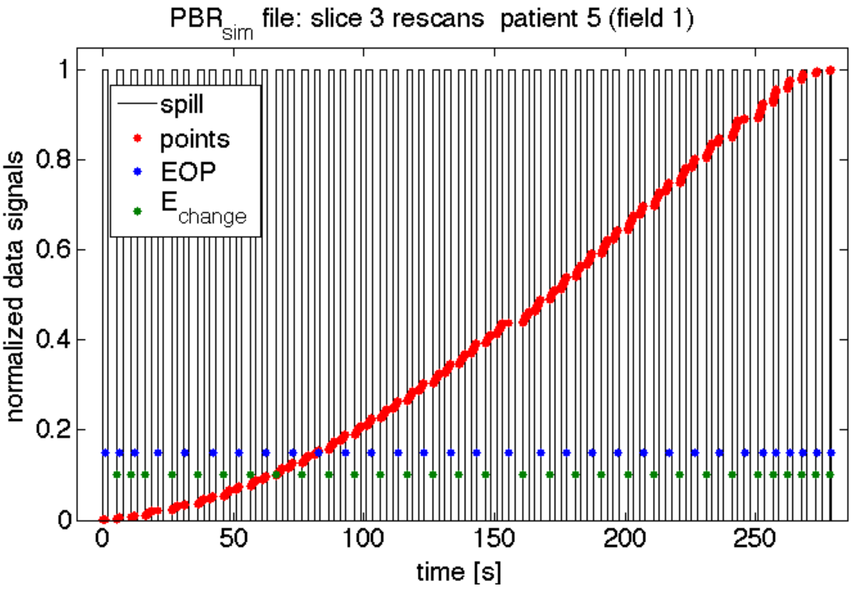

Figure 3.8.: *Slice-by-slice re-scanning* simulated physical beam record file calculated for patient 5 with 3 *re-scans*. The black line represents the spill signal (a value of one means that particles are extracted and the beam is on). The red points are the rasterpoint counter. If the irradiation of a point is finished this value is incremented by one. The rasterpoint counter is normalized to one. The blue points indicate when the irradiation of an IES is finished and the green points display if the energy of the particles was changed.

The same spill profiles were basically also used in case of *random-time-delay re-scanning* but it was assumed that the spill profile is being "frozen" in time during the *random-pauses* and that the spill extraction re-starts exactly after the *random-pause* is over. It follows that the total beam extraction time per spill is still 2.2 s but expanded to a longer time duration which depends on the *random-pauses*. The spill-on signal time $T_{\text{on, random}}$ can therefore have a length between $2.2\ \text{s} < T_{\text{on, random}} < (2.2 + N_{\text{random}}(i) \cdot T_{\text{random, max}})\ \text{s}$, with $T_{\text{random, max}}$ being the maximum *random-pause* length.

This change of the accelerator behavior compared to the current GSI accelerator was necessary because otherwise the *random-pause* will place the re-start of the irradiation to often into the period of spill pauses when no beam is available. However, these extraction characteristics can be realized by using an accelerator with variable spill length.

In case of *breath-sampled re-scanning* a square spill profile with a length of 10 s was used because the spill length needs to be at least as long as the breathing period. The intensity is then adjusted in a way that the particle extraction time equals the breathing period. Using a square spill is actually very close to the current spill shape implemented at HIT and the prolonged spill duration shall not bias the outcome of the 4D dose calculation since the irradiation starts in *breath-sampled re-scanning* anyway at an arbitrary phase for each IES. In addition, it will be shown in chapter 4.3.3 that the *breath-sampled re-scanning* dose calculation shows almost no dependence whether gained by a measured spill profile or by a square profile.

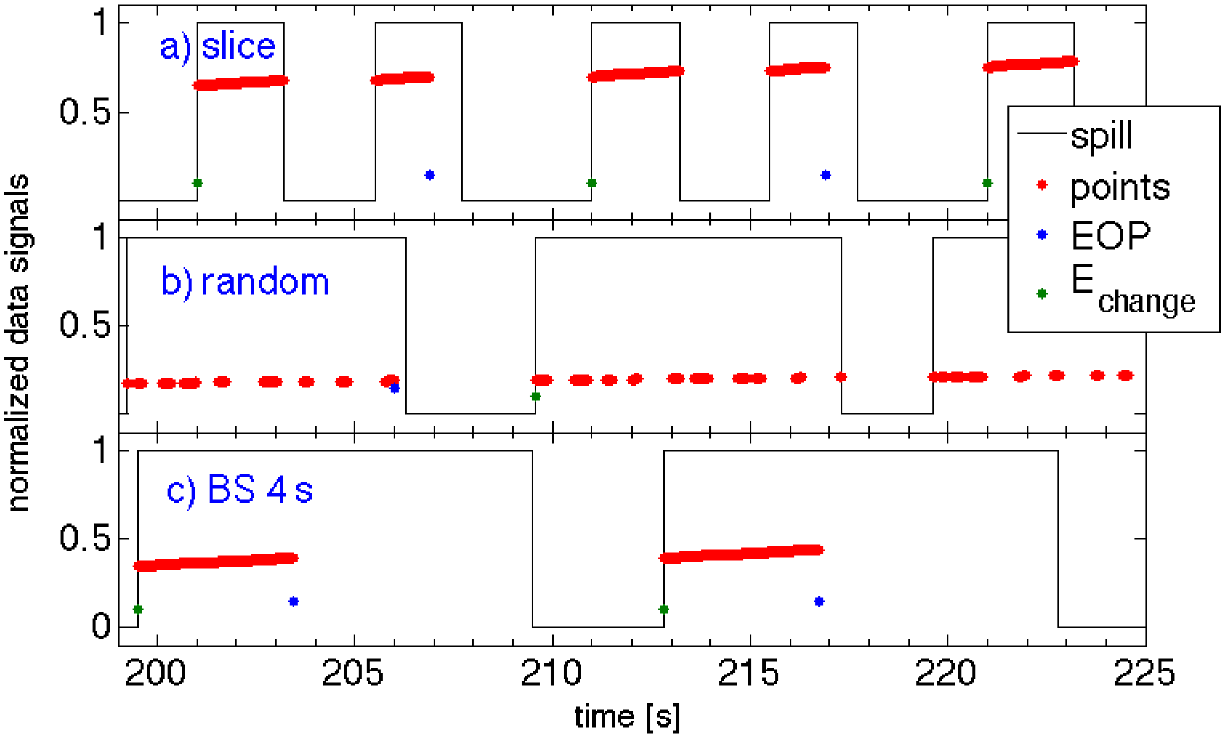

Figure 3.9.: Magnified cutout of the PBR_{sim} files in case of a *slice-by-slice re-scanning*, b) *random-time-delay re-scanning* with $\mu_{random} = 0.05$ and c) *breath-sampled re-scanning* with a spill length 10 s. The particle extraction time and the breathing motion period have a duration of 4 s.

The differences in beam delivery sequence between *slice-by-slice re-scanning*, *random-time-delay re-scanning* and *breath-sampled re-scanning* are illustrated in figure 3.9. The time which is necessary to finish an IES in *slice-by-slice re-scanning* and *random-time-delay re-scanning* mode is not constant and depends on the prescribed intensity and the total particle number of this slice. In case of *random-time-delay re-scanning* $\mu_{random} = 0.05$ was used. Not all 20 *random-pauses* are visible in the chosen temporal resolution. As requested, *breath-sampled re-scanning* finishes the irradiation of each IES in 4 s.

3.2.2 Patient simulation studies

This section refers to figure 3.1 (4. and 5.):

The 4D dose calculation is performed with TRiP. In addition to 4DCT data, the PBP$_{corr}$ and PBR$_{sim}$ files other input data like the motion trajectory or the starting phase have to be defined. A mandatory request for a treatment planning study is that it should include almost all relevant clinical cases and that it shows the variation of the 4D dose distribution if the input parameters are changed as it can happen in real patient treatments. Therefore the dose calculations have been performed over a broad range of parameters.

Standard cases

The standard cases represent the fundamental dose calculations in the scope of this thesis. The 4D dose distribution for all five patients (see table 3.1) and all *re-scan* modes (see table 3.2) were calculated over a broad range of parameters which should cover almost all relevant clinical situations. An overview is given in table 3.4.

simulation parameter	range or count
re-scan modes	6 (see table 3.2)
re-scan numbers	1, 3, 5, 9, 13, 17, 21
starting phase	0°, 90°, 180°, random (0° - 359°)
breathing period	3 s, 4 s and 5 s
patients	1, 2, 3, 4, 5

Table 3.4.: Overview of the parameter space for the standard calculations.

In addition to the fixed starting phases the 4D dose calculation was also performed with a starting phase that was randomly selected from the range of 0° - 359° for each field. To describe the trajectory of the tumors, Lujan-motion with $n = 2$ was used (Lujan et al., 1999).

The number of *random-pauses* was fixed to $\mu_{\text{random}} = 0.05$ and the maximum *random-pause* length to $T_{\text{random, max}} = 1\,\text{s}$, respectively.

The beam intensity for each treatment field is chosen to be the same as if this field is being irradiated in normal therapy mode at GSI without *re-scanning* functionality. An exception is the beam intensity selection in *breath-sampled re-scanning* mode which is being calculated in order to match the irradiation time per IES with the breathing period.

In total, over 2500 4D dose calculations were performed for the standard cases.

Special case I - *breath-sampled re-scanning* uncertainty

The standard cases assume *perfect* matching of the irradiation time of each IES with the breathing period. In real patient treatment the breathing motion of the patient will always fluctuate to some extent. Therefore, it is important to investigate the robustness of *breath-sampled re-scanning* with respect to these variations. The PBRSimEnv was adjusted to generate beam sequence files with an irradiation time per IES that perfectly matches the breathing period. To include the uncertainty, the breathing cycle of the motion traces, which are mandatory to calculate the 4D dose distribution with TRiP, were varied as listed in table 3.5. In total 480 4D dose calculations were performed with respect to variations in the motion period when irradiating in *breath-sampled re-scanning* mode.

simulation parameter	range or count
breath-sampled re-scanning length	4 s
breathing period	1 s , 3 s , 3.5 s, 3.75 s, 4 s, 4.5 s, 4.75 s, 5 s
re-scan numbers	1, 3, 5, 9, 13
starting phase	0°, 180°, random (0° - 359°)
patients	2, 3, 4, 5

Table 3.5.: Overview of the parameter space for *breath-sampled re-scanning* with uncertainties in the motion period.

Special case II - variation of the number and the maximum length of the *random-pauses*

The number and the maximum length of the *random-pauses* were also varied to study their influence. Since each *random-pause* prolongates the treatment time it is worthwhile to investigate the influence if these numbers are lowered. For these calculations only patient 5 with the largest motion amplitude was used along with a motion period of 4 s.

The beam intensity for each treatment field is chosen to be the same as if this field is being irradiated in normal therapy mode at GSI without *re-scanning* functionality. If the μ_{random} dependence is studied, the maximum random pause is fixed to $T_{\text{random, max}} = 1\,\text{s}$. If the $T_{\text{random, max}}$ is investigated, the number of random pauses is set to $\mu_{\text{random}} = 0.02$.

Further details are listed in table 3.6. In total 72 4D dose calculations were performed with respect to variations in the number and the maximum length of *random-pauses*.

3.2.3 Data analysis

The quantify and judge the quality of the dose distribution the measures D_x and V_x are used according to the ICRU recommendations (ICRU, 1993). The general definition is as follows:

simulation parameter	range or count
μ_{random}	0.05, 0.2
$T_{\text{random, max}}$	1 s, 0.1 s
re-scan numbers	1, 3, 5, 9, 13, 17
starting phase	0°, 180°, random (0° - 359°)
motion period	4 s
patient	5

Table 3.6.: Overview of the parameter space for a different number of *random-pauses* in the *random-time-delay re-scanning* mode.

- **D_x**: x% of the volume of interest has received a dose of at least D_x.
- **V_x**: A dose of at least x% of the target dose has been received by the volume V_x.

For comparison of the different *re-scanning* techniques the V_{95} and the V_{107} of the CTV have been analyzed as a measure for target coverage and overdose, respectively. In the ideal case $V_{95} = 100\%$ and $V_{107} = 0\%$ should be reached. The difference $D_5 - D_{95}$ is used to quantify the level of homogeneity. A sharper dose fall-off leads to a smaller $D_5 - D_{95}$ value and thus to a more homogeneous dose distribution. The analysis of these quantities is exemplary shown in figure 3.10.

The mean and standard deviation of the dose distributions were calculated over all motion parameters for each *re-scan* mode and each *re-scan* number for the measures of V_{95}, V_{107} and $D_5 - D_{95}$ for the standard and both special cases.

The values of all measures have been investigated for significant differences between the *re-scan* modes at fixed *re-scan* numbers. Since the requirements for parametric test procedures were not met it was necessary to use non-parametric significance tests. Hence, the different measures were tested by using the Kruskal-Wallis test in combination with the Wilcoxon–Mann–Whitney test at a significance level of $\alpha = 5\%$.

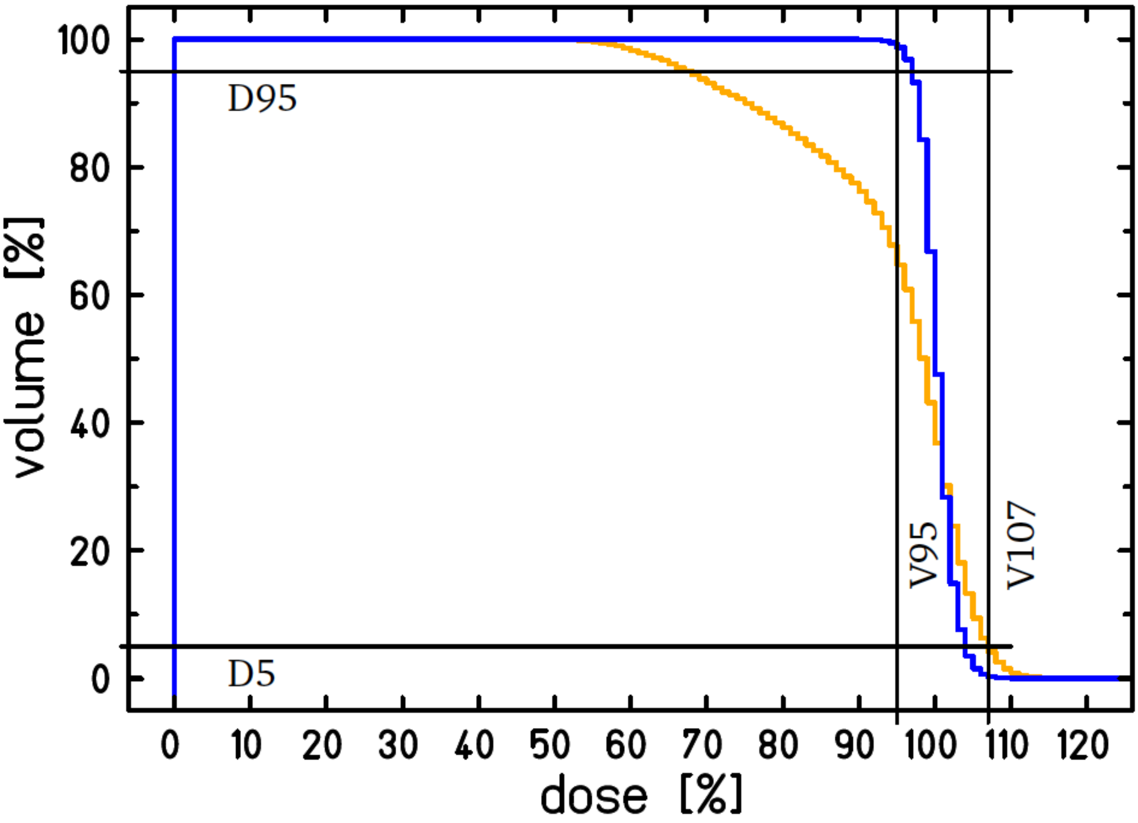

Figure 3.10.: Example of the analysis of V_{95}, V_{107}, and $D_5 - D_{95}$ comparing two different DVHs. The V_{95} and V_{107} are the volumes at the intersection of the vertical lines (at 95% and 107% dose level, respectiveley) and the according DVH curve. For the orange DVH $V_{95} = 64.7\%$ and $V_{107} = 4.2\%$, for the blue DVH $V_{95} = 98.7\%$ and $V_{107} = 0.2\%$. The D_5 is the dose at the intersection of the horizontal line at 5% volume level and the DVH curve. Accordingly, the D_{95} is the intersection of the horizontal line at 95% volume level and the DVH curve. The difference between these dose levels is the $D_5 - D_{95}$. For the orange DVH $D_5 - D_{95} = 39\%$ and for the blue DVH $D_5 - D_{95} = 7\%$. Figure and exemplary analysis are adopted from R. Luechtenborg (Lüchtenborg, 2012).

3.3 Results

3.3.1 The physical-beam-record simulation environment

The effect on the dose application due to the overdose which results from the finite time spacing of the therapy control units at GSI is shown in figure 3.11 a) - d) for a *re-scan* number of 25.

Figure 3.11 a) shows that the combination of high intensity irradiation in *slice-by-slice re-scanning* mode with a *re-scan* number of 25 leads to a broad distribution of the relative errors between the applied and the planned dose on the rasterpoints of patient plan. Some points get only 50% of the prescribed dose while others receive up to 175%.

Taking the weighting into account, then figure 3.11 b) shows a a much narrower distribution, the minima and maxima deviation values are very close to the ones of 3.11 c) which includes the *re-scan* effect on the dose application.

Figure 3.11 d) accounts for the weighting as well as for the *re-scan* effect and therefore represents the case which is closest to reality. The distribution is very narrow with a maximal deviation of 1% which can be seen in the enlarged detail.

Further calculations have been done in case of the *re-scan* numbers 5 and 11. The results are shown in table 3.7. The distributions get rapidly smaller for lower *re-scan* numbers.

The total prescribed particle number $N_{\text{planned}} = 7,199,586,070$ is identical for all *re-scan* cases. The total applied particle numbers for $N_{\text{GSI}\,\textit{re-scan}=5} = 7,199,603,400$, $N_{\text{GSI}\,\textit{re-scan}=11} = 7,199,603,386$ and $N_{\text{GSI}\,\textit{re-scan}=25} = 7,199,602,986$ are so close to N_{planned} that they can be considered as being identical in terms of total dose.

The effect on the total number of particles at GSI is so small because over- and underdosage cancel each other out which is different from the therapy control system used at HIT which is displayed in figure 3.11 e) - h).

Figure 3.11 e) shows that no rasterpoint is irradiated with too less dose and that the maximum deviation of overdose is 20% in case of the same patient plan, the same *re-scan* number and the identical intensity settings as for the calculations shown in figure 3.11 a).

Figures 3.11 f) and 3.11 g) illustrate that the deviation from the planned dose level is reduced when including the weighting and the *re-scanning* of the individual rasterpoints, respectively. Like in the former case at GSI, the best result at HIT is gained when combining both effects which is presented in figure 3.11 h). The deviation of the dose level is then expected to be less than 1% for all rasterpoints. Further calculations have been done in case of the *re-scan* numbers 5 and 11. The results are shown in table 3.7.

The corresponding numbers are $N_{\text{HIT}\,\textit{re-scan}=5} = 7,212,603,725$, $N_{\text{HIT}\,\textit{re-scan}=11} = 7,228,041,989$ and $N_{\text{HIT}\,\textit{re-scan}=25} = 7,294,277,434$ which results in a total particle deviation of 1.3% in case of 25 *re-scans*.

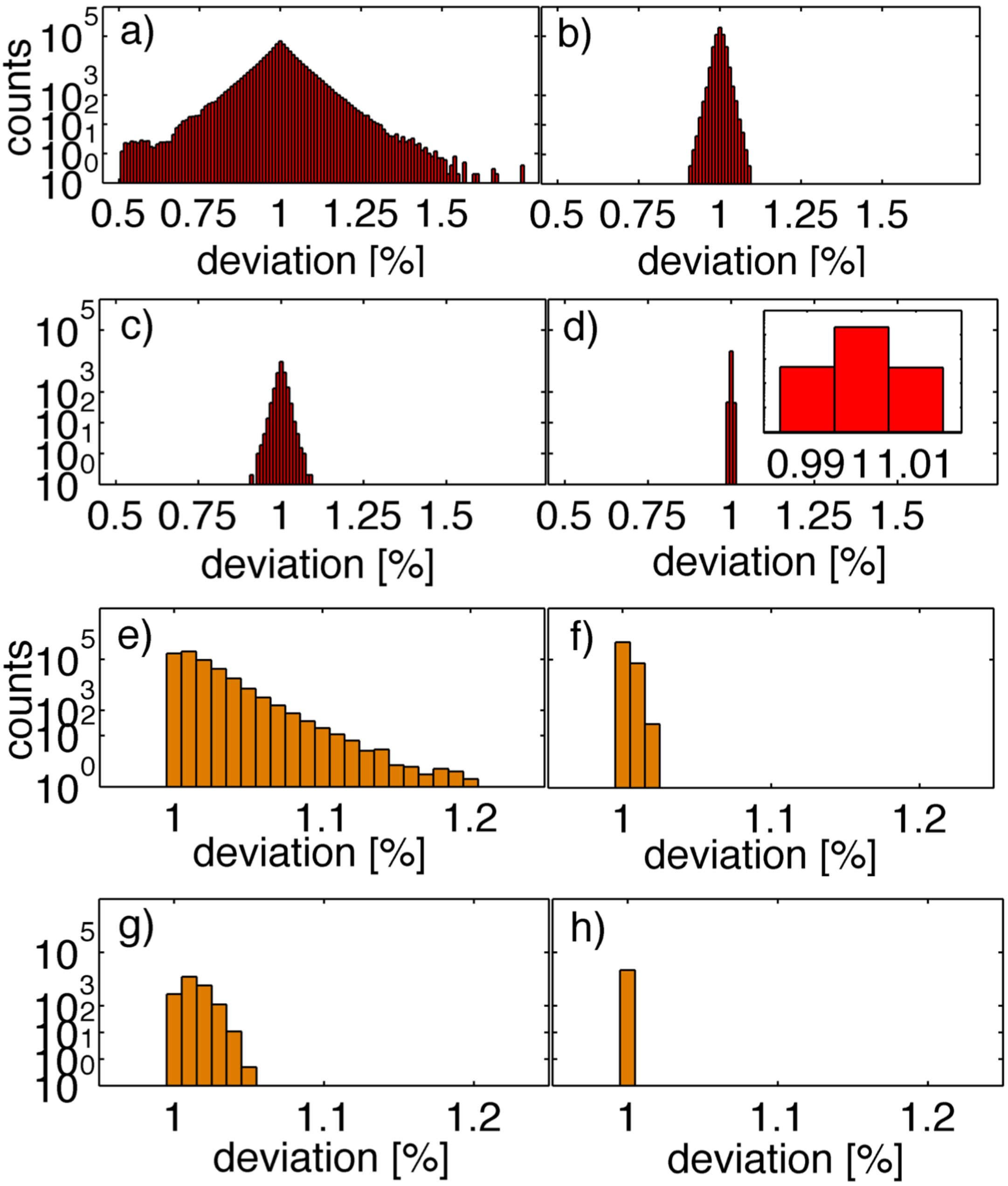

Figure 3.11.: Histograms showing the influence of the therapy control units (SAMS) on the dose application for a *re-scan* number of 25. More data can be found in table 3.7. Each subfigure shows the relative deviation of the actually irradiated and the planned dose. a) - d) displays the results for the TCU at GSI and e) - h) for the TCU at HIT, respectively. a) for each rasterpoint (see formula 3.2), b) for each rasterpoint, but weighted concerning its relative importance on the total dose for the TCU at GSI. c) as a) and d) as b) but including formula 3.4 which basically sums up the deviation for each individual rasterpoint over all *re-scan* runs. The width of each bin is 1%. e) corresponds to a), f) to b), g) to c) and h) to d), respectively.

re-scans	facility	min/max [%] (individual, not weighted)	min/max [%] (summed, weighted)
5	GSI - sample spill	0.89/1.14	1/1
11	GSI - sample spill	0.70/1.27	0.99/1.01
25	GSI - sample spill	0.51/1.75	0.99/1.01
5	HIT - sample spill	1.00/1.03	1.00/1.00
11	HIT - sample spill	1.00/1.07	1.00/1.00
25	HIT - sample spill	1.00/1.2	1.00/1.00
5	HIT - square spill	1.00/1.01	1.00/1.00
11	HIT- square spill	1.00/1.03	1.00/1.00
25	HIT - square spill	1.00/1.06	1.00/1.00

Table 3.7.: Quantitative results of figure 3.11 with additional values for the *re-scan* numbers 5 and 11.

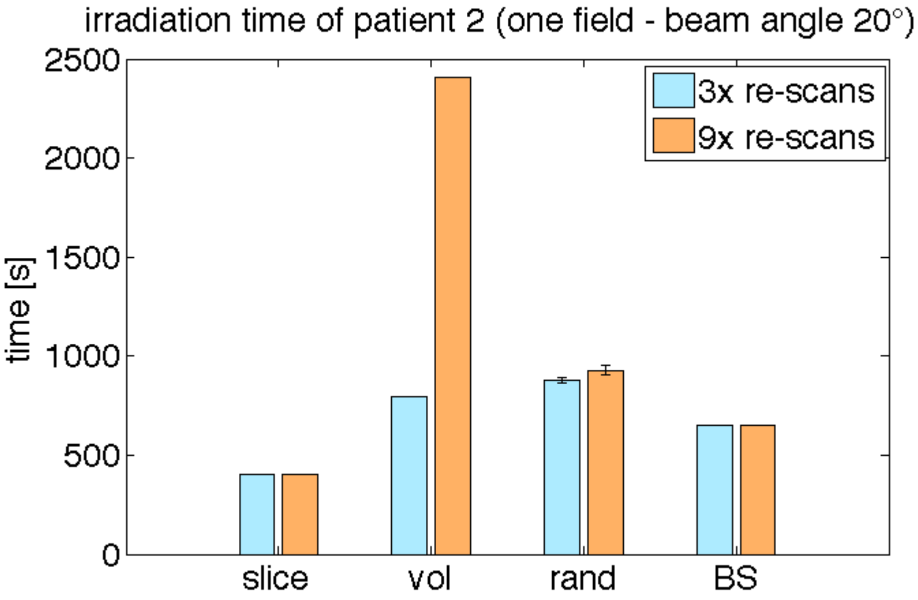

Figure 3.12.: Comparison of the irradiation duration in case of *slice-by-slice re-scanning*, *volumetric re-scanning*, *random-time-delay re-scanning* and *breath-sampled re-scanning*. The information was gained by analyzing the PBR$_{sim}$ of patient 2. The choice for this patient was arbitrary and shall not affect the conclusion of the results.

The time information of the generated PBR_{sim} files can be used to compare the different *re-scanning* modes with regard to the individual irradiation length. The data were analyzed in case of patient 2. Due to the implementation of the simulation environment *mixed-scanpath*, *local-parameter* and *slice-by-slice re-scanning* exhibit identical irradiation times so that figure 3.12 shows only a comparison of the treatment duration of *slice-by-slice*, *volumetric*, *breath-sampled* and *random-time-delay re-scanning* in case of $r = 3$ and $r = 9$. *Slice-by-slice re-scanning* is the technique which finishes the irradiation fastest and shows no dependence on the *re-scan* number. *Breath-sampled re-scanning* irradiation, which was planned in case of breathing period of 4 s, is the second fastest mode and shows no dependence on the *re-scan* number, too. *Random-time-delay re-scanning* is the only technique with an uncertainty of the irradiation time length due to the random pauses. The number of random pauses was defined as $\mu_{\text{random}} = 0.02$ with a maximum length of 1 s. Nevertheless, this mode shows only a minor dependence on the *re-scan* number. On the other hand, the irradiation time in case of *volumetric re-scanning* is almost tripled. In the current implementation *volumetric re-scanning* is certainly the mode which uses the accelerator beam most inefficiently.

3.3.2 Patient simulation studies

Standard cases

The results and data analysis of the dose distribution of patient 1 (smallest amplitude), patient 3 (medium amplitude) and patient 5 (greatest amplitude) will be presented in the following. The V_{95}, V_{107} $D_5 - D_{95}$ data were analyzed and visualized in figures. In addition, some general statements about quality of the individual *re-scan* modes with respect to their efficiency in reducing interplay patterns shall be given in this section. The complete set of data can be found in the appendix A.1.4 where the mean values, the standard deviation and the corresponding significance test are summarized in tables.

Representative dose distributions of patient 5 are shown in figure 3.13. The dose cuts are displayed for thee selected *re-scan* modes namely *slice-by-slice*, *breath-sampled* and *random-time-delay re-scanning* for patient 5 in case of $r = 1$ and $r = 9$, respectively. The calculations illustrated the outcome of a breathing period of 4 s, a starting phase of 0°. Distinct interplay patterns can be seen in the case of $r = 1$ for all three *re-scanning* flavors. No dose inhomogeneities are visible inside the CTV when increasing the *re-scan* number to $r = 9$ in case of *breath-sampled* and *random-time-delay re-scanning*, respectively. *Slice-by-slice re-scanning* also shows an improved dose distribution at $r = 9$, but some cold and hot spots are still visible.

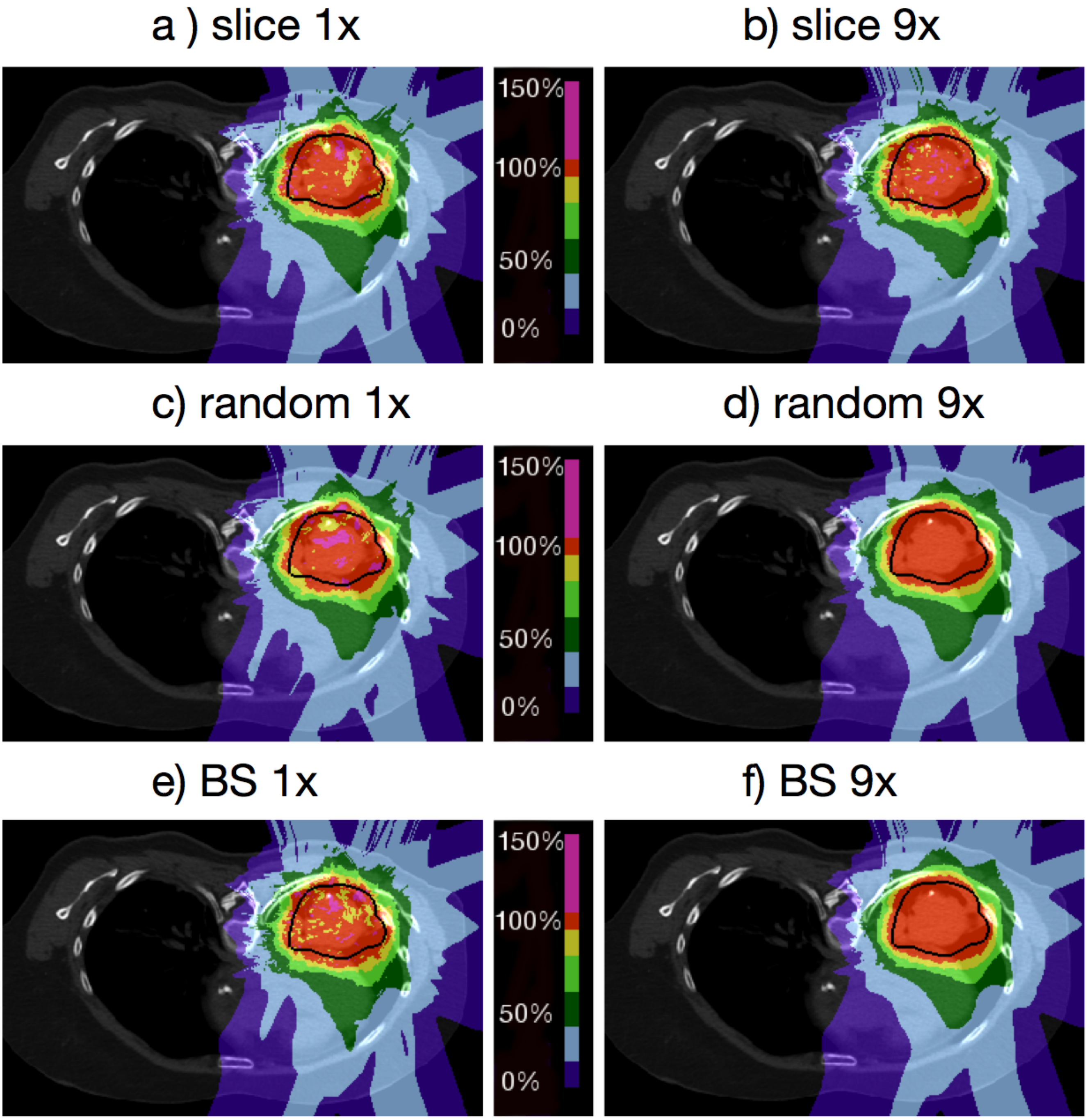

Figure 3.13.: Exemplary dose cuts of three selected *re-scan* modes, namely *slice-by-slice*, *breath-sampled* and *random-time-delay re-scanning* for patient 5 in case of $r = 1$ and $r = 9$, respectively. It can bee seen that *breath-sampled* and *random-time-delay re-scanning* reduce the interplay patterns very efficiently. The CTV represents the target contour and is outlined in black.

The upper parts of figure 3.14 a), 3.14 b) and 3.14 c) show the V_{95} analysis of patients 1, 3 and 5, respectively. It can bee seen that a larger motion amplitude results in less target coverage which cannot be efficiently compensated by *slice-by-slice re-scanning*, *volumetric re-scanning*, *mixed-scanpath re-scanning* and *local-parameter re-scanning* in all cases even for *re-scan* numbers up to $r = 17$. *Breath-sampled re-scanning* and *random-time-delay re-scanning* on the other hand can compensate the motion effects very well. The *breath-sampled re-scanning* mode requires a maximum number of $r = 9$ to reach a mean value of $V_{95} = 100\%$ in case of all five different patients. *Random-time-delay re-scanning* is also able to reach $V_{95} = 100\%$ for all patients but usually needs a larger *re-scan* number with a maximum up to $r = 17$. *Volumetric re-scanning* reaches total target coverage only in case of patient 3. *Slice-by-slice re-scanning*, *local-parameter re-scanning* and *mixed-scanpath re-scanning* are very close to $V_{95} = 100\%$ in case of the two patients with the smallest motion amplitude but they fail marginally. The significance analysis shows that *breath-sampled re-scanning* performs almost in all cases better than *slice-by-slice re-scanning*, *volumetric re-scanning*, *mixed-scanpath re-scanning* and *local-parameter re-scanning*. In case of larger motion amplitudes and medium *re-scan* numbers it sometimes also performs better than *random-time-delay re-scanning*. But altogether *random-time-delay re-scanning* is clearly the second best choice to gain good target coverage. No significant difference between *slice-by-slice re-scanning*, *mixed-scanpath re-scanning* and *local-parameter re-scanning* was found.

The lower parts of figures 3.14 a), 3.14 b) and 3.14 c) show the V_{107} analysis of patients 1, 3 and 5, respectively. It can bee seen that a larger motion amplitude results in larger overdose of the CTV which cannot be efficiently compensated by *slice-by-slice re-scanning*, *volumetric re-scanning*, *mixed-scanpath re-scanning* and *local-parameter re-scanning* in all cases even for *re-scan* numbers up to $r = 17$. The *breath-sampled re-scanning* technique needs a maximum number of $r = 3$ to reach a mean value of $V_{107} = 0\%$ in case of all five different patients. *Random-time-delay re-scanning* is also able to reach a value of $V_{107} = 0\%$ for all patients with a maximum *re-scan* number up to $r = 5$. The *volumetric re-scanning*, *local-parameter re-scanning*, *slice-by-slice re-scanning* and *mixed-scanpath re-scanning* modes can efficiently reduce the overdose to the CTV for patients 1 and 2. The V_{107} significance analysis shows the same trend as in the V_{95} case.

The corresponding $D_5 - D_{95}$ values for the three patients are shown in figure 3.15. The steepness of the dose volume histograms (DVHs) can be assessed by the corresponding $D_5 - D_{95}$. The lower this value the more homogeneous is the dose distribution of the CTV. In case of all patients the *breath-sampled re-scanning* technique resulted for a *re-scan* numbers $r \geq 13$ in a dose distribution which is almost as homogeneous and steep as an irradiation in the static case. For instance, the mean $D_5 - D_{95}$ values of patient 5 irradiated with $r = 13$ are 1.9% and 3.8% for *breath-sampled re-scanning* and *random-time-delay re-scanning*, respectively. The corresponding DVHs of the *random-time-delay re-scanning* mode are in general less steep than the ones of *breath-sampled re-scanning*. *Volumetric re-scanning* is less homogenous than those two techniques but outperforms *slice-by-slice re-scanning*, *local-parameter re-scanning* and *mixed-scanpath re-scanning*. Those three modes exhibit almost the same level of homogeneity. The $D_5 - D_{95}$ significance analysis shows the same tendencies as in the V_{95} and V_{107} cases.

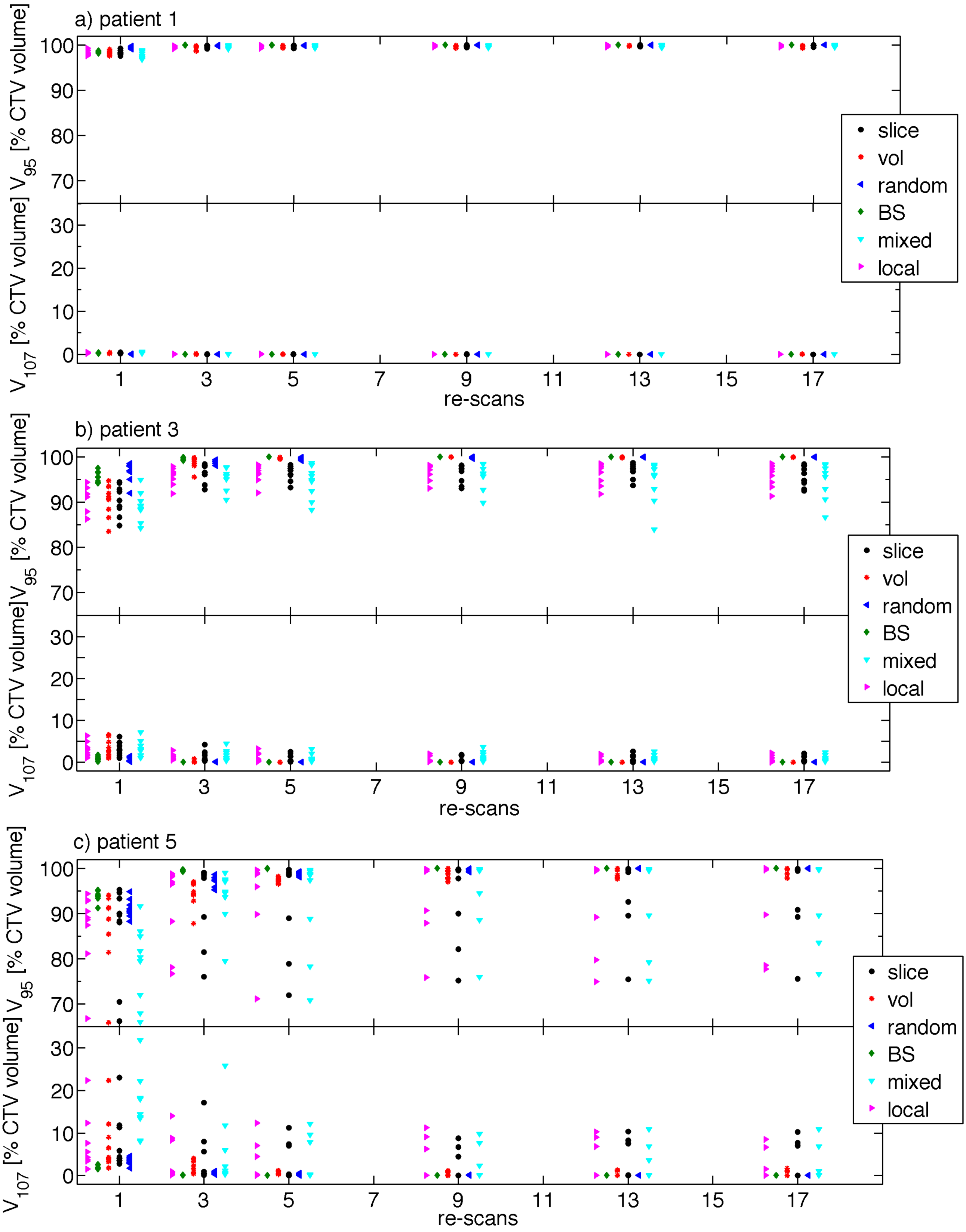

Figure 3.14.: V_{95} and V_{107} values for the different *re-scan* modes as a function of the *re-scan* number in case of a) patient 1, b) patient 3 and c) patient 5, respectively. Every case consist of twelve data points (due to the variation of the starting phases and the breathing periods) which might not be visible due to clustering of the points when increasing the *re-scan* number.

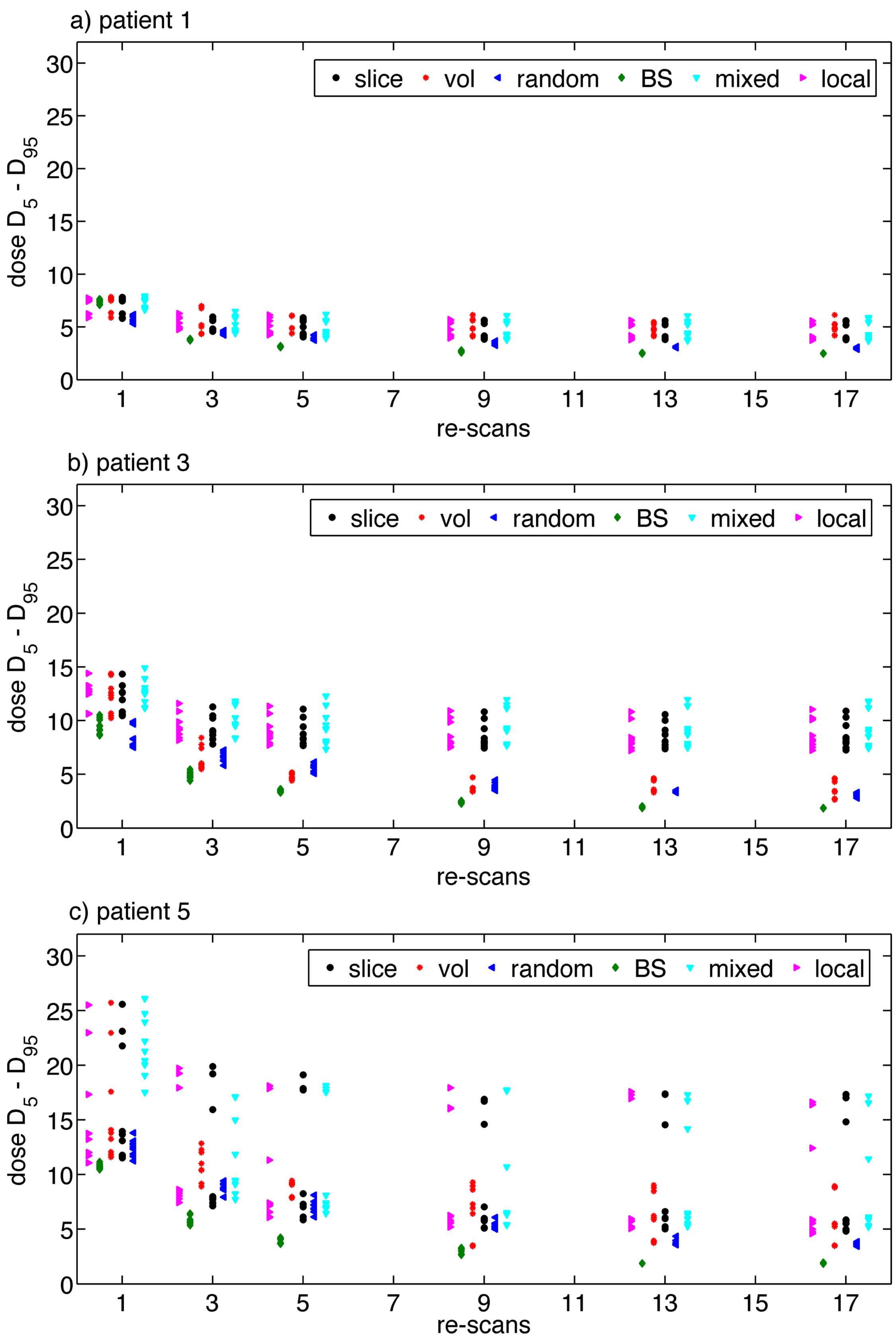

Figure 3.15.: The $D_5 - D_{95}$ values for the different *re-scan* modes as a function of the *re-scan* number in case of a) patient 1, b) patient 3 and c) patient 5, respectively. Every case consist of twelve data points which might not be visible due to clustering of the points when increasing the *re-scan* number.

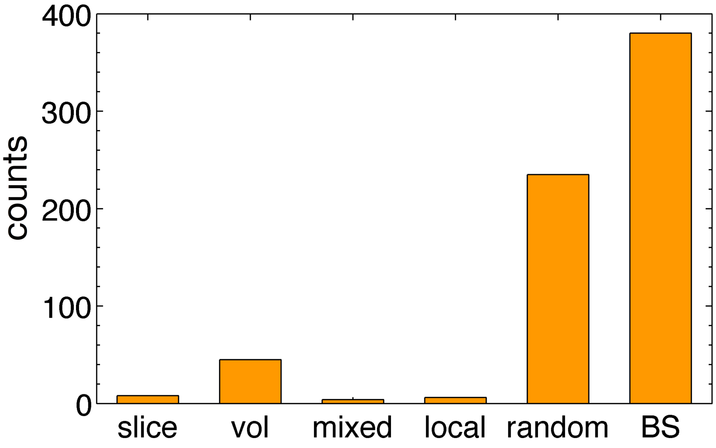

Figure 3.16.: The results of the V_{95} , V_{107} and the $D_5 - D_{95}$ significance tests are summarized in this figure. If a technique was significantly better than the other it got a count. Therefore the height of the individual bars indicates the quality of each *re-scan* mode.

About 1500 significance test have been performed for the results of the standard cases. Figure 3.16 gives an overview which technique performed best. The V_{95}, V_{107} and the $D_5 - D_{95}$ results were analyzed and if a significant difference between two *re-scan* modes was observed, the technique which performed better got a count. The numbers illustrate that *breath-sampled re-scanning* would be the best *re-scanning* choice to reduce interplay effects in the parameter space of this section. The second best option was clearly *random-time-delay re-scanning*. *Volumetric re-scanning* only got some counts when tested against the *slice-by-slice re-scanning*, *mixed-scanpath re-scanning*, *local-parameter re-scanning* modes.

Special case I - *breath-sampled re-scanning* uncertainty

The results and data analysis of the dose distribution of patients 5 will be presented in the following. The V_{95}, V_{107} $D_5 - D_{95}$ data was analyzed and visualized. The complete set of data can be found in the appendix A.1.5 where the mean values and the standard deviation are summarized in tables as well as significance tests of every case.

Figure 3.17 a) and b) illustrate that the deviations between the various motion periods get smaller when increasing r form 1 to 5 as well for the V_{95} and V_{107} analysis but that there is still a difference visible. Nevertheless, the data in the appendix shows that only one simulation (motion period 4.5 s patient 4) is not able to reach mean values of $V_{95} = 0\%$, $V_{107} = 100\%$ for the investigated range of *re-scan* numbers.

The differences between the various motion periods are more apparent by looking at the mean values of the $D_5 - D_{95}$ analysis displayed in figure 3.17 c). The $D_5 - D_{95}$ values show that the motion period of 4 s which corresponds to perfect matching of the motion period and

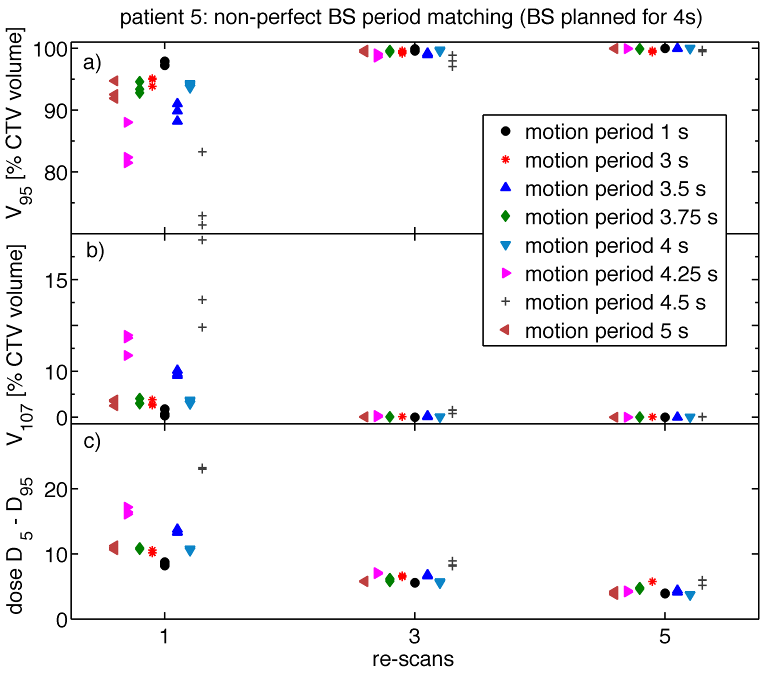

Figure 3.17.: V_{95}, V_{107} $D_5 - D_{95}$ and values for non-perfect *breath-sampled re-scanning* period matching as a function of the *re-scan* number in case of patient 5. The V_{95} is a measure of the dose coverage, the V_{107} of the overdose and the $D_5 - D_{95}$ of the homogeneity, respectively.

the *breath-sampled re-scanning* irradiation process leads in general to more homogeneous dose distributions than compared to the other motion periods. However, the difference is often not significant.

In figure 3.18 the V_{95} data of patients 4 and 5 are arranged as a function of the motion period to make dependencies of the period mismatch best visible. Independent of the *re-scan* number and the patient the curves exhibit three local maxima and two local minima. The shape of the "W" like curve is asymmetric. Small deviation of 0.25 s from the desired motion amplitude have larger impact if the motion period is longer than the irradiation time per IES. If the motion periods are 1 s and 5 s, respectively, the V_{95} results approach the level which was obtained when using the perfect matching period of 4 s.

Special case II - variation of the number and the maximum length of the *random-pauses*

The results and data analysis of the dose distribution of patients 5 for two different numbers of random pauses will be presented in the following. $\mu_{\text{random}} = 0.05$ is equivalent to 20 and $\mu_{\text{random}} = 0.2$ equivalent to 5 random pauses, respectively. The complete set of data can be found in the appendix A.1.6 where the mean values and the standard deviation are summarized in tables along with the significance tests of every case.

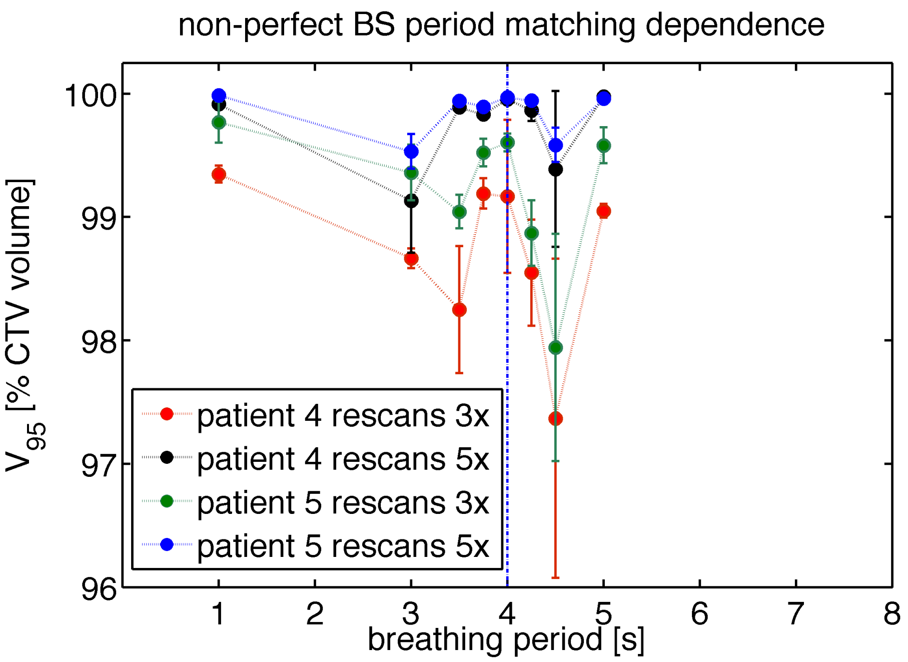

Figure 3.18.: Mean and standard deviation of the V_{95} data of patients 4 and 5 as a function of the motion period in case of the *re-scan* numbers $r = 3$ and $r = 5$, respectively. The blue line indicates the motion period of perfect *breath-sampled re-scanning* matching.

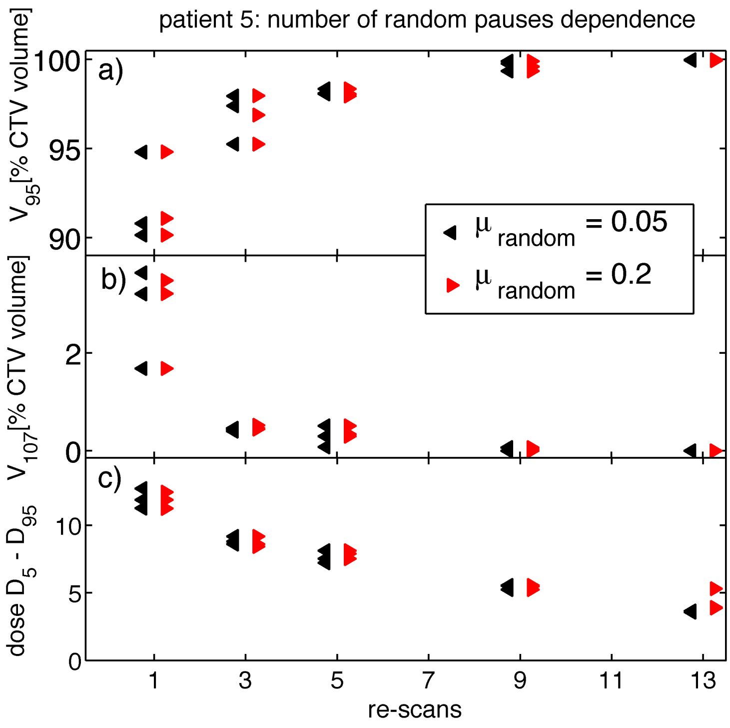

Figure 3.19.: V_{95}, V_{107} $D_5 - D_{95}$ and values for two different numbers of random pauses as a function of the *re-scan* number in case of patient 5. The maximum random pause is fixed to $T_{\text{random, max}} = 1\,\text{s}$. The V_{95} is a measure of the dose coverage, the V_{107} of the overdose and the $D_5 - D_{95}$ of the homogeneity, respectively.

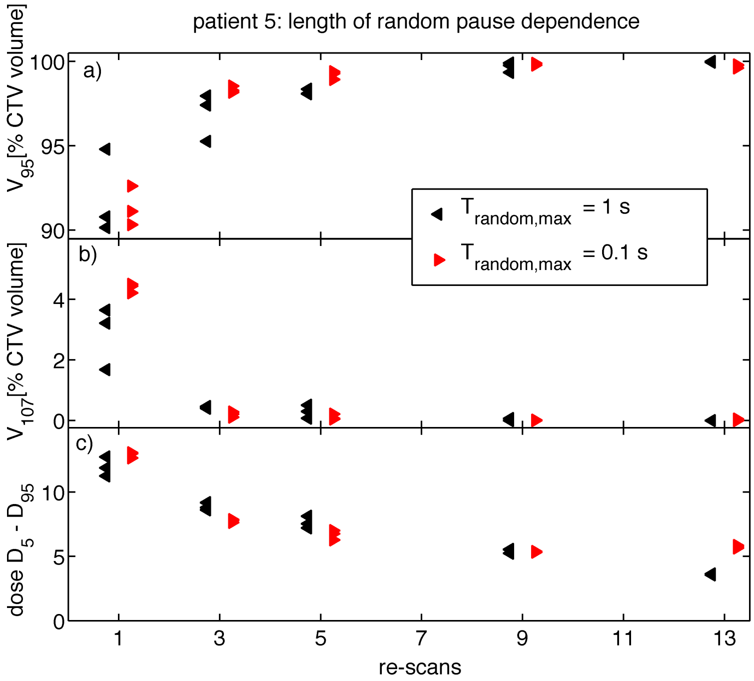

Figure 3.20.: V_{95}, V_{107} $D_5 - D_{95}$ and values for two different values of the maximum random pause length as a function of the *re-scan* number in case of patient 5. The number of random pauses is set to $\mu_{\text{random}} = 0.02$. The V_{95} is a measure of the dose coverage, the V_{107} of the overdose and the $D_5 - D_{95}$ of the homogeneity, respectively.

Figure 3.19 shows that the variation between those two numbers of random pauses has very little influence on the V_{95}, V_{107} and the $D_5 - D_{95}$ results. The statistical analysis showed only for the $D_5 - D_{95}$ values at $r = 13$ a significant better result of the higher number of random pauses.

Figure 3.20 shows that the variation of the maximum length of the random pauses has very little influence on the V_{95}, V_{107} and the $D_5 - D_{95}$ results, too. The statistical analysis showed that $T_{\text{random, max}} = 0.1\,\text{s}$ is the better option in three cases and $T_{\text{random, max}} = 1\,\text{s}$ in two cases. However, the absolute difference is actually so small that it is not expected to influence the outcome of a treatment.

3.4 Discussion

The simulation results of the patient study give an extensive overview of the properties of motion mitigation when using scanned particle beams in combination with *re-scanning*.

Uncertainties in the beam application are addressed as well as specific uncertainties in the *breath-sampled re-scanning* and the *random-time-delay re-scanning* mode. Especially these two *re-scan* modes show very promising results and facilitate the irradiation of the CTV with a satisfying quality even for large tumor motion. The consideration of uncertainties is essential to predict the outcome of real patient irradiations.

The adequately adapted parameter space ensures that the simulation results are not statistically unlikely outliners. Due to the experience at our group at GSI, the *re-scanning* technique can be easily classified in a broader context by comparing the results with other motion mitigation techniques like *beam tracking* (Lüchtenborg, 2012; Eley, 2013) and the *fractionation effect* (Woelfelschneider, 2011) investigated at our institute. In addition, the results were also compared with the findings of other research groups from all over the world (e.g. (Mori et al., 2013; Knopf et al., 2011; Phillips et al., 1992; Seco et al., 2009)).

3.4.1 The physical-beam-record simulation environment

The broad distribution of figure 3.11 a) reveals that some points would receive a particle level which is over 50% off the prescribed values. At a first glance this seems to be unacceptable because too much dosage can lead to necrotic tissue and too less will increase the surviving of cancer cells inside the CTV. The error in the number of particles is inversely proportional to the total treatment time of this point which means that the proximal IESs will certainly be the one with the biggest variations because the nominal particle number is lowest in these slices. But the rasterpoints in those regions receive pre-irradiation from the more distal slices which also contributes to their integral dose (see figure 2.10). Weighting the rasterpoints relative to their importance improves the error of the particle number to ±9% (see figure 3.11 b)) which is still considered to be too large. Almost the same effect can be observed by including the influence of *re-scanning* in the analysis (see figure 3.11 c)). The intrinsic feature of *re-scanning*, namely statistical averaging, is not only limited to smoothing interplay patterns which emerge because of the influence of intra- and inter fractional motion, but of a more general nature. Combining the two features yields the best approximation to the real system and shows that only 4% of the rasterpoints are irradiated with an error of ±1% in terms of the particle counts. Furthermore, smaller *re-scan* numbers and a lower intensity, which might be sufficient to compensate interplay patterns, will further decrease these deviations. Table 3.7 also includes calculations using an artificial spill with a perfect square shape. The results are even better because large spikes in a beam spill profile cause the largest deviations.

In contrast to the nearly gaussian shaped deviation curve which is caused by the therapy control system at GSI the deviations at HIT yield a systematic tendency towards too large particle numbers because the information of the previously irradiated rasterpoint is not used to correct the particle number of the next one. Figure 3.11 e) shows that the most frequent particle number is the one with an excess of 1%. Due to the finer sampling rate the maximum error is reduced by 30% compared to GSI. Including the effects of pre-irradiation (see 3.11 f)) clearly improves the irradiation quality better than the *re-scanning* effect (see 3.11 g)). The reason is that the systematic errors at HIT cannot be compensated as efficiently as the random errors at

GSI by statistical averaging. Figure 3.11 h) illustrates that the combination of both corrections results in particle deviations below 1% of each rasterpoint.

Until now the focus was on the irradiated particle numbers of each rasterpoint which is a slightly different issue than looking at the total dose deviation. The analysis of the particle numbers according to equation 3.3 does not take the pre-irradiated dose contributions into account which is in general a complex RBE-weighted value of the mixed radiation field[2]. The purpose of the weighting factor in equation 3.3 is only to scale the rasterpoints with respect to their relative importance like already mentioned.

The total dose corresponds therefore simply to the total number of particles which are applied in the investigated case. The total over- and underdosage contributions cancel out at GSI whereas the overdose sums up to 1.3% of the total planned dose at HIT at 25 *re-scans* and maximum intensity when using the measured spill profile. This is therefore a kind of worst case scenario but nevertheless worthwhile to keep in mind.

Both approaches tackle the issue of the dose application from different sides and shall therefore be both considered. Only looking at the total dose can lead to overlooking cases when, e.g., two IES are irradiated with wrong dose levels which could cancel each other out. On the other hand, only looking at the irradiated particle numbers could, e.g., underestimate to total applied dose.

In order to mimic the existing systems as close as possible it is therefore advisable to use the PBP_{corr} data input for the simulations environment since this data includes all the necessary information as it was done throughout this thesis when calculating dose distributions with TRiP. The analysis indicates that the influence of the therapy control systems at HIT and GSI should be small enough to facilitate *re-scan* irradiation.

With respect to economic considerations a fast irradiation process is desirable. Figure 3.12 displays the duration of different *re-scan* modes to finish the dose application. Within the simulation environment which was created in the scope of this theses there is no difference of the irradiation times of the *mixed-scanpath re-scanning*, *local-parameter re-scanning* and *slice-by-slice re-scanning* techniques. Hence, only *slice-by-slice re-scanning* is shown which is also the fastest method for this investigated case.

Volumetric re-scanning takes longer because after each *re-scan* run the energy is changed which takes each time additional 3.3 s. When increasing the number to $r = 9$ *re-scans* the number of additional pauses of the synchrotron to chance its energy is multiplied by three and therefore the time duration increasing accordingly, too.

For the case of $r = 3$ *random-time-delay re-scanning* is even longer than *volumetric re-scanning*. That is due to the fact that the number of random pauses was set to 20 ($\mu_{\text{random}} = 0.05$). These twenty random pauses of a duration with a maximum length of 1 s added up so that *random-time-delay re-scanning* took longer than *volumetric re-scanning*. This is the only mode with an

---

[2] These calculations are incorporated when performing the simulations with TRiP

uncertainty with respect to treatment length. When increasing the number of *re-scans* to $r = 9$ the number of random pauses keeps constant. Therefore it could even happen that the time duration is shorter than in case of $r = 3$. In this example it was slightly longer but this time approximately 250% faster than the corresponding *volumetric re-scanning* irradiation. In the current implementation of the *breath-sampled re-scanning* method the full spill length has to pass even if the irradiation of has been finished before. *Breath-sampled re-scanning* is calculated with a spill having a length of 10 s and *slice-by-slice re-scanning* with duration of 2.2 s which therefore results in longer irradiation time of the *breath-sampled re-scanning* technique.

3.4.2 Patient simulation studies

Standard cases

In this treatment planning study six difference *re-scanning* modes *slice-by-slice re-scanning*, *volumetric re-scanning*, *mixed-scanpath re-scanning*, *local-parameter re-scanning*, *random-time-delay re-scanning* and *breath-sampled re-scanning* have been compared for the treatment of lung tumors. Due to the very large number of simulation results the V_{95}, V_{107} and the $D_5 - D_{95}$ data is an appropriate option to present the outcomes in a compact and instructive way.

As it is already shown in other reports (e.g. (Mori et al., 2013; Knopf et al., 2011; Phillips et al., 1992; Bert and Durante, 2011)) the interplay effect is more distinct in case of greater motion amplitudes. The data illustrates that in case of the patients with the smallest amplitude the V_{95} and V_{107} saturate already for a *re-scan* number of $r = 5$. There is only a small difference between the individual techniques. However, only *random-time-delay re-scanning* and *breath-sampled re-scanning* reach a mean value of $V_{95} = 100\%$. The other techniques generally yield their maximum value already at $r = 5$ but they do not improve when increasing the *re-scan* number. For instance, in case of patient 2 the mean values of V_{95} are 99.5% and 99.4% at $r = 5$ and $r = 21$, respectively. The reason might be that those four techniques do not exhibit an extra feature which was merely introduced to break up a possible synchronicity between beam application and tumor motion. Even if a certain correlation, which creates a distinct interplay pattern, is broken up by changing the number of *re-scans* it can happen that another correlation emerges. Those two interplay patterns are likely to look different but both prevent that a value of $V_{95} = 100\%$ can be achieved.

The corresponding $D_5 - D_{95}$ analysis backs up this explanation. It is a measure of homogeneity and shows larger diversion of the data point than the V_{95} analysis. Two dose volume histograms (DVH) can look different but both having values of $V_{95} = 100\%$ and $V_{107} = 0\%$, respectively. Hence, the $D_5 - D_{95}$ data must be used to investigate the results more thoroughly. The analysis of patients 1 and 2 reveals that *breath-sampled re-scanning* and *random-time-delay re-scanning* both have lower $D_5 - D_{95}$ values than the other modes. However, the more crucial point is that the results of *breath-sampled re-scanning* and *random-time-delay re-scanning* not only get significantly better when increasing r but the variation of the data points is also greatly reduced so that both modes yield the same results independent of the starting conditions. It follows that both techniques can break up correlation without introducing new synchronicity effects. On the other hand, when inspecting the *slice-by-slice re-scanning*, *volumetric re-scanning*, *local-parameter re-scanning* and *mixed-scanpath re-scanning* results the fluctuation of the data points is almost constant in case of $r \geq 5$ which means that the homogeneity is not really improved when increasing the *re-scan* number.

In case of larger motion amplitudes (patients 3, 4 and 5) the differences between *random-time-delay re-scanning* and *breath-sampled re-scanning* and the four other *re-scanning* modes get more evident. Only *random-time-delay re-scanning* and *breath-sampled re-scanning* turn out to be a possible treatment modality in case of larger motion amplitudes. Nevertheless, the reason of these differences is again that only those two techniques can efficiently reduce the interplay effect.

The analysis of patient 5 shows that a high correlation between beam application and tumor motion was reached for a period of 5 s in case of the techniques *slice-by-slice re-scanning*, *local-parameter re-scanning* and *mixed-scanpath re-scanning*, respectively. The three data points having the worst results throughout all of the figures of this patient turned out to be related to this breathing period.

But also for all other patients *slice-by-slice re-scanning*, *local-parameter re-scanning* and *mixed-scanpath re-scanning* yield very similar results and the significance analysis showed in principle no difference between these threes modalities. In case of the distal slices, the number of *re-scans* per IES of the *slice-by-slice re-scanning* and *random-time-delay re-scanning* mode are identical or deviated only slightly which has only minor influence on the outcome for $r \geq 5$. The proximal slices exhibit a larger difference between the number of *re-scans*. For instance in *local-parameter re-scanning* mode, the most distal slice of patient 5 (field beam entrance angles of 20°) is irradiated with $r = 17$ and the most proximal IES with $r = 2$. But due to pre-irradiation, the weighting of those more proximal slices with respect to the total dose is obviously so much less that the irradiation quality stays on almost the same level like using the *slice-by-slice re-scanning* technique.

Knopf et al. (Knopf et al., 2011) report more satisfying dose distributions in the presence of motion if more fields are used and if the motion direction is parallel to the main direction of the pencil beam. In the present simulations four individual fields contribute to the total dose distribution which results in an *effective re-scan number* that is four times the *re-scan* number which is displayed in all the figures. Hence, the dose distributions get rapidly better as a function of the *re-scan* numbers compared to simulations using only a single field approach.

In the scope of this thesis (see section 4.3.3) it was also found that less interplay patterns emerge when the motion direction is parallel to the main direction of the pencil beam. In fact, this was the motivation to introduce *mixed-scanpath re-scanning*. A *re-scanning* mode which changes the main direction of the pencil beam for every consecutive run should be more robust than a mode with a fixed scanpath direction. However, the results show no significance difference between *slice-by-slice re-scanning* and *mixed-scanpath re-scanning*. The data points lie almost always on the same level. The reason is that in the experiments (see section 4.3.3) the setup was designed so that the motion directions were parallel as well as perpendicular to the main scanning path. When calculating the patient studies it is unlikely that these conditions are met as accurate as in the designed experiments. In addition, even if one field would meet the requirements, the other three fields will most likely not because in case of lung tumor motion there is typically only one dominant motion direction. Therefore, it might be worthwhile to investigate the differences of *mixed-scanpath re-scanning* and *slice-by-slice re-scanning* for irradiation with less irradiation fields than used in this study.

Figure 3.16 illustrates that *breath-sampled re-scanning* is the most efficient and in principle the best method to reduce interplay effects because it is the technique which is in most cases significantly better compared to all the other modes. Even if *breath-sampled re-scanning* is not in many cases better than *random-time-delay re-scanning*, the difference in the height of the corresponding bars emerges from the fact, that *breath-sampled re-scanning* is simply much more often better significantly better as *random-time-delay re-scanning* compared to the other four *re-scanning* flavors. This discrepancy of *random-time-delay re-scanning* and *breath-sampled re-scanning* arises from the fact that the irradiation of *random-time-delay re-scanning* is not exactly matched to the motion period so that some motion phases receive more irradiation than others. In the simulations the number of random pauses was sufficiently high so that the irradiations took longer than the motion period. If the number of random pauses is chosen too low it might happen that correlations are not being broken as efficiently and that the irradiation is being finished in a time duration which is shorter than the motion period. The later case could result in motion phases which would receive no irradiation at all.

Figure 3.16 also confirms that *slice-by-slice re-scanning*, *mixed-scanpath re-scanning* and *local-parameter re-scanning* are approximately identical efficient in reducing the interplay patterns of the investigated patient studies but that they are less efficient than *volumetric re-scanning*. However, since *volumetric re-scanning* has no extra feature to break up synchronicity it seems that it could happen that the reduction of interplay patterns might be less efficient in case of another combination of patients and beam application properties.

Mori et al. (Mori et al., 2013) also observed in their studies with a motion phantom that *volumetric re-scanning* yields better results than *slice-by-slice re-scanning*. In addition, they simulated a technique called Phase-Controlled Volumetric *re-scanning* which is in principle beam application in the *volumetric re-scanning* mode within one ore more *gating* windows. They matched the intensity so that the irradiation is finished at the end of a *gating* window. In their case study they used the whole motion period as a *gating* window and compared it to Phase-Controlled

Layered *re-scanning* which is basically their implantation of *breath-sampled re-scanning*. In all investigated cases Phase-Controlled Layered *re-scanning* was superior to Phase-Controlled Volumetric *re-scanning*. The data presented in the scope of this theses indicate a better reduction of interplay effects for *breath-sampled re-scanning* than presented by Mori et al. One reason might be due to the fact that they used a single field approach.

Furthermore Mori et al. show the effect of different dose levels on the interplay patterns. Their data reveal no tendency as a function of the prescribed dose but only fluctuations. A possible explanation could be that changing the dose levels simply can increase or decrease the correlation between beam application and tumor motion because the sweeping velocity of the pencil beam is changed. They further investigated the effect of motion amplitude and motion direction. The results are qualitatively in accordance with the findings in the scope of this thesis.

In accordance to the initial studies by Seco et al. (Seco et al., 2009) who compared different *re-scan* modes with respect of a box shaped target immersed in water in the presence of water with a single field approach *breath-sampled re-scanning* turned out to be the most efficient method to reduce interplay patterns.

R. Lüchtenborg (Lüchtenborg, 2012) performed studies in the presence of motion for exactly the same patients as done in this thesis. R. Lüchtenborg investigated how efficiently *beam tracking* (BT) and *real-time dose compensation combined with beam tracking* (RDBT) can reduce interplay patterns. RDBT is an advanced version of BT. In this flavor the prescribed number of particles of the rasterpoints which have not been irradiated yet are online corrected due to unwanted pre-irradiation levels. The analysis in his thesis showed that the dose distributions of a whole treatment course of RDBT and BT yield in general worse or similar results than all *re-scanning* modes at $r \geq 9$ for patients 1 and 2 with respect to the mean values of V_{95}, V_{107} and the $D_5 - D_{95}$.

In case of the two patients with the largest motion amplitude, namely patient 4 and 5, the results of RDBT and BT are worse than those of *breath-sampled re-scanning* and *random-time-delay re-scanning* but better than *slice-by-slice re-scanning*, *mixed-scanpath re-scanning* and *local-parameter re-scanning* in case of $r \geq 9$. The analysis of R. Lüchtenborg showed for instance that the dose distribution can get worse when using RDBT and BT even if the motion amplitude is decreased when inspecting the data of patients 3 and 4, respectively[3]. This indicates that there is still another factor which introduces some uncertainty but the size of the motion amplitude. Van de Water et al. (van de Water et al., 2009) also simulated BT on heterogenous phantoms and found that BT can produce dose inhomgeneities for heterogeneous targets. This might be the reason why interplay patterns cannot be as efficiently be compensated as with *breath-sampled re-scanning* and *random-time-delay re-scanning*.

---

[3] The analysis of the patients 4 and 2 in the thesis of R. Lüchtenborg correspond to the patients 3 and 4 of this thesis.

On the other hand, the irradiation of the healthy tissue is greatly reduced in case of BT and RDBT. *Re-scanning* needs an ITV which covers all motion phases whereas perfect BT or RDBT stresses the healthy tissue virtually to the same level as in the case of static irradiation. This gets especially important if organ at risk (OAR) are close to the tumor.

An even better sparing of healthy tissue is achieved by the *4D optimization for scanned ion beam tracking of moving tumors* developed and studied in the scope of the thesis of J. Eley (Eley, 2013). The principle idea of this method is that the dose levels are not constant over all motion phases but increased if the tumor is farther away from the OAR. In addition, the *4D optimized beam tracking* also improves target dose homogeneity for the investigates lung tumor patients compared with *3D optimized tracking* which is used in the thesis of R. Lüchtenborg (Lüchtenborg, 2012). *4D optimization* does in general potentially allow better treatment characteristics. An alternative option to the one of J. Eley has recently been reported by Graeff et al. (Graeff et al., 2013). They showed a solutions based on dedicated structuring of the CTV and included experimental studies which show the feasbility to actually apply such a treatment plan.

Furthermore, J. Eley (Eley, 2013) investigated the robustness of scanned ion beam tracking with respect to realistic motion and beam application uncertainties. The investigated patient was identical to patient 5 of this thesis. J. Eley confirmed the results of Van de Water et al. (van de Water et al., 2009), namely that even perfect *beam tracking* cannot reduce inhomgeneities as reliable as *re-scanning* when irradiating heterogeneous targets in the presence of motion. By incorporating realistic motion detection and beam application related errors, J. Eley received dose distributions in case of patient 5 which resulted in worse results of the V_{95}, V_{107} and the $D_5 - D_{95}$ measures than obtained with *breath-sampled* or *random-time-delay re-scanning*.

The dose levels to the OAR (heart, spinal cord and esophagus) for patients 1, 3, 4 and 5 were already studied in the thesis of J. Wölfelschneider (Woelfelschneider, 2011) who investigated the reduction of interplay effects as a function of the number of treatment fractions. For those 4 patients exactly the same ITV was used as in this thesis so that the dose distributions should be very similar inside the OAR. For instance, the analysis of J. Wölfelschneider showed that the mean dose of patient 5 to the heart exceeded the dose limit of 7 Gy (Hof et al., 2007). This OAR could not be spared, because its location was close to the target volume. All other mean doses were below the corresponding dose limits of the corresponding OAR.

The analysis of the efficiency of the number of the treatment fractions to reduce interplay effects (Woelfelschneider, 2011) shows that *breath-sampled re-scanning* and *random-time-delay re-scanning* yield significantly better results than increasing the number of fractions with respect to the mean values of V_{95}, V_{107} and the $D_5 - D_{95}$. Only patient 1 with the smallest motion amplitude reaches mean values of $V_{95} = 100\%$ and $V_{107} = 0\%$, respectively. The inspection of all the data points indicates that *volumetric re-scanning* is the *re-scanning* flavor whose results are closest to those of the *fractionation effect*. This is in accordance with the statement of J. Wölfelschenider that irradiating patients with four fields and ten fractions is physically comparable to a 40 times volumetric *re-scanning* (Woelfelschneider, 2011).

Special case I - *breath-sampled re-scanning* uncertainty

As expected, the irradiation duration of 4 s which exactly matches the breathing period yields the best results because all motion phases are equally covered. Figure 3.18 illustrates, if the breathing period is -0.25 s shorter than the irradiation duration it has only a small impact on the dose distribution. In this case all motion phases were irradiated even if some motion phases receive more dose than others. On the other hand, if the breathing period is $+0.25$ s longer than the irradiation duration the effect on the dose distribution especially for low *re-scan* numbers is larger because not all motions phases received irradiation.

A further increase of the deviation leads to local minima at both arms of the "W" shaped curve because the relationship of the dose levels of the individual motion phases gets most disadvantageous. However, increasing the deviation even more improves the dose distribution again. In case of a motion period of 1 s[4] the target moves four times through all its motion phases which decreases the imbalance of the motion phases. In addition, the total irradiation time in this case is an integer number of times of the respiration cycle. Furukawa et al. (Furukawa et al., 2010a) already stated that this is especially efficient in reducing interplay patterns.

If the motion period gets longer the target approaches the case of a static irradiation. Therefore it is not surprising that dose distributions will also get better when increasing the breathing period. However, it is quite surprising that already a breathing period of 5 s leads to a dose distribution which is not much worse than the one with the perfect matching period. Another smoothing effect compared to the standard cases could be the fact that the irradiation length per IES is prolonged to 4 s whereas the spill length was 2.2 s in case of *slice-by-slice*, *volumetric*, *local-paramter* and *mixed-scanpath re-scanning* modes in the corresponding simulations (see section 3.3.2) with a breathing period of 5 s of the patients.

The study of Shirato et al. (Shirato et al., 2004) showed an average standard deviation of 0.5 s of the investigated lung tumor breathing periods from different patients. Those variations in the breathing periods are in the range as to shift the dose distributions into the local minima. Systematic shifts of the breathing period could be accounted for by measuring the breathing period during the treatment and online adjustment of the spill intensity as to match the motion period. However, there is no way to predict the duration of the next breathing cycle. Further simulations could be performed to investigate the effect of changing breathing periods on the outcome of the treatment course. For instance, a probability distribution of the breathing periods could be incorporated into a Monte-Carlo simulation environment as to calculate the dose distributions. S. Hild et al. (Hild et al., 2013) report on new methods that allow quantification

---

[4] this rather short breathing period was included in the simulations due to academic curiosity

of uncertainties and their visual presentation for treatments of intra-fractionally moving tumors using a scanned ion beam.

If those simulations would yield that *breath-sampled re-scanning* needs some improvements due to the uncertainty in the breathing cycle, there are many possible ways to adapt the method. For instance, the irradiation of each slice could be subdivided in several parts - the irradiation of each part matching the best guess of the upcoming breaching cycle.

Special case II - variation of the number and the maximum length of the *random-pauses*

The results show almost no dependence if the number of *random-pauses* is reduced from $n_{random-pauses} = 20$ to $n_{random-pauses} = 5$. The reason might be that it is especially important to have a larger number of *random-pauses* than *re-scans*. Interplay patterns due to correlation emerge if the subsequent *re-scan* runs start relative to the moving tumor at the same position. A *random-pause* after every *re-scan* run reduces the probability that every *re-scan* run starts in the same motion phase. Introducing even more random pauses during a *re-scan* run does therefore not necessarily increase the probability that the correlation is broken more efficiently.

Therefore it is not surprising that both $n_{random-pauses} = 20$ and $n_{random-pauses} = 5$ yield similar results in case of $r \leq 5$. However, even for *re-scan* numbers $r > 5$ the outcomes for both numbers of *random-pauses* yield dose distribution of the same quality. The reason should be that the statistical averaging effect gets more and more dominant when increasing the *re-scan* number. This is likely to compensate the lower number of *random-pauses*.

The variation ($T_{\text{random, max}} = 1\,\text{s}$, $T_{\text{random, max}} = 0.1\,\text{s}$) with respect to the maximum length of the random pauses showed only very little difference of the measures V_{95}, V_{107} and $D_5 - D_{95}$, respectively.

A shorter $T_{\text{random, max}}$ will slightly decrease the treatment time and the likelihood that the end of a *random-pause* will be placed into a spill pause so that additional time will pass by until the irradiation can continue if $T_{\text{on, random}}$ is greater than the total spill length (see section 3.2.1). On the other hand, if the $T_{\text{random, max}}$ is too short the correlation between the beam application and the motion might not broken as efficiently than using longer *random-pauses*. The reason is, if the length approaches $T_{\text{random, max}} = 0\,\text{s}$ the dose distribution of the *random-time-delay re-scanning* mode will also align with the dose distribution of *slice-by-slice re-scanning*. However, this was obviously not the case when using $T_{\text{random, max}} = 0.1\,\text{s}$.

Furthermore, the longer $T_{\text{random, max}}$ is chosen the higher is the probability that all motion phases are being irradiated which is likely to increase the quality of the irradiation process. Of course, the irradiation time per IES can also be expanded by reducing the intensity of the beam.

Overall, it follows that *random-time-delay re-scanning* is a very effective and robust method to reduce interplay patterns. No additional online motion monitoring and no online adaption of the parameters of the therapy system should be necessary to yield satisfying irradiation quality.

3.5 Conclusion and outlook

Six different *re-scanning* modes have been analyzed with respect to their effectiveness in reducing the interplay effects of tumor motion by simulating patient treatments. In the ideal case, *breath-sampled re-scanning* is the best and *random-time-delay re-scanning* the second best option to reduce interplay effects. Even the rather large tumor motion of 26 mm of patient 5 can be compensated very efficiently with both techniques.

Out of the six investigated *re-scan* flavors only *breath-sampled re-scanning* depends on patient information (breathing period) during the treatment course. Prior to the irradiation of an IES, the intensity needs to be adjusted according to the best guess of the upcoming breathing period. However, this time duration cannot always be predicted with sufficient precision. If, e.g., a patient needs to cough during the irradiation, it might follow that the motion pattern can be changed so that the pre-adjusted intensity is too high or too low and the dose distribution is being shifted to the local minima like displayed in figure 3.18. Nevertheless, the measures at those two minima still outperform the corresponding values of *slice-by-slice*, *volumetric*, *mixed-scanpath* and *local-parameter re-scanning*. Further investigations (e.g. a finer time spacing) with respect to the period mismatch seem worthwhile.

On the other hand, *random-time-delay re-scanning* does not need any patient monitoring during the treatment and no accelerator system with the capability to adjust the intensity according to the breathing period. *Random-time-delay re-scanning* is very robust with respect to the investigated uncertainties and the efforts to implement this *re-scanning* flavor in an existing system should be less complex than for *breath-sampled re-scanning*.

Overall, both *random-time-delay re-scanning* and *breath-sampled re-scanning* yield excellent results with respect to reducing interplay effects in the presence of motion. These two modes should be the first choice when clinics aim to compensate tumor motion by *re-scanning*.

It is a general trend in the field of medicine that the therapy approaches get more and more adapted to the individual patient in consideration. Therefore, physicians aim for very flexible treatment options. To meet these requirements, it is also possible to combine *re-scanning* with *gating* (Furukawa et al., 2010a; Mori et al., 2013) or *beam tracking* (van de Water et al., 2009) to increase the number of possible treatment options. For example, the combination of *re-scanning* with either of the two techniques should decrease the ITV and hence reduce the irradiation of healthy tissue - which might be most beneficial if organs at risk are located close to the tumor.

It seems especially worthwhile to perform extensive studies in the future which investigate if *re-scanning* could improve the dose homogeneity of *beam tracking*. It is shown that even perfect *beam tracking* causes dose inhomogeneities when irradiating heterogeneous targets (van de Water et al., 2009; Eley, 2013). J. Eley (Eley, 2013) illustrated that *realistic beam tracking* is biased by random and systematic errors of various kinds. The influence of theses errors could be weakened by using *re-scanning* in combination with *beam tracking*. Compared to using *re-*

scanning alone, the combination could lead to a greatly reduced ITV. Possible modes which could be combined with *beam tracking* are *slice-by-slice*, *volumetric*, *mixed-scanpath* and *local-parameter re-scanning*.

4 Dosimetry and feasibility aspects of *re-scanning* irradiation

4.1 Introduction

Clinical unacceptable under- and overdosages are likely to result when scanned particle therapy is applied to a moving tumor (Phillips et al., 1992; Lambert et al., 2005; Bert et al., 2008b). This chapter shows experimental and simulation results of *re-scanning* irradiation with carbon ions in active scanning mode to mitigate the effects of target motion with respect to its dosimetric feasibility and reproducibility.

If constant irradiation duration is planned, the delivery time per beam position is in general proportionally reduced with the number *re-scans* r. Therefore, beam application in the *re-scan* mode sets new demands on deflecting magnets, energy variation and dosimetry detectors because the pencil beam has to sweep much faster across an iso-energy slice (IES).

This increased scan speed might manipulate the ionization chamber output that controls the irradiation due to recombination effects which could result in a falsified dose application (Leroy and Rancoita, 2009; Brusasco et al., 2000). Especially since some facilities tend to decrease the number of fractions by simultaneously increasing the dose per irradiation (Tsujii and Kamada, 2012) a reliable dosimetry gets even more important because, for example, so called cold spots (areas with underdosage in the clinical target volume (CTV) during the irradiation process) will have larger impact when reducing the number of fractions as shown by Wölfelschneider et al. (Woelfelschneider, 2011).

As a first step *slice-by-slice re-scanning* was implemented at GSI Helmholtzzentrum für Schwerionenforschung GmbH (GSI) and at Heidelberg Ion-Beam Therapy Centre (HIT) and fundamental irradiations were performed with regular target volumes to investigate whether the dose can be delivered as prescribed. Step by step the complexity of the experiments was increased and it was investigated how efficiently *re-scanning* is able to reduce interplay patterns which result when irradiating moving radiographic Kodak X-Omat V films vertical and horizontal in beams's eye view free in air. Finally, 3D plans were irradiated at HIT in *slice-by-slice re-scanning* and *breath-sampled re-scanning* in the presence of motion with the help of phantoms which were designed to mimic real patient treatment (Steidl et al., 2012b). The question, if *re-scanning* can be technically implemented at HIT so that it might be a treatment option in the future for patient with moving tumors shall be discussed. For all experimental measurements a simulation environment was created which took the setup parameters into account to validate the results.

4.2 Material & methods

4.2.1 *Re-scan* implementation - general aspects

The decision which *re-scan* technique to implement mainly depends upon the following two criteria:

- **Technical feasibility:** In general, every therapy facility has its unique design of treatment planning, accelerator, beam steering and detector systems. These combinations along with the interaction of software and hardware can inhibit the implementation of one or more of the different *re-scanning* techniques. For example, *random-time-delay re-scanning* interrupts the irradiation many times for a random time interval or *breath-sampled re-scanning* needs spill lengths of at least the duration of the breathing period. The currently existing system at GSI has not been designed to inherently exhibit these features.

- **Clinical relevance:** Other *re-scan* modes might be technically feasible but they could have other drawbacks. For example, *volumetric re-scanning* changes the beam's energy after each *re-scan* run of every single IES, so that the whole volume is scanned *n-times*. The synchrotron of GSI needs 3.3 s to change the particle's energy. So the additional time duration for *volumetric re-scanning* compared to *slice-by-slice re-scanning* would roughly be

  $$T_{additional} = 3.3\ \mathrm{s} \cdot (r-1) \cdot n_{IES}, \qquad (4.1)$$

  with r as the number of *re-scans* and n_{IES} as the number of iso energy slices. If two *re-scanning* techniques show similar dose distribution they choice will always be the one with the shortest irradiation time. This will lower the costs of the clinical treatment and more patients can benefit from the therapy. Other centers use range shifters to achieve a fast energy variation. They report a time of 80 ms (Zenklusen et al., 2010) and 500 ms (Furukawa et al., 2010b) to change the energy, respectively. In those cases *volumetric re-scanning* becomes a sensible option.

In the scope of this thesis *slice-by-slice re-scanning* was integrated at GSI and *slice-by-slice re-scanning* as well as *breath-sampled re-scanning* have been implemented at HIT. The rationale of this choice is as follows. *Slice-by-slice re-scanning* required the fewest changes to the beam application system of GSI and HIT. Moreover, it should be compatible with most of the existing and planned therapy facilities and can therefore serve as reference basis if various institutes try to compare their results. *Breath-sampled re-scanning* is the most promising type (see chapter 3.3) but also more challenging in its demands of the accelerator properties. As mentioned: In the ideal case, the irradiation time of every single IES should exactly match the motion period of the tumor. Various groups showed that the large majority of breathing periods lies between 3 s and 5 s (Ionascu et al., 2007). Shirato et al. (Shirato et al., 2004) report an average value of 3.6 ± 0.8 seconds by studying motion traces for 21 lung tumor patients. The prerequisite for the therapy accelerator is therefore that its extraction time is at least as long as the corresponding period. In addition the intensity has to be regulated in a way that the necessary dose can be delivered in this period. The extraction time for the synchrotrons in standard therapy mode of GSI and HIT are 2.2 s and 5 s, respectively. This means that even if a dedicated intensity regulation could be implemented at GSI, the current maximum spill on time is too short for experiments with realistic breathing periods. On the other hand one can expect the extraction time of HIT's synchrotron to be sufficient long in almost all cases.

4.2.2 Dosimetry - detectors & methods

Without reliable and accurate dose application of the static target it is not possible to deliver a satisfying homogenous dose distribution to a target in the presence of motion. Therefore it is crucial in a first step to validate if irradiation of a static target in *re-scan* mode is of comparable quality to the currently used standard irradiation modes at GSI and HIT. It was necessary to perform these initial experiments with static targets in order to isolate the effect of technical *re-scan* implementation on the dosimetric outcome.

The minimum requirement is the fulfillment of the recommended ICRU-50 (ICRU, 1993) bench marks, which aim a dose coverage of the target volume between 95% and 107% of the prescribed dose. Since these limits must also include uncertainties due to motion it follows that the static dose distribution needs to be even better. Compared to the standard irradiation, *re-scanning* changes for instance the temporal charge distribution inside the sensitive volume of the ionization chambers.

All detectors at GSI were designed to fulfill the demands of the patient irradiation mode and due to the technology transfer from GSI to HIT both beam measuring system are very similar. Before going into the experimental details an overview of the detectors and other measuring devices used both at GSI and HIT shall be given:

- **MP3 water phantom with Pin point chambers (PTW, Freiburg):** A system for three-dimensional dosimetric verification of treatment plans in intensity-modulated radiotherapy with heavy ions. Its components are an array of 24 ionization chambers (pin points) with 0.03 cm^3 sensitive volume of air. The ionization chambers (IC) are connected to two multichannel electrometers (Multidos, PTW, Freiburg, Germany), each of which controls the measurement of 12 ionization chambers. Within one row, the spacing between two ICs is 12 mm. The distance between two rows is 10 mm and the ICs of each two consecutive rows are shifted laterally by 6 mm against each other to prevent shading. At a nominal voltage of 400 V the pin points have an ion collection time of 50 μs. The system was routinely used for 3D plan verification at the heavy ion therapy project at the GSI (Karger et al., 1999). It measures the dose with a high precision (uncertainty $1\% - 2\%$) at different LET values. A similar device is currently used at HIT. The pin points are usually placed in a water phantom for the dose verification measurements of the treatment fields (Karger et al., 1999). This is a rational approach since the density of water is similar to the density of soft tissue. The phantom has three computer controlled motorized arms, which can be used to position the pin point chambers within a precision of 0.1 mm. The phantom is made of polymethyl methacrylate (PMMA). A thin entrance window of $250 \cdot 250 \cdot 5$ mm^3 PMMA reduces the influence on the radian field compared to the thicker walls.

- **Farmer chamber 30010 (PTW, Freiburg):** The Farmer chamber 30010 is a wide spread ionization chamber for absolute dose measurement in radiation therapy with 0.6 cm^3 sensitive volume of air. At a nominal voltage of 400 V the ionization chamber has an ion collection time of 140 μs (PTW, 2013).

- **Kodak X-Omat V films:** The Kodak X-Omat V films are classical silver bromide films commonly used in conventional radiation therapy. The films consist of polyester coated with an emulsion layer on each side, which is protected by an especially hard gelatine layer. Films are still very useful because of their unmatched spatial resolution. For instance, foci and interplay patterns can easily be checked and visualized. The size of a film is $24 \cdot 30$ cm^2. Each film comes in a light-tight ready pack. Detailed measurements have been done by Spielberger et al. (Spielberger et al., 2001) to characterize the films for irradiation with carbon ions at GSI. The film detector signal is called the *net* optical density (OD) (OD minus the background OD). For the sake of simplicity the term ‘optical density’ is used in the following, when referring to net optical density. The general formula of the dose-response curve can be expressed as

$$\mathrm{OD} = \mathrm{OD}_{max} \left[1 - \exp(-mD)\right], \tag{4.2}$$

with OD_{max} as the saturation optical density, $m = m(Z, E)$ as the exponential slope which is in general a function of the particle charge (Z) and the energy (E) and D as the dose in Gray. The analysis of the dose-response curves revealed that the OD can strongly depend on the processing conditions, such as temperature, concentration and activity of the developer and probably also on the film batch (Bathelt, 2000). Therefore we always irradiated a well defined referenced field on every single film. Comparing these reference fields amongst each other and expressing the results relative to those reference fields made the experiments independent of the processing conditions. The Kodak X-Omat V films were developed as soon as possible after irradiation with a Kodak M35 processing machine, using DX31 as developer and FX31 as fixer components from the company Typon. The

$$\mathrm{OD} = \log \frac{I_0}{I} \tag{4.3}$$

with I_0 being the incident light intensity and I the transmitted light intensity was measured using the Densonorm 21 E (Pehamed, PEHA med. Geräte GmbH) hand densitometer and the VIDAR DosimetryPRO® film scanner. In the scope of this thesis these devices have been calibrated and their performance was evaluated.

The homogeneity

$$H = 1 - \frac{\delta}{\mu}\,, \tag{4.4}$$

which is a measure of the smoothness of a dose distribution, was calculated (standard deviation δ and mean film response μ) in the region of interest (ROI) was is set in the center of the radiation field .

To isolate the dosimetric impact of *re-scanning*, some experiments were performed without target motion. In addition, the dose readings of the *re-scan* irradiations were normalized by the outcome of a standard irradiation as formerly used for patient treatment.

The fact that a relative dose measurement was performed rather than an absolute one reduces potential calibration errors and uncertainties. Therefore

$$relative\ dose = \frac{dose_{\textit{re-scan}}}{dose_{normal}} \tag{4.5}$$

was calculated as a function of the *re-scan* number.

In case of the Kodak X-Omat V films a reference band was irradiated in patient treatment mode on every single film and compared to the rescan mode on the very same film. This procedure reduces the effect of fluctuations in the film processing. There is hardly any information in data sheets on the precision of the ionization chambers when irradiated with heavy ions (Karger et al., 2010). In addition there is also an uncertainty in beam properties. Therefore the precision of a measured value was calculated as follows: For each experiment with the same nominal irradiation parameters the standard deviation of the data (e.g. dose for the ionisation chambers) was computed and the average of these values was defined as the standard error for each ionization chamber with the spread as the corresponding uncertainty.

A Pearson's r-test at the $\alpha = 1\%$ significance level was calculated to investigate the probability of linear correlation between the output of the dosimetry devices and the number of *re-scans*.

4.2.3 Implementation & dosimetry at GSI

The basis of every *re-scan* irradiation is the original physical-beam-plan (PBP) that assigns a unique energy, intensity, focus and particle number to every point of the irradiation grid. The data, generated as a part of the treatment planning, are transferred to an external scanner control unit.

At GSI, an essential part of the VME-based scanning control unit (Grözinger, 2004) is the fast autonomously running treatment sequencer which consists of seven control modules (SAM), which are responsible for beam measurement, beam request, beam positioning, data logging, interlock measurement etc. These modules can be loaded with dedicated *slice-by-slice re-scanning* programs so that a given PBP is automatically irradiated with the chosen *re-scan* number (Bert et al., 2008a).

The treatment of patients with heavy ions requires to measure and control particle fluence and beam position with high accuracy. At GSI the therapy control system checks every 12.5 μs (Haberer et al., 1993) if the prescribed particle number is reached for each rasterpoint. Due to the fact that these checks have finite spacing in time the signal to step over to the next rasterpoint is sent for an actual particle value that always exceeds the prescribed value. The therapy control unit at GSI subtracts this overdose of the previous rasterpoint from the nominal dose of the next one within the same IES (see figure 3.6). This is a rational assumption since the rasterpoint spacing is approximately one third of the full width at half maximum (FWHM) of the Gaussian shaped beam width so that one rasterpoint contributes to its neighbors which have, for example, a radial distance of 1 mm step size by a factor of 93% of its own dose. The effect of over-irradiation gets more prominent for lower particle numbers and higher beam intensities. Therefore the treatment planning system selects an appropriate intensity for each IES that is determined by the rasterpoint with the lowest particle counts within that IES which means that the system suggests a lower beam intensity when increasing the *re-scan* number. Changing the intensity results in an altered signal-to-noise relationship inside the ionisation chambers. To account for this, the amplification of the output signal of the chambers is automatically adjusted as a function of the particle fluence. However, the automatically generated amplification settings and intensity levels can be replaced independently from each other with a manual chosen selection so that their influence can be studied.

For safety reasons interlock units can abort the irradiation within microseconds. For instance, in patient irradiation mode at GSI the beam width and beam position are checked every 150 μs by 2 Multi-Wire Proportional Chambers with a precision of 1 mm. It might happen when using high speed *re-scanning* irradiation that the exposure time of a rasterpoint is beneath that threshold, which results in a termination of the treatment. Therefore, the interlock devices and the position measurement are switched off for the measurements.

4.2.4 Testing the implementation & dosimetry at GSI

Initial attempts have been done to check if the SAM programs are actually able to perform *re-scan* irradiation mode. It was tested if the system is able to irradiate 2D plans and 3D volume with *re-scanning* as fast as in standard mode. The rectangular 2D plan was designed to have a target area of $100 \cdot 100$ mm^2, energy 200.28 MeV/u and $2 \cdot 2$ mm^2 raster point grid. The sphere was designed to have a volume of 1000 cm^3, a rastergrid of $3 \cdot 3$ mm and a separation of the iso energy slides of 3 mm. Both plans were optimized to a physical dose of 2 Gy.

The time duration of each irradiation process is logged in data files at GSI. This information was used to compare the length of the *slice-by-slice re-scanning* versus *standard mode* irradiation using the same intensity levels in both cases.

Further experiments were focused on how precise the dose can be applied in *re-scan* mode compared to the standard irradiation. Karger et al. (Karger et al., 2010) state that the dose uncertainty should be well below 3% for measurements in phantoms. This includes variations in the beam application as well as the measuring accuracy of the detectors.

Hence a target area of $100 \cdot 100\,\mathrm{mm}^2$ was planned to be irradiated homogeneously with carbon ions (treatment plan parameters: single energy 200.28 MeV/u, $2 \cdot 2\,\mathrm{mm}^2$ raster point grid. 6.7 mm lateral beam FWHM, scan path: horizontal lines, $5 \cdot 10^5 \frac{\text{particles}}{\text{rasterpoint}}$) with different numbers of *re-scans* as well as in the patient beam delivery mode for comparison.

The following setup was used (see figure 4.1): The pin points were placed in the MP3 water phantom in a region around the Bragg Peak. In the entrance channel in air four detectors were used. First a PPIC1 with a constant flow of Kr/CO$_2$ gas (80/20 mass -%) with 2 l/h at atmospheric pressure and a high voltage of -1000 V (Brusasco et al., 2000). The current of the PPIC1, which is proportional to the beam current, is amplified[1] and converted into a voltage. This voltage is digitized by an analog-to-digital converter (ADC) with a sampling rate of $\Delta t = 12.5\ \mu$s and summed up. This sum is constantly compared with the prescribed particle number. PPIC1 controls the irradiation by sending a signal if the prescribed particle number has been received. Its size in beam's eye view (BEV) is larger than the maximum lateral extension of the treatment field as to minimize position dependencies of the PPIC1 signals (Voss et al., 1998) because the chamber's efficiency decreases at its edges. Secondly, the PPIC3, which is identical in construction to PPIC1 but with air as the sensitive volume was used. A charge-frequency convertor gives the readout of PPIC3 in terms of monitor units (MU) into the therapy control room (TKR). Thirdly, a Farmer chamber was placed in front of the water phantom as not to

---

[1] The settings of the amplification factor are in general individually set for each IES as a function of the beam's intensity.

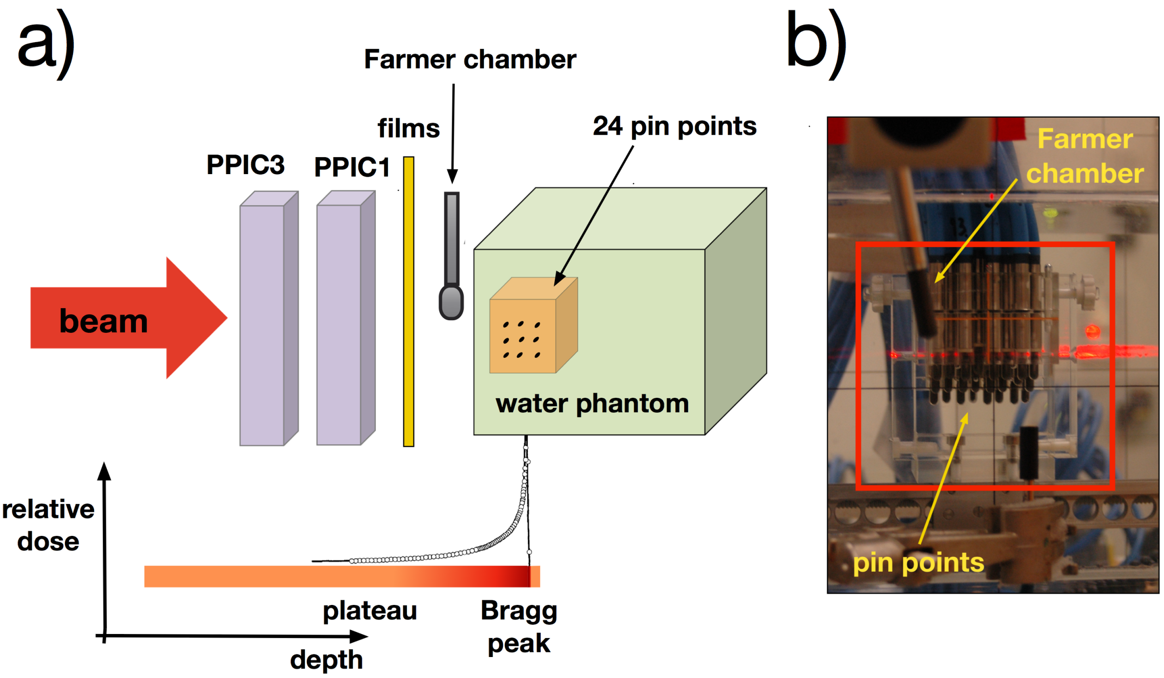

Figure 4.1.: a) sketch of the dosimetry setup at GSI. Behind the beam exit window the particles pass through PPIC3, PPIC1, Kodak X-Omat V films and the Farmer chamber in air. The beam then enters the MP3 water phantom and irradiates the 24 pin points. The first four detectors are placed in the beam's plateau region while the pin points are placed around the Bragg peak. The outline of the Bragg peak serves to guide the eye. b) photograph taken in beam's eye view of the MP3 water phantom made of PMMA with its entrance window. The red rectangle outlines the size of the treatment field. The detectors do not shadow each other with respect to the particle beam.

shadow the pin point array. The last detector instruments were the Kodak X-Omat V films. Via remote control new films could be moved into the beam with the help of a conveyor belt as to save time between consecutive irradiations. The detectors were arranged without overlap in BEV as indicated in figure 4.1.

Many experiments were performed with the same high intensity as in the case of *re-scan* number $r = 1$ since it should be investigated if accurate dosimetry can still be obtained with an irradiation as fast finished as possible. For this purpose, the intensity levels of the accelerator and the signal amplification settings of the PPIC1 has to be adapted manually.

Figure 4.2 displays the corresponding workflow.

1.: The TCU selects the standard intensity levels I_0 and the standard amplification settings for the spill signals Amp_0 in case of a standard PBP.

2.: The PBP is changed to the corresponding *re-scan* version so that the TCU selects new settings I_{auto} and Amp_{auto}.

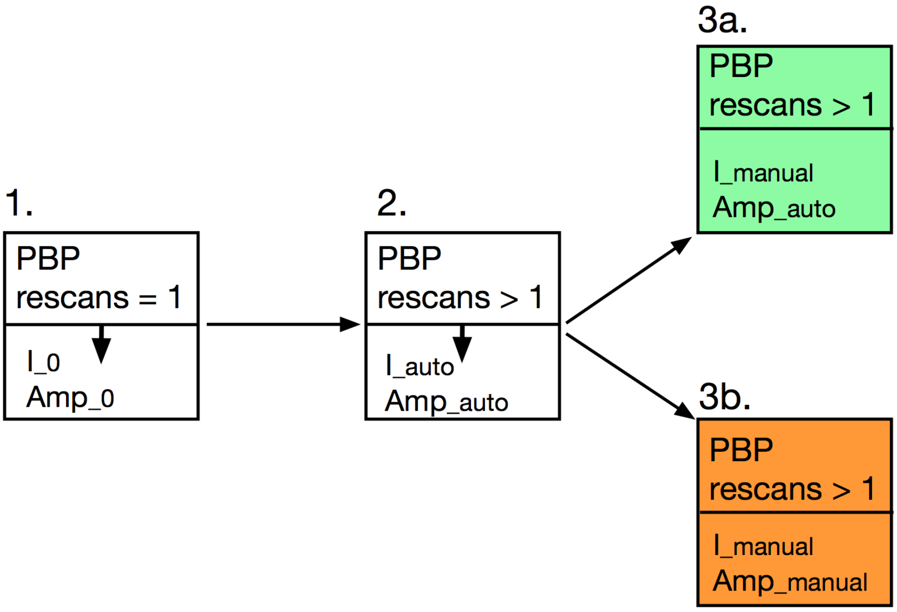

Figure 4.2.: Schematic workflow of the settings of the intensity levels and the amplification of the beam signal of the TCU.

3a. and 3b.: Before starting the irradiation the settings for the intensity and amplification can manually be replaced. Two different version have been measured. In both cases I_{manual} was set to $I_{manual} = I_0$, which means an irradiation with a beam fluence as high as in the normal irradiation. Version 3a. was set to Amp_{auto} and 3b. to $Amp_{manual} = Amp_0$.

It was investigated if changing between 3a. and 3b. would alter the outcome of the measurement

To summarize:

- The following parameters were measured with and without *slice-by-slice re-scanning* mode by irradiating 2D plans: 1) the total dose with large ionization chambers with two different amplification settings, local doses with small ionization chambers. 2) optical density with Kodak X-Omat V films. 3) exposure time with recorded data of the therapy control system 4) different settings for the signal amplification of the PPIC1.

4.2.5 Implementation & dosimetry at HIT

The HIT facility is run by scientific staff of the university of Heidelberg. To guarantee safe patient treatment the level to which experimental changes of the system are allowed is greatly reduced compared to a research facility like GSI. Since the pilot project at GSI served as a prototype for the HIT facility both systems are very similar. The implementation of the *re-scan* mode into the system at Heidelberg was done in collaboration with colleagues from HIT and with A. Gemmel from Siemens.

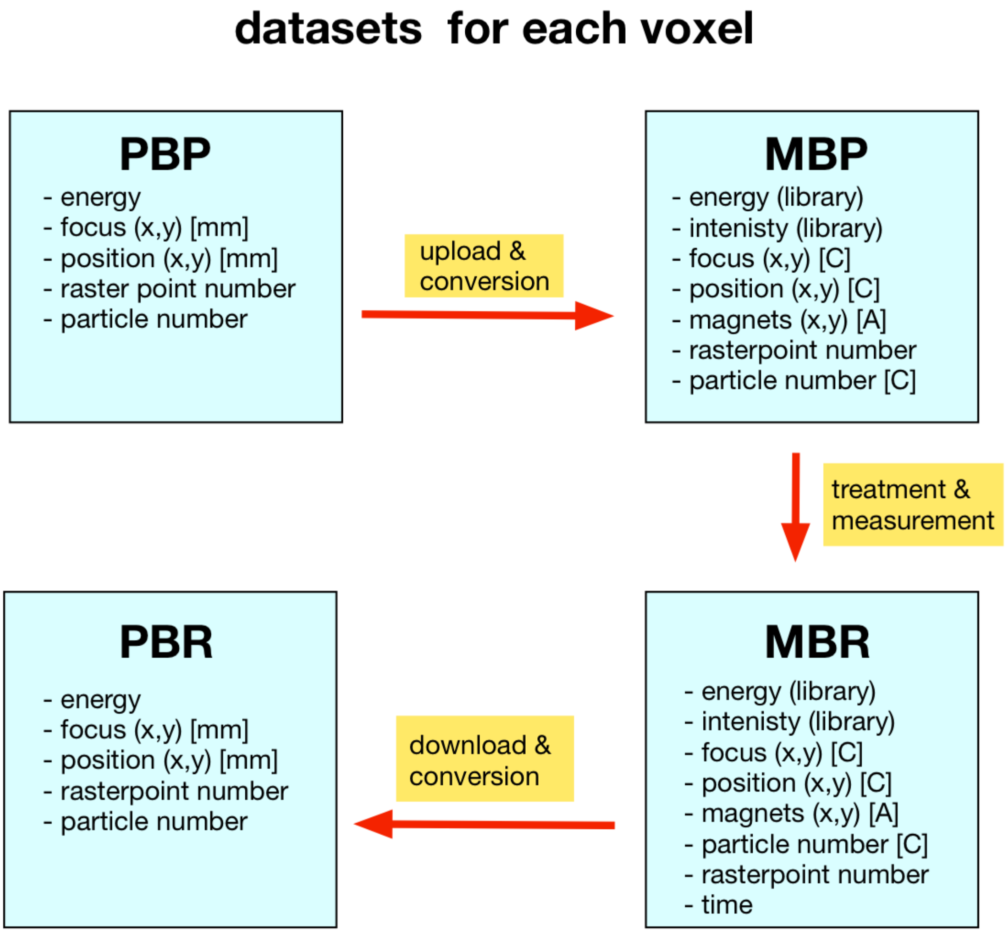

Figure 4.3.: Data file conversion scheme at HIT. The input data PBP is translated into values which are readable by the treatment control devices whose measured values are again transformed into the PBR data format. [lib] means that the value is taken from a pre defined library, [mm] is in millimeter and [C] represents the charge. The PBR files at GSI also provide the time information about the treatment course.

The treatment control at HIT cannot convert a standard PBP online as to irradiate it in *slice-by-slice re-scanning* mode. For this purpose dedicated software tools have been written which transform the original PBP into a *re-scan*-PBP which is then uploaded to the system. In a physical sense both methods are equivalent. Before treatment, the PBP files are translated into machine beam plan (MBP) files (see figure 4.3). In this process the input data is analyzed and the appropriate values for the treatment devices are set. Like done at GSI, the HIT system automatically selects the intensity value with respect to the point with the lowest particle number. Nevertheless, at this first level of *re-scanning* implementation at HIT it was possible to set the intensity manually for the whole plan by editing a line of the PBP file. Nominally HIT supplies 10 intensity levels with a maximum of $8 \cdot 10^7 \frac{\text{particles}}{\text{second}}$, but at the time when those measurements have been performed the maximum available particle rate was of $5 \cdot 10^7 \frac{\text{particles}}{\text{second}}$. The prescribed particle numbers of each voxel can then be written as a charge value into the MBP which can be be compared directly to the output of the ionization chamber. This procedure is also done in a similar way with the other parameters of the MBP. While performing the irradiation the values of the MBP are measured by the TCU[2] and written into a machine beam record (MBR) file which also contains the time stamp at which the irradiation of each voxel was finished. Finally, this plan is then translated into a PBR which contains the measured positions and particle numbers (see figure 4.3).

Figures 3.7 and 3.11 display the properties of the dose application of the treatment control system which checks every 2 μs if the prescribed dose has been irradiated.

Like at GSI, the position feedback loop and the corresponding interlocks had to be switched of because the *re-scanning* irradiation is too fast for those measurements. Unlike at GSI, at HIT the position data is still recored. Therefore a plan was irradiated as to investigate the influence of increasing *re-scanning* number on dose and position accuracy of the treatment control system by comparing PBP and PBR files. The course of the irradiation process uniquely relates each planned and actually irradiated point so that the applied dose and the mean radial position error can be calculated with reference to this information. The dose value is obtained by simply summing the parts which belong to the same rasterpoint. The position accuracy was addressed as the mean radial position error which was defined to be

$$\Delta r(i) = \sqrt{(x(i)_{\text{planned}} - \bar{x}(i)_{\text{measured}})^2 + (y(i)_{\text{planned}} - \bar{y}(i)_{\text{measured}})^2}, \tag{4.6}$$

with $x(i)_{\text{planned}}$ and $y(i)_{\text{planned}}$ being the values of the corresponding PBP points of each rasterpoint i and with $\bar{x}(i)_{\text{measured}}$ and $\bar{y}(i)_{\text{measured}}$ being the mean position[3] of the corresponding points of the PBR.

The second level of *re-scanning* implementation allowed the selection of each of the ten discrete intensity levels for each individual IES by the following procedure: Like shown in figure 4.3 the PBP is transformed into the MBP. The irradiation process which then starts is interrupted and the MBP is edited. Manually, the same intensity levels as in the standard irradiation case are inserted in the appropriate lines and the process is being continued. This procedure is therefore well suited for e.g. *slice-by-slice re-scanning* but of course not for *breath-sampled re-scanning* which needs continuously intensity variation.

The third level of *re-scanning* implementation allows for active intensity regulation by means of a feedback loop which controls the particle fluence by sending signals to the radio-frequency-knout-out-exciter (Schoemers et al., 2011). The intensity levels for each IES of the MBR are

---

[2] Three TCUs are implemented at HIT. Each TCU unit consists of an ionization chamber and a multiwire proportional chamber (MWPC). TCU1 controls the treatment.

[3] In case of a *re-scan* number $r > 1$ the mean of the vales was calculated.

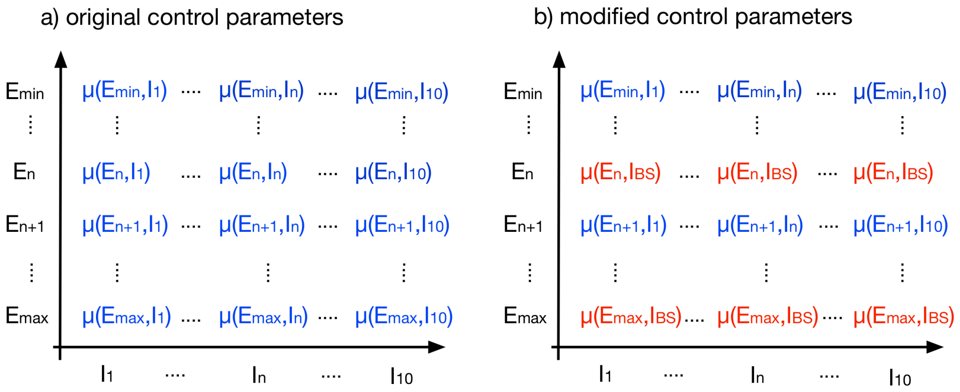

Figure 4.4.: Read-in table for the feedback loop at HIT. a) The coefficient $\mu = \mu(E, I)$ represents the nominal current value of the TCU output. The intensity is adjusted to meet the value. b) an individual μ value is calculated for the used energy levels to match the desired *breath-sampled re-scanning* intensity (reddish coefficients) and up-loaded to the system which adjusts the intensity appropriately.

translated into intensity and energy dependent current values which are constantly compared against the output of the TCUs. If the value of the TCU output is larger than the original control parameters (see figure 4.4 a)) a signal is sent so that the particle fluence is reduced by the radio-frequency-knout-out-exciter and vice versa. These original parameter values can be edited to facilitate *breath-sampled re-scanning*. The desired intensity of each IES is being calculated as a function of the breathing period and the modified control parameter is used to replace the corresponding original values in the read-in table of figure 4.4. Therefore, independently of the particle rate stated in the MBP, the feedback loop tries to match the current of the TCU output with the modified values of figure 4.4 b). Because it is a priori not known which particle rate was chosen by the system it is best to replace the whole row by the desired value. At the time when the experiments were done, the spill extraction characteristics are approximately the following: 5 s spill extraction time, spill pause of 2.5 s without changing the particle's energy and 5 s when changing the energy. This means that purely *breath-sampled re-scanning* experiments require breathing periods smaller than 5 s. Otherwise techniques which combine *gating* and *re-scanning* must be used (Furukawa et al., 2010a).

4.2.6 Testing the implementation & dosimetry at HIT

To test the *re-scanning* implementation at HIT the following measurements were performed:

Sixteen 2D fields were irradiated by carbon ions with an energy of 270.55 MeV/u, $2 \cdot 2$ mm^2 raster point grid, 6 mm lateral beam FWHM. The fields were divided in 4 rows with an increasing particle number per rasterpoint $0.8 \cdot 10^6$, $1.6 \cdot 10^6$, $3.2 \cdot 10^6$ and $6.4 \cdot 10^6$, respectively. Then, the four fields of each row have been irradiated with increasing *re-scan* numbers of 1, 3, 9 and 19 in the *slice-by-slice re-scanning* mode and with intensity of $5 \cdot 10^7 \frac{\text{particles}}{\text{second}}$.

The tests addressing the *breath-sampled re-scanning* implementation have been performed with 3D plans of the density-variation-phantom (DeVarPho) (see figure 4.5), a motion period was assumed to be 4 s and a *re-scan* number of $r = 1$ was used.

The purpose by analyzing PBR and MBR files was to check if the *breath-sampled re-scanning* mode could actually be irradiated when changing the read-in parameters of the treatment control according to figure 4.4 and to compare it against standard[4] *slice-by-slice re-scanning* irradiation of the same plan.

Irradiations with three different plans have been performed in order to test if the prescribed dose can be applied at the isocentre. While testing the *re-scan* implementation with the 2D plans described above, a Farmer chamber was placed at the isocenter and the relative dose (see equation 4.12) was measured for the $r = 3, 9$ and 19. Only one Kodak X-Omat V film was placed between the Farmer chamber and the beam entrance window so that the beam suffered almost no energy loss and the chamber was basically free in air in the plateau region of the dose.

In addition, phantoms have been used to study 3D motion mitigation by *re-scanning*. Before performing measurements in the presence of motion, static dose distributions were measured with one of the phantoms as to test the dosimetry for 3D *re-scan* irradiation. Hence, this phantom is being introduced in this section and the properties of the motion parameters will be listed in section 4.2.7.

Like addressed in (Rietzel and Bert, 2010; Graeff et al., 2012), heavy ion irradiation is much more sensitive with respect to density variations than photon therapy, so that an expansion of the CTV to an internal target volume (ITV) which simply geometrically covers all motion phases is not sufficient. Recently, a new algorithm (Graeff et al., 2012) was incorporated in TReatment planning for Particles (TRiP) which accounts for density variations and also includes all motion phases in the optimization process. Therefore the phantoms have been designed to show density variations.

The setup of the DeVarPho is illustrated in figure 4.5. Its main focus was on very defined and large density variations. Therefore two slits have been cut into a block of PMMA (406 Hounsfield unit (HU)) and one has been filled with a slab of teflon (1990 HU) and the other simply by air (-1000 HU). This phantom was placed in front of the MP3 water (0 HU) tank. With these HU values (Schneider et al., 1996; Morin et al., 2007; Richter et al., 2008) a computed tomography (CT) was created and an ITV with a prescribed dose of 5 Gy was optimized[5] to cover a CTV with a width of 50 mm, a hight 25 mm and a length of 40 mm in BEV.

---

[4] with automatic intensity selection

[5] The prescribed dose was taken to be 5 Gy because otherwise the particle numbers in the proximal slices would have become too low when using high *re-scan* numbers.

It was irradiated in *slice-by-slice* ($r = 5$ and 11) and *breath-sampled re-scanning* ($r = 1$) mode, the relative doses are reported (see equation 4.12). The measurements werde done by using the pin point array. Regions close to the ITV which exhibit large dose gradients were left out in the analysis since even small set up uncertainties can have a large effect when reporting relative doses in those areas.

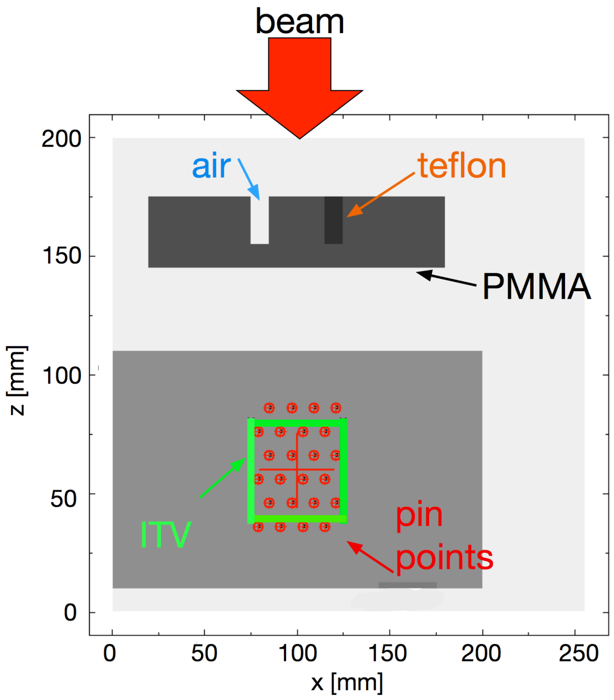

Figure 4.5.: Schematic draw of the set up for the DeVarPho. The beam enters from the positive z-direction. First traversing the phantom with the density variations and then entering the MP3 water tank filled with water. Details can be found in B.1.1.

To summarize, the following measurements have been performed to test the implementation and to validate the dosimetry:

- *Slice-by-slice re-scanning* as well as *breath-sampled re-scanning* were implemented at HIT. Experiments to validate the performance have been made with focus on the spill structure as well as the position and the dosimetry data. These values were obtained by analyzing the PBR files created by the TCUs.

- irradiation of a homogeneous plan 2D in *slice-by-slice re-scanning* mode without motion with different *re-scan* numbers

- irradiation of a 3D phantom in *slice-by-slice re-scanning* and *breath-sampled re-scanning* mode without motion with different *re-scan* numbers

4.2.7 Motion effects mitigation by *re-scanning*

This section is focused on experiments that show how efficiently motion effects can be reduced by using the *re-scanning* technique. The various experimental setups and parameters have also been incorporated in a simulation environment to validate the outcome and to further extent the range of parameter sets.

All experiments have been performed with carbon ions even if the physicians at HIT also use protons to treat patients. Carbon ions are more sensitive concerning interplay effects. Hence the mitigation of motion effects when using carbon ion beams is even more challenging. The reason is that their lateral deflection is smaller than for protons which results in a narrower FWHM of the beam.

The focus of the initial simulations and experiments was on 2D plans because interplay effects are not reduced due to pre-irradiation as in case of 3D plans. Furthermore, the most distal IES of every 3D plans is de facto a 2D plans because it is not pre-irradiated. Hence, the dependence of motion related parameters can be studied more accurate when simulating 2D plans.

The next step was the irradiation of 3D plans to two different phantoms in the presence of motion in the *slice-by-slice re-scanning* and *breath-sampled re-scanning* mode as to investigate how fast the dose distribution gets homogenous in these cases.

2D irradiation: Experiments - Amplitude, period, phase and scanpath dependence

The effectiveness of *re-scanning* on dose smoothing was studied by simulating target motion with the Kodak X-Omat V films which moved sinusoidal vertical and horizontal in beam's eye view free in air (peak-to-peak motion amplitude: 1 cm ± 0.1 cm and 1.5 cm ± 0.2 cm and a period of 3 s ± 0.2 s).

A target area was planned to be irradiated homogeneously ($90 \cdot 60$ mm^2 and $60 \cdot 90$ mm^2, respectively, single energy 244.21 MeV/u, $3 \cdot 3$ mm^2 grid, 9.2 mm beam FWHM scan-path: horizontal lines). To account for target motion 1 cm and 1.5 cm margins were added in the motion direction, respectively. Irradiation was performed in the *slice-by-slice re-scanning* method with up to 21 *re-scans*. The rationale behind starting the reduction of interplay effects with *re-scanning* by the irradiation of simple rectangular areas with a single energy is the following:

The temporal patterns of scanned beam application and respiratory motion are comparable which means that a correlation can occur between beam application and motion of the target. This would violate the basic assumption of *re-scanning* as being a process with an underlying random nature (Rietzel and Bert, 2010). The probability that these correlations emerge is higher when irradiating regular shapes with a homogeneously dose distribution. In general, the geometrical field shape of patients will be more irregular.

In addition, it was investigated if *re-scanning* is also able to mitigate motion effects for larger motion amplitudes. Large amplitudes are in general more critical in the treatment course, because of increased exposure of healthy tissue and more severe interplay effects.

These measurements are some sort of a worst case study, because if *re-scanning* will be able to compensate interplay effects for large amplitudes it is highly unlikely to fail for smaller amplitudes. Since interplay patterns are very sensitive to the a priori unknown starting position of the target, a multi-phase phantom was constructed (see figure 4.6) which can move up to six films simultaneously, each separated by a phase shift of 60 degree. In contrast to the previous experiment we could not change the motion direction of the phantom, therefore we changed the primary scanning direction, so that it was parallel or perpendicular to the motion direction.

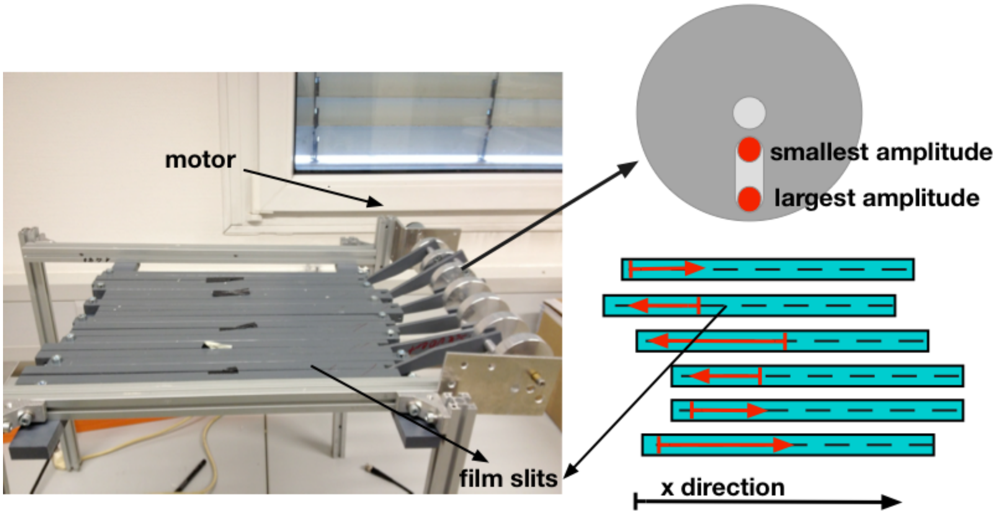

Figure 4.6.: The left part of the figure shows a picture of the multi-phase phantom. The right part illustrates the most important features of it. The films were fixed in small slits (indicated as dashed black lines) and moved perpendicular to beam's eye view in the x direction. The red arrows symbolize the velocity vector of each rod. The amplitude of the motion could be changed by screwing the rods at a different radius with respect to the crank.

A peak-to-peak amplitude of 5 cm ± 0.3 cm, a period of 4 s ± 0.2 s and 5 s ± 0.2 s, were chosen respectively. A target area was planned to be irradiated homogeneously ($50 \cdot 50\ \text{mm}^2$, single energy 200.28 MeV/u, $2 \cdot 2\ \text{mm}^2$ grid, 6.7 mm FWHM, scan-path: horizontal lines and vertical lines). To account for target motion, 5 cm geometrical margins were added in the motion direction and irradiation was done in the slice-by-slice *re-scanning* method. Irradiations were performed with up to 29 *re-scans*. Interplay patterns of the films were analyzed by visual inspection and the homogeneity relative to a stationary irradiation within the ROI.

All measured OD values were corrected for the *re-scan* effect which is shown in figure 4.9 d). The corrected OD value is obtained by multiplying the measured OD value with the inverse of the fit of the appropriate *re-scan* number.

2D irradiation: Simulations - Amplitude, period, phase, intensity, scanpath and spill profile dependence

A simulation environment based on TRiP4D (Richter, 2012) was set up in order to recalculate experiments or to predict results. The actual PBP, the spill shape, the intensity and the irradiation mode were given as input parameters to the dedicated physical-beam-record simulation environment (PBRSimEnv) which creates a file (with the temporal progress of the irradiation of each rasterpoint) which is in the following referred as being the *simulated*-PBR. This file is necessary for TRiP4D to include the temporal dimension of the irradiation. Dose distributions resulting from the foregoing experiments have been compared with simulations to investigate the dependence of motion mitigation by *re-scanning*.

The simulated intensity range varied from 10^6 to 10^{10} particles within a spill of a length of 2.2 s. In case of the *breath-sampled re-scanning* mode of spill of a length of 10 s was used and breathing period of 4 s was assumed.

Starting phases varied from 0° to 360° in steps of 5°. Peak-to-peak amplitudes of 1 cm, 1.5 cm, 2 cm and 5 cm were simulated. The main beam application direction was simulated as being parallel as well as being perpendicular to the motion of the target. The range of *re-scan* numbers was varied from $r = 1$ to $r = 29$. The PBP used in the simulations were the same as in the foregoing experiments. In addition, it was examined whether different spill shapes influence the outcome of the simulations. If there would be a strong dependence on the spill shape it would be questionable if forward calculations to predict clinical outcomes make any sense at all. For this purpose different spills were measured and down-sampled to a time resolution of 10 μs and have been compared to an artificial square spill profile. All spills were normalized to 1 particle per spill, hence it was possible to multiply the spill profiles with an arbitrary particle number to get the desired intensity.

The simulated results are reported in several ways: 1) dose area histogram (DAH) curves, which are the projection of the well known dose volume histogram (DVH) to one CT slice in depth. The ROI was analyzed with respect to variations in amplitude, period, intensity and spill shape. 2) Visual display of dose distributions in 2D and 3D surface plots. 3) Quantitative analysis of the dose distribution with focus on amplitude-, phase-, period and intensity dependence, penumbra width and homogeneity.

To summarize:

- Interplay effects have been studied by irradiation and simulation of 2D plans.

- The influence of motion was introduced by 1) moving Kodak X-Omat V films with a motor (experiment) or 2) by incorporating the motion in the simulation environment.
- The dependence of *re-scanning* in the presence of motion was investigated with respect to the following parameters: Amplitude, period, starting phase, intensity, scanpath and spill profile shape.

3D irradiation: Experiments with phantoms

The 2D motion mitigation experiments were a good start to tackle the issue. The necessary next step had been the irradiation of 3D phantoms in the presence of motion which is addressed in this section. Two phantoms have been used, both planned and constructed at GSI to fit our very specific demands. The DeVarPho has already been introduced in section 4.2.5. Now, the motion related parameters are added. The DeVarPho was planned to be placed on the very same sliding table as the MP3 phantom with the pin points. It follows that there was no relative movement between the pin points and the MP3 phantom. The motion was adjusted to have a period of 4 s ± 0.2 s, 2 cm ± 0.2 cm peak-to-peak amplitude in horizontal direction (x-axis) and a sinusoidal motion trace. The fields have been optimized with a horizontal as well as with a vertical scanpath of the pencil beam. A CT was constructed with 21 different amplitude based phases in order to allow for the calculation of the ITV in the presence of motion. Measurements in *slice-by-slice re-scanning* mode with the *re-scan* numbers of 1, 5 and 11 in horizontal as well was vertical scan path have been performed. In addition, simulations have been performed with parameters as to mimic the experiments. Nominal, the same intensity levels and motion traces were chosen. The starting phase of the simulation was chosen to be 0°. The starting phase of the phantom is subjected to an uncertainty of circa ±15°.

The second phantom is named breathing-thorax-phantom-with-6D-target-motion (BreThoPho). It was build at GSI and its details and parameters can be found in the thesis of P. Steidl (Steidl, 2011). It was constructed as to mimic real patient cases better than any existing solution at that time. It mainly consists of an artificial thorax which can mimic breathing motion and a robotic arm with detectors which can independently mimic tumor motion inside the thorax. The HUs of the CT scan have been converted into water-equivalent path length (WEPL) for the use of particle irradiation.

The tumor is represented by an ITV of the size (35 × 35 × 35) mm^3. The dose distribution is measured with 20 pin points which are placed into a detector head that is made of PMMA. In beam's eye view, the pinpoints have a lateral distance of 1 cm from each other. The rows are at a distance of 12 mm from each other (Steidl et al., 2012b). The setup up is shown in figure 4.7. The ITV was optimized using a grid size of 2 mm with a horizontal as well as with a vertical scan path. The motion parameters of the detector head were chosen to be 2 cm ± 0.06 cm peak-to-peak amplitude in horizontal direction (x-axis) in a sinusoidal motion trace with a period

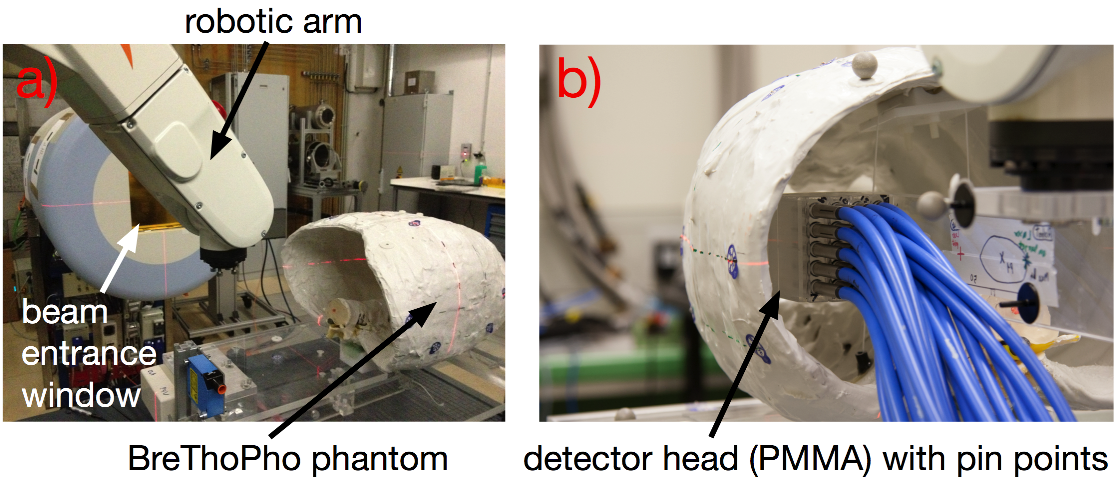

Figure 4.7.: a) Overview of the setup with the BreThoPho phantom. The beam crosses the entrance window and enters the phantom where the detector head, shown in b), can be moved by the robotic arm in predefined motion traces.

of 4 s ± 0.01 s. The thorax was adjusted to mimic breathing with a period of 4 s ± 0.1 s, too. The plan was optimized with a prescribed dose of 5 Gy[6]. The measurements were performed in the presence of motion in *slice-by-slice re-scanning* mode with the *re-scan* numbers 1, 3, 5, 9, and 11 and in *breath-sampled re-scanning* mode with the *re-scan* number of 5. As done above, simulations have been performed with same parameters as used in the experiments.

For both phantoms, regions close to the ITV, which exhibit large dose gradients were left out in the analysis, because even small set up uncertainties can have a large effect when reporting relative doses. In case of the BreThoPho phantom pin points inside the area of $10\text{ mm} \leq x \leq 30\text{ mm}$ and $12\text{ mm} \leq y \leq 24\text{ mm}$ lie well inside the ITV region without sharp dose gradients. The pin points of the DeVarPho experiments are within an area of $6\text{ mm} \leq x \leq 36\text{ mm}$ and $10\text{ mm} \leq y \leq 70\text{ mm}$ lie well inside the ITV region without sharp dose gradients. Therefore these pin points were used when the efficiency of the two *re-scan* modes to mitigate motion effects in case of 3D irradiations was analyzed by calculating the corresponding homogeneity values. Additional information can be found in section B.1.1.

3D irradiation: Simulations with phantoms

A simulation environment was set up in order to recalculate experiments or to predict results for the 3D irradiations in the presence of motion similar to the previous 2D case. The focus in this section was to see if simulations and experiments agree with respect to their outcome. In case of *slice-by-slice re-scanning* a measured spill with a length of 2.2 s and for the *breath-sampled re-scanning* mode a square spill profile of a length of 10 s was used, respectively. The motion

---

[6] At this time there was a minimal particle limit of 8000 particles per rasterpoint. Since it was a priori not obvious which would be the highest *re-scan* number, it was necessary to increase the particle numbers per rasterpoint by increasing the prescribed dose.

parameters were adapted from the experimental conditions listed in the previous section. The corresponding CT data was generated because they are mandatory to optimize the PBP which are used to irradiated the phantoms. Starting phases were randomly chosen from 0° to 360° in steps of 5°. The PBP used in the simulations were the same as in the foregoing experiments. The range of *re-scan* numbers in the simulations was $1 \leq r \leq 11$. The beam's intensity was nominally the same as in the MBP of the corresponding experiment.

To summerize:

- 3D motion mitigation experiments and simulations have been performed with two different phantoms (with density variations) in *breath-sampled re-scanning* and *slice-by-slice re-scanning* mode with a *re-scan* number up to $r = 11$. The detectors moved sinusoidally in horizontal direction with an amplitude of 2 cm peak-to-peak. The period was chosen to be 4 s.

4.3 Results

Table 4.1 gives an overview of a selected number of experiments and simulations. Its purpose is to give the reader a review of the foregoing *material* & *methods* section and an outlook of the *results* section of this chapter which is focused on presenting the most important information of the studies.

4.3.1 Implementation & dosimetry at GSI

If the interlock mask was set properly the modified SAM programs ran successfully until irradiation was finished in *re-scan* mode.

The analysis of the physical beam records shows (see figure 4.8) that the mean irradiation time variation is below 5 % in case of a single energy plan (left picture) as well as for a plan of a sphere (right picture). Therefore, a *re-scan* number of 15 does not necessarily cause a significant change in treatment time which can also be expected for other *re-scan* numbers.

To continue with the dosimetric measurements: The red data points in figure 4.9 symbolize Amp_{auto} setting. In this case the amplification of PPIC1 was adjusted for each *re-scan* case individually according to the recommendation of the plan optimization procedure (see figure 4.2). The green data points represent experiments performed with Amp_{manual}, so that every irradiation was done with the settings of the $r = 1$ case.

Figure 4.9 a) shows the results of the Farmer ionization chamber. The data points fluctuate randomly about $relative\ dose = 1$ with a maximum deviation of around 3%. Assuming PPIC1[7] works correctly in the *re-scan* mode (see chapter 4.4) the readout of the farmer chamber lies well

---

[7] Any malfunctioning of PPIC1 has an influence on the dose measurements of all the detectors which are positioned behind PPIC1 in beam's direction.

section - figure	study - dependence	plan - scanpath	detectors	motion	*re-scan* mode	type
implementation & dosimetry - figure 4.8	irradiation time	2D homogeneous field 3D iso-dose sphere - horizontal	TCU	no	slice (1x, 5x, 9x, 15x, 19x)	experiment at GSI
implementation & dosimetry - figures 4.10, 4.12 and 4.13	irradiation time, position accuracy, dose levels	2D homogeneous field - horizontal	TCU, X-ray films, Farmer chamber	no	slice (1x, 3x, 9x, 19x)	experiment at HIT
implementation & dosimetry - figure 4.15	irradiation time	3D DeVarPho - horizontal	TCU pin points	no	BS (1x)	experiment at HIT
implementation & dosimetry - figure 4.9	dose levels	2D homogeneous field - horizontal	TCU, pin points Farmer chamber, X-ray films	no	slice (1x, 3x, 5x, 9x, 15x, 19x)	experiment at GSI and HIT
implementation & dosimetry - figures 4.18 and 4.19	dose levels	3D DeVarPho - horizontal	pin points	no	slice (5x, 11x) BS (1x)	experiment at HIT
motion mitigation - figures 4.20 and 4.21	homogeneity - amplitude, scan-path	2D homogeneous field - horizontal	X-ray films	1 cm, 1.5 cm, period 3 s, vertical and horizontal	slice (1x, 5x, 9x, 13x, 17x, 21x)	experiment at GSI
motion mitigation - figures 4.21, 4.22 and 4.23	homogeneity - amplitude, scan-path	2D homogeneous field - horizontal	dose cubes	1 cm, 1.5 cm, period 3 s vertical and horizontal	slice and BS (1x, 3x, 5x, 7x, 9x, 11x, 13x, 15x, 17x, 19x, 21x)	simulation
motion mitigation - figure 4.24	homogeneity - amplitude, scan-path	2D homogeneous field - vertical	X-ray films	5 cm, period 4 s horizontal	slice (1x, 5x, 9x, 11x, 13x, 17x, 21x, 29x)	experiment at GSI and HIT
motion mitigation - figure 4.25	homogeneity - amplitude, scan-path	2D homogeneous field - vertical	X-ray films	5 cm, period 4 s, horizontal	BS (1x, 5x, 9x, 11x, 13x, 17x, 21x, 29x)	simulation
motion mitigation - figures 4.26 and 4.27	DAH - amplitude, period intensity, *re-scans*	2D homogeneous field - horizontal	dose cubes	1 cm, 2 cm,5 cm, period 4 s, vertical	slice and BS (1x, 5x, 13x, 25x)	simulation
motion mitigation figure 4.30	DAH - starting phase	2D homogeneous field - horizontal	dose cubes	1.5 cm, period 4 s, vertical	slice and BS (1x, 9x, 19x)	simulation
motion mitigation - figure 4.3.3	DAH - spill profile	2D homogeneous field - vertical	dose cubes	1 cm, 5 cm, period 4 s, horizontal	slice (1x, 25x) and BS (1x, 5x, 7x, 25x)	simulation
motion mitigation - figure 4.34	homogeneity	3D DeVarPho - vertical and horizontal	pin points	2 cm, period 4 s, horizontal	slice (1x, 5x, 11x)	experiment at HIT
motion mitigation - figure 4.34	homogeneity	3D DeVarPho - vertical and horizontal	dose cubes	2 cm, period 4 s, horizontal	slice and BS (1x, 3x, 5x, 7x, 11x)	simulation
motion mitigation - figure 4.35	homogeneity	3D BreThoPho - vertical and horizontal	pin points	2 cm, period 4 s, horizontal	slice (1x, 3x, 5x, 9x, 11x) and BS (5x)	experiment at HIT
motion mitigation - figure 4.35	homogeneity	3D BreThoPho - vertical and horizontal	dose cubes	2 cm, period 4 s, horizontal	slice and BS (1x, 3x, 5x, 7x, 11x)	simulation

Table 4.1.: Overview of the most important data of the studies which are presented in the following. The motion trajectory is always performed in a sinusoidal fashion. The amplitude is always reported as being the peak-to-peak distance. Details can be found in the material & methods section 4.2.

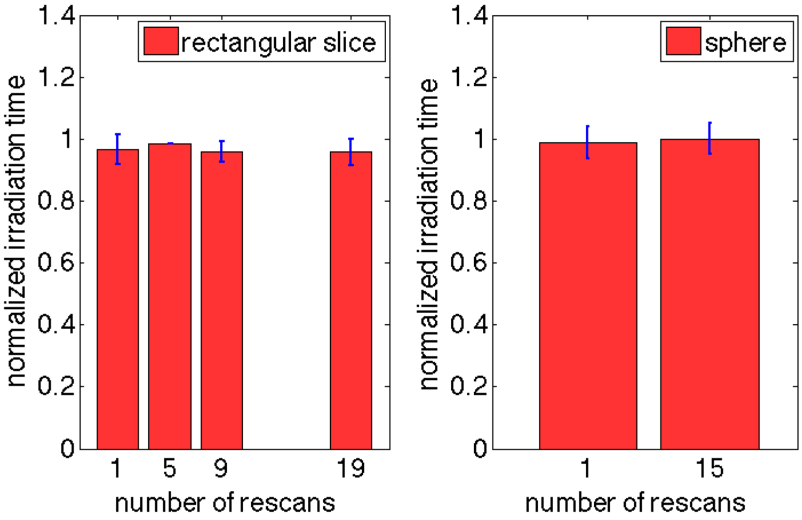

Figure 4.8.: The left part of the figure shows the time duration for irradiating a rectangular slice as a function of the rescan number, the right part for irradiation a sphere, respectively. The time is normalized to the case which took the longest time. The overall treatment time could be maintained by *re-scan* irradiation in the *slice-by-slice re-scanning* technique if the intensity is kept at the values of the standard mode.

between the 95 – 107% intervention thresholds to reduce the risk of failure in tumor control (ICRU, 1993). In addition, a Pearson's r-test at the $\alpha = 1\%$ significance level that benchmarks the probability of linear correlation was performed. It states that there is no correlation between the dose in *re-scan* mode and the number of *re-scans* in case of the Farmer chamber. A summary of the Pearson's r values for all detectors is shown in table 4.2.

detector	Pearson's r_P	correlation $\alpha = 1\%$
Farmer chamber	$0.11 < r_P < 0.12$	no correlation
PPIC3	$0.98 < r_P < 1$	correlation
pin points	$-0.11 < r_P < 0.6$	no correlation
Kodak X-Omat V films	$-0.88 < r_P < -0.85$	correlation

Table 4.2.: The table shows the Pearson's r_P correlation coefficient regarding an significance level of $\alpha = 1\%$ for the different detectors.

The measurement of the pin points is shown in figure 4.9 b). This chart was created by adding the output of the 24 individual pin points which were placed in six different linear energy transfer (LET) regions to a single value. The data points are also randomly distributed around $relative\ dose = 1$ with a maximum variance less than 2.5% so that no correlation could be observed. In addition, each of the six different LET regions was analyzed separately. The position nearest to the Bragg-Peak did not show any tendency different from the global one, as well as all the other positions. This indicates that there is no major LET dependence in $relative\ dose$ measurements for the pin points with our settings.

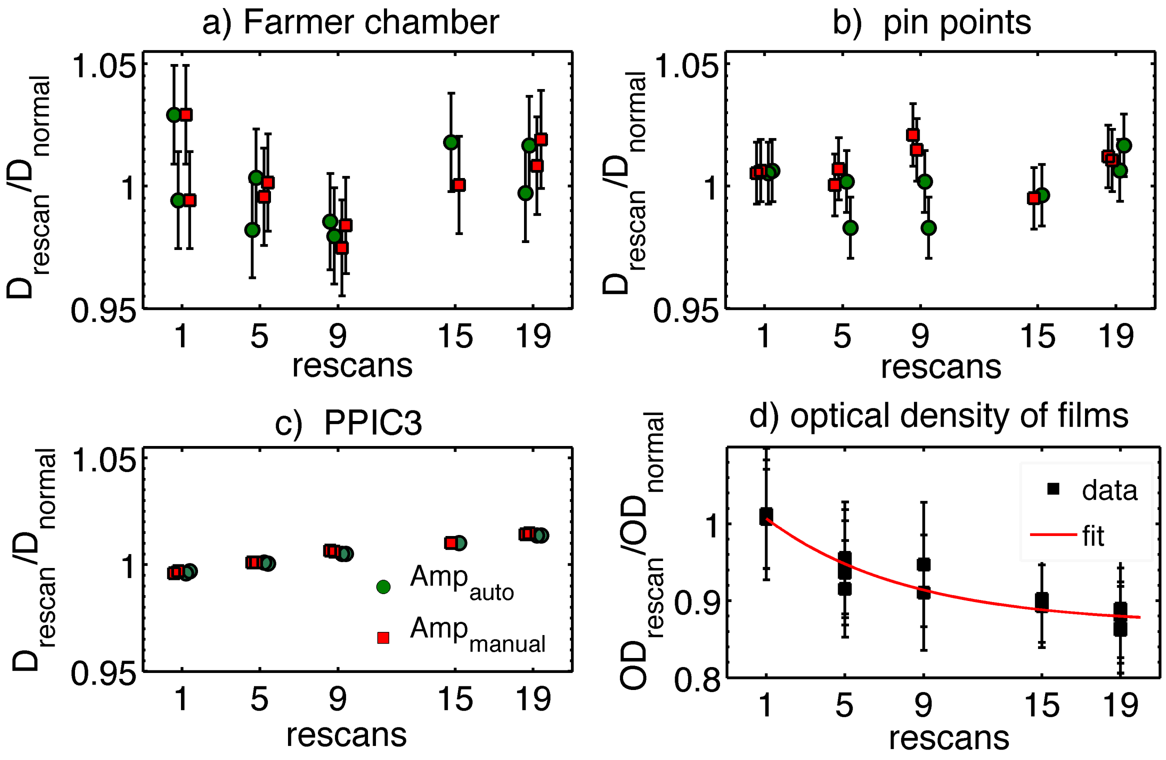

Figure 4.9.: Summary of dosimetric data without motion irradiated at GSI. For better visibility, the points are distributed around the actual *re-scan* number. a) shows the relative dose D_{rescan}/D_{normal} of the Farmer chamber with no linear correlation at the Pearson's $r_P = 1\%$ sig level. b) displays the corresponding pin point data with no linear correlation Pearson's $r_P = 1\%$ sig level. c) PPIC3 shows a correlation between dose and the number of rescans. The error bars are too small to be visible in this representation. d) the relative optical density OD_{rescan}/OD_{normal} of the Kodak X-Omat V films with the corresponding fit function.

Figure 4.9 c), on the other hand, reveals a dependency of the dose as a function of the rescan number for PPIC3, but with a deviation of less than 2% which lies well between the limits of the ICRU-50 report. All three types of ionization chambers demonstrate no systematic difference between the settings for Amp_{auto} and Amp_{manual} so that the settings of the charge to voltage amplification of PPIC1 did not influence the $relative\ dose$ measurement strongly.

Figure 4.9 d) shows the result of the Kodak X-Omat V films. The correlation between the OD, which is function of dose, and r is clearly visible. Underdosage up to 14% occurred in our experiments. Using equation 4.2, an average value of $\mathrm{OD}_{max} = 4$ (see (Spielberger et al., 2001)), the absolute values $\mathrm{OD}_{re-scan} = 0.46$ and $\mathrm{OD}_{normal} = 0.51$ for $r = 19$ and the fact that $m_{re-scan} = m_{reference}$ (both fields have been analyzed on the very same film) it follows:

$$\frac{D_{re-scan}}{D_{normal}} = \frac{\ln(1 - \mathrm{OD}_{re-scan}/\mathrm{OD}_{max})}{\ln(1 - \mathrm{OD}_{normal}/\mathrm{OD}_{max})} \approx 0.9. \tag{4.7}$$

This means, that a dose verification calculated from the optical density values of the Kodak X-Omat V films can have a relative deviation as large as 10% for $r = 19$.

Nevertheless, the films showed good homogeneity values in the range of $0.96 < H < 0.98$ and can therefore still be used to analyze interplay patterns. The exponential function $relative\ dose = a \cdot e^{-br} + c$, with a, b and c as free parameters and r as the *re-scan* number, was fitted to the data points. The result of the parameters (with 95% confidence bounds) is:

$$a = 0.16\,(0.097,\ 0.216) \tag{4.8}$$

$$b = 0.10\,(-0.03,\ 0.231) \tag{4.9}$$

$$c = 0.87\,(0.779,\ 0.931) \tag{4.10}$$

The motivation of the fit was to extract experimental correction factors of the optical densities for the films which can compensate the decreasing of the OD with increasing *re-scan* number.

To summarize:

- *Slice-by-slice re-scanning* was successfully implemented at GSI. The overall irradiation time can in principle be kept equal to the standard mode.
- The measurements of all gas filled ionisation chambers show relative errors smaller than ±3% when irradiated in *slice-by-slice re-scanning* mode with a *re-scan* number up to 19.
- The optical density of the Kodak X-Omat V films decreases significantly when increasing the *re-scan* number.

Figure 4.10 displays the mean irradiation time in *slice-by-slice re-scanning* mode of all rasterpoint multiplied by the *re-scan* number ($0.8 \cdot 10^6 \frac{\text{particles}}{\text{rasterpoint}}$ and maximum intensity level at HIT).

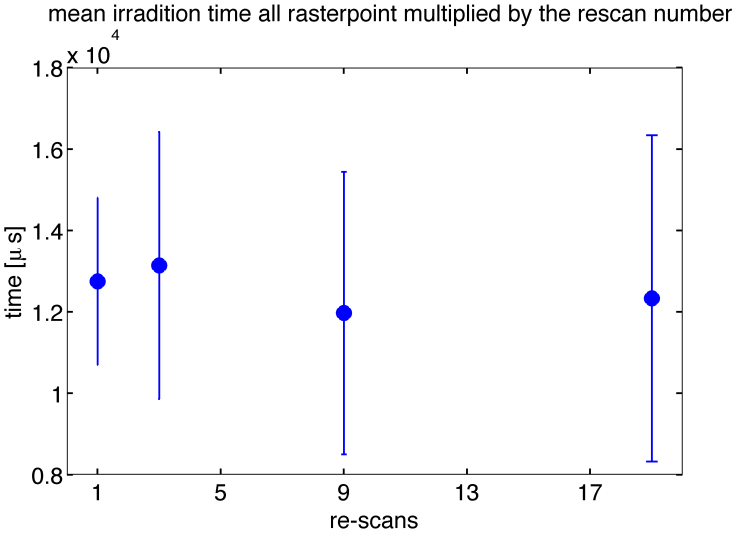

Figure 4.10.: Mean irradiation time of all rasterpoints of a 2D field with $0.8 \cdot 10^6 \frac{\text{particles}}{\text{rasterpoint}}$ is almost independent of the *re-scan* number. In this case the total irradiation time of each rastpoint is roughly 1.3 ms.

The analysis of the corresponding MBR data shows that the *re-scan* irradiation can in principle be finished as fast as in the normal irradiation mode.

As already mentioned, even if the position feedback loop is offline, the PBR and MBR data are still recorded. The comparison of those data with the reference values of the PBP and MBP exhibits the accuracy of the irradiation process.

Figure 4.11 a) depicts the nominal position versus the measured values as a function of the *re-scan* numbers. Figure 4.11 b) is a magnified cutout of a). Without active position feedback control the beam is not corrected due to the values obtained by the MWPCs. It can be seen that there is a influence of < 1 mm in y and x direction for the center of irradiation which increases in case of increasing *re-scan* numbers.

Figure 4.12 a) shows the corresponding quantitative analysis of the mean radial position error (see equation 4.6) for $0.8 \cdot 10^6 \frac{\text{particles}}{\text{rasterpoint}}$ which yields a maximum mean radial position error of 2.9 mm. Figure 4.12 b) with a particle density of $6.4 \cdot 10^6 \frac{\text{particles}}{\text{rasterpoint}}$ results in a maximum mean radial position error of 2.1 mm. As seen many times before, irradiating with a slower sweeping pencil beam generally yields better results.

In case of a $0.8 \cdot 10^6 \frac{\text{particles}}{\text{rasterpoint}}$ the mean radial position error gets much better when irradiating at higher *re-scan* numbers. This is due to the fact the *re-scanning* seems to have an averag-

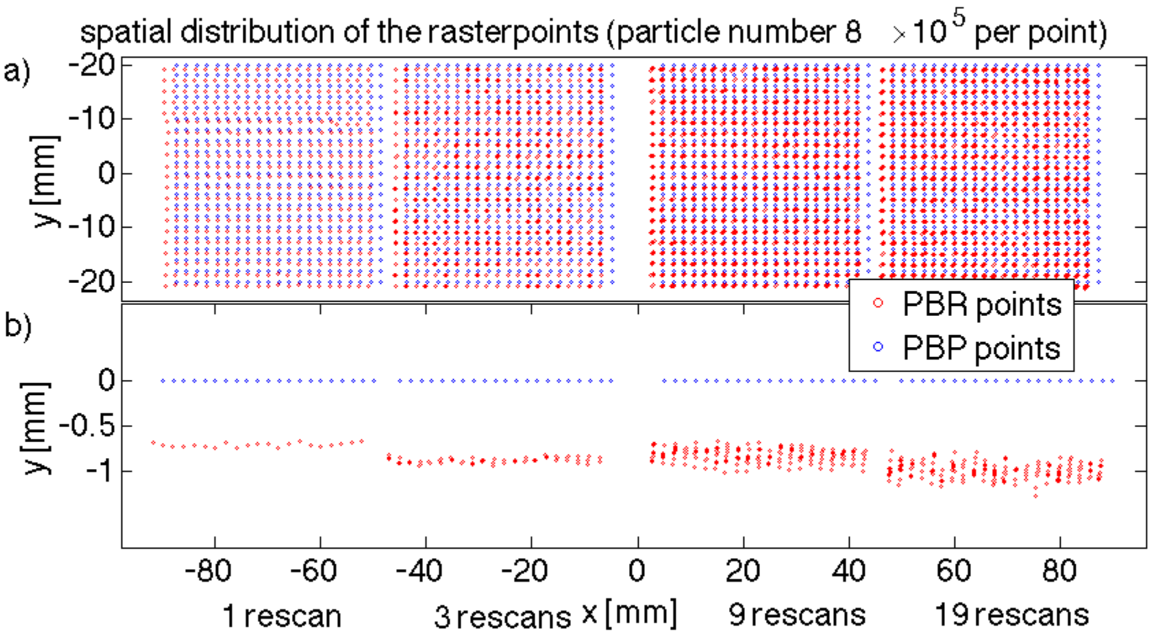

Figure 4.11.: The figure shows the spatial distribution of the planned and measured rasterpoints as a function of the *re-scan* number with *slice-by-slice re-scanning*. In case of the PBP the data points of each *re-scan* run lie exactly over each other. In case of the PBR data points the *re-scanning* irradiation is clearly visible.

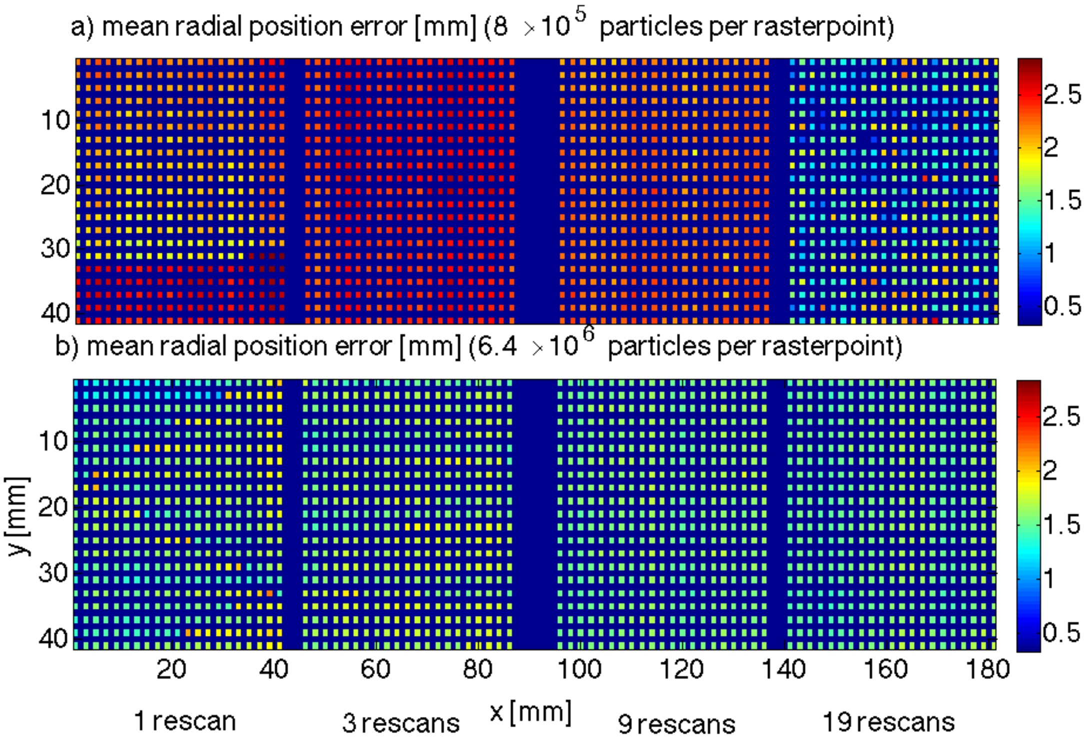

Figure 4.12.: The figure shows the mean radial position error in mm (see equation 4.6) for two fields with a different particle density as a function of the *re-scan* number.

ing effect which reduces the initial beam offset. For this measurement, that was done with a horizontal scanpath, the smoothing effect was dominant for the x position of the beam.

No less important than hitting the right position is applying the right dose. This analysis is addressed in figures 4.13 and 4.14. The first one sets up the same rasterpoint matrix as above and shows as results the relative dose error for densities of a) $0.8 \cdot 10^6 \frac{\text{particles}}{\text{rasterpoint}}$ and b) $1.6 \cdot 10^6 \frac{\text{particles}}{\text{rasterpoint}}$ as a function of the *re-scan* number.

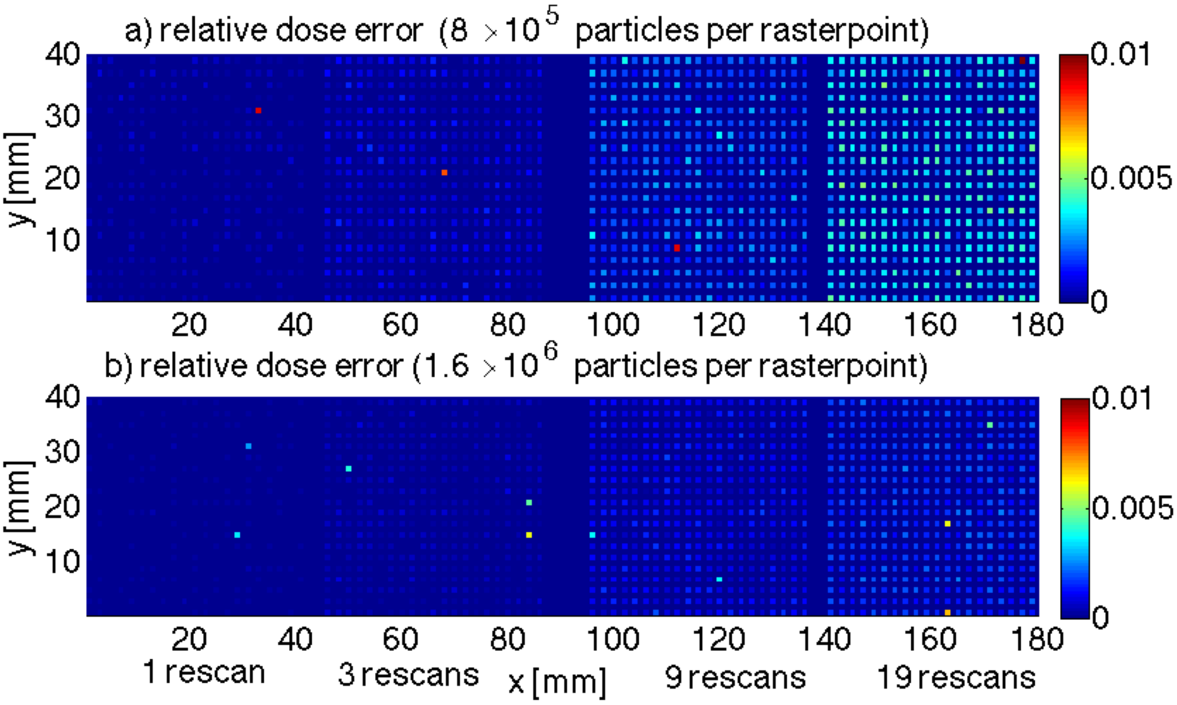

Figure 4.13.: Dose deviations by comparing the data of the PBP and PBR as a function of the *re-scan* numbers for two different particle densities. a) $0.8 \cdot 10^6 \frac{\text{particles}}{\text{rasterpoint}}$ and b) $1.6 \cdot 10^6 \frac{\text{particles}}{\text{rasterpoint}}$.

As predicted in chapter 3, the influence on the dose deviation is greater in case of lower particle densities and higher *re-scan* numbers. A deviation of approximately 1% occurs only four times in a) and not at all in b) by irradiation with the maximum available intensities. Hence, accurate dose application can be expected considering the finite dose sampling intervals of the TCUs at HIT.

Figure 4.14 is the experimental analog of to the simulations showed in 3.11 which displays the data of 4.13 b) in a histogram. Whereas single visits of some rasterpoints might have a deviation of 3%, which will most likely happen when irradiating with 19 *re-scans*, the comparison with the summed dose of each rasterpoint versus the planned dose yields a deviation below 1%.

Figure 4.15 shows an extract of the spill structure when irradiating the DeVarPho 3D plan with a) *slice-by-slice re-scanning*, b) *breath-sampled re-scanning* and c) as a cutout of b) with a *re-scan* number of 1. Figure 4.15 a) illustrates the time structure of the spill when irradiating in *slice-by-*

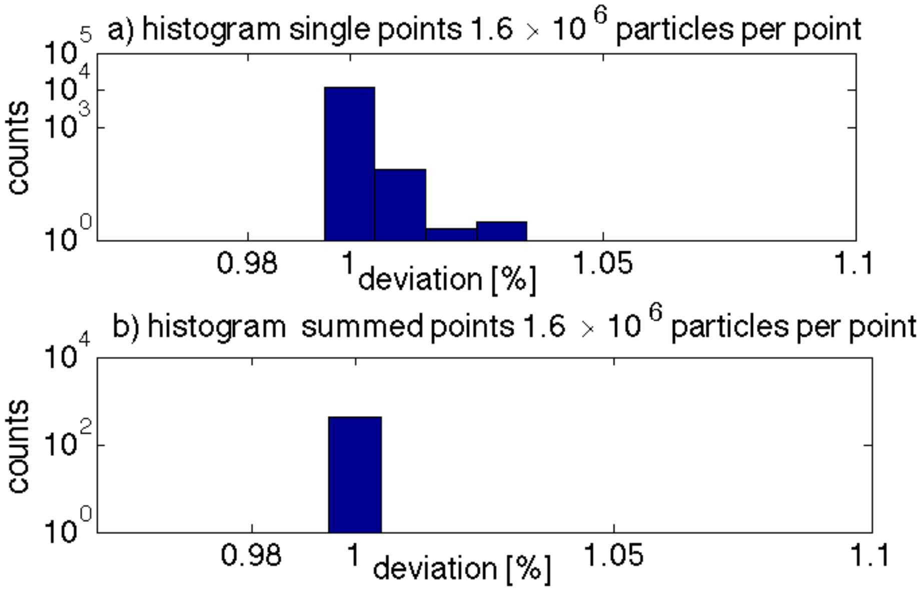

Figure 4.14.: Histogram of figure 4.13 b). The upper picture shows the deviation of each individual *re-scan* run and the lower picture the deviation of a rasterpoint if the fraction dose of all *re-scan* runs are summed up to a total dose of the corresponding rasterpoint.

slice re-scanning mode. As irradiation begins with the distal slices (these slices have in general higher particle numbers) the duration to finish a slice is longer for the more distal and shorter for the more proximal slices. In this case the treatment of the last slice was finished within 0.6 s. Figures 4.15 b) and c) on the other hand reveal a very regular irradiation pattern like it is expected in the *breath-sampled re-scanning* mode. The spill-on time was planned to be 4 s and the average irradiation time in the experiment was measured to be $\bar{T}_{breath\text{-}sampled\ re\text{-}scanning} = 3.89 \pm 0.1$ seconds per IES.

A further comparison between *slice-by-slice* and *breath-sampled re-scanning* in terms of applied dose: Figure 4.16 a) shows the particle numbers for both modes as a function of the IES number. The differences between the two modes are only visible in figure 4.16 b) where the

$$\text{relative deviation} = \frac{\mathrm{N}_{breath\text{-}sampled\ re\text{-}scanning} - \mathrm{N}_{slice\text{-}by\text{-}slice\ re\text{-}scanning}}{\mathrm{N}_{slice\text{-}by\text{-}slice\ re\text{-}scanning}} \tag{4.11}$$

is plotted, with N being the particle numbers of each IES.

The relative deviation between both modes is below 0.07%. The deviation gets greater when the difference in the intensities is larger. Differences in dose levels as low as presented in Figure 4.16 will not alter the outcome of a treatment.

Up next, the dosimetry results at the isocentre are presented:

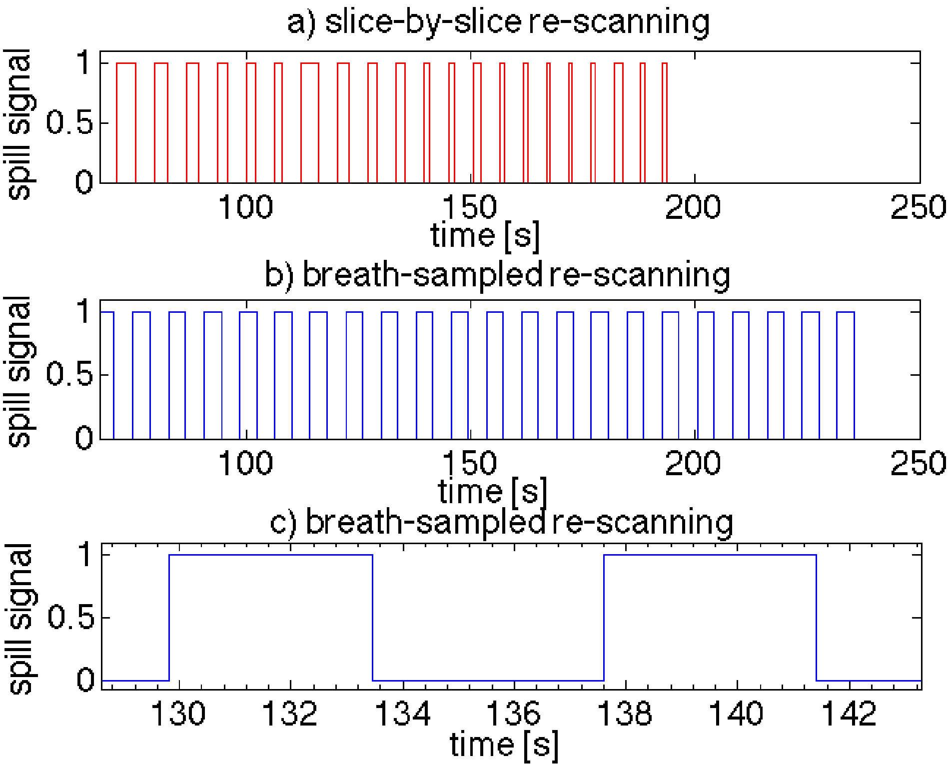

Figure 4.15.: Spill structure obtained when irradiating the DeVarPho 3D plan with a) *slice-by-slice re-scanning*, b) *breath-sampled re-scanning* for a period of 4 s with a *re-scan* number of 1. c) is a cutout of b). A spill signal of 1 means that beam is irradiating an IES and 0 represents the spill off status.

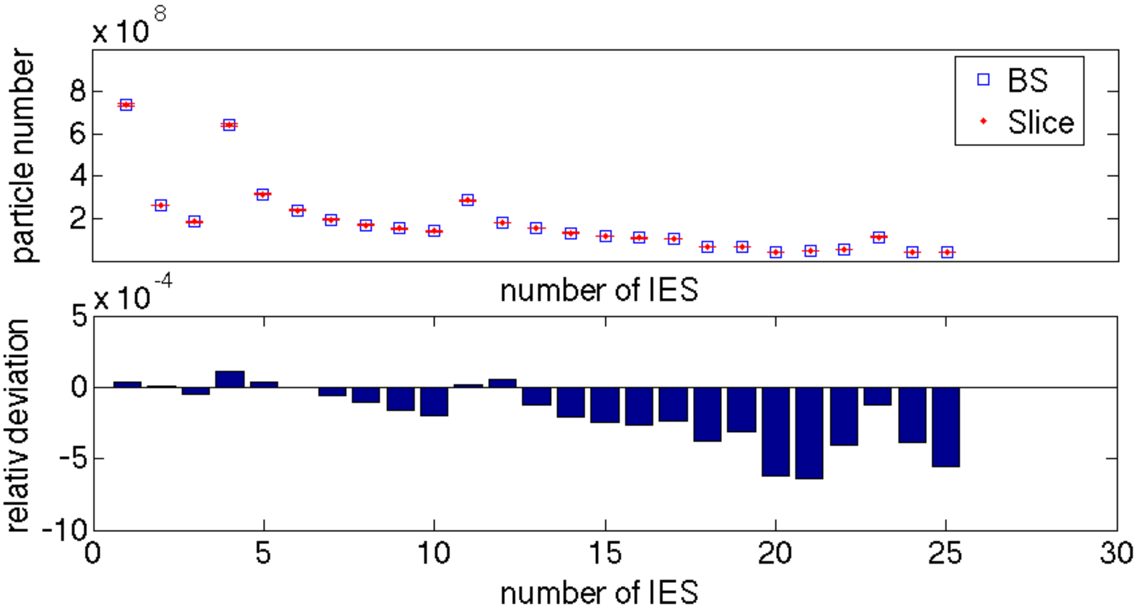

Figure 4.16.: Comparison of the particle numbers recorded in the PBR files after irradiating the DeVarPho 3D plan with 1 *re-scan* in *breath-sampled re-scanning* and *slice-by-slice re-scanning* mode. The relative deviation is calculated according to equation 4.11.

Figure 4.17 illustrates that irradiating 2D plans with the *re-scan* numbers of 3, 9 and 19 results in a *relative dose* deviation of well below 2.5 % when measured with the Farmer chamber. The data points are randomly distributed around 1 and show no visible dependence with respect to the *re-scan* number.

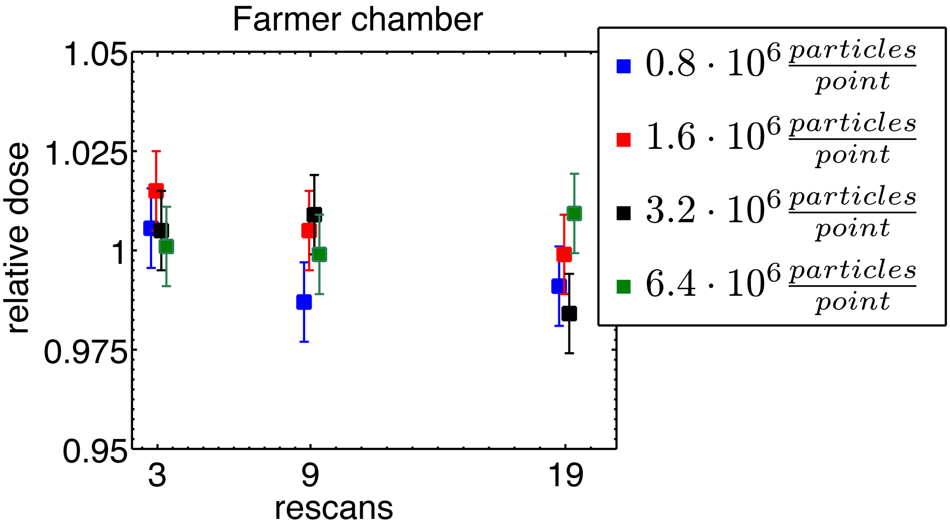

Figure 4.17.: Farmer chamber data obtained by irradiating the plans of section 4.2.5.

Figure 4.18 displays the pin point doses of *breath-sampled re-scanning* (1 *re-scan*) versus standard mode when irradiating the DeVarPho. All pin points inside the region without sharp dose gradients have a relative deviation smaller than ±5% (red color). The analysis of those pin points yields an average relative dose of 0.985 ± 0.021 which shows that 3D dose plans can be irradiated at HIT in *breath-sampled re-scanning* mode.

Figure 4.19 displays the corresponding experiment but with *slice-by-slice re-scanning* and $r = 5$. The analysis of the pin points yields an average relative dose of 1.023 ± 0.031. One pin point value inside the ITV region shows a relative deviation greater than ±5%. The pin point at $x = 12$ mm and $y = 50$ mm is the pin point around the region with the sharpest dose gradients and outside of the ITV (see figure B.2) so that its large relative deviation is not surprising. The irradiation with *slice-by-slice re-scanning* and 11 *re-scans* results in an average relative dose of 1.037 ± 0.048.

To summarize:

- *Slice-by-slice re-scanning* and *breath-sampled re-scanning* have been successfully implemented at HIT.
- The irradiation of a *slice-by-slice re-scanning* plan can be finished as fast in standard mode.
- With switched off position feedback loop, the maximum mean radial position error is 2.9 mm. *Re-scanning* even improves the positioning errors slightly.

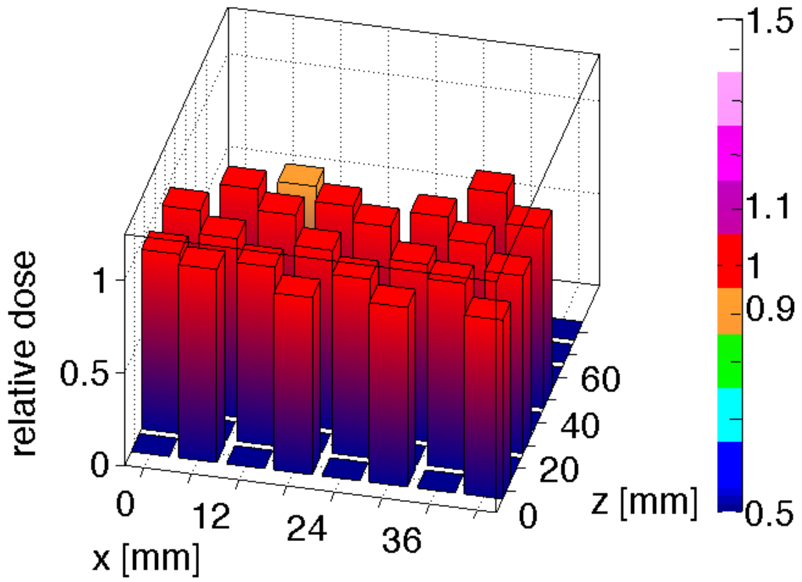

Figure 4.18.: Static pin point doses of *breath-sampled re-scanning* (1 *re-scan*) relative to the standard mode. The pin points inside the area of 6 mm $\leq x \leq$ 36 mm and 10 mm $\leq y \leq$ 70 mm lie well inside the ITV region without sharp dose gradients. Therefore these, pin point are used when quantitative results are reported.

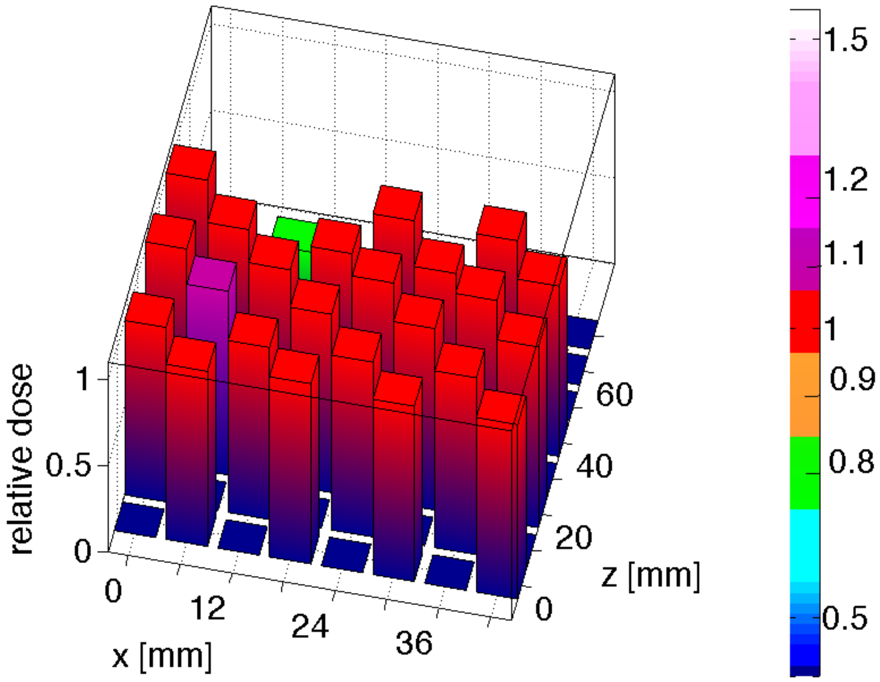

Figure 4.19.: Static pin point doses of *slice-by-slice re-scanning* (5 *re-scans*) relative to the standard mode. The pin points inside the area of 6 mm $\leq x \leq$ 36 mm and 10 mm $\leq y \leq$ 70 mm lie well inside the ITV region without sharp dose gradients. Therefore, these pin point are used when quantitative results are reported.

- The measured dose of the TCUs is within 1% to the prescribed one.
- *Breath-sampled re-scanning* can be irradiated with a intensity so that the irradiation of each IES takes as long as the motion period.
- Irradiations of 2D and 3D plans (without motion) with *breath-sampled re-scanning* and *slice-by-slice re-scanning* modes yield dose distributions with satisfying accuracy and precision.

4.3.3 Motion effects mitigation by *re-scanning*

2D irradiation: Amplitude, period, intensity and scanpath dependence

Figure 4.20 and figure 4.21 show the experimental film responses and the influence of the number of *re-scans* on the homogeneity for a horizontal scanpath, a motion period of 4 s in vertical and horizontal direction and peak-to-peak amplitudes of 1 cm and 1.5 cm, respectively.

Visual inspection of figure 4.20 illustrates that the two motion directions yield very different dose distributions. Interplay leads to a distinct interference pattern for a standard irradiation (1 *re-scan*) of the vertical moving film inside the ROI. There is even some chance that the outcome gets worse when increasing the *re-scans* which is clearly visible for the *re-scan* 5 case. For the *re-scan* numbers 13, 17 and 21 no significant difference is visible inside the ROI, CTV and ITV, respectively. When the target was moved horizontally the blackening of all ROIs looks alike and the movement is only visible because of the structure of the envelope outside the CTV.

Figure 4.22 displays the corresponding simulation results. The accordance with the experimental results is visible. The basic features of the measured dose distributions can be found in the forward calculations as well. As in the experimental case, the vertical motion results in a much greater distortion in the simulations, too. Particularly, the comparison of the *re-scan* numbers of 1 and 5 illustrates the power of the simulation environment to predict the outcome of a *re-scan* simulation.

Figure 4.21 shows the quantitative analysis of the ROI of the Kodak X-Omat V films. For a small number of *re-scans* interplay is not always reduced and can even decrease homogeneity for an unfortunate combination of parameters like starting phase, motion amplitude, motion period, scan path and beam application. Generally, a larger amplitude increases interplay effects. It follows that more *re-scans* are needed to yield an acceptable dose homogeneity value. In these experiments the peak-to-peak 1 cm vertical motion amplitude had a homogeneity minimum of $H = 0.61$ at 5 *re-scans* and the 1.5 cm peak-to-peak vertical motion amplitude of $H = 0.30$ at 3 *re-scans*. For both amplitudes static irradiation quality is reached after 15 *re-scans*. For the horizontal motion the minima of the homogeneity of both amplitudes had a value of $H = 0.96$ and was even for low *re-scan* numbers superior to the static reference irradiation. To reach static

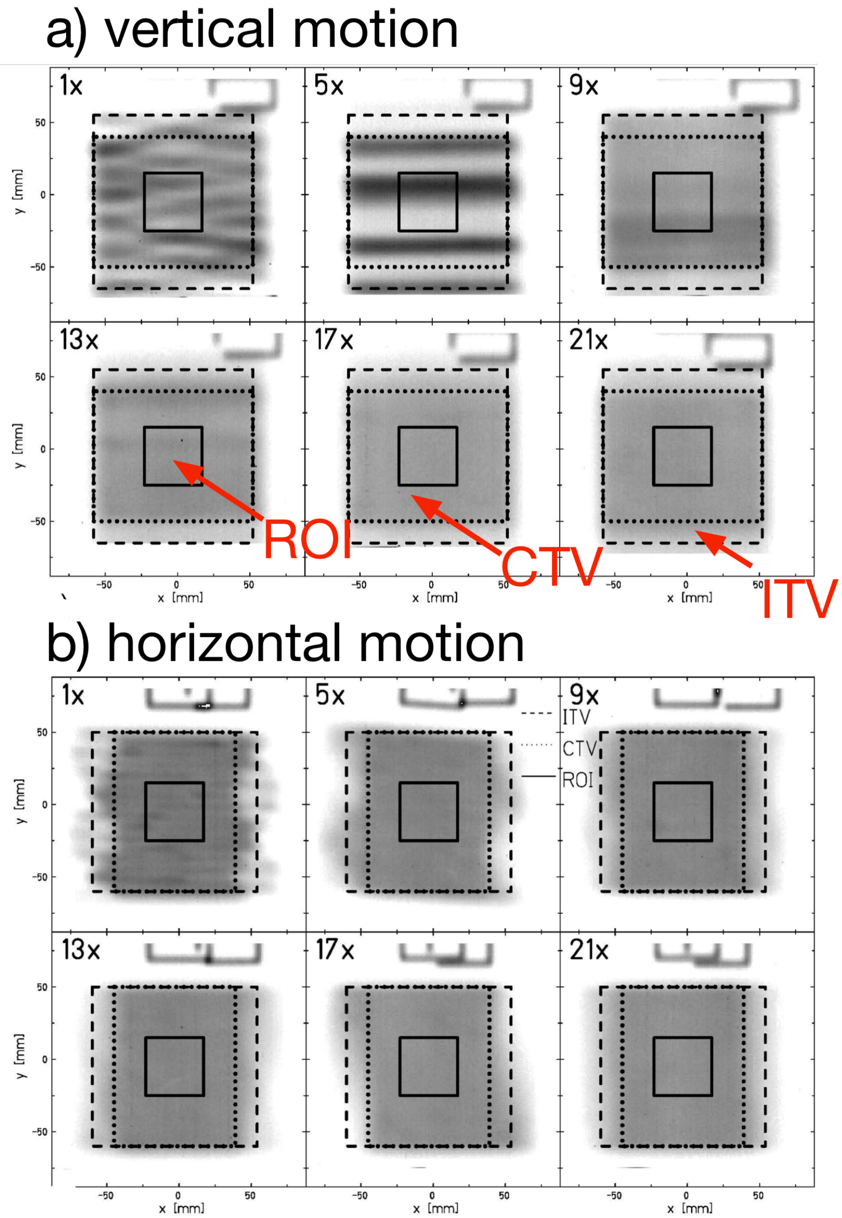

Figure 4.20.: Normalized measured film response as a function of the number of *re-scans* for 15 mm amplitude target motion and a horizontal scanpath. a) vertical motion b) horizontal motion (ROI: solid line; CTV: dotted line; ITV: dashed line). In case of the vertical motion distinct interplay patterns are visible. The specific combination of all the irradiation parameters even yields to a decreasing homogeneity value when increasing the *re-scan* number from 1 to 5. Figure 4.21 reports the corresponding data. Even without *re-scanning* compensation the horizontal motion does not distort the dose distribution significantly. The impact of motion is only visible at the shape of the envelope of the dose distribution. Measurement performed by C. Bert (Bert et al., 2008a).

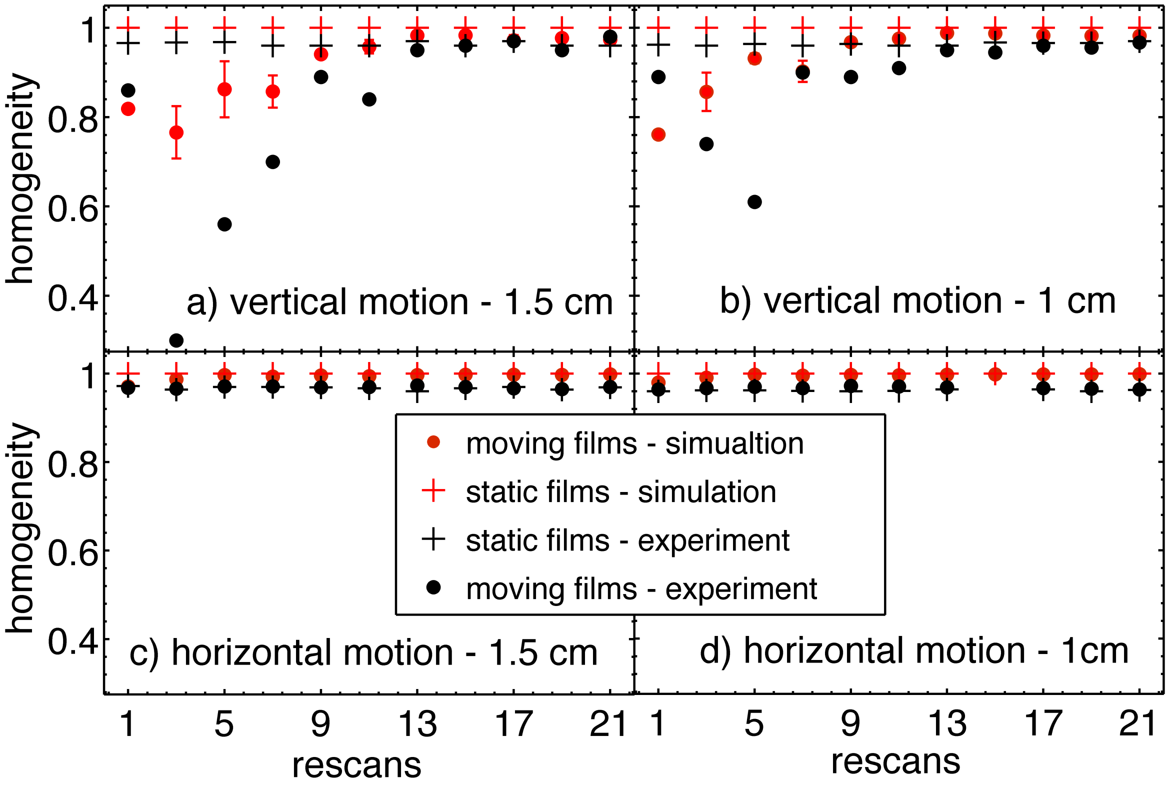

Figure 4.21.: Homogeneity within the ROI of the irradiations and the corresponding simulations as a function of the number of *re-scans*. The static Kodak X-Omat V films were irradiated without *re-scan* functionality on the very same film in normal therapy mode to obtain reference homogeneity values. The simulation of a static target results in a perfect homogeneity of $\mathrm{H} = 1$ and is independent of the film developing process.

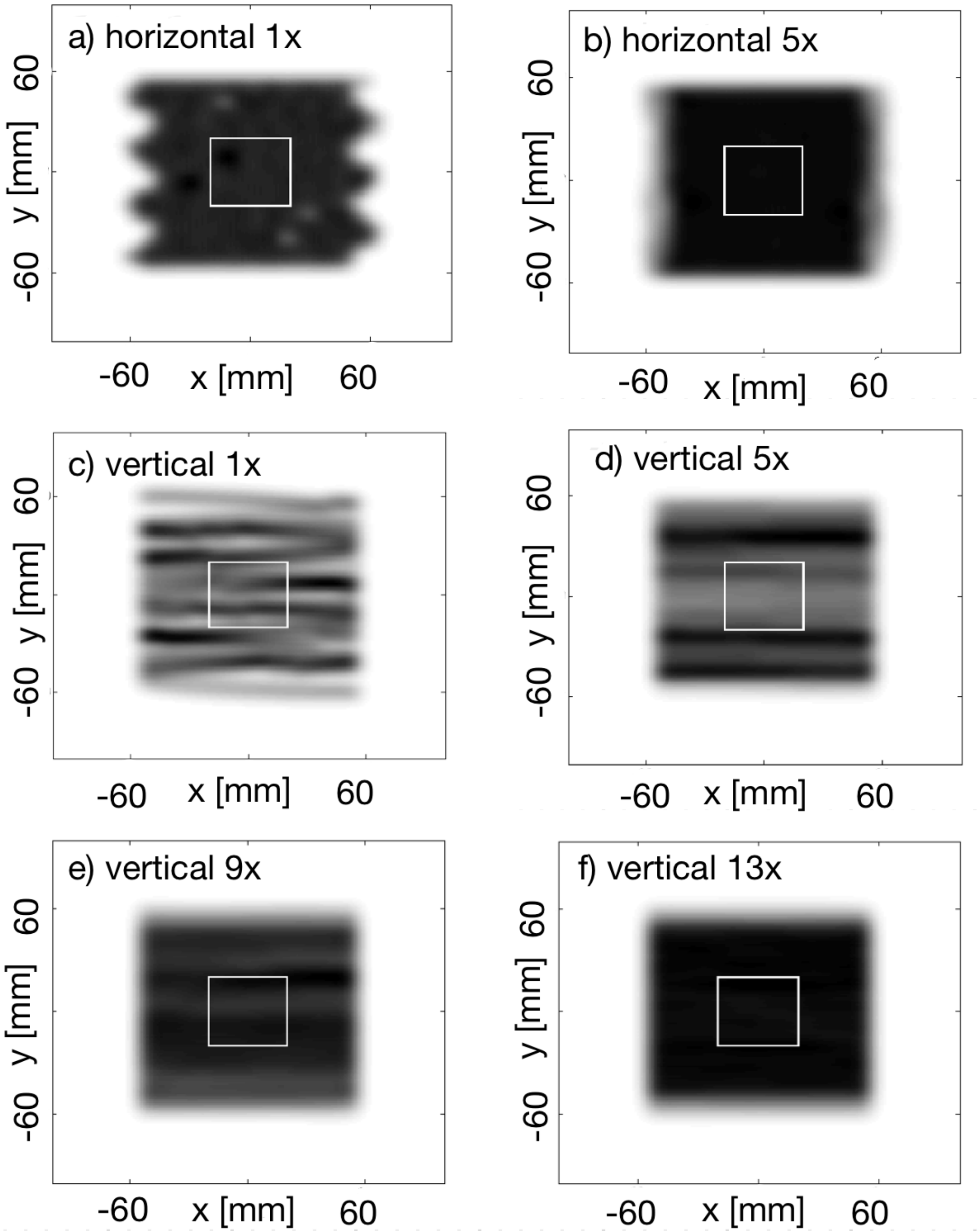

Figure 4.22.: 2D simulation of interplay patterns irradiated in the *slice-by-slice re-scanning* mode to compare with the experimental results of figure 4.20. a) - b) horizontal and c) - f) vertical sinusoidal motion with a period of 3 s and a peak-to-peak amplitude of 1.5 cm.

irradiation quality no *re-scan* irradiation is needed in case of both horizontal amplitudes for this parameter set.

The corresponding simulation results are also presented in figure (4.21). In contrast to the experiments three different starting phases (0°, 90° and 180°) were used to calculate the dose cubes. In these simulations the peak-to-peak 1 cm vertical motion amplitude has both the absolute homogeneity minimum of $\mathrm{H} = 0.75$ and the minimum of the mean homogeneity $\mathrm{H} = 0.76$ at 1 *re-scan*. In case of the 1.5 cm vertical peak-to-peak motion amplitude, both the absolute homogeneity minimum of $\mathrm{H} = 0.71$ and the minimum of the mean homogeneity $\mathrm{H} = 0.77$ occurred at 3 *re-scans*. Again a larger amplitude increases interplay effects which is also visible in the wider spread of the standard deviation error bars. For both horizontal motion amplitudes static irradiation quality is almost reached after 5 *re-scans*. The 1 cm peak-to-peak horizontal motion amplitude has both the absolute homogeneity minimum of $\mathrm{H} = 0.97$ and the minimum of the mean homogeneity $\mathrm{H} = 0.98$ at 1 *re-scan*. The 1.5 cm horizontal peak-to-peak motion amplitude has both the absolute homogeneity minimum of $\mathrm{H} = 0.96$ and the minimum of the mean homogeneity $\mathrm{H} = 0.97$ at 1 *re-scan*. The simulated homogeneity values for a static target results in a perfect homogeneity of $\mathrm{H} = 1$ whereas the experimental homogeneity values can even be smaller than those measured in the presence of target motion. The reason is that the Kodak X-Omat V films are not perfectly homogeneous because errors can be introduced in the developing and analyzing process as already mentioned. Furthermore, the transversal beam profile always deviates more or less from a perfect circle which is used in the optimization process. *Re-scanning* can smoothen these inhomogeneities resulting from an elliptical beam shape by the same statistical means as it reduces interplay effects due to motion.

The simulations above were also calculated for *breath-sampled re-scanning* and the results are shown in figure 4.23 for a peak-to-peak amplitude of 1.5 cm in vertical motion. The planned dose was 1 Gy. Figure 4.23 a) and 4.23 c) show that the different temporal structure of the beam application results in a dose profile which almost never matches the prescribed dose of 1 Gy.

Inherently *re-scanning* is best suited for small motion amplitudes because the exposure of the healthy tissue will then be closest to the static case. But our investigations also include larger motion amplitudes as a worst case scenario. Films have been irradiated with six different starting phases at the same time by using the multi-phase phantom. The peak-to-peak amplitude was set to $\mathrm{A} = 5$ cm, the period to $\mathrm{P} = 4$ s, the intensity to $\mathrm{I} = 0.8 \cdot 10^7 s^{-1}$ and the motion direction was perpendicular to the scan path. Figure 4.24 a) shows the dependence of the homogeneity on the starting phase and the *re-scan* number. There is a large phase dependence for low *re-scan* numbers which means that even a small change in the starting phase can yield a totally different interplay pattern. More *re-scans* are needed to reach the static irradiation homogeneity (29 *re-scans* in the *slice-by-slice re-scanning* mode) than in the cases of smaller amplitudes presented above. Figure 4.24 b) plots the minima, mean and maxima along with

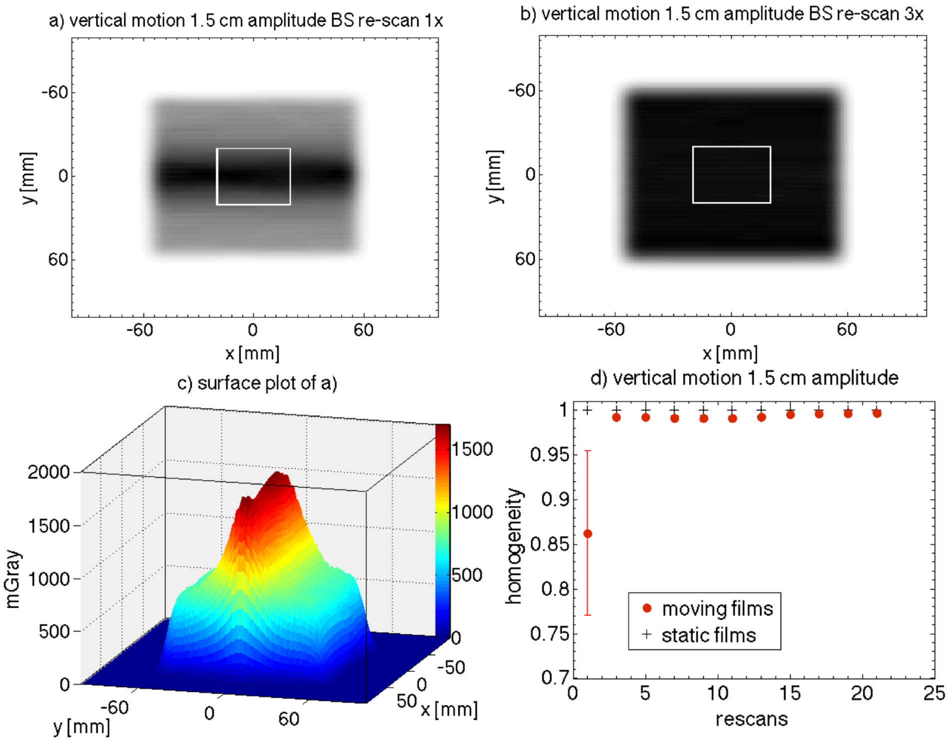

Figure 4.23.: Simulations with the *breath-sampled re-scanning* technique in case of vertical motion with a peak-to-peak amplitude of 1.5 cm. a) 1 *re-scan* b) 3 *re-scans* c) surface plot of 1 *re-scan* d) homogeneity as a function of *re-scan* number.

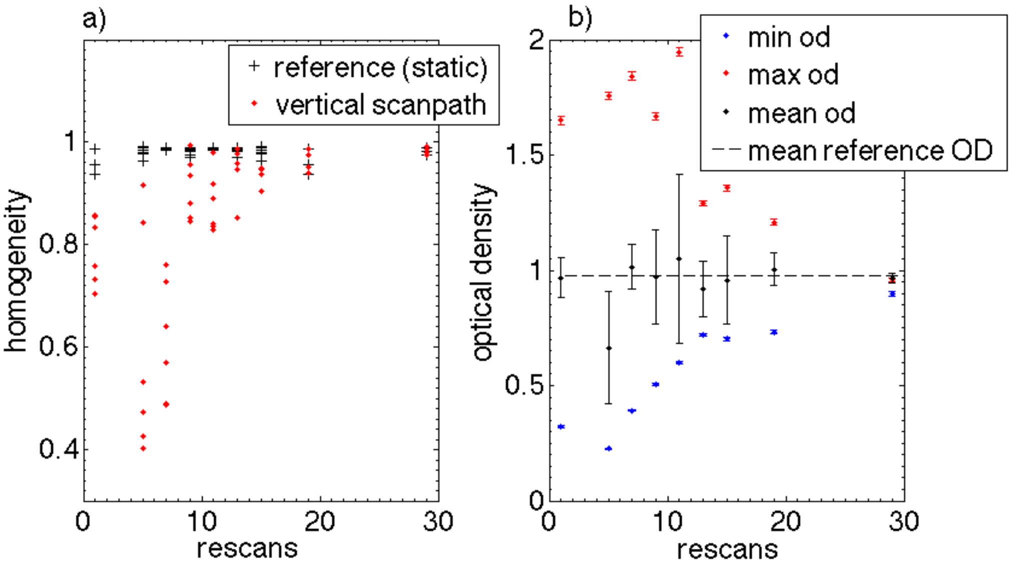

Figure 4.24.: a) Homogeneity within the CTV. The peak-to-peak motion amplitude was 5 cm and the motion period of 4 s. Six different starting phases (separated by $60°$) were used and irradiation was done in the *slice-by-slice re-scanning* mode. The static films were irradiated in normal therapy mode to get reference homogeneity values on each film. b) Shows the absolute min, mean and max optical density values for the same CTV area. These values converge to the static reference measurements for increasing r.

the mean optical density for static irradiation versus the *re-scan* number. For the case of 5 *re-scans* the CTV was obviously not irradiated most of the time which results in large underdosage. In addition to the foregoing irradiation, a simulation with the same nominal parameter space was performed with *breath-sampled re-scanning* (see figure 4.25). For all motion amplitudes the *breath-sampled re-scanning* simulations converge faster to static irradiation quality than the *slice-by-slice re-scanning* simulations. But compared to figure 4.23 the homogeneity values are 1-2% lower for identical *re-scan* numbers in case of the 5 cm amplitude compared to the 1.5 cm.

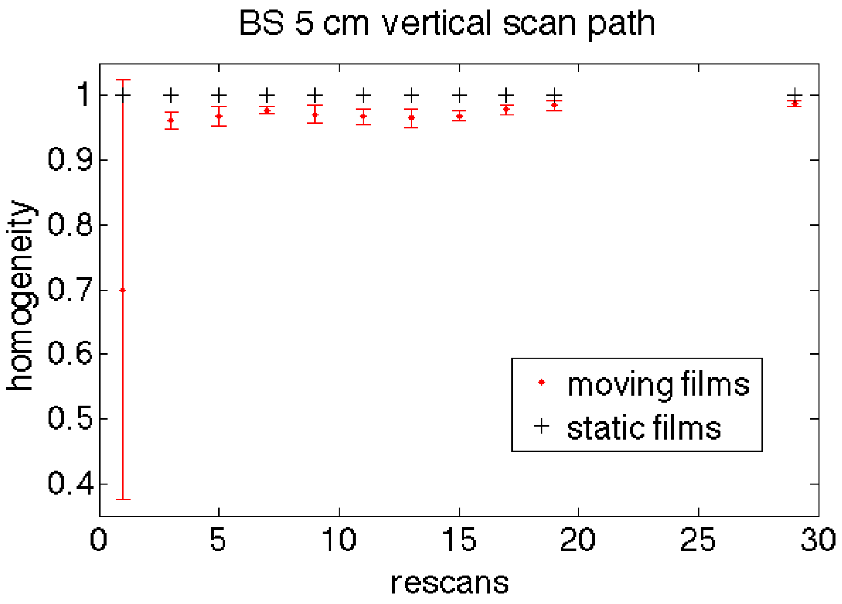

Figure 4.25.: Mean homogeneity values within the CTV area as a function of r. The peak-to-peak motion amplitude was 5 cm and the motion period of 4 s. Six different starting phases (separated by 60°) were used and simulations were in the *breath-sampled re-scanning* mode.

Figures 4.26 (for *slice-by-slice re-scanning*) and 4.27 (for *breath-sampled re-scanning*) present the simulation results for a wide range of parameters (see table 4.3) and display their influence on DAHs[8].

In Figure 4.26 a) the dependence of the motion amplitude on the DAHs was studied. As expected, the DAH improves for smaller amplitudes. This is again in accordance with the experimental results shown before - the data of 4.21 demonstrate that *re-scanning* compensates interplay effects for small amplitudes faster than for larger ones. Figure 4.26 b) exhibits the influence of a variation and the duration of the motion. The shorter the period the worse become the DAHs with this specific parameter set. Figure 4.26 c) shows the intensity dependence and that our a priori chosen intensity (see table 4.3) apparently results in a DAH of minimum quality. To gain the best possible DAH curve with this specific simulation setting one could use very high or very low intensity values. In the limit of an infinite intensity value the target seems

---

[8] DAHs are basically a special case of the well known dose volume histograms but with the depth dimension of one CT voxel.

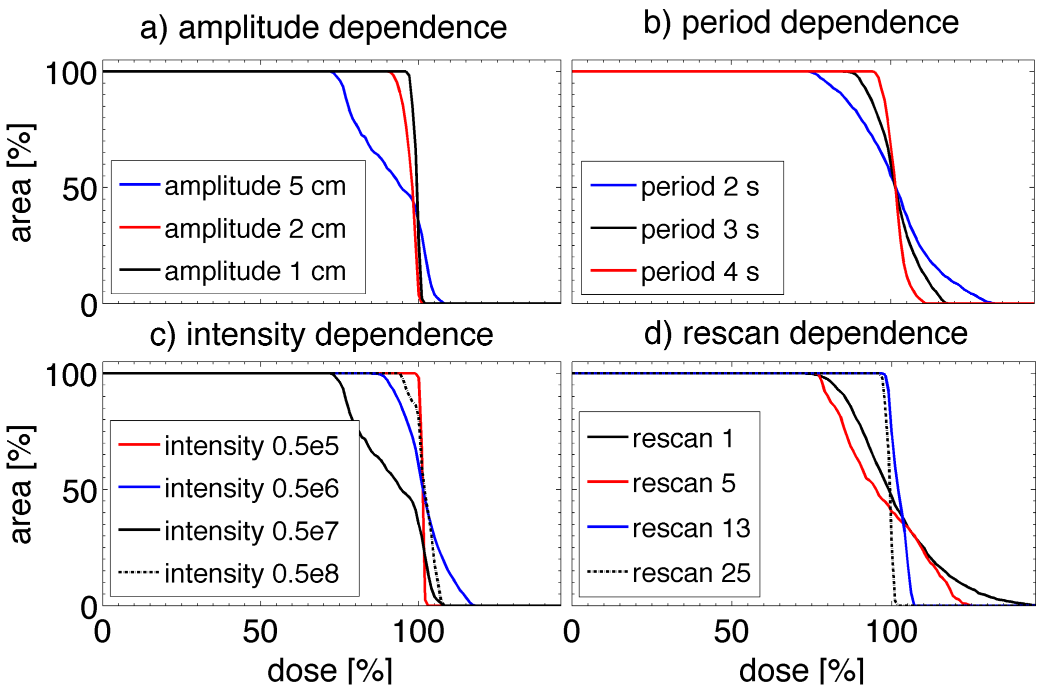

Figure 4.26.: DAHs simulated for *slice-by-slice re-scanning* mode (motion being perpendicular to the scan path) as a function of parameters which play a crucial role in shaping interplay patterns. Table 4.3 gives an overview of the actual parameter set of each figure.

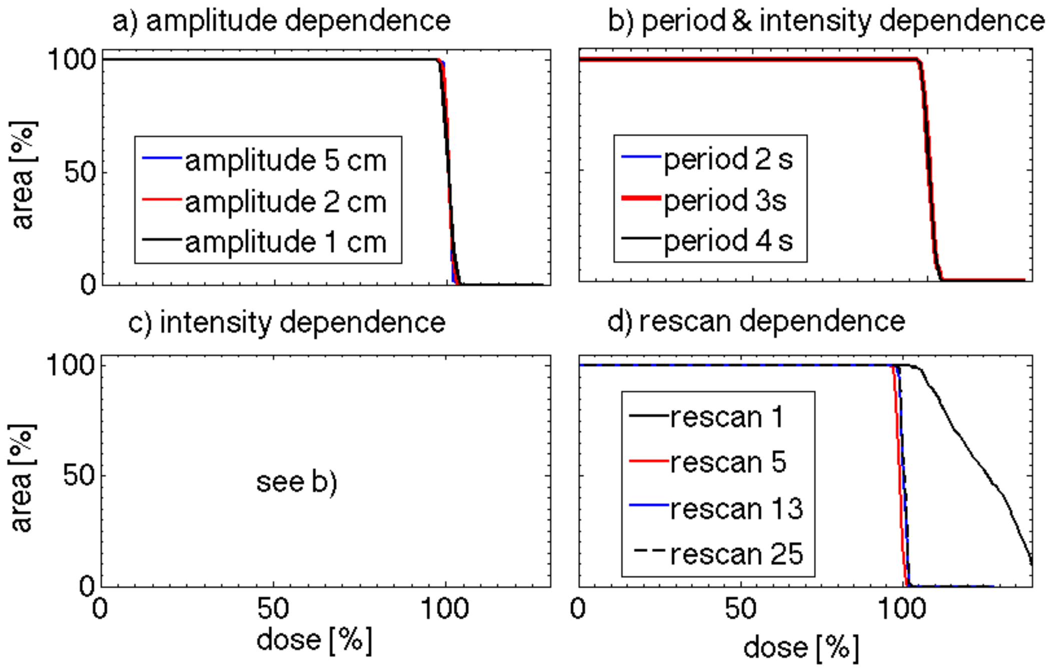

Figure 4.27.: DAHs simulated for *breath-sampled re-scanning* mode (motion being perpendicular to the scan path) as a function of parameters which play a crucial role in shaping interplay patterns. Table 4.3 gives an overview of the actual parameter set of each figure.

to be stationary whereas for very low intensity values the particles are evenly distributed many times over all motion phases. Figure 4.26 d) displays the influence on the number of *re-scans*. Analog to our experiments the quality of the DAH decreases when comparing the *re-scan* 1 and 5 cases and reaches static irradiation quality after 25 *re-scans*.

Compared to the foregoing results in *slice-by-slice re-scanning* mode the *breath-sampled re-scanning* technique shows almost no influence on the used parameter set. In figure 4.27 a) the variance of each single DAH curve is minimal and the dose values for all amplitudes are within the limits of the ICRU-50 (ICRU, 1993) report. Inspecting figure 4.27 b) suggest that there might be no influence of the chosen period at all. This point will be addressed in the discussion section. Figure 4.27 c) was left empty to make clear that the dependence on the period and the intensity are coupled and that there exists no subjection on the intensity on its own. The relationship between the two parameters is

$$I = \frac{N}{T_{PE}}, \tag{4.12}$$

with I being the intensity, N the number of particles and T_{PE} the period of the motion. Static irradiation quality is already reached after 5 *re-scans* (see figure 4.27 d)).

figure	*re-scans*	amplitude [cm]	intensity [1/s]	period [s]	phase [°]
4.26 a)	slice 25	-	$0.5 \cdot 10^7$	4	0
4.26 b)	slice 25	5	$0.5 \cdot 10^7$	-	0
4.26 c)	slice 25	5	-	4	0
4.26 d)	slice	1	$0.5 \cdot 10^7$	4	0
4.27 a)	BS 25	-	automatic	4	0
4.27 b)	BS 25	5	automatic	-	0
4.27 d)	BS	1	automatic	4	0
4.28 a)	slice	5	$1 \cdot 10^8$	4	0
4.28 b)	BS	5	automatic	4	0
4.3.3	slice	5	$0.5 \cdot 10^7$	4	0
4.33 a)	slice	1	$1 \cdot 10^8$	4	0
4.33 b)	BS	5	automatic	4	0
4.33 c)	BS	1	automatic	4	0
4.33 d)	BS	5	automatic	4	0

Table 4.3.: Summary of the parameters used for the simulation of the listed figures. The amplitude length is meant to be from peak-to-peak.

Figures 4.28 a) and b) compare the DAHs for the rather large peak-to-peak amplitude of A = 5 cm when irradiated in *slice-by-slice re-scanning* and *breath-sampled re-scanning* mode, respectively. The left pictures indicates that, even in case of 25 *re-scans*, *slice-by-slice re-scanning* cannot guarantee satisfying irradiation quality[9] for larger amplitudes. In contrast to this finding, for 13 *re-scans breath-sampled re-scanning* is already very close the limits of the ICRU-50 report and the numbers 17 and 25 lie well between these limits even of they both show a small overdosage of the target volume.

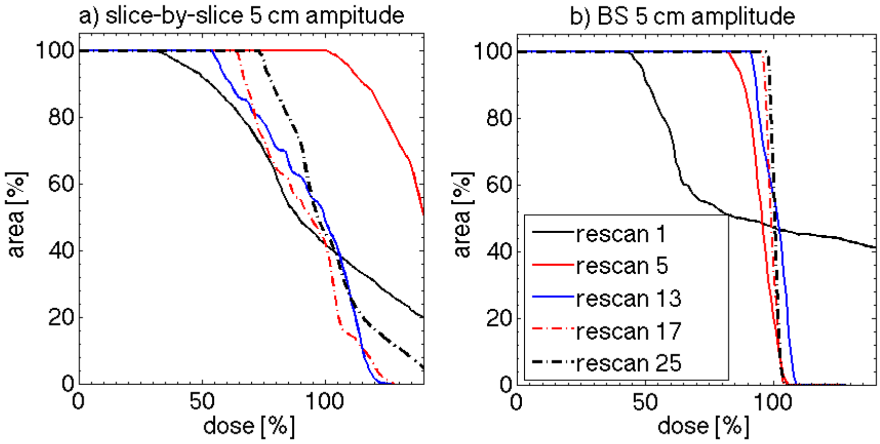

Figure 4.28.: DAHs simulated for *slice-by-slice re-scanning* and *breath-sampled re-scanning* mode (motion being perpendicular to the scan path) in case of a large amplitude of A = 5 cm. Table 4.3 gives an overview of the actual parameter set of each figure. The legend is valid far a) and b).

2D irradiation: Size of the field penumbra

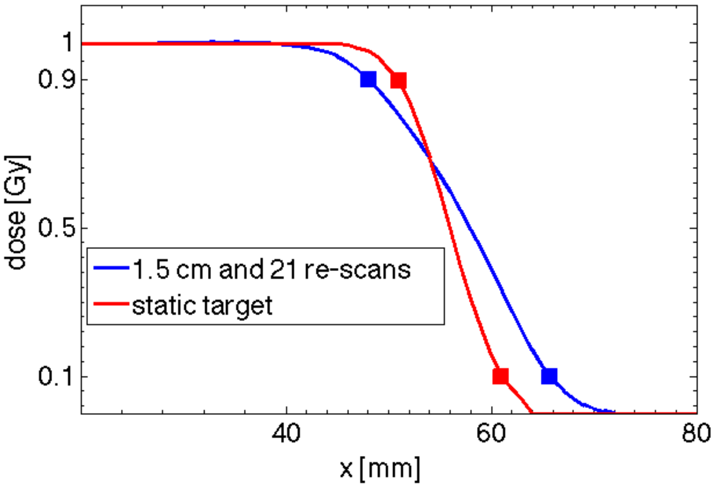

Figure 4.29.: Comparison of the penumbra width: The moving target (peak-to-peak amplitude 1.5 cm, starting phase of 0° and 21 *re-scans*) results in a 90% to 10% penumbra width of 18 mm in case of the static target the width is 10 mm, respectively.

---

[9] The limits of the dose axis was kept constant in relation to the foregoing pictures as to make the comparison more convenient.

Irradiating a moving target leads to a blurred dose distribution which means that the sharp dose gradients of the static case cannot be preserved so that the beam penumbra at the field edges will increase. Mathematically, the blurring can be described by a convolution of the static dose distribution that would result without motion with a characteristic motion kernel (Bortfeld et al., 2004). The shape of the penumbra depends on the amplitude, the characteristics of the motion, the *re-scan* number and on the sharpness of the static dose distribution. Figure 4.29 shows the comparison of the penumbra between the static dose distribution and the case of 21 *re-scans*, an amplitude of 1.5 cm and a starting phase of 0°. The distance between 90% and 10% levels of the prescribed dose defines the width of the penumbra. The values were calculated as 10 mm for the static target and 18 mm for the moving one, respectively.

2D irradiation: Starting phase dependence

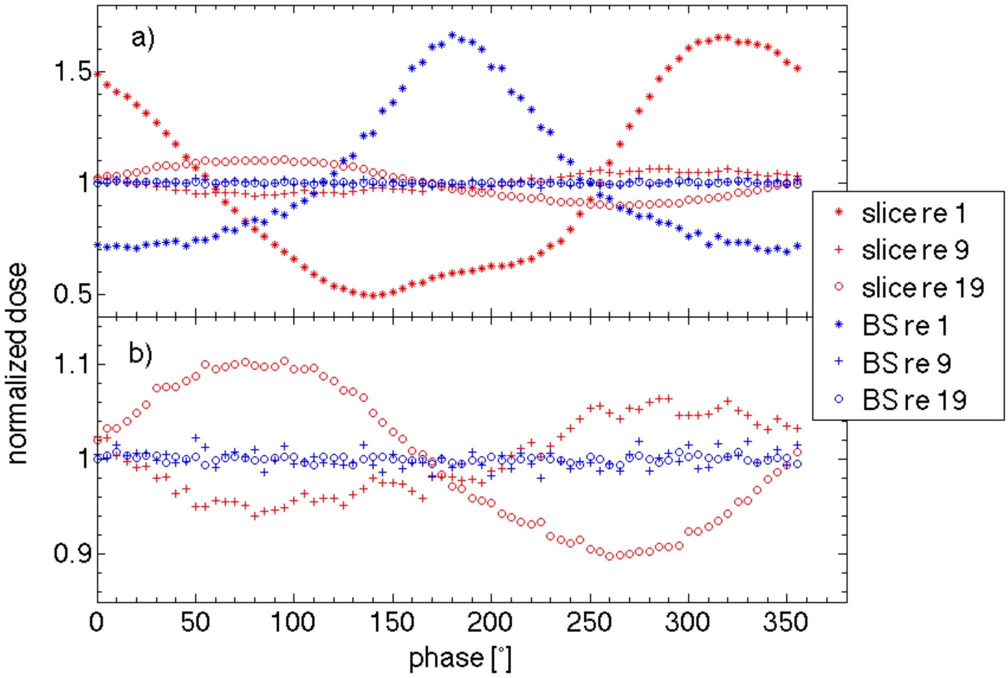

Figure 4.30.: Starting phase dependence for 1.5 cm peak-to-peak amplitude in vertical motion direction, a horizontal scan path and a period of 4 s. The dose values were taken from the voxel in the centre of the radiation field and normalized to the prescribed dose. a) shows the results of *slice-by-slice re-scanning* and *breath-sampled re-scanning* with the *re-scan* numbers 1, 9 and 19. b) magnified cutout of a)

The starting phase of any *re-scan* mode is in general unknown in advance and experiments with a large number[10] of phases are in reality very time consuming and often not feasible. Therefore figure 4.30 shows the phase dependence of a single energy slice for *slice-by-slice re-*

---

[10] For example with a phase shift of 5° for every irradiation.

mode	a) % of dose inside 95-107%	b) deviation in % max vs. min
slice 1	0.06	338
slice 9	0.94	12
slice 19	0.41	22
BS 1	0.07	241
BS 9	1	3
BS 19	1	0.8

Table 4.4.: Analysis of figure 4.30. Column a) shows the percentage of dose of the centre voxel inside the radiation field which is inside the limits of the ICRU-50 (ICRU, 1993) standard. Column b) compares the deviation of the values of the maximum and minimum dose in percent.

scanning and *breath-sampled re-scanning* with a peak-to-peak amplitude of 1.5 cm, a period of 4 s and a motion perpendicular to the scan path direction. The dose was extracted at one voxel in the centre of the radiation field. A strong phase dependence is clearly visible with both modes at a *re-scan* number of 1. Surprisingly, the *slice-by-slice re-scanning* phase dependance is smaller for 9 than for 19 *re-scans*, but in both cases the dose variance is largely reduced. *Breath-sampled re-scanning* reduces the phase dependence by a much larger amount than the other technique and gets constantly better by increasing the *re-scan* number. Interestingly, all *slice-by-slice re-scanning* curves mimic the shape of the underlying sinusoidal motion. Despite all calculations having exactly the same parameters[11] the maxima are shifted by approximately 90° and 270°, respectively. The more the curve mimics a sinusoidal shape the greater the correlation between beam application and motion must have been. To overcome this correlation is an important prerequisite to ensure satisfying irradiation of the patient. Inspecting figure 4.30 b) shows that *breath-sampled re-scanning* not only reduces the dose variance by a much larger amount but that it is also able to break up the correlation between motion and beam amplification for the *re-scan* numbers 9 and 19. The values are randomly distributed around the mean and no projection of the underlying motion can be observed. Table 4.4 displays results from figure 4.30 concerning the dose variations.

Bortfeld et al. (Bortfeld et al., 2002) calculated that the probability density function (PDF) of the dose distribution of a voxel will transform into a Gaussian shape after a few fractions. Figure 4.31 shows histograms of the foregoing simulations. All distributions are centered around the prescribed dose of 1 Gy. The asymmetry, which is most pronounced in a) and d), is most likely to vanish by increasing the number of simulations. Both techniques indicate that it is very unlikely for a point to receive the planning dose for 1 *re-scan*. The minima and maxima dose values have the highest probability. In case of the *slice-by-slice re-scanning* mode this behavior tends to vanish at first by applying 9 *re-scans*, but appears again for 19 *re-scans*. *Breath-sampled re-*

---

[11] Besides the different *re-scan* numbers

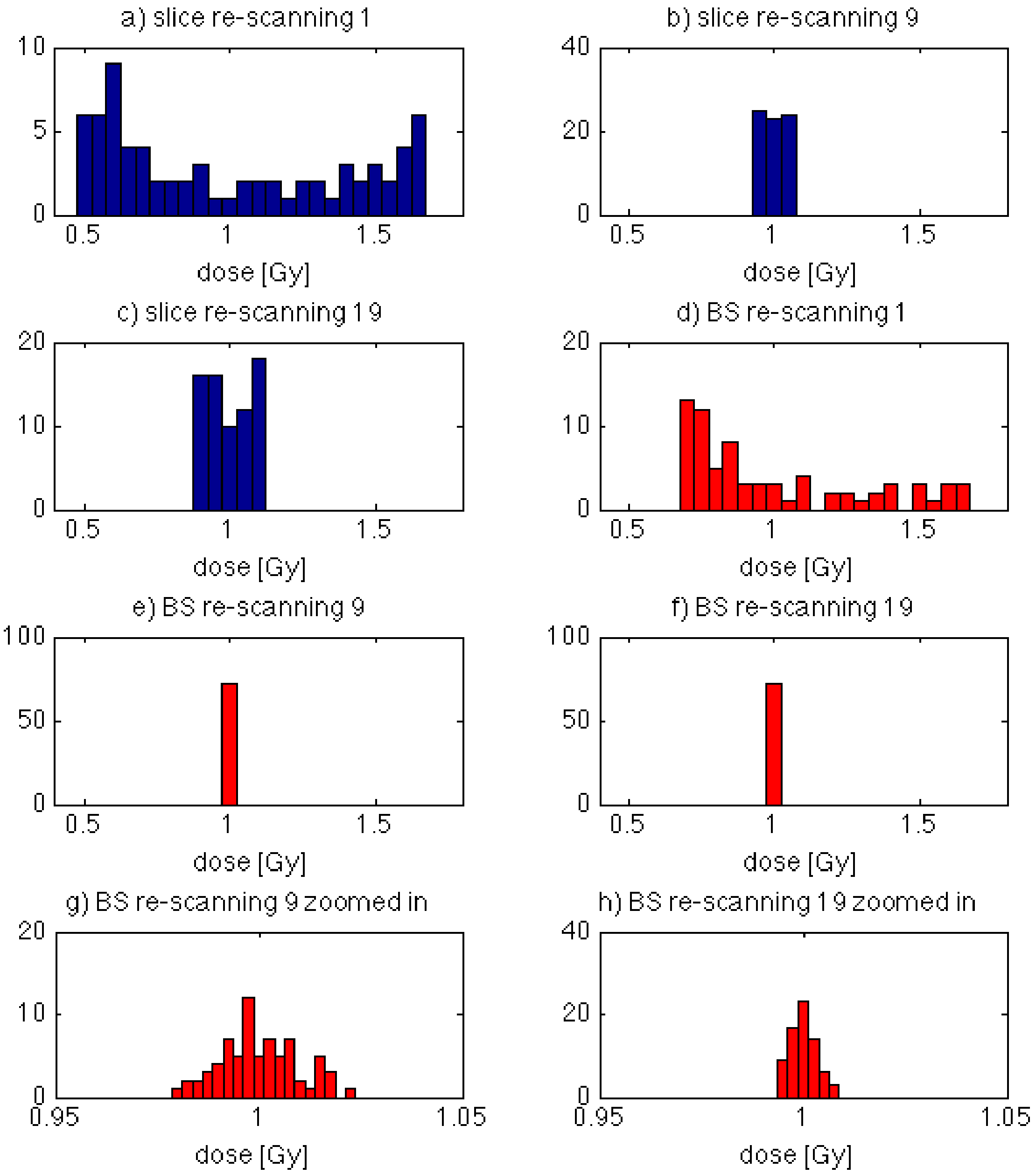

Figure 4.31.: Histograms of figure 4.30. a) - c) show the results of *slice-by-slice re-scanning* with the *re-scan* numbers 1,9 and 19. d) - f) show the corresponding histogram for the *breath-sampled re-scanning* mode. g) and h) are the magnified versions of e) and f), respectively. For viewing purpose the limits of both axes are not constant.

scanning is definitely much closer to the findings of Bortfeld et al., who assert that distributions like a) and d) should transform into a Gaussian shape after a few *re-scans*.

2D irradiation: Spill profile dependence

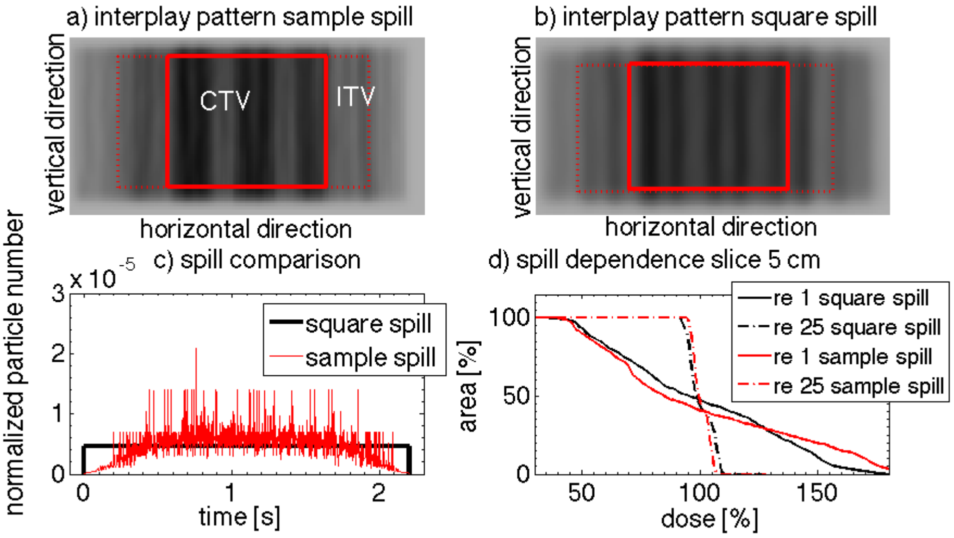

Figure 4.32.: The dependence of the spill shape on the dose pattern. Simulation parameters are listed in table 4.3. Qualitatively, the interplay between a) the ideal square and b) the measured spill profile is almost identical in case of 1 *re-scan*. c) displays both spill structures normalized to one particle per spill and d) the DAHs of 1 and 25 *re-scans* for both spill shapes.

In experiments with motion phantoms or when calculating simulations, the frequency, amplitude and *re-scan* number can be adjusted quite precisely, but there can be large deviations between the actual intensity and the one used in the simulation. Furthermore, every spill shape deviates from one another more or less. Therefore an ideal rectangular spill shape was compared with a typical measured spill file, which was used for the previous simulations. Figure 4.3.3 a) and b) shows the interplay patterns of the measured spill and the ideal square profile (see figure c)) for 25 *re-scans* in *slice-by-slice re-scanning* mode, respectively. Qualitatively, both are basically identical so that cold and hot regions appear at the same position if all the other simulation parameters are kept constant. The DAHs of figure 4.3.3 d) differ distinctly for 1 *re-scan* but only marginally for 25 *re-scans* which is again due to an averaging effect of *re-scanning*.

To extent theses findings figure 4.33 presents further simulation results. The core message is that the DAH can deviate from each other independent of the used irradiation mode for 1 *re-scan* due to different spill profiles but that a *re-scan* number of 25 basically entirely reduces the differences. Figure 4.33 d) shows that already a *re-scan* number of 5 yields in marginal differences of the corresponding curves when irradiating in *breath-sampled re-scanning* mode.

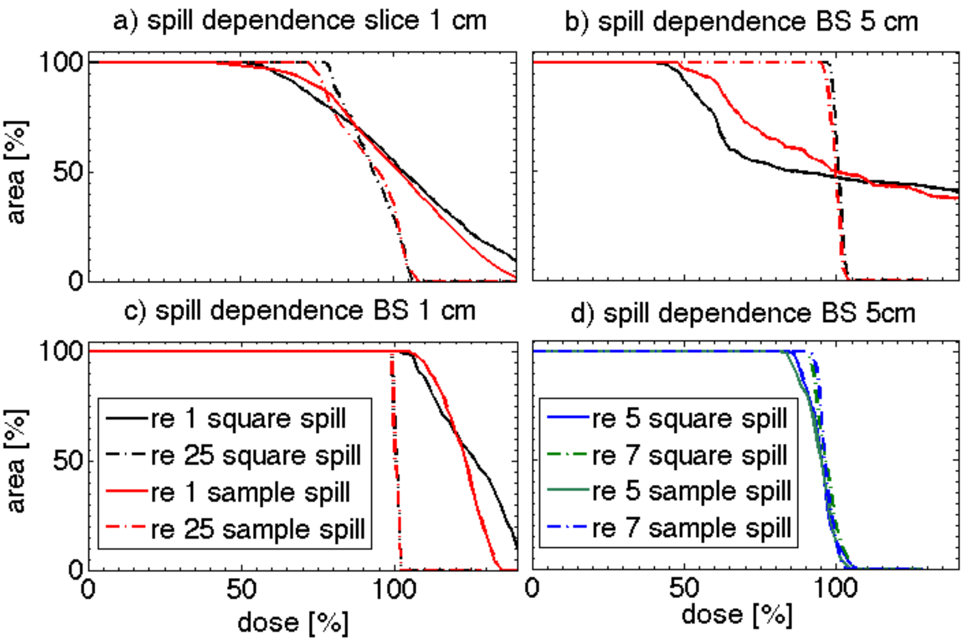

Figure 4.33.: Supplement of figure 4.3.3. It shows the dependence on the spill shape for a) *slice-by-slice re-scanning* and b) - c) *breath-sampled re-scanning* technique (see table 4.3 for details).

Therefore realistic dose distributions can be calculated without knowing the exact spill shape in advance.

To summarize:

- Experiments show:
  - *Slice-by-slice re-scanning* efficiently reduces interplay patterns due to motion when irradiating 2D plans. Interplay effects are being compensated faster if the motion is in parallel with the primary scanpath.
  - The larger the motion amplitude the stronger are the interplay patterns.
- Simulations show:
  - The interplay patterns of the experiments can also be generated with the simulation environment.
  - *Breath-sampled re-scanning* reduces interplay patterns much faster than *slice-by-slice re-scanning*.
  - The dependence of the dose distribution on parameters like starting phase, spill shape, period, amplitude and *re-scan* number is much smaller in case of *breath-sampled* than with *slice-by-slice re-scanning*.

- The *re-scan* number which is needed to guarantee satisfying to application cannot be assessed with a general formula so far. Simulations with the specific irradiation parameters are mandatory.

3D irradiation: Density variation phantom

Figure 4.34 reports experimental as well as simulation homogeneity results of the DeVarPho in the presence of motion as a function of the *re-scan* number. As expected, the homogeneity improves when increasing the *re-scan* number. Comparing the corresponding *re-scan* modes along with the scan path it seems that saturation has almost been reached at a *re-scan* number of 5. Both in the simulation as well as in the experiment only minor improvement regarding the homogeneity can be observed when increasing the *re-scan* number to 11. Like observed before, irradiations parallel to the scan path (horizontal) yield better results than irradiations being perpendicular to the motion.

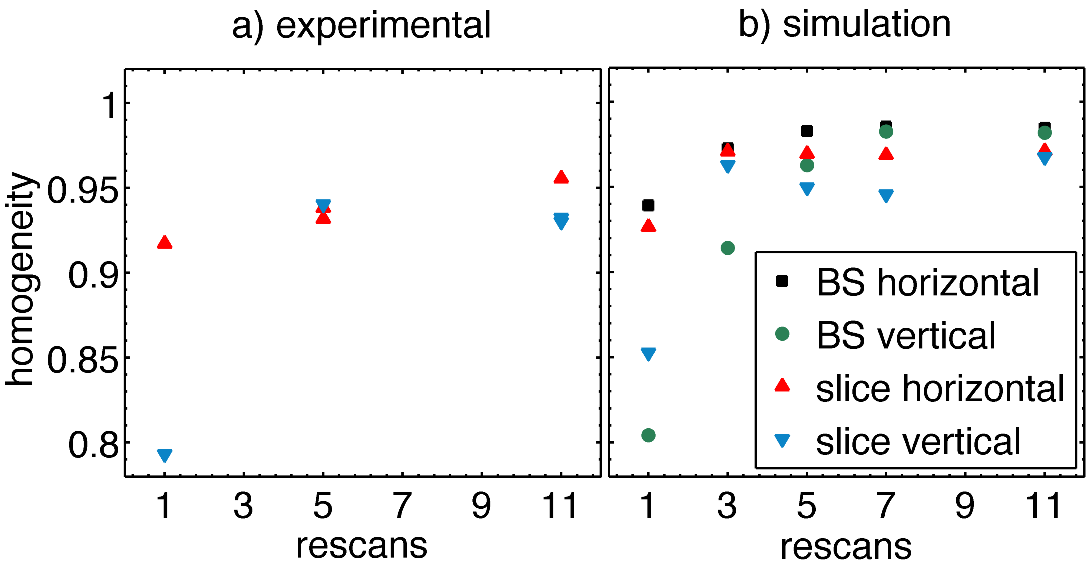

Figure 4.34.: Homogeneity values for a) experiments and b) simulations of the DeVarPho in the presence of motion as a function of the *re-scan* number. Experiments have only been performed in *slice-by-slice re-scanning* mode. Simulations were calculated for *breath-sampled* and *slice-by-slice re-scanning* irradiations.

In addition, the simulations show that *breath-sampled re-scanning* is significantly better than *slice-by-slice re-scanning* for a *re-scan* number $r \geq 7$ and shows less scanpath dependence. In the experiments as well as in the simulations, *slice-by-slice re-scanning* with a vertical scanpath is the only mode which shows a small, but clearly visible, region of decreasing inhomogeneity when increasing the *re-scan* number. The homogeneity of the static measurements was calculated to be 0.969 ± 0.007. Therefore the simulations predict that all *breath-sampled re-scanning* simulation with a *re-scan* number $r \geq 7$ and all simulation $r \geq 11$ have at least static irradiation quality.

The experimental results for *slice-by-slice re-scanning* mode are a little bit worse than the static measurements. They result in a homogeneity of H = 0.956 and H = 0.932 in case of the horizontal and vertical scanpath, respectively. This shows that *re-scanning* was able to reduce interplay effects very efficiently so that almost static irradiation quality is reached.

3D irradiation: Breathing thorax phantom with 6D target-motion

Figure 4.35 shows experimental as well as simulation homogeneity results of the BreThoPho in the presence of motion as a function of the *re-scan* number.

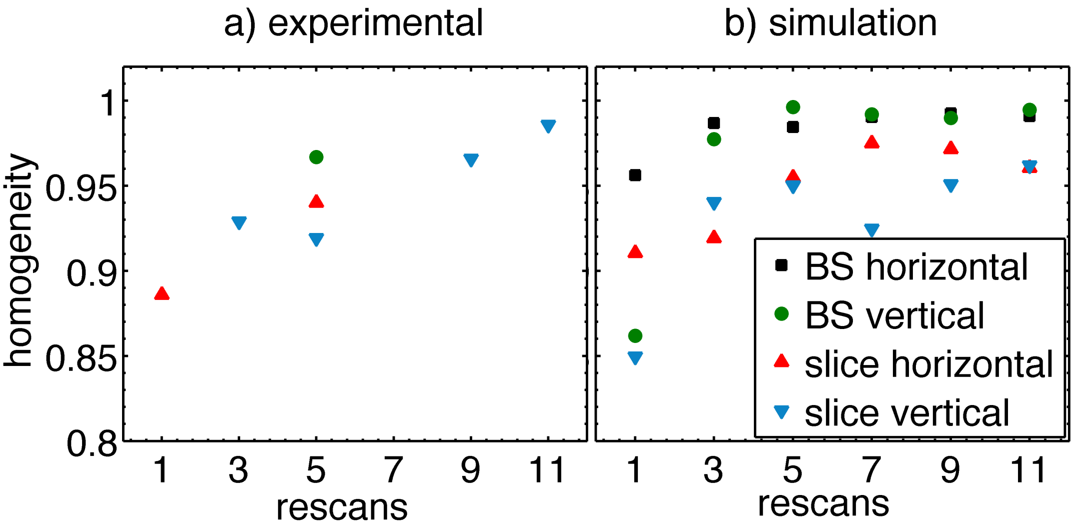

Figure 4.35.: Homogeneity values for a) experiments and b) simulations of the BreThoPho in the presence of motion as a function of the *re-scan* number. Experiments and simulations have been performed for *slice-by-slice* and *breath-sampled re-scanning* mode.

As expected, the homogeneity gets better when increasing the *re-scan* number. The general tendency, especially of the simulation figure 4.35 b), is similar to what has been written when reporting the results of figure 4.34. It shall be emphasized that figure 4.35 a) shows the only irradiation that succeeded when trying to irradiate in *breath-sampled re-scanning* motion in the presence of motion. Therefore it offers the possibility to actually compare experimentally *breath-sampled re-scanning* and *slice-by-slice re-scanning*. *Breath-sampled re-scanning* was irradiated with the unfavorable vertical scanpath, nevertheless it showed a much better homogeneity (H = 0.967) than *slice-by-slice re-scanning* in horizontal scanpath.

The homogeneity of the static measurements was calculated to be 0.977 ± 0.005. Therefore, the simulations predict that all *breath-sampled re-scanning* simulation with a *re-scan* number $r \geq 3$ have at least static irradiation quality. The experimental results for *slice-by-slice re-scanning* mode (vertical scnapath) with a *re-scan* number $r = 9$ and $r = 11$ result in a homogeneity of

$H = 0.966$ and $H = 0.981$, respectively. This shows that *re-scanning* was able to reduce interplay effects very efficiently so that almost static irradiation quality is reached.

Additional results can be found in section B.2.1.

To summarize:

- Experiments and simulations showed that interplay effects for both the DeVarPho- and the BreThoPho have been efficiently reduced by *slice-by-slice* and *breath-sampled re-scanning*. In experiments and in simulations *breath-sampled* was superior to *slice-by-slice re-scanning*.

4.4 Discussion

4.4.1 Implementation & dosimetry - a general view

In addition to the efforts done at GSI and HIT to implement the *re-scanning* technique other groups work on that topic as well. Recently, the group at Paul Scherer Institut (PSI) provided data for *re-scanning* experiments at their new Gantry 2 (Schätti et al., 2013). They report a lateral scanning speed with protons of roughly 1 mm/ms and 80 ms to change the particle's energy (Zenklusen et al., 2010). The National Institute of Radiological Sciences (NIRS) on the other hand presents both experimental and simulation results (Furukawa et al., 2010b). Their efforts tend towards very short irradiation times[12] and intensity control of the beam with RF-knockout extraction (Furukawa et al., 2005). The Heavy-Ion Medical Accelerator in Chiba (HIMAC) can accelerate up to $2 \cdot 10^{10}$ ions, so that almost all irradiations require only one or two injections. They chose to implement a very promising *re-scanning* variation which they named *phase-controlled re-scanning* (PCR) - a combination of *gating* and *re-scanning*. This technique is assumed to reduce the phase dependence very effectively since it is very similar to *breath-sampled re-scanning* but with the advantage of sparing more healthy tissue. The drawback is that PCR needs motion monitoring to determine the breathing period.

A very short treatment time can be important because of several reasons. If the tumor is subjected to large baseline drifts or if patient monitoring[13] is necessary, which stresses the body with additional dose, a fast irradiation is preferable. In addition, economics and patient comfort must be considered, both will benefit by the fastest treatment that can preserve the quality standards. In practice, the clinics will have to find the optimal compromise between irradiation quality and irradiation speed, which are in general conflictive aims and might yield to individual solutions for each patient. Furukawa et al. (Furukawa et al., 2010b) report a lateral scanning speed with carbon ions of roughly 100 and 50 mm/ms and 500 ms to change the particle's energy. Similar to the experiments done in the scope of this thesis, they did careful measurements

---

[12] The system took only 20 s to deliver the physical dose of 1 Gy to a spherical target having a diameter of 60 mm with eight *re-scans*.

[13] with the use of X-rays

to check if the prescribed dose can be applied in *re-scan* mode because even a sufficiently high scanning speed, realized by the deflecting magnets, does not guarantee correct dosimetry since it is only one element of the dosimetry chain.

Running the *re-scan* mode with a modified interlock mask (as it is currently done at GSI and HIT), which basically means that the position feedback loop is switched off, is surely not an ideal solution. The development of a complete interlock mask which also works in *re-scan* mode is mandatory. A possible approach could be that some thresholds scale with the chosen *re-scan* number in order to keep the system as flexible as possible. Furukawa et al. (Furukawa et al., 2010b) briefly report about their interlock system and state a lateral position tolerance of 2 mm but without going into *re-scan* specific details. They also switched off the position correction loop.

Experiments which tackle the problem of correct dosimetry in the *re-scan* mode with heavy ions without the interference of motion have also been reported by Furukawa et al. (Furukawa et al., 2010b) and in the previous chapters. The fewer *re-scans* are being needed in the irradiation process the closer the dosimetry will be to the standard irradiation case. The goal was therefore to investigate beam application for high *re-scan* numbers. If those can fulfill the criteria of patient treatment quality, it can be expected that all lower numbers will also satisfy these demands. Both GSI and NIRS use the raster scanning technique which means that the beam is not switched off when moving from one spot to the next[14]. This reduces dead time but in the case of high *re-scan* numbers the transient dose between spots may become significant compared to low speed irradiation. Since especially NIRS tries to implement high speed irradiation they included the influence of the transient dose in their planning software. Furukawa et al. (Furukawa et al., 2010b) also cared about the influence of position, size, time and structure of the beam, saturation of the electrons or recombination effects when irradiating in high speed mode with sub millisecond delivery time of each rasterpoint. They irradiated a 3D box and report that the precision of the scanned beam position was less than ±0.5 mm. In addition, they report almost no difference when compering their standard irradiation with 8 *re-scans*.

4.4.2 Implementation & dosimetry at GSI

Figure 4.8 shows that *slice-by-slice re-scanning* irradiation can in principle be finished as fast as standard irradiation by the treatment control system when a modified interlock mask is set.

As already mentioned, in the current implementation the read out of the MWPCs was switched of because of the short sampling time when using *re-scan* irradiation mode. Therefore, it was not possible to record the position data of the irradiated rasterpoints. Hence, every information concerning the lateral position of the pencil beam could only be obtained at the isocentre with

---

[14] PSI uses the discrete spot scanning method. Every time the irradiation position needs to be changed the beam will be switched off.

appropriate detector devices like Kodak X-Omat V films or pin points chambers. The interlocks at GSI are not designed for the *slice-by-slice re-scanning* irradiation mode. Even if dosimetry measurements at the iso-center show that a plan could be irradiated within the recommended limits of the ICRU, it might be necessary to choose a lower *re-scan* number so that the interlock system needs not to be switched off[15]. But a lower *re-scan* number can result in an interplay pattern outside the 95% - 107% threshold. Therefore, the *re-scan* technique of choice would the one which can guarantee homogeneous irradiation along with a low *re-scan* number in a short irradiation time.

At GSI, if a certain *re-scan* number would be needed to yield satisfying homogenous dose application one is able to reduce the intensity of every slice individually[16] so that position feedback loop could be switched on. However, with the current system this will, in general, result in unacceptable long irradiation times.

The influence of the treatment control system on dosimetry measurements has already been addressed in chapter 3.3. Calculations yield a dose uncertainty of less than 1% for the individual rasterpoints so that larger deviations should not be caused by this effect.

Beam application in the *re-scan* mode alters the temporal space charge distribution inside the ionization chambers (see figure 4.36) which might lead to falsified dose measurements due to recombination effects in chambers with a large sensitive volume like PPIC1 and PPIC3. The applied electric field inside the chambers is parallel to the beam direction.

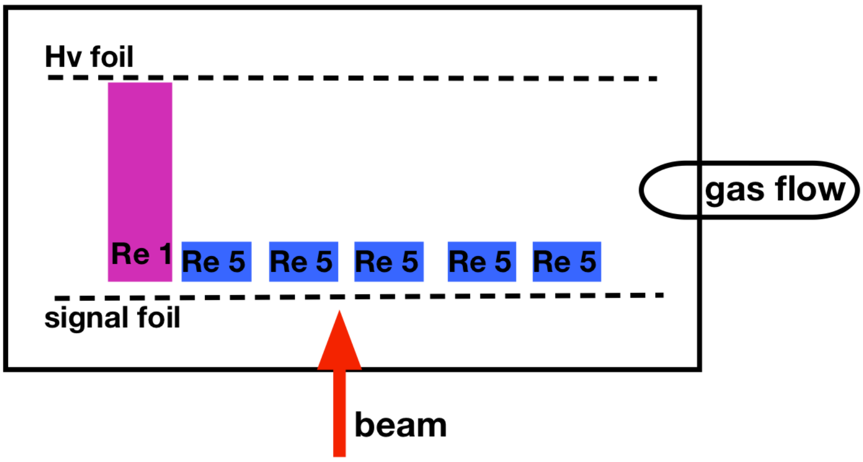

Figure 4.36.: Schematic drawing of the modified charged distribution due to *re-scanning* inside PPIC1 and PPIC3. Assuming a homogeneous PBP: If T_0 is the time to irradiate a rasterpoint for one *re-scan* then five *re-scans* will deposit the charge across a larger area. The height symbolizes the amount of charge.

---

[15] It is mandatory that all interlocks are switched on when irradiating a patient

[16] to a minimal value of roughly $\mathrm{I} = 1 \cdot 10^6 s^{-1}$.

Experiments done by D. Schardt et al. (Schardt et al., 2011) show, for measurements done with ions at the Bragg peak region with an ionization chamber filled with air, a strong dependency of the recombination rate as a function of the orientation of the electric field. A field angle of 90°, relative to the beam direction, results in a correction factor of approximately 2% whereas a field parallel to the beam yielded a correction factor of over 20%. This clearly shows that space charge effects play a role in the Bragg peak region for chambers like PPIC1 and PPIC3. In the experiment of figure 4.1, both chambers were placed in the plateau region. The *re-scanning* effect is not exactly the same as changing the orientation of the field, but a small influence on the dose measurement can be seen in figure 4.9 c). PPIC1 and PPIC3 contain a different sensitive volume which leads to different recombination coefficients $\alpha_{\mathrm{PPIC3}} < \alpha_{\mathrm{PPIC1}}$ (see (Fridman and Kennedy, 2011)). The volumetric recombination rate can be expressed as

$$\frac{dn^+}{dt} = \alpha\, n^+\, n^-, \tag{4.13}$$

with n^+ as the ion and n^- as the electron density. The larger value of the recombination rate is responsible that PPIC1 is more sensitive to recombination effects. Therefore, PPIC3 measures the particles more efficiently. PPIC1, which controls the course of the treatment, stops the irradiation if the prescribed particle number is reached. The increasing space charge effects due to *re-scanning* lead to less efficient measurement of this chamber. Since PPIC3 is not so much affected by that effect its dose slightly increases relative to PPIC1. When designing the ionization chambers in the starting phases of the therapy pilot project at GSI, test were done to find the gas with an optimal W-value for the PPIC1 (Brusasco et al., 2000) because this is a major source of dose uncertainty. Anyway, the variation between the two chambers according to the data is only 2% for $r = 19$ and the maximum intensity of the particle beam.

The data of the Farmer chamber in figure 4.9 a) and the pin points in figure 4.9 b) show that both of these chambers and the PPIC1 are not much influenced by space charge effects due to the *re-scanning* irradiation. PPIC1 builds up a signal chain with each of the other two chambers. Any systematical error in the output of PPIC1 would be transformed in a visible tendency in the data points of those two other devices. For example, if the PPIC1 measurement with increasing *re-scan* numbers yields in a distinct underdosage then the data points of 4.9 b) and 4.9 c) would fluctuate around a curve with a negative slope. In addition, every systematical error of the small chambers would also show a correlation with the *re-scan* number. Only if the systematical errors of all three chambers exactly compensate each other, fluctuation around a $relative\ dose = 1$ can occur but this is very unlikely, since the chamerbs are different from each other, filled with different gases and placed at different LET positions. Therefore, the dosimetry is affected by a level which still ensures safe patient irradiation inside the limits of the ICRU-50 (ICRU, 1993) report.

Several experiments, with different beam parameters, performed with the Kodak X-Omat V films showed a decreasing of the OD with an increasing *re-scan* number. The *re-scan* results were compared relative to a small reference field was irradiated on each film in therapy mode. Hence, the decreasing of the OD cannot be caused by the developing procedure of the films.

Consequently, the photochemical reactions in the film do not only depend on the product of intensity and time of exposure. This is called failure of reciprocity and is already known for X-rays (Martens et al., 2002). To our knowledge, it is the first time that this phenomena has been observed with heavy ions. Martens et al. state that for "photon and electron beams, grains are normally rendered developable by the energy transferred during a single electron hit. However, the highest energy secondary electrons produced in the phantom by mega voltage photon beams have a very low linear energy transfer coefficient at the beginning of their paths (Hamilton 1966b) that results, for some emulsions, in failure of the single hit theory, and thus in failure of the reciprocity law. This is obviously the case for the KODAK X-Omat V films". Apparently, these findings can be extended to irradiation with heavy ions as well. The films can still be used to examine interplay patterns but without determination of appropriate correction factors for *re-scanning* irradiation the films cannot be used for dose verification purposes.

To summarize:

- The implementation of *slice-by-slice re-scanning* at GSI was feasible. To guarantee a high quality of the beam application the interlock mask has to be redesigned to facilitate *re-scan* irradiation.
- The current system at GSI delivers the particle beam in *slice-by-slice re-scanning* mode to the target with a dose which is well inside the ICRU-50 (ICRU, 1993) report.

4.4.3 Implementation & dosimetry at HIT

It could be shown that *slice-by-slice* and *breath-sampled re-scanning* have been successfully implemented at HIT. In principle, it is possible to irradiate a patient in *slice-by-slice re-scanning* mode as fast as in the standard patient mode without introducing severe changes to the dose application so that patient treatment should be possible. Though, the position feedback loop had to be switched off in *re-scanning* mode because the fast irradiation would have resulted in interlocks. Figure 4.37 shows schematically why the position feedback loop is needed to achieve precise irradiation in the lateral plane. The accuracy with which the beam can be tuned by the accelerator team is limited. This has several reasons. Often it is not possible to tune the position of the beam for every energy, focus and intensity separately[17]. That means, optimizing the parameters of the accelerator for one energy and focus pair can make the accuracy of another

---

[17] as I learned when implementing the Gantry along with the accelerator crew at HIT

set worse. The second source of uncertainty is simply that the accelerator is subjected to small day-by-day changes.

Despite both perturbations, the position of the beam must lie inside a fine-tuning-grid with the size of a few millimeters[18]. With the position feedback switched on, the deflection magnets of the rasterscanning system can shift the beam to its prescribed position. This is indicated in figure 4.37 with the help of the greenish arrows. To conclude: Comparing the irradiations for 1 *re-scan* (which is identical to the standard irradiation without position feedback loop) and 19 *re-scans* in figures 4.11 and 4.12 shows that *re-scanning* even improves position accuracy slightly. It follows, if the position feedback functionality will be adapted to the increased speed of *re-scanning*, irradiation in *breath-sampled re-scanning* and *slice-by-slice re-scanning* mode shall be possible with almost the same precision as in the current standard mode - which means sub-millimeter precision. The histograms of figure 3.11 (simulation) and 4.14 (measurement) are in good agreement and small deviations might arise because of different particle numbers and intensities. The measured doses by the TCU units and the prescribes ones deviate so less from each other that (see figure 4.13) that no concerns regarding the dose level application should arise.

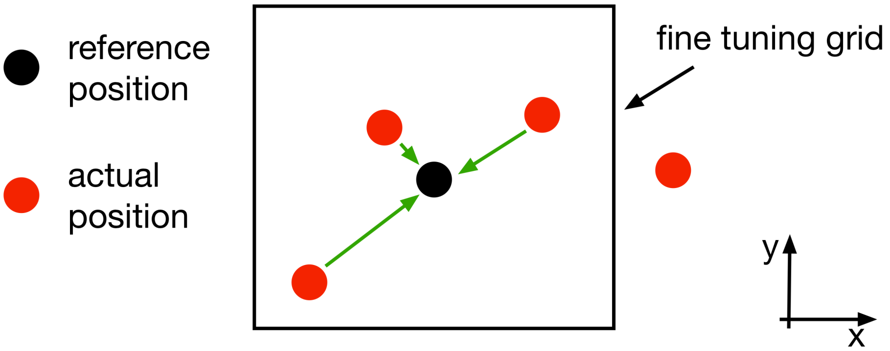

Figure 4.37.: shows schematically the influence of the position feedback loop. The distance and direction of the actual beam position is measured with respect to its reference position. The correctional factors are applied to the deflecting magnets which shift the beam closer to the reference position.

The difference between the desired *breath-sampled re-scanning* period of 4 s and the average irradiation time in the experiment of $\bar{T}_{breath\text{-}sampled\ re\text{-}scanning} = 3.89 \pm 0.1$ lies within a tolerable range for a feasibility study. Furthermore, the results can surely be improved by further optimizing the control parameters for *breath-sampled re-scanning* at HIT. Efforts in this direction are ongoing. Recently, it is even possible to irradiate individual rasterpoint with a predefined intensity (Schoemers et al., 2011).

At first, the particle numbers per rasterpoint ($0.8 \cdot 10^6$, $1.6 \cdot 10^6$, $3.2 \cdot 10^6$ and $6.4 \cdot 10^6$) which have been used for the dosimetry measurements in figure 4.17 appear quite large compared

---

[18] the size of the fine-tuning-grid is not for the public domain

to conventional treatments with many fractions. However, in the regime of hypofractionation (Miyamoto et al., 2007), a particle number per rasterpoint of $0.8 \cdot 10^6$ is a fairly good approximation with respect to the IESs at the distal region of the tumor.

Figure 4.18 shows that in case of *breath-sampled re-scanning* (1 *re-scan*) the continuously variation of the intensity level can be executed without introducing additional errors to the dosimetry. On the other hand, comparing these results with the *slice-by-slice re-scanning* with 5 (see figure 4.19) and 11 *re-scans*, the average dose increases by 3.8% and 5.3%, respectively. It can be observed that the pin points within one row of the same z-value have very small standard deviations but that the values from rows with other z-values show different dose values. In general, it was observed that the more distal the row, the lower the dose value of the corresponding pin points. This leads to the finding that the pin points might be less accurate when the dose per rasterpoint visit gets smaller. This was not observed when performing the experiments of section 4.3.1 (see figure 4.9). This could be due to following facts: The irradiated plans were 2D and 3D plans. Therefore, the proximal pin points receive many pre-irradiations with low doses which did not happen in the 2D case. Especially those proximal pin points showed the largest deviation. The distal pin points showed almost no dependence on the *re-scan* number, like observed before. Furthermore, all measurements lie within a relative deviation of ±4%. Even irradiation under the same conditions can sometimes result in deviations of this order.

To summarize:

- First experiments to implement *slice-by-slice re-scanning* and *breath-sampled re-scanning* at HIT were successful. To guarantee a high quality and safe beam application the interlock mask has to be redesigned to facilitate *re-scan* irradiation.
- Irradiations of 2D and 3D plans with *breath-sampled re-scanning* and *slice-by-slice re-scanning* modes at HIT yield dose distributions with respect to the reference irradiation which are well between the limits of the ICRU-50 report. The pin point doses at proximal regions should be carefully analyzed when irradiating with higher *re-scan* numbers.

4.4.4 Motion mitigation

This section is focused on motion mitigation with *re-scanning*. Motion mitigation by gating (Bert et al., 2009) and tracking (Bert et al., 2007) are addressed elsewhere. In principle it is always possible to combine *re-scanning* with tracking and gating.

Van de Water et al. (van de Water et al., 2009) compared *re-scanning*, perfect tracking (no position error, no time delay), imperfect tracking (with position errors and time delays) and retracking (a hybrid solution combining tracking and *re-scanning*) for dose homogeneity (difference between D_5 and D_{95} in the CTV) in a homogeneous and a heterogeneous (simulated rib proximal to target) phantom. They found that the nominal dose homogeneity could not be obtained with perfect tracking as well as imperfect tracking for pencil irradiation with protons in case of a heterogeneous phantom, which was moving with an amplitude of 15 mm. Retracking with 4 *re-scans* was not really superior to perfect tracking but better as *re-scanning* with 4 *re-scans*. The best results yielded *re-scanning* with 8 *re-scans*. They state that the results are due to the highly sensitive nature of proton beams to small spatial errors.

Furukawa et al. worked out that the *total-irradiation-time* (T_{total}) for each IES needs to be: $T_{total} = n \cdot T_{breathing}$, with n being an integer number and $T_{breathing}$ the duration of the respiration cycle, that *re-scanning* reduces interplay effects very efficiently. Hence they introduced so called PCR in which the intensity is adjusted to exactly match into a predefined gating window. In principle this is the same as combining *breath-sampled re-scanning* with gating. They moved their phantom with a period of 4 s and an amplitude of 10 mm. In the comparison between the static measurements and the moving measurements with the PCR method, they report a dose difference of less than 2% for the pin point chambers in the target volume, which also agrees with their simulations.

Seco et al. (Seco et al., 2009) analyze dose distributions of five different *re-scanning* techniques. Even if the tools written in the scope of this thesis could mimic each of those five methods, the simulations in this chapter have only been performed for the cases that have also been implemented in the facilities at HIT and GSI, namely *slice-by-slice re-scanning* and *breath-sampled re-scanning*.

The investigations of *re-scanning* started in almost all research groups with irradiation or simulation of 2D fields or simple 3D phantoms. Some publications at facilities without an active beam scanning system tackled the effect of statistical averaging of *re-scanning* only in simulations (Kraus et al., 2011; Bortfeld et al., 2002). The report very useful results but the they neglect the influence of an real existing beam scanning system which can influence the dose distribution to a degree which transforms a dose distribution beyond the limits of the ICRU-50 report. Therefore it is strongly recommended to validate the simulation tools versus the experiment as it was done many times at GSI with TRiP (Richter, 2012; Gemmel et al., 2011) and at NIRS (Furukawa et al., 2010a).

2D irradiation: Amplitude and scanpath dependence

The visual inspection of figure 4.20 as well as the quantitative analysis of figure 4.21 reveals a strong dependence of the interplay pattern concerning the relative orientation of the primary scanning path and the motion direction. If the motion direction is parallel to the scanpath only a few *re-scan* numbers are needed to yield a very homogeneous dose distribution. Similar findings have been observed by Knopf et al. (Knopf et al., 2011). Since the complete scanning for one complete line of the PBP was, with the used settings, roughly ten times faster than the tumor motion period for $r = 1$, the dose distortion will be very small if the motion direction is along that line (see figure 4.38 a). In case of high *re-scan* numbers the target may even be considered as being quasi static so that small fluctuations will only occur if the irradiation of each line always starts at the same motion phase.

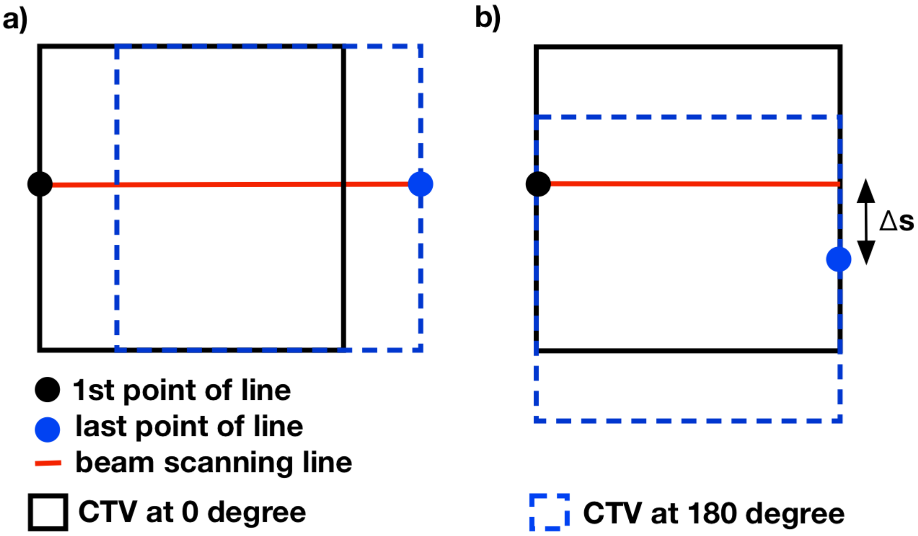

Figure 4.38.: shows the origin of dose patterns of the CTV due to the relative moving direction of the pencil beam versus the target. a) the pencil beam and the target move parallel. The relative dose error of each point long the line its very small. b) the pencil beam and the target move perpendicular. The further the beam moves to the right the larger is the spatial separation Δs between the planned and the actual irradiated rasterpoint which leads to massive underdosage if Δs is too large.

Being roughly ten times faster in this experiment is not enough if the motion is perpendicular to the scanpath. If one assumes that the irradiation starts at the 1st point of figure 4.38 b) then the target moves down while the pencil beam moves to the right. Taking the maximum velocity of the sinusoidal motion and multiplying it with the time the pencil beam needs to cross the line yields that the target has moved down by roughly $\Delta s = 0.8$ cm in this experiment. Hence, the Gaussian beam profile of the pencil beam can deliver approximately 10% of the prescribed dose to the planned rasterpoint and as a consequence the diagonal stripes appear which can easily be seen for the $r = 1$ case. Increasing the *re-scan* number while maintaining the intensity reduces Δs. In case of $r = 7$, Δs will be so small that the dose error is within ±5%. In fact it can be seen that for $r = 5$ the diagonal stripes have disappeared, unfortunately there is a strong temporal correlation between beam application and motion which results in the horizontal stripes. For $r = 9$ this correlation is strongly reduced and the CTV gets homogeneous. This illustrates that increasing both the *re-scan* number and decreasing the intensity by a factor of e.g. two will not cause those diagonal stripes to disappear if the irradiation time of the IES and the motion cycle are strongly correlated. Therefore, whenever it is possible the beam angles should be chosen that the motion of the tumor is perpendicular to the IESs and that the scanning direction is parallel to the motion direction. As expected, interplay effects get worse for larger amplitudes and the measurements indicates that *slice-by-slice re-scanning* might be of limited use when the motion amplitudes get large. On the other hand, the simulation results of figure 4.25 show that *breath-sampled re-scanning* can even compensate an peak-to-peak amplitude of 5 cm. A general finding in all experiments and simulations done in the scope of this thesis is that the interplay effect of smaller amplitudes can be compensated more easily than for larger ones. This is not surprising because reducing the amplitude more and more will end in the well known static case. A general expression which states how the dose distributions change with increasing amplitude is hard to find because it depends strongly on the specific treatment parameters.

2D irradiation: Reducing the size of the field penumbra

The lateral motion of the target still yields in a widespread penumbra (see figures 4.29 and 4.39 b)) and in additional irradiation of healthy tissue. Figure 4.39 displays a proposal how to optimize the irradiation field in order to reduce the additional dose which is more sophisticated than a simple geometrical extension of the CTV (Engelsman et al., 2006) to account for lateral motion. An inhomogenous particle number distribution can spare organ at risk (OAR) in the presence of motion even if the nominal dose is identical for all rasterpoints inside the CTV.

2D irradiation: Correlation effects, phase dependence and the statistical nature of *re-scanning*

Very surprisingly at first glance, the experiments in figure 4.20 and the corresponding simulations in figure 4.21 display a drop in homogeneity for 5 and 3 *re-scans* compared to 1 *re-scan* in the case of the peak-to-peak amplitude of 1.5 cm and motion direction perpendicular to the scan path. The reason is that the effect of the vertical stripes are less severe than the correlation between beam application and motion which results in those thick horizontal lines. These horizontal lines which emerge at low *re-scan* numbers are very sensitive with respect to the starting motion phase, intensity and field properties which is also indicated by the rather large error bars in figure 4.21 where six different motion phases have been used wheres the corresponding experiments have been measured at a random starting phase. Basically, this explains the difference between the simulation and the measurements for low *re-scan* number. Qualitatively (see figures 4.20 and 4.22), both basically look identical but small deviations can shift the horizontal lines in or outside the ROI which leads to these deviations. Larger ROIs and the averaging when using the mean of more different starting phases effect should align the results.

The implication for treatment planning is therefore that precise knowledge about all starting parameters is needed to do forward calculations which show how a patient can be irradiated with the largest benefit. It follows that the system should be as reproducible as possible, because fluctuations will influence the interplay pattern. In real treatment it is favoured that *re-scanning*

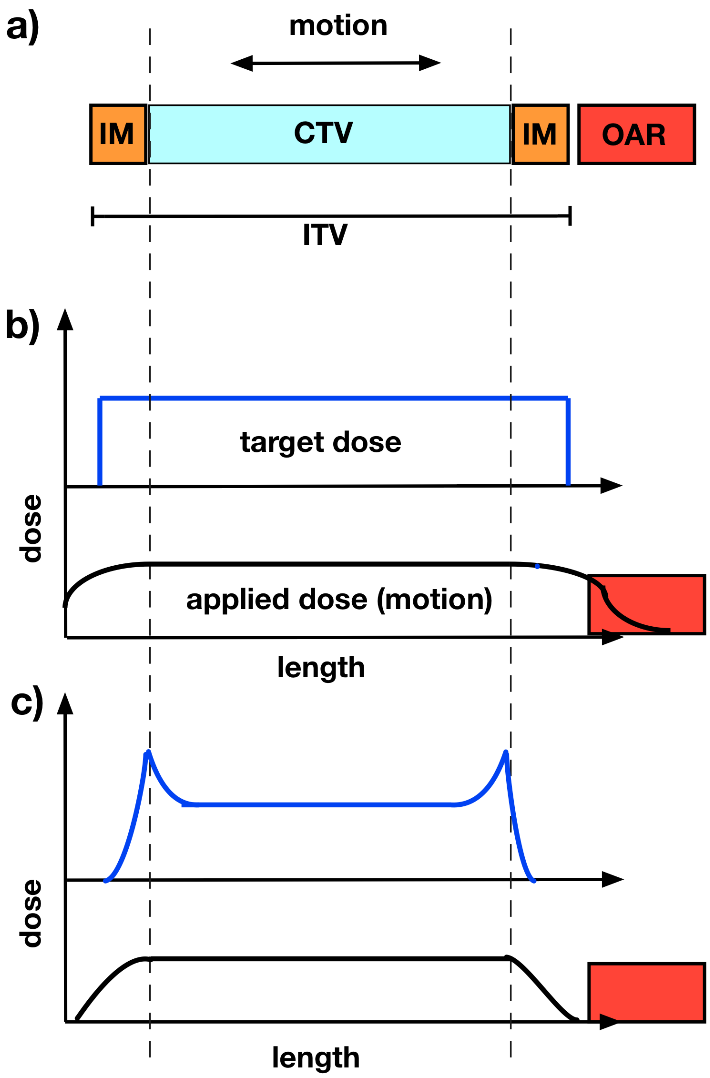

Figure 4.39.: Optimization of treatment planning in the presence of motion. a) The CTV is assumed to be very close to an OAR. To account for the moving target an ITV has to be used. b) the standard procedure is to simply extend the spatial dose region homogeneously to include the motion. Some percentage of the applied dose will than be shifted inside the OAR. c) Weighting the planned dose distribution by the use of a probability function of the target results in a non homogeneous target dose distribution (upper part) which shall spare the OAR in the presence of motion (lower part) (Muessig et al., 2012).

starts at a random motion phase because this reduces tumor monitoring efforts and therefore additional dose from diagnostic devices. The variations in *slice-by-slice re-scanning* are too large to ensure satisfying dose homogeneity even for moderate motion amplitudes in case of low *re-scan* numbers and scan path being perpendicular to the motion direction. On the other hand, if motion and scanpath are parallel the homogeneity gets, even for low *re-scan* numbers, better than the static measurement[19] on the same film. The explanation is that the planned circular beam profile look sometime more or less elliptical which can lead to small fluctuations in spatial dose deposition which is compensated by *re-scanning*. If a distorted beam focus sweeps only once over the film the homogeneity is of course worse than planned. In the *re-scan* mode the pencil beam sweeps many times over the area, the center point of the pencil beam and the beam focus will be slightly shifted every time, resulting in averaging the dose distribution. Since the corresponding simulations are computed with perfectly circular beam profiles this effect is not visible in 4.21.

The statistical nature of *re-scanning* leads to the fact that there is always some likelihood of fluctuations. These fluctuations get severe if a correlation between the beam application and the target motion exists. The conclusion shall not be drawn that $r = 5$ is in general worse than no compensation.

Independently to our interference effects for low *re-scan* numbers it is shown that the averaging effect really begins to start at $r = 5$. Bortfeld et al. (Bortfeld et al., 2002) showed that fractionated treatment (see also (Woelfelschneider, 2011)) has a much smaller cumulative error as the irradiation on a single day which can be described by statistical methods. With the assumption that there is no correlation between beam scanning and target motion in the *re-scan* irradiation, their results can be adapted to *re-scanning*. They calculate that the expected dose value $\langle D \rangle$ is a weighted average of the dose distribution without motion. The deviation ΔD of a well defined rasterpoint can be expressed as a probability density function $f(\Delta D)$ which will converge to a Gaussian shape after about five fractions (or *re-scans*); the width of the distribution is a function of the treatment technique, the motion amplitude and other factors. Their analysis for a sinusoidal motion yields the following: At a low *re-scan* number the probability distribution has two peaks symmetrically distributed around $\langle D \rangle$ with a high likelihood of getting a large deviation. For higher *re-scan* numbers the curve turns into a Gaussian shape with a distinct peak and a low probability of a large dose deviation. Calculating the foregoing simulations with *breath-sampled re-scanning* instead of *slice-by-slice re-scanning* reveals that the treatment field reaches already at $r = 3$ static homogeneity values in case of the most unfavourable parameter set presented above. The large variation in the calculated dose values in figure 4.23 d) for 1 *re-scan* vanishes abruptly. Therefore *breath-sampled re-scanning* is very robust compared to *slice-by-slice re-scanning* because it minimizes the correlation effects between motion and beam application.

---

[19] The static measurements have been irradiated without *re-scanning*.

A recently published article by Knopf et al. (Knopf et al., 2011) presents simulation results for proton beam therapy which show only small a dependence on the starting motion phase within the CTV. This could be due to the fact that they used liver patient data and that they only investigated three different staring phases wheres the outcome of figure 4.30 was calculated with 72 different starting phases. Interestingly, the underlying sinusoidal motion characteristics are transferred into the shape of all the *slice-by-slice re-scanning* rescan numbers which further strengthens the statement that target motion and beam application are much more correlated in case of *slice-by-slice re-scanning* than for *breath-sampled re-scanning*. For the *breath-sampled re-scanning* numbers 9 and 19, the data points fluctuate randomly around the nominal dose value. The sinusoidal shape of the *slice-by-slice re-scanning* curves lead the the following consequence. If a plan is to be irradiated with a precise starting phase than small deviations related to the starting phase shall yield only in small deviations of the expected dose. If this statement can remain valid when using other parameter sets has to be investigated for every single case individually. The dose values for *breath-sampled re-scanning* indicate that the deviations from the nominal dose value is anyhow very small so that any effort to start the irradiation at a distinct starting phase seems to be needless.

Phillips et al. (Phillips et al., 1992) and Bortfeld et al. (Bortfeld et al., 2004) predict that *re-scanning* improves the dose uniformity roughly as the square root of *re-scans*. Bortfeld et al. state that the PDF is lowest at the expected dose value when using only 1 *re-scan* and that the central limit theorem transforms the shape of the PDF to a Gaussian centered around the expected dose value for about 5 *re-scans*. A central assumption in their works is that no correlation between beam application and motion shall be present. In the case of 1 *re-scan* the histograms displayed in figure 4.31 look for both *slice-by-slice re-scanning* and *breath-sampled re-scanning* like the ones shown in (Bortfeld et al., 2002). Increasing the *re-scan* number transform the PDF of *breath-sampled re-scanning* to a Gaussian shape with very small deviations from the expected dose value. In contrast, the PDF of *slice-by-slice re-scanning* even gets broader when comparing 9 *re-scans* with 19 *re-scans* leaving the expected dose value with the lowest likelihood. This is an additional evidence that the correlation between target motion and beam application is present even when irradiating with higher *re-scan* numbers in *slice-by-slice re-scanning* mode. Therefore the proposed improvement of dose uniformity as being roughly the square root of *re-scans* cannot be applied in heavy ion therapy with active beam scanning. Therefore it was not possible to fit the data points to a curve which reflects the square root behavior.

2D irradiation: Intensity and spill profile dependence

When irradiating static tumors, the intensity level is selected to minimize irradiation time to a value which can at the same time ensure proper beam monitoring, i.e. position and dose measurement for safe treatment delivery.. Figure 4.26 c) demonstrates that the intensity level can influence the DAH strongly in *slice-by-slice re-scanning* mode and unfortunately the highest intensity level at GSI is the one with the worst DAH curve. It follows that the intensity that would be selected for static treatment is most unfavorable when motion is present. The switching to lower intensities, which will increase dose coverage, should be easy. Selecting higher intensities, which will increase the facilities' efficiency, might require extensive hardware upgrade.

Figure 4.27 displays simulations for the *breath-sampled re-scanning* mode with an otherwise identical parameter set to figure 4.26. The intensity level is in this technique adjusted according to the motion period, therefore both dependencies are merged into a single one. The shorter the period the faster the beam application so that each rasterpoint will be irradiated in the same motion phase, independent of the period. In all cases *breath-sampled re-scanning* compensates interplay patterns almost perfectly and reveals almost no dependence on patient- and machine-specific parameters. This reduction of parameter dependence is immensely important to guarantee quality assurance of the treatment. Prior to every patient irradiation with *re-scanning* with moving tumors, forward calculations have to be performed as to check if the selected mode results in DVH curves which satisfy the physicians. The input parameters used in theses simulations will deviate to a certain degree from the actual treatment, therefore a method - like *breath-sampled re-scanning*- which is robust with respect to those deviations is desirable.

The temporal beam spill profile is a further source of error. The input sample spill profile which is used to predict the dose distribution will deviate more or less form the actual used beam. Figures 4.3.3 and 4.33 display that the fluctuations due to the spill shape are largest when using only 1 *re-scan*. For instance, the DAH curves of *breath-sampled re-scanning* show almost no dependence with respect to the spill shape when using 5 *re-scans* because the statistical averaging effect of *re-scanning* already smoothes the influence of spikes in the spill profiles. The difference between the two chosen spills, used in this calculations, will most likely be much larger than the difference between two spills of a reliable therapy system. Therefore a sample spill which reflects the average properties shall be well suited to perform forward calculations in the *breath-sampled re-scanning* mode.

To summarize:

- *Breath-sampled re-scanning* reduces interplay effects much more efficiently as *slice-by-slice re-scanning*. In addition, *breath-sampled re-scanning* is far less dependent on all investigated parameters like amplitude, *re-scan* number, motion period, intensity and spill profile.

3D irradiation of phantoms

The simulation data of figures 4.35 and 4.34 are in both cases better than the experimental results. This is not surprising since the simulation is not affected by the uncertainty of experimental parameters which are numerous in such measurements. For instance, its homogeneity value in for the static dose distribution depends only on the optimization process and the dose calculation algorithm and is generally very close to 1 as seen in section 4.3.3.

Actually one has to mention another source of uncertainty. Some pin points have not been considered in the calculation. As mentioned in section 4.2.7, these are the pin points which lie very close to sharp dose gradients so that even small set up errors can lead to large differences in dose measurement. This means that the most distal IES slices are not included in the calculation of the homogeneity, but exactly these slices are subjected to the largest interplay effects because they do not benefit from the intrinsic *re-scanning* effect due to pre-irradiation. On the other hand, the irradiated 2D plans of section 4.3.3 are basically the equivalent of the most distal IES slice of a 3D plan and there it could be shown that *re-scanning* was able to reduce interplay pattern very efficiently, too.

Due to limited availability of beam time and an increasing level of complexity much more measurements have been performed in *slice-by-slice re-scanning* mode than in *breath-sampled re-scanning*. The measurement of the *breath-sampled re-scanning* mode is very promising. All simulations show that *breath-sampled re-scanning* is by far less dependent on parameters like starting phase etc., so that uncertainty of a single *breath-sampled re-scanning* dataset is certainly much smaller than in case of the *slice-by-slice re-scanning* mode.

In case of the DeVarPho the detector head and the phantom do not have relative motion. Such a setup would perhaps not be appropriate when performing experiments with *beam tracking* or *gating*, because both techniques rely on the time dependent position information of the detector head relative to the phantom. The presented case would therefore be closer to a periodical motion of the whole patient during treatment. Since *re-scanning* does not need any time dependent position information of the detector head this experiment was a sensible choice when making *re-scanning* experiments. One plan with different CT phases was optimized with the goal that *re-scanning* should be able to deliver satisfying dose distribution to all motion phases, therefore it does actually not matter if the motion of the detector head is relative (as it had been in case of the BreThoPho phantom) or parallel to it.

To summarize:

- The demands for *re-scanning* to effectively reduce interplay effects in case of the used 3D phantoms can be compared to those of real patients. Therefore the results of section 4.3.3 are quite promising and suggest that *re-scanning* shall be a sensible treatment option for moving tumors.

4.5 Conclusion

This chapter shows that *re-scanning* is an option to treat moving tumors with carbon ions at HIT and at GSI[20].

---

[20] Patient treatment stopped at GSI in the year 2008.

Dosimetry measurements showed that these new irradiation modes can deliver dose distribution to the static target which are well inside limits of the ICRU-50 (ICRU, 1993) bench marks, which aim a dose coverage of the target volume between 95% and 107% of the prescribed dose. It was illustrated that interplay effects are reduced more efficiently in *breath-sampled re-scanning* mode. *Breath-sampled re-scanning* shows only very little dependence on treatment parameters like amplitude of motion, breathing period and spill shape. In case of *breath-sampled re-scanning*, static homogeneity quality is almost reached for $r = 5$ for a peak-to-peak amplitude of 5 cm and the uncertainty is greatly reduced compared to *slice-by-slice re-scanning*. It follows that simulated dose distributions for *breath-sampled re-scanning* irradiation will only slightly deviate from irradiated ones, which is very important if a physician needs to judge the outcome of a patent treatment on the basis of simulations. It is even possible to combine *re-scanning* with *gating* and with *beam tracking* as improve their outcome.

To conclude:

- *Breath-sampled re-scanning* is a very promising technique to treat moving tumor with carbon ions and showed that it can efficiently reduce interplay patterns. It is easier to implement than *beam tracking* and can therefore be the one of the first options at facilities which use heavy ions treatment. If the interlock mask at HIT is changed to enable *breath-sampled re-scanning* irradiation with an active position feedback loop it shall be possible and sensible to treat patients with moving tumors in the clinic in the near future.

5 Discussion and summary

The *re-scanning* method has been assessed via simulations in a patient treatment study (chapter 3) and via experiments performed at GSI Helmholtzzentrum für Schwerionenforschung GmbH (GSI) and Heidelberg Ion-Beam Therapy Centre (HIT) (chapter 4). This chapter shall provide a summarizing discussion including an outlook on possible research directions.

Intensity modulated radiotherapy (IMRT) as well as intensity modulated particle therapy (IMPT) aim to deliver the dose as conformal as possible to the tumor in order to reduce the integral dose to the body and especially to the organs at risk (OARs) (Durante and Loeffler, 2013). The corresponding treatment fields got more complex (Krämer and Durante, 2010) and the applied radiation fluence is usually a function of space and time $F = F(\vec{r}, t)$ to facilitate a very conformal tumor irradiation.

Hence, interference effects can emerge if moving tumors (e.g., in the lung) are treated with scanned ion particle beams (Phillips et al., 1992). As a consequence, the dose distribution of a tumor can exhibit sub-volumes with under- and overdosage. This effect, which is also called interplay, is most severe if the beam application and the intra-fractional tumor motion happen on a comparable time scale (Rietzel and Bert, 2010), which unfortunately is the case with existing therapy systems (Rietzel and Bert, 2010; Furukawa et al., 2010a).

Especially in scanning particle therapy, these interplay effects get so severe in case of thoracic tumors that, up-to date, almost no center performs treatments. Exceptions are the Rinecker Proton Therapy Center (RPTC) in Munich that uses apneic oxygenation to allow treatments of tumors in the thorax and upper abdomen (Bert and Durante, 2011) and, recently, the MD Anderson Cancer Center (MDACC) in Texas (MDACC, 2013). Both clinics only treat indications with rather small motion amplitudes.

Hence, techniques which mitigate the effects of tumor motion to the dose distribution are in the focus of many research groups (Bert and Durante, 2011). The most prominent techniques are:

- ***Re-scanning***: This method is investigated in the scope of this thesis, but is also studied by other research groups (Seco et al., 2009; Zenklusen et al., 2010; Mori et al., 2013). *Re-scanning* is based on statistical averaging. Repeated applications of the treatment field reduce dose inhomogeneities as to facilitate patient treatment in presence of tumor motion. The total number of repetitions is called the *re-scan* number r. *Re-scanning* exists in various flavors (see sections 2.3.6 and 3.2.1) which differ in the efficiency to reduce interplay patterns and the technical application complexity. *Re-scanning* is technically less complex and hence easier to implement in an existing therapy system than the other methods mentioned below. The *re-scanning* techniques investigated in the scope of this thesis do not require spatio-temporal knowledge of the tumor position during treatment which makes this method especially suitable for patients with non-periodic motion trajectories. The drawback is the loss of tumor conformity because the corresponding internal target volume (ITV) (Graeff et al., 2012) needs to cover the clinical target volume in all motion states.

- ***Gating***: This technique aims to irradiate the tumor only when its location is in or close to the exhale state which can increase the treatment time considerably. In this position the tumor motion is greatly reduced which decreases the interplay effects. In general, the motion monitoring of the tumor causes additional dose to the patient but compared to *re-scanning* the tumor conformity is increased since the ITV can be decreased. Uncertainties are being induced because the position of the tumor cannot be located with absolute precision (Steidl, 2011). *Gating* is currently already used in passive particle beam delivery (Miyamoto et al., 2003) and intensity modulated radiotherapy (IMRT) (Keall et al., 2006). The first liver patients have recently been treated with a particle scanning system at HIT by using *gating* (Richter, 2012).

- ***Beam tracking***: This technique is technically the most challenging approach. It needs precise spatio-temporal knowledge of the tumor's location. The beam positions are adapted to the tumor motion and, in principle, the tumor can be irradiated as conformal as without motion. The beam adaption cannot be performed instantly and with perfect spatial precision which might violate accurate dose application (Eley, 2013). Recently, a 4D treatment planning concept that considers motion during particle number optimization was implemented at GSI (Graeff et al., 2013; Eley, 2013). By using this method, an even better sparing of OARs is possible.

In the scope of this thesis, patient simulations with scanned carbon ion beams were performed by using *slice-by-slice*, *volumetric*, *mixed-scanpath*, *local-parameter*, *random-time-delay* and *breath-sampled re-scanning* (see chapter 3). The aim was to investigate which technique can most efficiently reduce the interplay patterns in the presence of motion.

The MDACC kindly provided the time resolved computed tomography (4DCT) data of the five lung cancer patients which were used in the study. The patients in the study covered a tumor motion range from 1 mm to 25 mm. The investigation was based on a fractionation scheme applied in passive carbon radiotherapy at National Institute of Radiological Sciences (NIRS) (Miyamoto et al., 2007). The treatment planning approach in this works mimics the case that a patient is being irradiated with four different fields on a single day. Based on the clinical findings at NIRS, the relative biological effectiveness (RBE) weighted dose for one fraction was calculated using local effect model (LEM) to be 17.70 Gy(RBE). The dose per field was the fraction dose divided by the number of fields (Woelfelschneider, 2011; Lüchtenborg, 2012).

Different measures were used to judge the quality of the simulations results of the different *re-scanning* modes inside the clinical target volume (CTV). The dose coverage was evaluated by V_{95}[1], the overdose via V_{107} and the homogeneity by $D_5 - D_{95}$[2]. The different measures were tested by using the Kruskal-Wallis test in combination with the Wilcoxon–Mann–Whitney test at a significance level of $\alpha = 5\%$.

At first, 4D dose distribution for all five patients and all *re-scan* modes were calculated over a broad range of parameters which should cover almost all relevant clinical situations. The influence of different *re-scan* numbers r, various breathing periods or changing starting phases were investigated in the presence of tumor motion.

It was shown that a larger motion amplitude > 5 mm results in less target coverage which cannot be efficiently compensated by *slice-by-slice*, *volumetric*, *mixed-scanpath* and *local-parameter re-scanning* even for higher *re-scan* numbers because the correlation between tumor motion and beam application cannot be broken up efficiently.

On the other hand, *breath-sampled* and *random-time-delay re-scanning* compensate the motion effects very well. In case of all patients *breath-sampled* and *random-time-delay re-scanning* reach mean values of $V_{95} = 100\%$ and $V_{107} = 0\%$ for $r \geq 9$ and $r \geq 17$, respectively. Consequently, both methods also yielded the lowest $D_5 - D_{95}$ values. The $D_5 - D_{95}$ analysis shows that the dose distribution can get nearly as homogeneous as in the static case without motion, if the *re-scan* number is chosen appropriately ($r \geq 17$). The corresponding significance analysis shows that *breath-sampled re-scanning* turns out to be the best and *random-time-delay re-scanning* to be the second best *re-scanning* mode.

The reason might be that those two techniques exhibit an extra feature which was merely introduced to break up a possible synchronicity between beam application and tumor motion. In case of *breath-sampled re-scanning* the irradiation of each iso-energy slice (IES) is matched to the breathing period and in case of *random-time-delay re-scanning* a predefined number of *random-pauses* is integrated in the irradiation process.

The robustness of the two modes was also investigated. In case of *breath-sampled re-scanning*, the irradiation duration was varied so that the perfect matching with the breathing period was no longer valid. In case of *random-time-delay re-scanning*, the number and the maximum length of the *random-pauses* were varied.

In case of a period mismatch of 0.5 s - 1 s, the measures of *breath-sampled re-scanning* degraded but still stayed on a level which clearly outperforms the corresponding values of *slice-by-slice*, *volumetric*, *mixed-scanpath* and *local-parameter re-scanning*. Further investigations (e.g., a

---

[1] V_x: A dose of at least x% of the target dose has been received by the volume V_x

[2] D_x: x% of the volume under consideration has received a dose of at least D_x

finer time spacing) with respect to the period mismatch seem worthwhile. *Random-time-delay re-scanning* turned out to be very robust with respect to the investigated uncertainties.

Overall, both *random-time-delay re-scanning* and *breath-sampled re-scanning* yield excellent results with respect to reducing interplay effects in the presence of motion. These two modes should be the first choice when clinics aim to compensate tumor motion by *re-scanning*.

Due to the same 4DCT data set and the identical simulation environment (TReatment planning for Particles (TRiP)), the results of this thesis can be compared in a very instructive way with other studies of the medical physics group at GSI which investigated *beam tracking* (Lüchtenborg, 2012; Eley, 2013).

Breath-sampled and *random-time-delay re-scanning* show better dose coverage measures of the CTV than any *beam tracking* flavor. On the other hand, the tumor conformity of *re-scanning* can certainty be increased if the technique is used in combination with *gating* or *beam tracking* which will be most beneficial of organ at risk (OAR) could be spared.

Mori et al. (Mori et al., 2013) recently published results of method called *phase-controlled re-scanning* (Furukawa et al., 2010a). This is a combination of *gating* and *re-scanning* which reduces the size of the ITV in contrast to using only *re-scanning*. They performed a study, with phantoms and the 4D data set of one patient (lung tumor patient, motion amplitude of 13 mm), which showed that *slice-by-slice re-scanning* was not able to improve the dose distributions for an increasing number of *re-scans*. This confirms the results of this work, namely, that *slice-by-slice re-scanning* is not always able to break up the correlation between beam application and target motion. On the other hand *phase-controlled re-scanning* could improve the dose distributions efficiently. The patient study, using the *phase-controlled re-scanning* technique, shows less improvement of the dose distributions than the corresponding results (i.e., similar motion amplitude and *re-scan* number) presented in this work in case of *breath-sampled* or *random-time-delay re-scanning*. This deviation might be due to the fact that the treatment planning studies in this work include the usage of four fields from different directions whereas Mori et al. use a single field approach. It was already reported by Knopf et al. (Knopf et al., 2011) that an increasing number of fields has the capability to improve the dose distribution as multiple field also provide additional averaging

It seems especially worthwhile to perform extensive studies in the future which investigate if *re-scanning* could improve the dose homogeneity of *beam tracking*. It is shown that even perfect *beam tracking* causes dose inhomogeneities when irradiating heterogeneous targets (van de Water et al., 2009; Eley, 2013; Lüchtenborg, 2012). Due to the statistical averaging effect, it can be expected that the combination of *re-scanning* and *beam tracking* might lead to a robust and homogeneous dose distributions along with a greatly reduced ITV.

In addition, in the scope of this thesis *slice-by-slice* (at GSI and at HIT) and *breath-sampled re-scanning* (at HIT) were also successfully implemented in a research version and irradiations with carbon ions were performed. Compared to the normal therapy mode, *re-scanning* sets higher demands on the beam irradiation system because the pencil beam moves much faster over the irradiation volume. This might cause errors with respect to dosimetry and the beam application in general (e.g., position accuracy). Therefore, dedicated experiments were planned and performed to validate if satisfying dose application is possible with this new technique.

Furukawa et al. (Furukawa et al., 2010b) also cared about the influence of position, size, time and structure of the beam, saturation of the electrons or recombination effects when irradiating in high speed mode with sub millisecond delivery time of each rasterpoint. They successfully implanted *re-scanning* and found their system to be able to deliver the dose with satisfying quality for $r = 8$. They did not observe recombination effects of more than 1% with their beam monitoring system. The precision of their scanned beam position was less than 0.5 mm.

At GSI and at HIT, the position feedback loop and the corresponding interlocks had to be switched off because the *re-scanning* irradiation is too fast for those measurements. In normal therapy mode, positioning errors of the pencil beam are detected by the therapy control unit (TCU) and the beam can be shifted by the magnets with the help of the position feedback loop to the prescribed position.

The implementations were tested by *slice-by-slice* and *breath-sampled re-scanning* irradiations with different *re-scan* numbers. At first, the experiments were performed without the presence of motion as to isolate the effects of the new techniques.

The physical-beam-plans (PBP) could successfully be irradiated. Due to the deactivation of the position feedback loop, the maximum mean radial position error was detected to be 2.9 mm inside the TCU system. In normal therapy mode, deviations of this order would be in the acceptable range inside the TCU detection system because the fine-tuning is done by the position feedback loop along with the beam steering magnets. Hence, *re-scanning* irradiation dose not overload the system in case of the investigated *re-scan* numbers. The maximum error was measured at $r = 1$ ($r_{max} = 19$ in this experiment) which basically exhibits the same scanning speed as normal therapy mode. The corresponding dose levels were also measured by the TCU devices. The dose slightly increased with an increasing *re-scan* number but all values were within 1% to the prescribed dose.

As a next step, it was investigated, if the dose levels in the isocentre are also in accordance with normal therapy mode. The measurements of all the gas filled ionisation chambers showed relative errors smaller than ±3% when irradiated in *slice-by-slice re-scanning* mode with a *re-scan* number up to $r = 19$ and a 2D plan.

Then, experiments have been designed which also included a moving target as to study the efficiency in reducing interplay patterns by using *slice-by-slice* and *breath-sampled re-scanning*. In case of each experiment setup, a simulation environment was created (see section 3.2.1 and 4.2.7) to mimic the experiment and to check if the findings of simulations and experiments are in accordance.

For this purpose Kodak X-Omat V films were irradiated with 2D plans in *slice-by-slice re-scanning* mode in the presence of motion studying the following parameters: Amplitude, period, starting phase, intensity, scanpath and spill profile shape. The corresponding investigations in the *breath-sampled re-scanning* mode were only assessed via simulations which were designed as to mimic the experimental setup. The experiments were in accordance with the simulations. This was expected because the capability of our simulation environment TRiP was already testet and validated elsewhere (see (Richter, 2012; Krämer and Durante, 2010; Bert et al., 2010)).

The experiments showed that *slice-by-slice re-scanning* efficiently reduces interplay patterns due to motion when irradiating 2D plans. Interplay effects are being compensated faster if the motion is in parallel to the primary scanpath. The larger the motion amplitude the stronger are the interplay patterns. The corresponding simulations showed that *breath-sampled re-scanning* reduces interplay patterns much faster than *slice-by-slice re-scanning* and shows less dependence on the investigated parameters.

To mimic real patient treatment more closely, two heterogenous phantoms (see section 4.2.5 and (Steidl et al., 2012a)) were irradiated with 3D plans. Appropriate ITVs (Graeff et al., 2012) were generated to account for the motion. The detectors moved sinusoidally in horizontal direction with an amplitude of 2 cm peak-to-peak. The period was chosen to be 4 s. Experiments and simulations showed that interplay effects for both phantoms have been efficiently reduced by *slice-by-slice* and *breath-sampled re-scanning*. In experiments and in simulations *breath-sampled* was superior to *slice-by-slice re-scanning*.

It follows that the therapy systems at HIT and GSI show no technical objections against a *re-scan* implementation under therapy conditions. On all accounts, the position feedback loop needs to be adapted to high-speed *re-scanning* irradiation so that the beam position can be corrected during treatment. Figure 5.1 illustrates in a schematic way how the position correction might be influenced by the *re-scan* irradiation. Figure 5.1 a) represents the case of standard patient irradiation. A rasterpoint is irradiated and after a predefined time T_{PCL} (position-correction-loop-reaction-time) the pencil beam can be shifted to the prescribed lateral position. In this example, 75% of the prescribed dose can be delivered to the corrected position. Figure 5.1 b) shows the same process for a rasterpoint in case of $r = 2$. The relativ fraction of the particles which are shifted due to the information of the position feedback loop has decreased to 50 %. In Figure 5.1 c) the system is not able to correct the pencil beam position at all. The influence of this effect needs to be investigated further and to be considered when defining new parameters and limits for the position feedback loop.

Further research efforts should also include the implementation and investigation of *random-time-delay re-scanning* in experiments since it showed very promising results in the treatment planning studies (chapter 3). For example, at HIT its implementation could be imagined in the following way which makes use of the existing *gating* functionality. The physical-beam-plan (PBP) is to be irradiated in *slice-by-slice re-scanning* mode. Then, a *gating* signal, which is

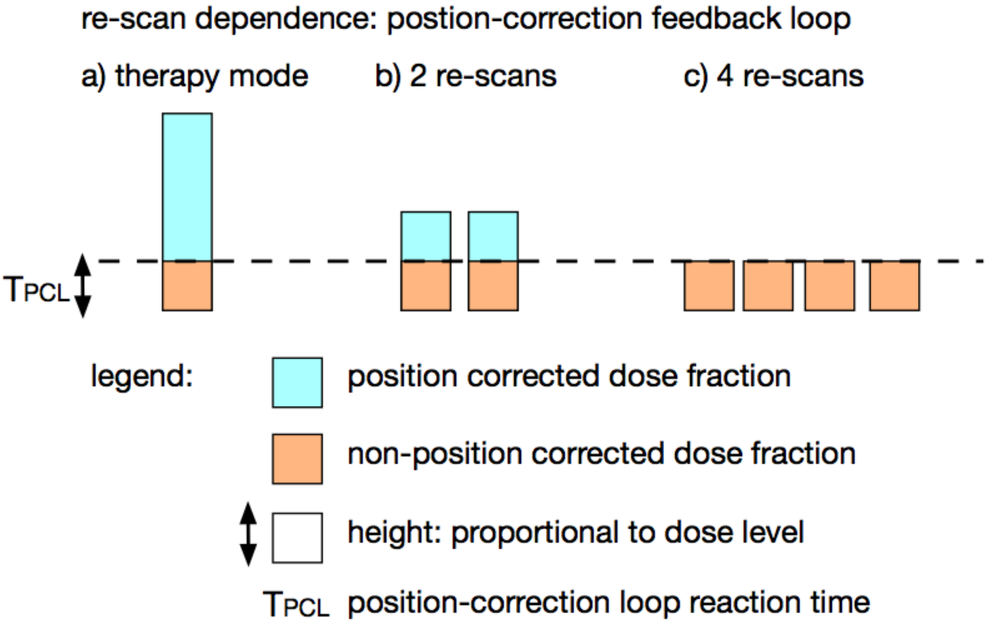

Figure 5.1.: The relative fraction of the particles of a rasterpoint which are corrected with respect to their lateral position due to the information of the position feedback loop decreases with the number of *re-scans*.

no longer coupled to the motion state, is send after a pre-defined irradiation progress. If the lengths of the *gating* pauses are produced by the use of a random number generator then this combination corresponds to the *random-time-delay re-scanning* flavor investigated in this thesis.

Moreover, a method should be implemented that accounts for changes in the breathing period when using *breath-sampled re-scanning*. So far, the intensity is pre-defined according to a given period. The breathing of a real patient might deviate from the planning breathing period or be subjected to a tendency towards a longer or shorter period. The corresponding motion patterns could be assessed via motion monitoring systems (Evans, 2008; Steidl, 2011) and the intensity could be adapted by sending signals to a radio-frequency-knock-out-exciter (Schoemers et al., 2011) in order that the irradiation time per IES gets again more aligned to the breathing period.

Even if the technical feasibility was investigated for a broad range of *re-scan* numbers, it is not guaranteed that the systems will still work properly if the *re-scan* number needs to be increased even further. Up to now, no real patient plan was irradiated in *re-scanning* mode. In general, the PBPs of patients exhibit large dose gradients. It needs to be investigated if this will introduce uncertainties in the beam application. In addition, the systems at GSI and at HIT have a defined minimal particle limit N_{min}. This basically means that irradiations will not be executed if a single rasterpoint has a prescribed particle number which is smaller than N_{min}. A rather high *re-scan* number in combination with a standard fraction schema of 2 Gy/day might fall below this limit. Therefore, further measurements need to be performed before patient treatment in the *re-scanning* mode can begin.

Including the findings of chapter 3 it is likely that a *re-scan* number of about $r = 9$ shall be sufficient when treating lung tumors in the *breath-sampled* or *random-time-delay re-scanning* mode in a four field scenario. This is well inside the experimentally investigated *re-scan* numbers.

If clinics try to implement *re-scanning* in the therapy workflow it would be desirable that prior to each treatment the resulting dose distribution is being simulated with the motion characteristics of the patient's tumor. It is important to investigate if the specific treatment plan of a patient and the beam application may result in dose inhomogeneities due to an unlucky combination of the used parameters. For instance, in case of $r = 9$ the simulation results of patients 5 (see figure 3.14) showed satisfying dose coverage in 9 out of 12 cases. Therefore, a dedicated pre-irradiation simulation environment in the clinical environment might be necessary to detect outcomes with an unacceptable dose distribution. In addition, especially for fractionated dose delivery, the quality assurance should incorporate 4D dose reconstruction based on the treatment records. Richter et al. showed the technical feasibility of such a process for liver patients treated with abdominal compression or gating at HIT (Richter et al., 2013).

Moreover, it must be stated that the experimental and simulation results obtained in the scope of this theses may not easily be transferred to other particle therapy systems. The efficiency in reducing the interplay effect in scanned particle therapy is highly depend on the individual combination of patient specific parameters and the beam application system.

This statement is also confirmed by the findings of a group from the Massachusetts General Hospital (MGH) (Dowdell et al., 2013). Via 4D Monte Carlo simulations, they studied the interplay effect in scanning proton therapy for lung cancer patients. They investigated the dependencies of the dose distribution with respect to the beam delivery parameters and state that the initial breathing phase can have a significant effect on the interplay patterns - particularly for shorter delivery times. This is in accordance with the findings in this work. They further report that increasing the spot size of the beam will decrease the interplay patterns - similar studies were performed at GSI for liver cancer patients (Richter, 2012). However, this procedure will result in less tumor conformity.

If a system provides *gating* or *beam tracking* functionality studies which combine any of these modes with *re-scanning* shall be made in order to investigate which individual technique or which combination of the methods will be most beneficial with respect to therapeutic considerations.

6 Conclusion

In the field of radiotherapy, heavy ion scanned particle therapy provides the best ratio of sparing healthy tissue versus damaging tumor cells when treating stationary tumors. Thus, carbon ion therapy has become a popular treatment option for some indications in the recent years. Currently, only tumors which exhibit very small motion amplitudes are being treated at a few therapy centers since the interaction of tumor motion and scanned beam application is likely to cause severe interference patterns. This so called interplay effect jeopardizes a uniform delivery of the prescribed therapeutic dose across the whole tumor volume.

Repeated application of the treatment dose within a therapy fraction has been shown to efficiently reduce such over- and underdosing of subvolumes within the tumor due to statistical averaging. The corresponding treatment fields need to be enlarged to cover all motion phases of the tumor. This approach, which exists in various flavors, is called *re-scanning*. The main difference between the modes is the spatial-temporal behavior of the scanned pencil beam which delivers the dose in localized packets across the tumor volume. Within the scope of this thesis, the possible dosimetric benefit of six different *re-scanning* modes has been assessed. These treatment planning studies were based on time resolved computed tomography (4DCT) data of five lung cancer patients.

The 4D dose distributions were calculated with the GSI treatment planning software TReatment planning for Particles (TRiP). The studies were performed by incorporating a wide range of realistic motion related parameters which cover typical lung tumor cases. For all five patients, two techniques, called *breath-sampled* and *random-time-delay re-scanning*, could increase the dose application quality to a level which shall enable successful treatment of lung tumor patients in the future. Especially *random-time-delay re-scanning* was very robust with respect to treatment related uncertainties.

In addition, research versions of *slice-by-slice* and *breath-sampled re-scanning* were implemented, tested and verified at GSI Helmholtzzentrum für Schwerionenforschung GmbH (GSI) and Heidelberg Ion-Beam Therapy Centre (HIT). First, it was investigated if these new techniques, which greatly increase the scanning speed of the pencil beam, could technically be applied with acceptable dosimetric outcomes. The measurements showed that a *re-scan* implementation in the therapy workflow should technically be possible. However, some functionalities, which guarantee safe and precise dose application, like the position monitoring of the pencil beam, still need to be adjusted to the increased demands of the *re-scanning* functionality. Second, the efficiency of *re-scanning* with respect to reducing dose inhomogeneities in the presence of motion was assessed by irradiating radiographic films and phantoms. Both, *slice-by-slice* and *breath-sampled re-scanning* were able to reduce dose inhomogeneities significantly, whereas the latter showed better results.

Further investigation of the *re-scanning* method, especially on the experimental side, will be needed before this technique can be used in patient treatment. Nevertheless, *re-scanning* shows very promising results and it can be expected to enable the treatment of moving tumors with scanned particle beams in the near future.

A Appendix of chapter 3

Results and additional information of the treatment planning studies chapter which have not been not presented in the text are shown here.

A.1 Results

The captions of many of the following tables will be identical. In order to make the presentation more compact, the captions are presented right now. A reference is than displayed under each table so that the appropriate caption can be easily found.

A.1.1 Caption: Mean and standard deviations of the V_x or $D_5 - D_{95}$ measures along with the corresponding significance tests

Mean and standard deviations of the V_x or $D_5 - D_{95}$ measure, respectively. The results are calculated for the whole treatment course and for different *re-scan* modes as a function of the *re-scan* number.

The corresponding significance test shall be interpreted as follows: The *re-scan* modes were labeled with numbers (e.g. slice (1)) in the table for presentation purposes. If the number of a certain *re-scan* mode is listed in the column of any other *re-scan* technique within the same row - than these modes differ significantly. For this purpose, the Wilcoxon-Mann-Whitney-Test and the Kruskal-Wallis-Test have been used at the 5% level.

A.1.2 Caption: *Breath-sampled re-scanning* uncertainty: Mean and standard deviations of the V_x or $D_5 - D_{95}$ measures along with the corresponding significance tests

Mean and standard deviations of the V_x or $D_5 - D_{95}$ measure, respectively. The results are calculated for the whole treatment course. The dose distribution was investigated for a possible mismatch between the *breath-sampled re-scanning* spill extraction time per iso-energy slice (IES) (varying from 1 s to 5 s) and the breathing period of the patient (4 s) as a function of the *re-scan* number.

The corresponding significance test shall be interpreted as follows: The irradiation periods were labeled with numbers (e.g. 1s(1) or 3.75s(4)) in the table for presentation purposes. If the number of a certain period is listed in the column of any other period within the same row

- than these results differ significantly. For this purpose, the Wilcoxon-Mann-Whitney-Test and the Kruskal-Wallis-Test have been used at the 5% level.

A.1.3 Caption: *random-time-delay re-scanning* uncertainty: Mean and standard deviations of the V_x or $D_5 - D_{95}$ measures along with the corresponding significance tests

Mean and standard deviations of the V_x or $D_5 - D_{95}$ measure, respectively. The results are calculated for the whole treatment course. The dose calculations are obtained in case of a different number of *random-pauses* or a different length of the *maximum random-pause.* as a function of the *re-scan* number.

The corresponding significance for the number *random-pauses* test shall be interpreted as follows: The number of the *random-pauses* were labeled with numbers ($\mu_{\text{random}} = 0.05(1)$) in the table for presentation purposes. If the number of a certain *random-pause* is listed in the column of any other *random-pause* within the same row - than these results differ significantly.

The corresponding significance for the maximum length of *random-pauses* test shall be interpreted as follows: The maximum length of the *random-pauses* were labeled with numbers ($T_{\text{random, max}} = 1\,\text{s}(1)$) in the table for presentation purposes. If the maximum length of a certain *random-pause* is listed in the column of any other *random-pause* within the same row - than these results differ significantly.

For this purpose, the Wilcoxon-Mann-Whitney-Test and the Kruskal-Wallis-Test have been used at the 5% level.

A.1.4 Standard cases: Figures, mean V_{95}, V_{107} $D_5 - D_{95}$ values along with corresponding significance testing

Patient 1

patient 1	V_{95} mean (standard deviation) [% CTV volume]					
re-scans	slice	vol	mixed	local	random	BS
1	98.4 (0.6)	98.3 (0.5)	98.1 (0.8)	98.3 (0.6)	99.5 (0.2)	98.4 (0.2)
3	99.7 (0.2)	99.4 (0.5)	99.6 (0.3)	99.6 (0.3)	99.8 (0.1)	99.9 (0.0)
5	99.7 (0.2)	99.7 (0.2)	99.8 (0.2)	99.7 (0.2)	99.9 (0.0)	100.0 (0.0)
9	99.8 (0.2)	99.7 (0.2)	99.8 (0.2)	99.8 (0.2)	100.0 (0.0)	100.0 (0.0)
13	99.9 (0.1)	99.8 (0.1)	99.8 (0.2)	99.8 (0.1)	100.0 (0.0)	100.0 (0.0)
17	99.8 (0.2)	99.8 (0.2)	99.8 (0.2)	99.8 (0.2)	100.0 (0.0)	100.0 (0.0)
21	99.8 (0.2)	99.8 (0.0)	99.8 (0.2)	99.8 (0.2)	100.0 (0.0)	100.0 (0.0)

Table A.1.: Patient 1 (caption: see section A.1.1)

patient 1	V_{95} significance test [% CTV volume]					
re-scans	slice(1)	vol(2)	mixed(3)	local(4)	random(5)	BS(6)
1	5	5	5	5	1/2/3/4/6	5
3	6	5/6	6	6	2	1/2/3/4
5	6	5/6	6	5/6	2/4	1/2/3/4
9	6	5/6	6	6	2	1/2/3/4
13	5/6	5/6	5/6	5/6	1/2/3/4	1/2/3/4
17	5/6	5/6	5/6	5/6	1/2/3/4	1/2/3/4
21	5/6	5/6	5/6	5/6	1/2/3/4	1/2/3/4

Table A.2.: Patient 1 (caption: see section A.1.1)

patient 1	V_{107} mean (standard deviation) [% CTV volume]					
re-scans	slice	vol	mixed	local	random	BS
1	0.3 (0.1)	0.3 (0.1)	0.3 (0.1)	0.3 (0.1)	0.0 (0.0)	0.2 (0.1)
3	0.0 (0.0)	0.1 (0.0)	0.0 (0.0)	0.0 (0.0)	0.0 (0.0)	0.0 (0.0)
5	0.0 (0.0)	0.0 (0.0)	0.0 (0.0)	0.0 (0.0)	0.0 (0.0)	0.0 (0.0)
9	0.0 (0.0)	0.0 (0.0)	0.0 (0.0)	0.0 (0.0)	0.0 (0.0)	0.0 (0.0)
13	0.0 (0.0)	0.0 (0.0)	0.0 (0.0)	0.0 (0.0)	0.0 (0.0)	0.0 (0.0)
17	0.0 (0.0)	0.0 (0.0)	0.0 (0.0)	0.0 (0.0)	0.0 (0.0)	0.0 (0.0)
21	0.0 (0.0)	0.0 (0.0)	0.0 (0.0)	0.0 (0.0)	0.0 (0.0)	0.0 (0.0)

Table A.3.: Patient 1 (caption: see section A.1.1)

patient 1	V_{107} significance test [% CTV volume]					
re-scans	slice(1)	vol(2)	mixed(3)	local(4)	random(5)	BS(6)
1	5	5	5	5	1/2/3/4/6	5
3		5/6	6	6	2	2/3/4
5		5/6		6	2	2/4
9		4/5/6		2	2	2
13		5/6			2	2
17	2	1/4/5/6		2	2	2
21		5/6			2	2

Table A.4.: Patient 1 (caption: see section A.1.1)

patient 1	$D_5 - D_{95}$ mean (standard deviation) [% prescribed dose]					
re-scans	slice	vol	mixed	local	random	BS
1	7.1 (0.9)	7.1 (0.8)	7.3 (0.5)	7.1 (0.8)	5.7 (0.3)	7.4 (0.2)
3	5.1 (0.5)	5.5 (1.1)	5.2 (0.7)	5.3 (0.6)	4.5 (0.1)	3.8 (0.0)
5	4.8 (0.7)	5.1 (0.7)	4.7 (0.8)	5.0 (0.7)	3.9 (0.2)	3.1 (0.0)
9	4.5 (0.8)	4.9 (0.7)	4.6 (0.8)	4.7 (0.7)	3.5 (0.1)	2.7 (0.1)
13	4.4 (0.8)	4.8 (0.5)	4.6 (0.8)	4.4 (0.7)	3.1 (0.1)	2.5 (0.0)
17	4.4 (0.8)	4.8 (0.6)	4.5 (0.9)	4.4 (0.8)	3.0 (0.1)	2.5 (0.0)
21	4.4 (0.8)	4.7 (0.4)	4.6 (0.9)	4.5 (0.8)	2.9 (0.1)	2.5 (0.0)

Table A.5.: Patient 1 (caption: see section A.1.1)

patient 1	$D_5 - D_{95}$ significance test [% prescribed dose]					
re-scans	slice(1)	vol(2)	mixed(3)	local(4)	random(5)	BS(6)
1	5	5	5	5	1/2/3/4/6	5
3	6	6	6	5/6	4	1/2/3/4
5	6	5/6	6	5/6	2/4	1/2/3/4
9	5/6	5/6	5/6	5/6	1/2/3/4	1/2/3/4
13	5/6	5/6	5/6	5/6	1/2/3/4	1/2/3/4
17	5/6	5/6	5/6	5/6	1/2/3/4	1/2/3/4
21	5/6	5/6	5/6	5/6	1/2/3/4	1/2/3/4

Table A.6.: Patient 1 (caption: see section A.1.1)

Patient 2

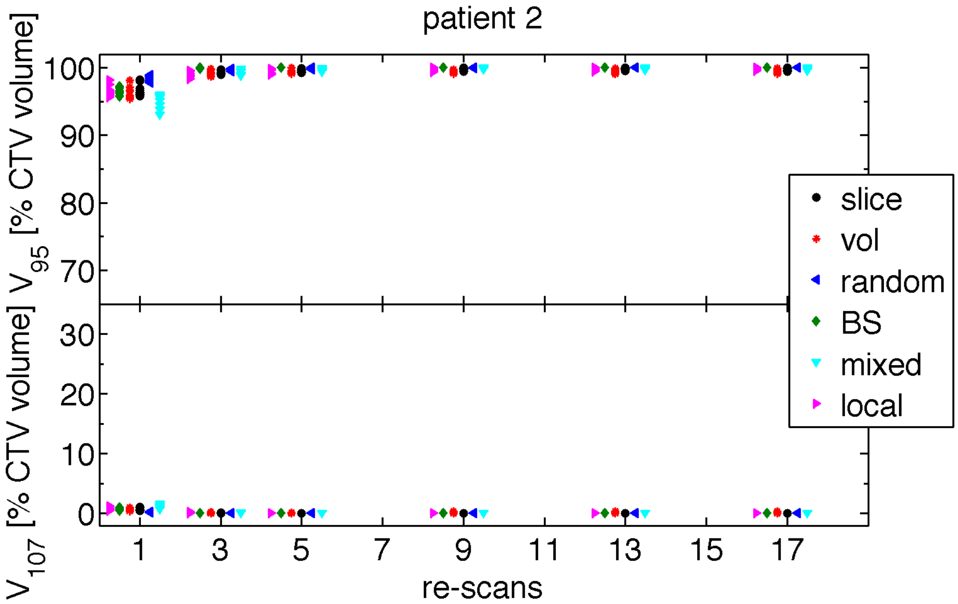

Figure A.1.: V_{95} and V_{107} values for the different *re-scan* modes as a function of the *re-scan* number in case of patient 2. The V_{95} is a measure of the dose coverage and the V_{107} of the overdose, respectively. Every case consist of twelve data points (due to the variation of the starting phases and the breathing periods) which might not be visible due to clustering of the points when increasing the *re-scan* number.

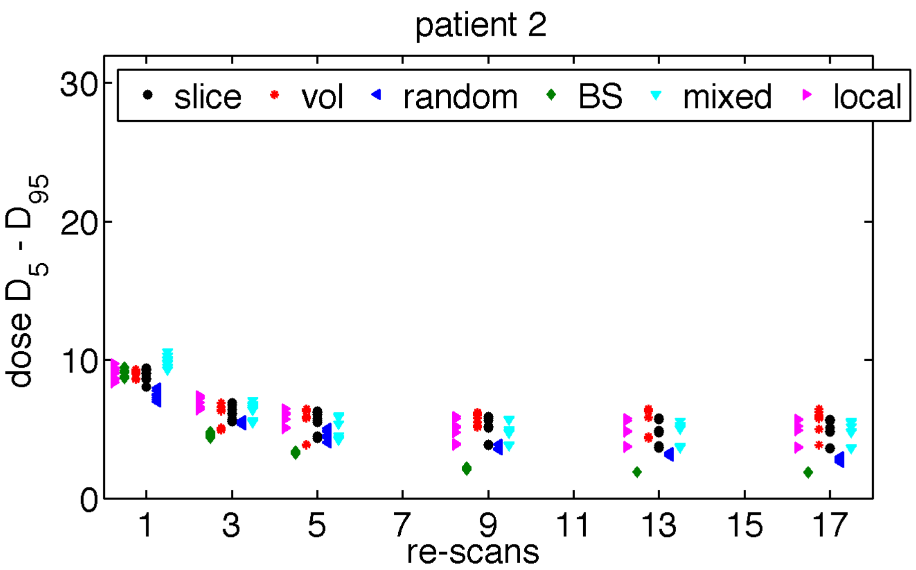

Figure A.2.: The $D_5 - D_{95}$ values for the different *re-scan* modes as a function of the *re-scan* number in case of patient 2. The $D_5 - D_{95}$ is a measure of the homogeneity. Every case consist of twelve data points which might not be visible due to clustering of the points when increasing the *re-scan* number.

patient 2	V_{95} mean (standard deviation) [% CTV volume]					
re-scans	slice	vol	mixed	local	random	BS
1	96.6 (0.8)	96.3 (0.8)	95.0 (1.1)	96.4 (0.8)	98.3 (0.4)	96.5 (0.5)
3	99.4 (0.3)	99.3 (0.4)	99.3 (0.4)	98.9 (0.4)	99.8 (0.1)	99.9 (0.0)
5	99.6 (0.2)	99.5 (0.4)	99.7 (0.2)	99.4 (0.4)	99.9 (0.1)	100.0 (0.0)
9	99.8 (0.2)	99.5 (0.2)	99.9 (0.1)	99.7 (0.2)	100.0 (0.0)	100.0 (0.0)
13	99.8 (0.2)	99.5 (0.3)	99.8 (0.1)	99.8 (0.2)	100.0 (0.0)	100.0 (0.0)
17	99.8 (0.2)	99.5 (0.3)	99.9 (0.1)	99.8 (0.2)	100.0 (0.0)	100.0 (0.0)
21	99.8 (0.2)	99.4 (0.4)	99.9 (0.1)	99.8 (0.2)	100.0 (0.0)	100.0 (0.0)

Table A.7.: Patient 2 (caption: see section A.1.1)

patient 2	V_{95} significance test [% CTV volume]					
re-scans	slice(1)	vol(2)	mixed(3)	local(4)	random(5)	BS(6)
1	3/5	5	1/5/6	5	1/2/3/4/6	3/5
3	6	6	6	5/6	4	1/2/3/4
5	6	6	6	5/6	4	1/2/3/4
9	6	5/6	6	5/6	2/4	1/2/3/4
13	5/6	5/6	5/6	5/6	1/2/3/4	1/2/3/4
17	5/6	5/6	5/6	5/6	1/2/3/4	1/2/3/4
21	5/6	5/6	6	5/6	1/2/4	1/2/3/4

Table A.8.: Patient 2 (caption: see section A.1.1)

patient 2	V_{107} mean (standard deviation) [% CTV volume]					
re-scans	slice	vol	mixed	local	random	BS
1	0.7 (0.3)	0.6 (0.2)	1.2 (0.3)	0.7 (0.2)	0.2 (0.1)	0.7 (0.2)
3	0.1 (0.0)	0.1 (0.1)	0.1 (0.1)	0.1 (0.1)	0.0 (0.0)	0.0 (0.0)
5	0.0 (0.0)	0.1 (0.1)	0.0 (0.0)	0.0 (0.0)	0.0 (0.0)	0.0 (0.0)
9	0.0 (0.0)	0.2 (0.1)	0.0 (0.0)	0.0 (0.0)	0.0 (0.0)	0.0 (0.0)
13	0.0 (0.0)	0.2 (0.1)	0.0 (0.0)	0.0 (0.0)	0.0 (0.0)	0.0 (0.0)
17	0.0 (0.0)	0.2 (0.1)	0.0 (0.0)	0.0 (0.0)	0.0 (0.0)	0.0 (0.0)
21	0.0 (0.0)	0.2 (0.1)	0.0 (0.0)	0.0 (0.0)	0.0 (0.0)	0.0 (0.0)

Table A.9.: Patient 2 (caption: see section A.1.1)

patient 2	V_{107} significance test [% CTV volume]					
re-scans	slice(1)	vol(2)	mixed(3)	local(4)	random(5)	BS(6)
1	3/5	3/5	1/2/5	5	1/2/3/4/6	5
3	6	6	6	5/6	4	1/2/3/4
5	6	5/6		5/6	2/4	1/2/4
9	2	1/3/4/5/6	2	2	2	2
13	2	1/3/4/5/6	2	2	2	2
17	2	1/3/4/5/6	2	2	2	2
21	2	1/3/4/5/6	2	2	2	2

Table A.10.: Patient 2 (caption: see section A.1.1)

patient 2	$D_5 - D_{95}$ mean (standard deviation) [% prescribed dose]					
re-scans	slice	vol	mixed	local	random	BS
1	9.0 (0.4)	9.0 (0.3)	9.9 (0.4)	9.1 (0.4)	7.5 (0.3)	9.1 (0.3)
3	6.2 (0.5)	6.0 (0.8)	6.2 (0.6)	6.8 (0.4)	5.4 (0.1)	4.5 (0.1)
5	5.4 (0.8)	5.4 (1.1)	5.2 (0.7)	5.8 (0.6)	4.5 (0.4)	3.3 (0.1)
9	4.9 (0.8)	5.8 (0.4)	4.7 (0.8)	4.9 (0.9)	3.6 (0.2)	2.1 (0.1)
13	4.8 (0.9)	5.5 (0.9)	4.8 (0.8)	4.8 (0.9)	3.2 (0.1)	1.9 (0.0)
17	4.7 (0.9)	5.4 (1.0)	4.6 (0.8)	4.8 (0.9)	2.8 (0.1)	1.9 (0.0)
21	4.7 (0.9)	5.5 (1.2)	4.6 (0.8)	4.7 (0.8)	2.5 (0.1)	1.8 (0.0)

Table A.11.: Patient 2 (caption: see section A.1.1)

patient 2	$D_5 - D_{95}$ significance test [% prescribed dose]					
re-scans	slice(1)	vol(2)	mixed(3)	local(4)	random(5)	BS(6)
1	3/5	3/5	1/2/4/5	3/5	1/2/3/4/6	5
3	6	6	6	5/6	4	1/2/3/4
5	6	6	6	5/6	4	1/2/3/4
9	6	5/6	6	5/6	2/4	1/2/3/4
13	5/6	5/6	5/6	5/6	1/2/3/4	1/2/3/4
17	5/6	5/6	6	5/6	1/2/4	1/2/3/4
21	5/6	5/6	6	5/6	1/2/4	1/2/3/4

Table A.12.: Patient 2 (caption: see section A.1.1).

Patient 3

patient 3	V_{95} mean (standard deviation) [% CTV volume]					
re-scans	slice	vol	mixed	local	random	BS
1	90.3 (3.1)	90.3 (3.4)	89.1 (2.8)	90.0 (3.3)	96.5 (2.3)	95.7 (1.2)
3	96.1 (1.8)	98.7 (1.5)	95.0 (2.2)	95.7 (1.7)	98.9 (0.3)	99.7 (0.2)
5	96.5 (1.5)	99.8 (0.1)	94.4 (3.1)	96.2 (1.7)	99.5 (0.2)	100.0 (0.0)
9	96.4 (1.9)	100.0 (0.0)	95.6 (2.6)	96.7 (1.6)	99.9 (0.1)	100.0 (0.0)
13	97.0 (1.5)	99.9 (0.1)	94.6 (4.2)	96.4 (2.2)	100.0 (0.0)	100.0 (0.0)
17	96.1 (2.1)	100.0 (0.0)	95.0 (3.6)	96.1 (2.2)	100.0 (0.0)	100.0 (0.0)
21	97.0 (1.6)	100.0 (0.1)	95.4 (2.5)	97.0 (1.9)	100.0 (0.0)	100.0 (0.0)

Table A.13.: Patient 3 (caption: see section A.1.1)

patient 3	V_{95} significance test [% CTV volume]					
re-scans	slice(1)	vol(2)	mixed(3)	local(4)	random(5)	BS(6)
1	5/6	5/6	5/6	5/6	1/2/3/4	1/2/3/4
3	6	3/4	2/5/6	2/5/6	3/4	1/3/4
5	2/6	1/3/4	2/5/6	2/5/6	3/4	1/3/4
9	2/5/6	1/3/4	2/5/6	2/5/6	1/3/4	1/3/4
13	2/5/6	1/3/4	2/5/6	2/5/6	1/3/4	1/3/4
17	2/5/6	1/3/4	2/5/6	2/5/6	1/3/4	1/3/4
21	2/5/6	1/3/4	2/5/6	2/5/6	1/3/4	1/3/4

Table A.14.: Patient 3 (caption: see section A.1.1)

patient 3	V_{107} mean (standard deviation) [% CTV volume]					
re-scans	slice	vol	mixed	local	random	BS
1	3.1 (1.8)	3.0 (2.0)	3.3 (2.1)	3.1 (1.8)	0.4 (0.4)	0.9 (0.4)
3	1.3 (1.2)	0.1 (0.2)	1.5 (1.2)	1.3 (0.8)	0.1 (0.0)	0.0 (0.0)
5	1.0 (1.0)	0.0 (0.0)	1.1 (1.1)	1.2 (1.1)	0.0 (0.0)	0.0 (0.0)
9	0.7 (0.7)	0.0 (0.0)	1.2 (1.1)	0.9 (0.8)	0.0 (0.0)	0.0 (0.0)
13	0.8 (0.8)	0.0 (0.0)	0.9 (0.9)	0.7 (0.7)	0.0 (0.0)	0.0 (0.0)
17	0.7 (0.7)	0.0 (0.0)	1.0 (0.8)	0.8 (0.8)	0.0 (0.0)	0.0 (0.0)
21	0.9 (1.0)	0.0 (0.0)	1.0 (0.8)	0.7 (0.7)	0.0 (0.0)	0.0 (0.0)

Table A.15.: Patient 3 (caption: see section A.1.1)

patient 3	V_{107} significance test [% CTV volume]					
re-scans	slice(1)	vol(2)	mixed(3)	local(4)	random(5)	BS(6)
1	5/6	5/6	5/6	5/6	1/2/3/4	1/2/3/4
3	2/5/6	1/3/4	2/5/6	2/5/6	1/3/4	1/3/4
5	2/5/6	1/3/4	2/5/6	2/5/6	1/3/4	1/3/4
9	2/5/6	1/3/4	2/5/6	2/5/6	1/3/4	1/3/4
13	2/5/6	1/3/4	2/5/6	2/5/6	1/3/4	1/3/4
17	2/5/6	1/3/4	2/5/6	2/5/6	1/3/4	1/3/4
21	2/5/6	1/3/4	2/5/6	2/5/6	1/3/4	1/3/4

Table A.16.: Patient 3 (caption: see section A.1.1)

patient 3	$D_5 - D_{95}$ mean (standard deviation) [% prescribed dose]					
re-scans	slice	vol	mixed	local	random	BS
1	12.2 (1.4)	12.2 (1.4)	12.7 (1.3)	12.4 (1.4)	8.5 (0.9)	9.5 (0.6)
3	9.4 (1.1)	6.5 (1.1)	9.9 (1.4)	9.6 (1.2)	6.6 (0.5)	4.9 (0.3)
5	9.0 (1.2)	4.8 (0.3)	9.6 (1.7)	9.2 (1.3)	5.6 (0.3)	3.4 (0.1)
9	8.7 (1.2)	4.0 (0.6)	9.5 (1.7)	8.8 (1.3)	3.9 (0.4)	2.4 (0.1)
13	8.6 (1.2)	3.9 (0.6)	9.4 (1.7)	8.6 (1.3)	3.4 (0.1)	1.9 (0.1)
17	8.8 (1.3)	3.6 (0.8)	9.4 (1.8)	8.8 (1.4)	3.1 (0.2)	1.8 (0.0)
21	8.5 (1.3)	3.4 (0.9)	9.3 (1.6)	8.6 (1.3)	3.0 (0.2)	1.8 (0.0)

Table A.17.: Patient 3 (caption: see section A.1.1)

patient 3	$D_5 - D_{95}$ significance test [% prescribed dose]					
re-scans	slice(1)	vol(2)	mixed(3)	local(4)	random(5)	BS(6)
1	5/6	5/6	5/6	5/6	1/2/3/4	1/2/3/4
3	2/5/6	1/3/4	2/5/6	2/5/6	1/3/4	1/3/4
5	2/6	1/3/4	2/5/6	2/5/6	3/4	1/3/4
9	2/5/6	1/3/4	2/5/6	2/5/6	1/3/4	1/3/4
13	2/5/6	1/3/4	2/5/6	2/5/6	1/3/4	1/3/4
17	2/5/6	1/3/4	2/5/6	2/5/6	1/3/4	1/3/4
21	5/6	3/4	2/5/6	2/5/6	1/3/4	1/3/4

Table A.18.: Patient 3 (caption: see section A.1.1)

Patient 4

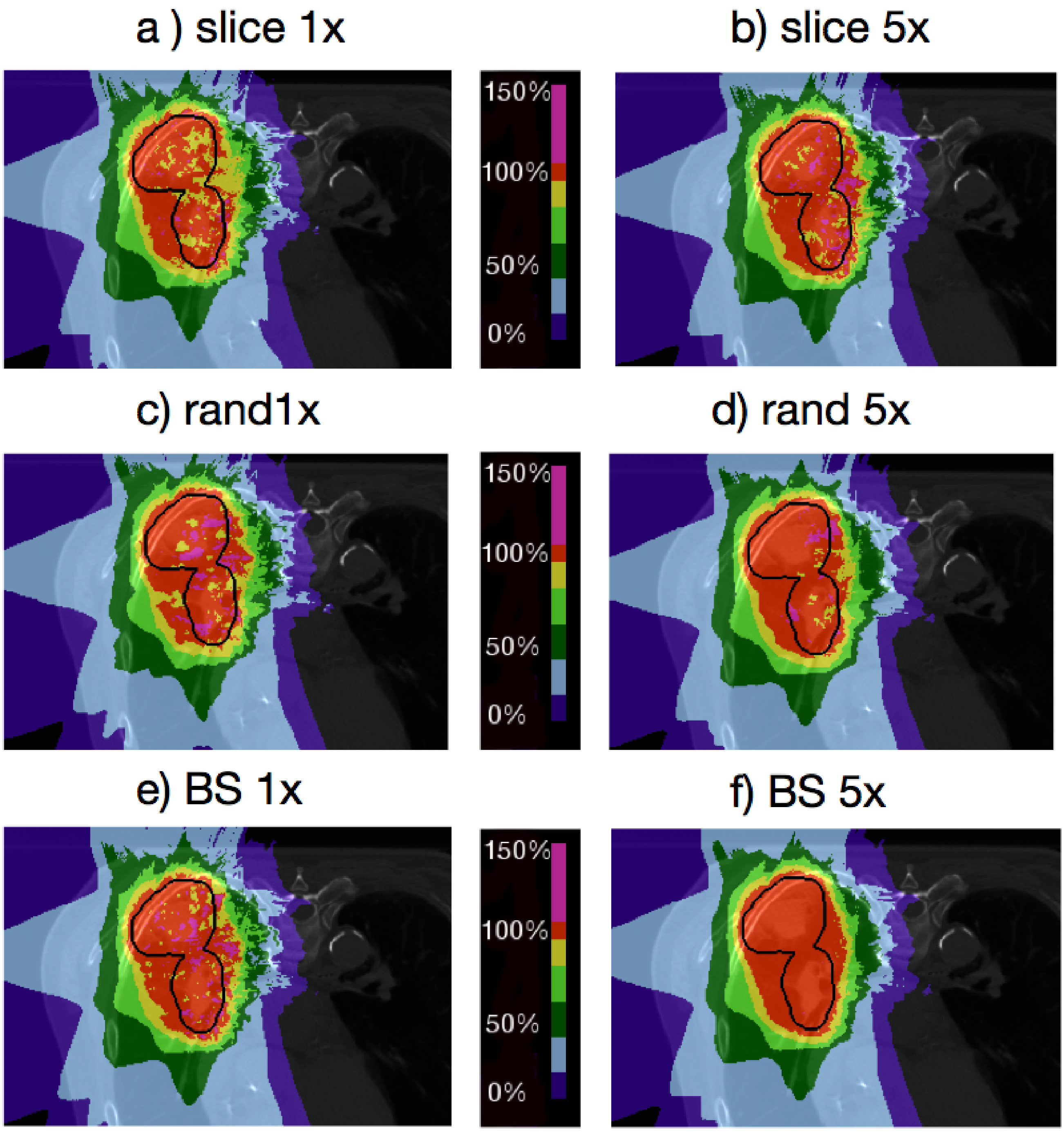

Figure A.3.: Exemplary dose cuts of three selected *re-scan* modes, namely *slice-by-slice*, *breath-sampled* and *random-time-delay re-scanning* for patient 4 in case of $r = 1$ and $r = 5$, respectively. It can bee seen that *breath-sampled* and *random-time-delay re-scanning* reduce the interplay patterns very efficiently. The CTV represents the target contour and is outlined in black.

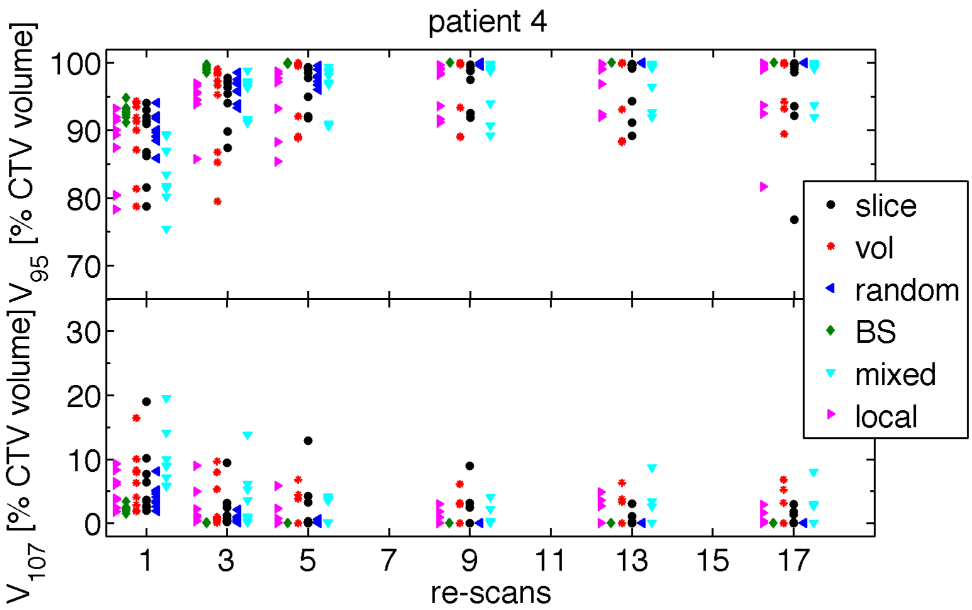

Figure A.4.: V_{95} and V_{107} values for the different *re-scan* modes as a function of the *re-scan* number in case of patient 4. The V_{95} is a measure of the dose coverage and the V_{107} of the overdose, respectively. Every case consist of twelve data points (due to the variation of the starting phases and the breathing periods) which might not be visible due to clustering of the points when increasing the *re-scan* number.

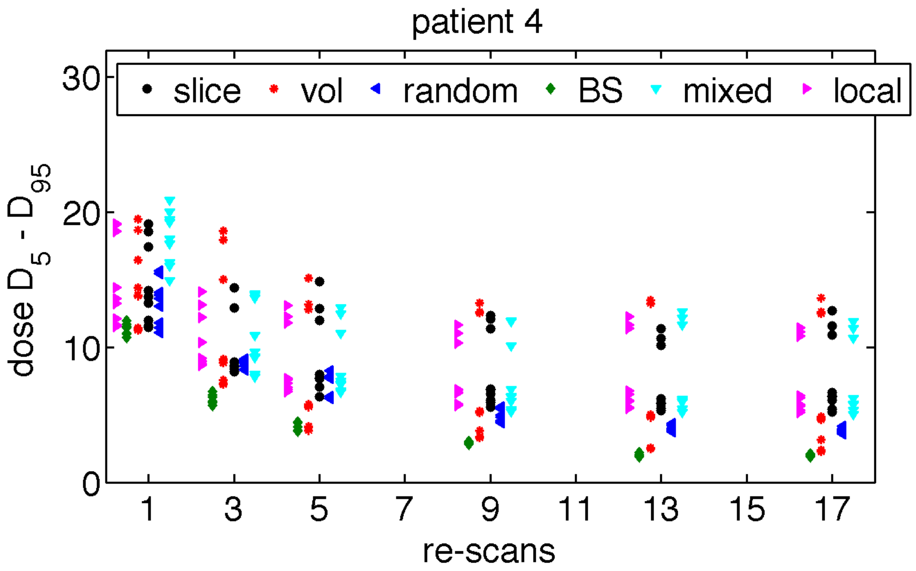

Figure A.5.: The $D_5 - D_{95}$ values for the different *re-scan* modes as a function of the *re-scan* number in case of patient 4. The $D_5 - D_{95}$ is a measure of the homogeneity. Every case consist of twelve data points which might not be visible due to clustering of the points when increasing the *re-scan* number.

patient 4	V_{95} mean (standard deviation) [% CTV volume]					
re-scans	slice	vol	mixed	local	random	BS
1	88.0 (5.2)	88.7 (5.6)	83.4 (5.0)	86.9 (5.6)	90.0 (2.7)	92.6 (1.0)
3	94.6 (4.0)	93.0 (6.8)	94.9 (3.2)	94.1 (4.0)	96.5 (1.6)	99.2 (0.4)
5	96.6 (3.0)	96.4 (5.0)	96.4 (3.4)	95.1 (5.0)	97.7 (1.0)	99.9 (0.1)
9	97.3 (3.2)	96.6 (4.9)	96.9 (3.9)	96.7 (3.6)	99.8 (0.2)	100.0 (0.0)
13	96.8 (4.1)	96.5 (5.3)	97.4 (3.3)	97.4 (3.3)	99.9 (0.0)	100.0 (0.0)
17	95.9 (6.8)	97.1 (4.3)	98.0 (3.0)	96.4 (5.5)	100.0 (0.0)	100.0 (0.0)
21	97.5 (3.0)	97.1 (4.4)	96.7 (4.9)	97.7 (3.0)	100.0 (0.0)	100.0 (0.0)

Table A.19.: Patient 4 (caption: see section A.1.1)

patient 4	V_{95} significance test [% CTV volume]					
re-scans	slice(1)	vol(2)	mixed(3)	local(4)	random(5)	BS(6)
1			6	6		3/4
3	6	6	6	6	6	1/2/3/4/5
5	6		6	6	6	1/3/4/5
9	6	6	6	6		1/2/3/4
13	5/6	6	5/6	5/6	1/3/4	1/2/3/4
17	5/6	6	5/6	5/6	1/3/4	1/2/3/4
21	5/6	6	5/6	5/6	1/3/4	1/2/3/4

Table A.20.: Patient 4 (caption: see section A.1.1)

patient 4	V_{107} mean (standard deviation) [% CTV volume]					
re-scans	slice	vol	mixed	local	random	BS
1	6.2 (4.9)	6.4 (4.4)	9.5 (3.9)	5.2 (2.6)	4.2 (1.6)	2.2 (0.5)
3	1.8 (2.6)	3.0 (4.0)	3.2 (4.1)	1.9 (2.6)	0.8 (0.6)	0.0 (0.0)
5	2.1 (3.8)	1.6 (2.4)	1.3 (1.8)	1.0 (1.8)	0.3 (0.3)	0.0 (0.0)
9	1.4 (2.7)	1.3 (2.1)	0.9 (1.6)	0.6 (1.0)	0.0 (0.0)	0.0 (0.0)
13	0.5 (0.9)	1.4 (2.2)	1.4 (2.6)	1.2 (1.8)	0.0 (0.0)	0.0 (0.0)
17	0.7 (1.0)	1.5 (2.5)	1.4 (2.4)	0.5 (1.0)	0.0 (0.0)	0.0 (0.0)
21	0.8 (1.3)	1.6 (2.6)	0.7 (1.2)	1.1 (1.9)	0.0 (0.0)	0.0 (0.0)

Table A.21.: Patient 4 (caption: see section A.1.1)

patient 4	V_{107} significance test [% CTV volume]					
re-scans	slice(1)	vol(2)	mixed(3)	local(4)	random(5)	BS(6)
1	6	6	5/6	6	3	1/2/3/4
3	6	6	6	6	6	1/2/3/4/5
5	6	6	6	6	6	1/2/3/4/5
9	6		6	6		1/3/4
13	5/6		5/6	5/6	1/3/4	1/3/4
17	5/6		5/6		1/3	1/3
21	5/6			5/6	1/4	1/4

Table A.22.: Patient 4 (caption: see section A.1.1)

patient 4	$D_5 - D_{95}$ mean (standard deviation) [% prescribed dose]					
re-scans	slice	vol	mixed	local	random	BS
1	14.6 (2.9)	14.5 (3.1)	17.9 (1.9)	14.8 (3.1)	13.4 (1.7)	11.3 (0.4)
3	10.1 (2.4)	11.3 (4.7)	10.6 (2.5)	10.4 (2.1)	8.8 (0.3)	6.1 (0.3)
5	9.1 (3.0)	7.8 (4.4)	8.8 (2.6)	8.9 (2.6)	7.4 (0.9)	4.0 (0.3)
9	8.2 (2.7)	7.1 (4.2)	7.8 (2.8)	7.9 (2.3)	5.0 (0.5)	2.9 (0.1)
13	7.5 (2.4)	6.9 (4.8)	7.8 (3.1)	8.0 (2.8)	4.1 (0.2)	2.0 (0.1)
17	7.8 (2.8)	6.7 (4.6)	7.5 (2.8)	7.5 (2.6)	3.8 (0.2)	1.9 (0.1)
21	7.5 (2.5)	6.7 (4.8)	7.4 (2.9)	7.6 (2.6)	3.4 (0.1)	1.8 (0.0)

Table A.23.: Patient 4 (caption: see section A.1.1)

patient 4	$D_5 - D_{95}$ significance test [% prescribed dose]					
re-scans	slice(1)	vol(2)	mixed(3)	local(4)	random(5)	BS(6)
1	6	6	5/6	6	3	1/2/3/4
3	6	6	6	6	6	1/2/3/4/5
5	6	6	6	6	6	1/2/3/4/5
9	5/6	6	6	5/6	1/4	1/2/3/4
13	5/6	6	5/6	5/6	1/3/4	1/2/3/4
17	5/6	6	5/6	5/6	1/3/4	1/2/3/4
21	5/6	6	5/6	5/6	1/3/4	1/2/3/4

Table A.24.: Patient 4 (caption: see section A.1.1)

Patient 5

patient 5	V_{95} mean (standard deviation) [% CTV volume]					
re-scans	slice	vol	mixed	local	random	BS
1	85.3 (11.0)	85.4 (9.9)	78.3 (9.4)	85.9 (9.6)	90.9 (1.8)	93.7 (1.3)
3	92.7 (9.4)	93.9 (3.1)	93.2 (6.9)	91.9 (9.1)	96.8 (1.2)	99.5 (0.2)
5	92.0 (11.1)	97.3 (0.7)	91.6 (11.5)	93.3 (10.7)	98.7 (0.5)	100.0 (0.0)
9	93.2 (10.0)	99.0 (1.0)	94.3 (9.2)	94.0 (9.3)	99.7 (0.2)	100.0 (0.0)
13	94.2 (9.3)	99.3 (0.8)	93.0 (10.4)	93.0 (10.4)	100.0 (0.0)	100.0 (0.0)
17	94.1 (9.4)	99.4 (0.8)	93.7 (9.5)	93.5 (9.8)	100.0 (0.0)	100.0 (0.0)
21	93.9 (9.7)	99.1 (1.3)	94.2 (9.4)	94.9 (9.1)	100.0 (0.0)	100.0 (0.0)

Table A.25.: Patient 5 (caption: see section A.1.1)

patient 5	V_{95} significance test [% CTV volume]					
re-scans	slice(1)	vol(2)	mixed(3)	local(4)	random(5)	BS(6)
1	6	6	6	6		1/2/3/4
3	6	6	6	6	6	1/2/3/4/5
5	6	6	6	6	6	1/2/3/4/5
9	6	6	6	6		1/2/3/4
13	5/6	6	5/6	5/6	1/3/4	1/2/3/4
17	5/6	6	5/6	6	1/3	1/2/3/4
21	5/6		5/6	5/6	1/3/4	1/3/4

Table A.26.: Patient 5 (caption: see section A.1.1)

patient 5	V_{107} mean (standard deviation) [% CTV volume]					
re-scans	slice	vol	mixed	local	random	BS
1	7.5 (6.0)	7.2 (5.9)	15.6 (6.8)	7.0 (5.9)	3.4 (1.0)	1.8 (0.4)
3	3.5 (5.3)	2.0 (1.4)	4.6 (7.5)	3.6 (4.9)	0.6 (0.2)	0.0 (0.0)
5	2.8 (4.2)	0.6 (0.4)	3.2 (4.7)	2.6 (4.1)	0.2 (0.1)	0.0 (0.0)
9	2.2 (3.4)	0.4 (0.5)	2.3 (3.7)	2.7 (4.2)	0.0 (0.0)	0.0 (0.0)
13	2.8 (4.2)	0.4 (0.6)	2.3 (3.8)	2.7 (4.1)	0.0 (0.0)	0.0 (0.0)
17	2.7 (4.0)	0.5 (0.7)	2.1 (3.8)	1.9 (3.2)	0.0 (0.0)	0.0 (0.0)
21	2.1 (3.7)	0.3 (0.4)	2.8 (4.3)	2.2 (3.4)	0.0 (0.0)	0.0 (0.0)

Table A.27.: Patient 5 (caption: see section A.1.1)

patient 5	V_{107} significance test [% CTV volume]					
re-scans	slice(1)	vol(2)	mixed(3)	local(4)	random(5)	BS(6)
1	6	6	5/6	6	3	1/2/3/4
3	6	6	6	6	6	1/2/3/4/5
5	6	6	6	6	6	1/2/3/4/5
9		6	6	6		2/3/4
13	5/6	5/6	5/6	5/6	1/2/3/4	1/2/3/4
17	5/6		5/6	5/6	1/3/4	1/3/4
21	5/6		5/6	5/6	1/3/4	1/3/4

Table A.28.: Patient 5 (caption: see section A.1.1)

patient 5	$D_5 - D_{95}$ mean (standard deviation) [% prescribed dose]					
re-scans	slice	vol	mixed	local	random	BS
1	16.4 (5.7)	16.2 (5.5)	21.6 (2.8)	16.1 (5.5)	12.5 (0.7)	10.7 (0.2)
3	11.3 (5.5)	10.7 (1.5)	11.6 (3.9)	11.8 (5.4)	8.8 (0.4)	5.9 (0.4)
5	10.6 (5.6)	8.8 (0.6)	10.8 (5.2)	10.0 (5.0)	7.1 (0.5)	3.9 (0.2)
9	9.3 (5.2)	6.4 (2.3)	9.3 (5.2)	9.4 (5.3)	5.3 (0.3)	3.1 (0.2)
13	9.4 (5.4)	6.2 (2.1)	9.3 (5.2)	9.4 (5.8)	3.8 (0.2)	1.9 (0.0)
17	9.1 (5.6)	5.9 (2.3)	9.0 (5.0)	8.7 (5.1)	3.6 (0.1)	1.9 (0.0)
21	8.9 (5.4)	5.7 (2.6)	9.3 (5.5)	8.6 (5.0)	3.3 (0.3)	1.8 (0.0)

Table A.29.: Patient 5 (caption: see section A.1.1)

patient 5	$D_5 - D_{95}$ significance test [% prescribed dose]					
re-scans	slice(1)	vol(2)	mixed(3)	local(4)	random(5)	BS(6)
1	6	6	5/6	6	3	1/2/3/4
3	6	6	6	6	6	1/2/3/4/5
5	6	6	6	6	6	1/2/3/4/5
9	6	6	6	6		1/2/3/4
13	5/6	6	5/6	5/6	1/3/4	1/2/3/4
17	5/6	6	5/6	5/6	1/3/4	1/2/3/4
21	5/6	6	5/6	5/6	1/3/4	1/2/3/4

Table A.30.: Patient 5 (caption: see section A.1.1)

A.1.5 Special case I - *breath-sampled re-scanning* uncertainty: Mean V_{95}, V_{107} $D_5 - D_{95}$ values along with corresponding significance testing

Patient 2

patient 2	BS period mismatch:V_{95} mean (standard deviation) [% CTV volume]							
re-scans	1s	3s	3.5s	3.75s	4s	4.25s	4.5s	5s
1	99.4 (0.1)	97.7 (0.1)	96.2 (0.6)	97.1 (0.2)	96.8 (0.5)	95.6 (0.4)	96.1 (1.2)	95.5 (0.4)
3	99.9 (0.0)	99.7 (0.1)	99.7 (0.1)	99.9 (0.0)	99.9 (0.0)	99.9 (0.0)	99.9 (0.0)	99.8 (0.0)
5	100.0 (0.0)	100.0 (0.0)	100.0 (0.0)	100.0 (0.0)	100.0 (0.0)	100.0 (0.0)	100.0 (0.0)	100.0 (0.0)
9	100.0 (0.0)	100.0 (0.0)	100.0 (0.0)	100.0 (0.0)	100.0 (0.0)	100.0 (0.0)	100.0 (0.0)	100.0 (0.0)
13	100.0 (0.0)	100.0 (0.0)	100.0 (0.0)	100.0 (0.0)	100.0 (0.0)	100.0 (0.0)	100.0 (0.0)	100.0 (0.0)

Table A.31.: Patient 2 (caption: see section A.1.2)

patient 2	BS period mismatch: V_{95} significance test [% CTV volume]							
re-scans	1s(1)	3s(2)	3.5s(3)	3.75s(4)	4s(5)	4.25s(6)	4.5s(7)	5s(8)
1	6/8	6				1/2		1
3		5/7	7		2		2/3	
5		5			2			
9								
13								

Table A.32.: Patient 2 (caption: see section A.1.2)

patient 2	BS period mismatch:V_{107} mean (standard deviation) [% CTV volume]							
re-scans	1s	3s	3.5s	3.75s	4s	4.25s	4.5s	5s
1	0.0 (0.0)	0.3 (0.0)	1.0 (0.1)	0.4 (0.1)	0.8 (0.0)	1.3 (0.2)	0.9 (0.1)	1.0 (0.1)
3	0.0 (0.0)	0.0 (0.0)	0.0 (0.0)	0.0 (0.0)	0.0 (0.0)	0.0 (0.0)	0.0 (0.0)	0.0 (0.0)
5	0.0 (0.0)	0.0 (0.0)	0.0 (0.0)	0.0 (0.0)	0.0 (0.0)	0.0 (0.0)	0.0 (0.0)	0.0 (0.0)
9	0.0 (0.0)	0.0 (0.0)	0.0 (0.0)	0.0 (0.0)	0.0 (0.0)	0.0 (0.0)	0.0 (0.0)	0.0 (0.0)
13	0.0 (0.0)	0.0 (0.0)	0.0 (0.0)	0.0 (0.0)	0.0 (0.0)	0.0 (0.0)	0.0 (0.0)	0.0 (0.0)

Table A.33.: Patient 2 (caption: see section A.1.2)

patient 2	BS period mismatch: V_{107} significance test [% CTV volume]							
re-scans	1s(1)	3s(2)	3.5s(3)	3.75s(4)	4s(5)	4.25s(6)	4.5s(7)	5s(8)
1	3/6	6	1	6		1/2/4		
3	6			6	6	1/4/5/7	6	
5								
9								
13								

Table A.34.: Patient 2 (caption: see section A.1.2)

patient 2	BS period mismatch:$D_5 - D_{95}$ mean (standard deviation) [% prescribed dose]							
re-scans	1s	3s	3.5s	3.75s	4s	4.25s	4.5s	5s
1	6.3 (0.0)	8.2 (0.1)	9.5 (0.2)	8.7 (0.0)	9.1 (0.1)	9.7 (0.2)	9.3 (0.2)	9.7 (0.1)
3	4.3 (0.1)	5.5 (0.0)	5.2 (0.0)	4.9 (0.1)	4.4 (0.1)	5.0 (0.0)	4.3 (0.1)	5.1 (0.0)
5	3.5 (0.0)	3.9 (0.0)	3.7 (0.0)	3.4 (0.0)	3.3 (0.1)	3.5 (0.0)	3.4 (0.0)	3.6 (0.0)
9	3.3 (0.0)	2.8 (0.0)	3.0 (0.0)	2.3 (0.0)	2.1 (0.0)	2.2 (0.1)	2.5 (0.1)	3.2 (0.1)
13	1.9 (0.0)	2.7 (0.1)	2.1 (0.1)	1.9 (0.0)	1.9 (0.0)	1.9 (0.0)	2.1 (0.1)	3.0 (0.0)

Table A.35.: Patient 2 (caption: see section A.1.2)

patient 2	BS period mismatch: $D_5 - D_{95}$ significance test [% prescribed dose]							
re-scans	1s(1)	3s(2)	3.5s(3)	3.75s(4)	4s(5)	4.25s(6)	4.5s(7)	5s(8)
1	6/8	6/8				1/2		1/2
3	2/3	1/5/7	1/7		2		2/3	
5		4/5/7	5	2	2/3		2	
9	4/5/6			1	1/8	1		5
13		5			2/8	8		5/6

Table A.36.: Patient 2 (caption: see section A.1.2)

Patient 3

patient 3	BS period mismatch: V_{95} mean (standard deviation) [% CTV volume]							
re-scans	1s	3s	3.5s	3.75s	4s	4.25s	4.5s	5s
1	99.4 (0.2)	97.8 (0.1)	93.1 (1.4)	96.4 (0.9)	95.7 (0.3)	88.6 (4.6)	87.5 (6.0)	93.4 (0.7)
3	100.0 (0.0)	99.6 (0.2)	99.3 (0.2)	99.6 (0.1)	99.9 (0.1)	99.6 (0.1)	99.8 (0.1)	99.5 (0.2)
5	100.0 (0.0)	100.0 (0.0)	100.0 (0.0)	100.0 (0.0)	100.0 (0.0)	99.9 (0.0)	100.0 (0.0)	100.0 (0.0)
9	100.0 (0.0)	100.0 (0.0)	100.0 (0.0)	100.0 (0.0)	100.0 (0.0)	100.0 (0.0)	100.0 (0.0)	100.0 (0.0)
13	100.0 (0.0)	100.0 (0.0)	100.0 (0.0)	100.0 (0.0)	100.0 (0.0)	100.0 (0.0)	100.0 (0.0)	100.0 (0.0)

Table A.37.: Patient 3 (caption: see section A.1.2)

patient 3	BS period mismatch: V_{95} significance test [% CTV volume]							
re-scans	1s(1)	3s(2)	3.5s(3)	3.75s(4)	4s(5)	4.25s(6)	4.5s(7)	5s(8)
1	6/7	7				1	1/2	
3	3		1/5		3			
5								
9								
13								

Table A.38.: Patient 2 (caption: see section A.1.2)

patient 3	BS period mismatch: V_{107} mean (standard deviation) [% CTV volume]							
re-scans	1s	3s	3.5s	3.75s	4s	4.25s	4.5s	5s
1	0.0 (0.0)	0.3 (0.1)	2.8 (0.4)	0.7 (0.3)	0.7 (0.3)	2.2 (1.3)	3.9 (2.3)	1.4 (0.3)
3	0.0 (0.0)	0.0 (0.0)	0.0 (0.0)	0.0 (0.0)	0.0 (0.0)	0.0 (0.0)	0.0 (0.0)	0.0 (0.0)
5	0.0 (0.0)	0.0 (0.0)	0.0 (0.0)	0.0 (0.0)	0.0 (0.0)	0.0 (0.0)	0.0 (0.0)	0.0 (0.0)
9	0.0 (0.0)	0.0 (0.0)	0.0 (0.0)	0.0 (0.0)	0.0 (0.0)	0.0 (0.0)	0.0 (0.0)	0.0 (0.0)
13	0.0 (0.0)	0.0 (0.0)	0.0 (0.0)	0.0 (0.0)	0.0 (0.0)	0.0 (0.0)	0.0 (0.0)	0.0 (0.0)

Table A.39.: Patient 3 (caption: see section A.1.2)

patient 3	BS period mismatch: V_{107} significance test [% CTV volume]							
re-scans	1s(1)	3s(2)	3.5s(3)	3.75s(4)	4s(5)	4.25s(6)	4.5s(7)	5s(8)
1	3/6/7	7	1			1	1/2	
3								
5								
9								
13								

Table A.40.: Patient 3 (caption: see section A.1.2)

patient 3	BS period mismatch:$D_5 - D_{95}$ mean (standard deviation) [% prescribed dose]							
re-scans	1s	3s	3.5s	3.75s	4s	4.25s	4.5s	5s
1	6.0 (0.1)	7.9 (0.2)	11.4 (0.1)	9.1 (0.0)	9.5 (0.1)	12.0 (0.4)	13.2 (1.1)	10.7 (0.2)
3	4.3 (0.1)	5.5 (0.0)	5.9 (0.1)	5.3 (0.0)	4.6 (0.2)	5.5 (0.2)	5.4 (0.2)	5.5 (0.1)
5	3.5 (0.0)	4.1 (0.1)	3.8 (0.1)	3.5 (0.0)	3.4 (0.0)	3.7 (0.1)	3.9 (0.2)	3.8 (0.1)
9	3.4 (0.1)	2.9 (0.1)	3.2 (0.1)	2.5 (0.0)	2.5 (0.0)	2.5 (0.1)	3.4 (0.2)	3.5 (0.0)
13	2.0 (0.1)	2.9 (0.1)	2.4 (0.1)	2.1 (0.0)	2.0 (0.1)	2.1 (0.2)	2.9 (0.6)	3.4 (0.0)

Table A.41.: Patient 3 (caption: see section A.1.2)

patient 3	BS period mismatch: $D_5 - D_{95}$ significance test [% prescribed dose]							
re-scans	1s(1)	3s(2)	3.5s(3)	3.75s(4)	4s(5)	4.25s(6)	4.5s(7)	5s(8)
1	6/7	6/7				1/2	1/2	
3	3/8		1/5		3			1
5	2	1/5			2/8			5
9	5			8	1/8	8		4/5/6
13	8				8			1/5

Table A.42.: Patient 3 (caption: see section A.1.2)

Patient 4

patient 4	BS period mismatch:V_{95} mean (standard deviation) [% CTV volume]							
re-scans	1s	3s	3.5s	3.75s	4s	4.25s	4.5s	5s
1	95.0 (0.5)	93.6 (1.9)	88.5 (1.3)	92.6 (0.6)	92.8 (0.4)	82.6 (1.6)	85.5 (3.1)	91.8 (1.0)
3	99.4 (0.1)	98.7 (0.1)	98.1 (0.5)	99.2 (0.1)	99.3 (0.6)	98.5 (0.4)	97.0 (1.3)	99.0 (0.0)
5	99.9 (0.0)	99.2 (0.4)	99.9 (0.0)	99.8 (0.0)	100.0 (0.0)	99.9 (0.1)	99.4 (0.5)	100.0 (0.0)
9	100.0 (0.0)	100.0 (0.0)	100.0 (0.0)	100.0 (0.0)	100.0 (0.0)	100.0 (0.0)	99.9 (0.1)	100.0 (0.0)

Table A.43.: Patient 4 (caption: see section A.1.2)

patient 4	BS period mismatch: V_{95} significance test [% CTV volume]							
re-scans	1s(1)	3s(2)	3.5s(3)	3.75s(4)	4s(5)	4.25s(6)	4.5s(7)	5s(8)
1	6/7					1	1	
3	7				7		1/5	
5		5/8			2			2
9								

Table A.44.: Patient 4 (caption: see section A.1.2)

patient 4	BS period mismatch:V_{107} mean (standard deviation) [% CTV volume]							
re-scans	1s	3s	3.5s	3.75s	4s	4.25s	4.5s	5s
1	1.3 (0.3)	2.1 (0.7)	4.9 (1.0)	2.6 (0.9)	2.1 (0.4)	8.6 (0.6)	11.3 (3.1)	2.3 (0.2)
3	0.0 (0.0)	0.2 (0.1)	0.1 (0.1)	0.0 (0.0)	0.0 (0.0)	0.1 (0.1)	0.5 (0.8)	0.0 (0.0)
5	0.0 (0.0)	0.0 (0.0)	0.0 (0.0)	0.0 (0.0)	0.0 (0.0)	0.0 (0.0)	0.0 (0.0)	0.0 (0.0)
9	0.0 (0.0)	0.0 (0.0)	0.0 (0.0)	0.0 (0.0)	0.0 (0.0)	0.0 (0.0)	0.0 (0.0)	0.0 (0.0)

Table A.45.: Patient 4 (caption: see section A.1.2)

patient 4	BS period mismatch: V_{107} significance test [% CTV volume]							
re-scans	1s(1)	3s(2)	3.5s(3)	3.75s(4)	4s(5)	4.25s(6)	4.5s(7)	5s(8)
1	6/7					1	1	
3	2	1						
5	2	1/3/4/5/6/8	2	2	2	2		2
9								

Table A.46.: Patient 4 (caption: see section A.1.2).

patient 4	BS period mismatch:$D_5 - D_{95}$ mean (standard deviation) [% prescribed dose]							
re-scans	1s	3s	3.5s	3.75s	4s	4.25s	4.5s	5s
1	9.8 (0.3)	10.9 (0.2)	14.0 (0.5)	11.5 (0.4)	11.2 (0.2)	17.9 (0.6)	19.0 (0.2)	11.7 (0.3)
3	5.7 (0.1)	7.1 (0.1)	7.3 (0.1)	6.1 (0.1)	5.9 (0.4)	7.3 (0.1)	7.8 (0.6)	6.3 (0.0)
5	4.4 (0.1)	6.0 (0.4)	4.6 (0.2)	4.5 (0.1)	3.8 (0.0)	4.5 (0.2)	5.0 (0.4)	4.0 (0.2)
9	3.8 (0.1)	3.2 (0.1)	3.6 (0.1)	3.1 (0.1)	3.0 (0.0)	3.0 (0.0)	3.6 (0.1)	3.4 (0.1)

Table A.47.: Patient 4 (caption: see section A.1.2)

patient 4	BS period mismatch: $D_5 - D_{95}$ significance test [% prescribed dose]							
re-scans	1s(1)	3s(2)	3.5s(3)	3.75s(4)	4s(5)	4.25s(6)	4.5s(7)	5s(8)
1	6/7	7				1	1/2	
3	3/6/7		1			1	1	
5		5/8			2/7		5	2
9	4/5/6			1	1/7	1	5	

Table A.48.: Patient 4 (caption: see section A.1.2)

Patient 5

patient 5	BS period mismatch:V_{95} mean (standard deviation) [% CTV volume]							
re-scans	1s	3s	3.5s	3.75s	4s	4.25s	4.5s	5s
1	97.7 (0.3)	94.4 (0.7)	89.3 (1.4)	93.8 (0.9)	94.0 (0.3)	85.0 (3.5)	74.7 (5.7)	92.9 (1.2)
3	99.7 (0.2)	99.4 (0.2)	99.1 (0.1)	99.5 (0.1)	99.6 (0.1)	98.9 (0.2)	97.9 (0.8)	99.5 (0.1)
5	100.0 (0.0)	99.5 (0.1)	99.9 (0.0)	99.9 (0.0)	100.0 (0.0)	99.9 (0.0)	99.6 (0.1)	100.0 (0.0)
9	100.0 (0.0)	100.0 (0.0)	100.0 (0.0)	100.0 (0.0)	100.0 (0.0)	100.0 (0.0)	99.9 (0.0)	100.0 (0.0)
13	100.0 (0.0)	100.0 (0.0)	100.0 (0.0)	100.0 (0.0)	100.0 (0.0)	100.0 (0.0)	100.0 (0.0)	100.0 (0.0)

Table A.49.: Patient 5 (caption: see section A.1.2)

patient 5	BS period mismatch: V_{95} significance test [% CTV volume]							
re-scans	1s(1)	3s(2)	3.5s(3)	3.75s(4)	4s(5)	4.25s(6)	4.5s(7)	5s(8)
1	6/7	7				1	1/2	
3	7						1	
5	2/7	1/5			2/7		1/5	
9		7			7		2/5	
13								

Table A.50.: Patient 5 (caption: see section A.1.2)

patient 5	BS period mismatch:V_{107} mean (standard deviation) [% CTV volume]							
re-scans	1s	3s	3.5s	3.75s	4s	4.25s	4.5s	5s
1	0.6 (0.4)	1.6 (0.3)	4.7 (0.3)	1.8 (0.3)	1.6 (0.2)	8.3 (1.1)	13.7 (4.0)	1.5 (0.3)
3	0.0 (0.0)	0.1 (0.0)	0.1 (0.0)	0.0 (0.0)	0.0 (0.0)	0.1 (0.1)	0.6 (0.2)	0.0 (0.0)
5	0.0 (0.0)	0.0 (0.0)	0.0 (0.0)	0.0 (0.0)	0.0 (0.0)	0.0 (0.0)	0.0 (0.0)	0.0 (0.0)
9	0.0 (0.0)	0.0 (0.0)	0.0 (0.0)	0.0 (0.0)	0.0 (0.0)	0.0 (0.0)	0.0 (0.0)	0.0 (0.0)
13	0.0 (0.0)	0.0 (0.0)	0.0 (0.0)	0.0 (0.0)	0.0 (0.0)	0.0 (0.0)	0.0 (0.0)	0.0 (0.0)

Table A.51.: Patient 5 (caption: see section A.1.2)

patient 5	BS period mismatch: V_{107} significance test [% CTV volume]							
re-scans	1s(1)	3s(2)	3.5s(3)	3.75s(4)	4s(5)	4.25s(6)	4.5s(7)	5s(8)
1	6/7					1	1/8	7
3	3/7		1		7		1/5	
5	7		7		7	7	1/3/5/6/8	7
9								
13								

Table A.52.: Patient 5 (caption: see section A.1.2)

patient 5	BS period mismatch:$D_5 - D_{95}$ mean (standard deviation) [% prescribed dose]							
re-scans	1s	3s	3.5s	3.75s	4s	4.25s	4.5s	5s
1	8.5 (0.3)	10.4 (0.3)	13.6 (0.2)	10.8 (0.1)	10.6 (0.1)	16.5 (0.5)	23.2 (0.1)	10.9 (0.2)
3	5.6 (0.0)	6.5 (0.1)	6.7 (0.1)	6.0 (0.2)	5.6 (0.1)	7.1 (0.1)	8.4 (0.4)	5.8 (0.1)
5	3.9 (0.0)	5.8 (0.0)	4.2 (0.1)	4.7 (0.1)	3.7 (0.0)	4.2 (0.1)	5.8 (0.4)	4.1 (0.2)
9	3.5 (0.0)	3.2 (0.1)	3.5 (0.1)	3.0 (0.1)	3.1 (0.1)	3.1 (0.1)	4.6 (0.6)	3.5 (0.1)
13	2.1 (0.4)	2.9 (0.0)	2.7 (0.2)	2.0 (0.0)	1.9 (0.0)	2.2 (0.0)	4.3 (0.5)	3.3 (0.1)

Table A.53.: Patient 5 (caption: see section A.1.2)

patient 5	BS period mismatch: $D_5 - D_{95}$ significance test [% prescribed dose]							
re-scans	1s(1)	3s(2)	3.5s(3)	3.75s(4)	4s(5)	4.25s(6)	4.5s(7)	5s(8)
1	6/7	7			7	1	1/2/5	
3	6/7				6/7	1/5	1/5	
5	7	5			2/7		1/5	
9				7	7	7	4/5/6	
13	7			7	7/8		1/4/5	5

Table A.54.: Patient 5 (caption: see section A.1.2)

A.1.6 Special case II - variation of the number and the maximum length of the *random-pauses*: Mean V_{95}, V_{107} $D_5 - D_{95}$ values along with corresponding significance testing

patient 5	V_{95} mean (standard deviation) [% CTV volume]	
re-scans	$\mu_{\text{random}} = 0.05$	$\mu_{\text{random}} = 0.2$
1	91.9 (2.3)	92.0 (2.2)
3	96.9 (1.3)	96.7 (1.2)
5	98.2 (0.1)	98.1 (0.2)
9	99.7 (0.3)	99.6 (0.3)
13	100.0 (0.0)	100.0 (0.0)

Table A.55.: Patient 5 (caption: see section A.1.3)

patient 5	V_{95} significance test [% CTV volume]	
re-scans	$\mu_{\text{random}} = 0.05(1)$	$\mu_{\text{random}} = 0.2(2)$
1		
3		
5		
9		
13		

Table A.56.: Patient 5 (caption: see section A.1.3)

patient 5	V_{107} mean (standard deviation) [% CTV volume]	
re-scans	$\mu_{\text{random}} = 0.05$	$\mu_{\text{random}} = 0.2$
1	2.8 (0.9)	2.8 (0.9)
3	0.4 (0.0)	0.5 (0.0)
5	0.3 (0.2)	0.4 (0.1)
9	0.0 (0.0)	0.0 (0.0)
13	0.0 (0.0)	0.0 (0.0)

Table A.57.: Patient 5 (caption: see section A.1.3)

patient 5	V_{107} significance test [% CTV volume]	
re-scans	$\mu_{\text{random}} = 0.05(1)$	$\mu_{\text{random}} = 0.2(2)$
1		
3		
5		
9		
13		

Table A.58.: Patient 5 (caption: see section A.1.3)

patient 5	$D_5 - D_{95}$ mean (standard deviation) [% prescribed dose]	
re-scans	$\mu_{\text{random}} = 0.05$	$\mu_{\text{random}} = 0.2$
1	12.0 (0.7)	11.9 (0.5)
3	8.9 (0.3)	8.7 (0.3)
5	7.6 (0.4)	7.9 (0.3)
9	5.4 (0.2)	5.4 (0.2)
13	3.6 (0.0)	4.4 (0.8)

Table A.59.: Patient 5 (caption: see section A.1.3)

patient 5	$D_5 - D_{95}$ significance test [% prescribed dose]	
re-scans	$\mu_{\text{random}} = 0.05(1)$	$\mu_{\text{random}} = 0.2(2)$
1		
3		
5		
9		
13	2	1

Table A.60.: Patient 5 (caption: see section A.1.3)

Variation of the maximum length of the *random-pauses*

patient 5	V_{95} mean (standard deviation) [% CTV volume]	
re-scans	$T_{\text{random, max}} = 1\,\text{s}$	$T_{\text{random, max}} = 0.1\,\text{s}$
1	91.9 (2.3)	91.4 (1.2)
3	96.9 (1.3)	98.3 (0.2)
5	98.2 (0.1)	99.2 (0.2)
9	99.7 (0.3)	99.8 (0.1)
13	100.0 (0.0)	100.0 (0.0)

Table A.61.: Patient 5 (caption: see section A.1.3)

patient 5	V_{95} significance test [% CTV volume]	
re-scans	$T_{\text{random, max}} = 1\,\text{s}(1)$	$T_{\text{random, max}} = 0.1\,\text{s}(2)$
1		
3	2	1
5	2	1
9		
13		

Table A.62.: Patient 5 (caption: see section A.1.3)

patient 5	V_{107} mean (standard deviation) [% CTV volume]	
re-scans	$T_{\text{random, max}} = 1\,\text{s}$	$T_{\text{random, max}} = 0.1\,\text{s}$
1	2.8 (0.9)	4.4 (0.3)
3	0.4 (0.0)	0.2 (0.1)
5	0.3 (0.2)	0.1 (0.1)
9	0.0 (0.0)	0.0 (0.0)
13	0.0 (0.0)	0.0 (0.0)

Table A.63.: Patient 5 (caption: see section A.1.3)

patient 5	V_{107} significance test [% CTV volume]	
re-scans	$T_{\text{random, max}} = 1\,\text{s}(1)$	$T_{\text{random, max}} = 0.1\,\text{s}(2)$
1	2	1
3		
5		
9		
13		

Table A.64.: Patient 5 (caption: see section A.1.3)

patient 5	$D_5 - D_{95}$ mean (standard deviation) [% prescribed dose]	
re-scans	$T_{\text{random, max}} = 1\,\text{s}$	$T_{\text{random, max}} = 0.1\,\text{s}$
1	12.0 (0.7)	12.9 (0.3)
3	8.9 (0.3)	7.8 (0.2)
5	7.6 (0.4)	6.9 (0.4)
9	5.4 (0.2)	5.4 (0.2)
13	3.6 (0.0)	5.7 (0.1)

Table A.65.: Patient 5 (caption: see section A.1.3)

patient 5	$D_5 - D_{95}$ significance test [% prescribed dose]	
re-scans	$T_{\text{random, max}} = 1\,\text{s}(1)$	$T_{\text{random, max}} = 0.1\,\text{s}(2)$
1		
3	2	1
5		
9		
13	2	1

Table A.66.: Patient 5 (caption: see section A.1.3)

B Appendix of chapter 4

Results and additional information of the dosimetry chapter which have not been not presented in the text are shown here.

B.1 Material & methods

B.1.1 Dosimetry at HIT

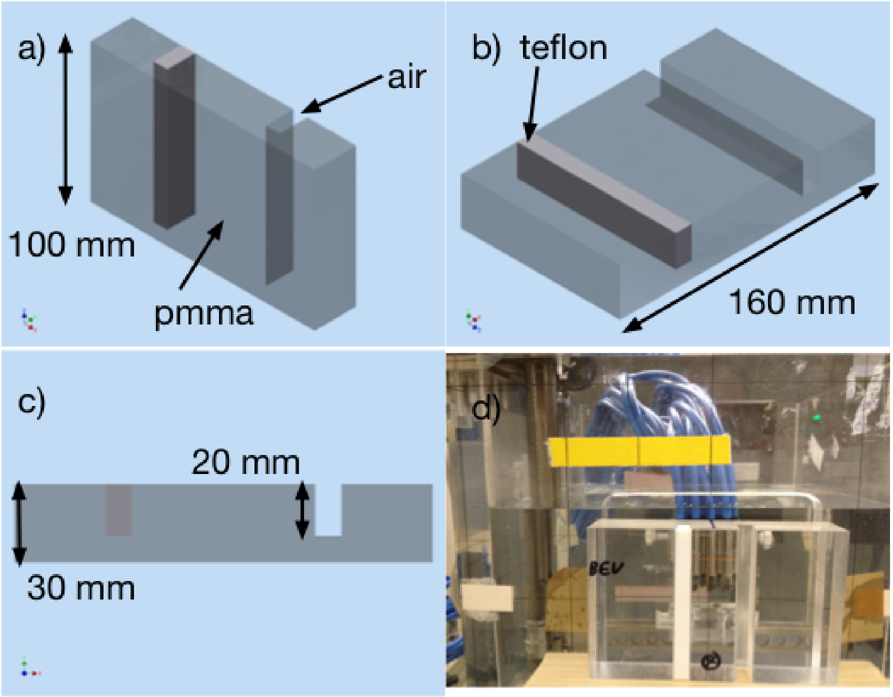

Figure B.1.: This figure shows in a) - c) the DeVarPho from different angles together with its dimension and materials. d) is a picture taken from the set up. The mp3 water phantom with the pin points can be seen behind the DeVarPho.

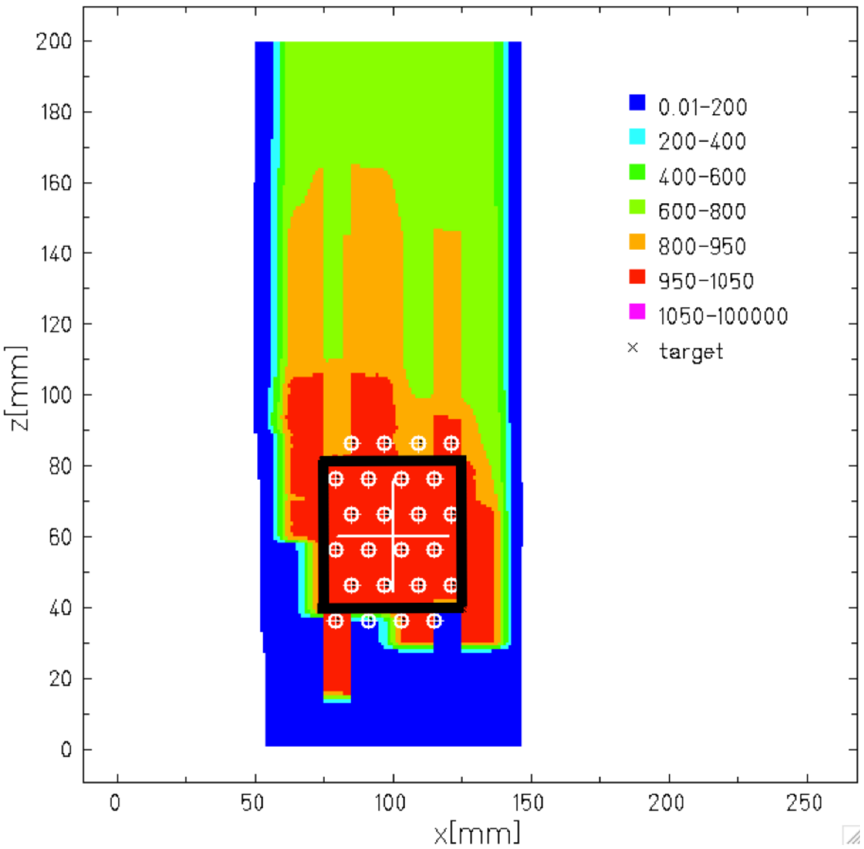

Figure B.2.: The ITV dose distribution of the reference phase of the DeVarPho optimized with the algorithm implemented by Graeff et. al. (Graeff et al., 2012). The overshoot in the lower left and lower right corner is due to the finite FWHM width of the beam an the density variations of the DeVarPho. This effect is explained in figure B.3. The white circles represent the pin point chambers.

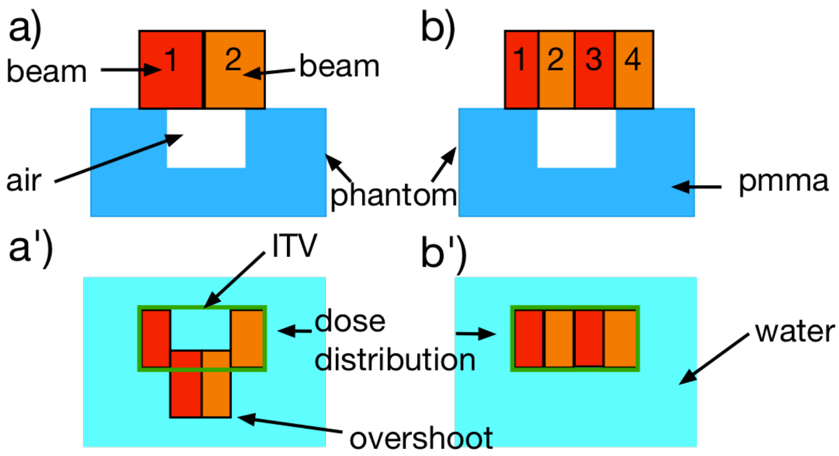

Figure B.3.: Schematic illustration of dose overshooting. The beams are colored differently and symbolized by rectangles. Like shown in a), if the width of the beam is broader than the slit of air or the rastergrid position causes a beam to cross materials of different density (in the upper half of the phantom) it will result in overshoot of the dose. In order to fill the ITV with the prescribed dose, beam 1 in a) must have enough energy to cross the PMMA, parts of this beam also travel trough air instead of PMMA. Consequently, those particles will move further into the medium (e.g. water) like shown in a'). b) shows the ideal case without overshooting.

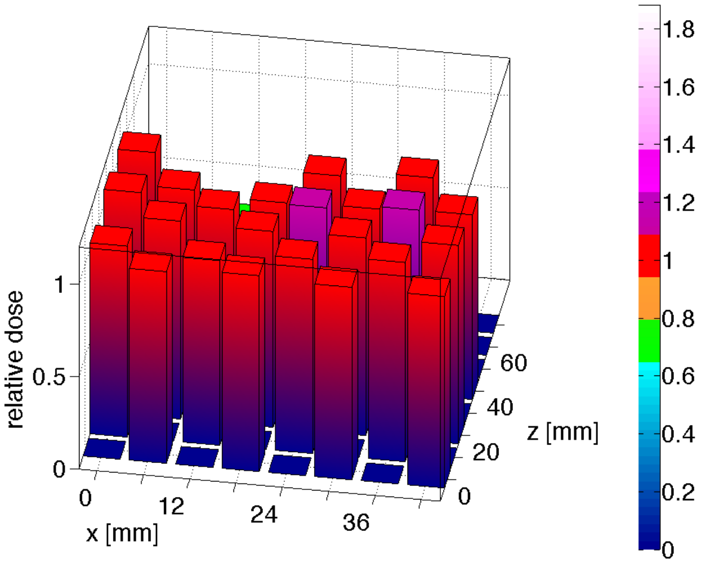

Figure B.4.: Pin point doses of *slice-by-slice re-scanning* (11 *re-scans*) relative to the standard mode of the DeVarPho. The pin points inside the area of 6 mm $\leq x \leq$ 36 mm and 10 mm $\leq y \leq$ 70 mm lie well inside the ITV region without sharp dose gradients. Therefore these pin point are used when quantitative results are reported. The phantom was not moving.

B.2 Motion effects mitigation

B.2.1 Motion effects mitigation by *re-scanning* at HIT

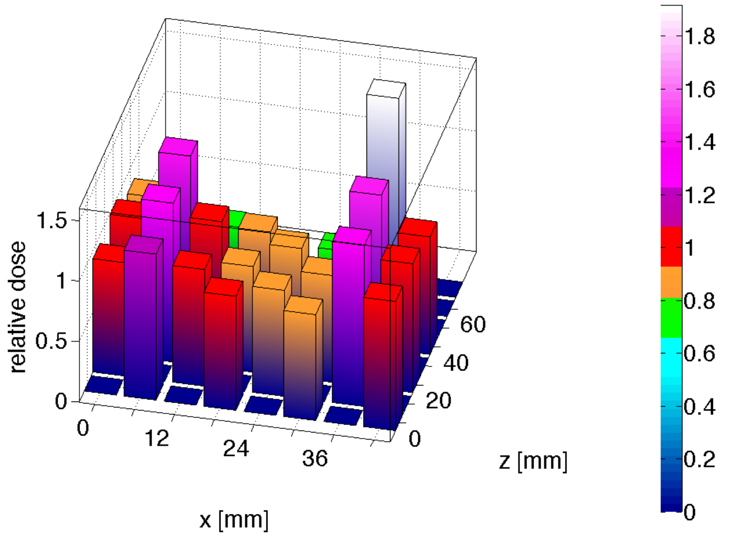

Figure B.5.: Pin point doses of *slice-by-slice re-scanning* ($r = 1$) in the presence of motion of the DeVarPho relative to the standard mode irradiation without motion. The motion causes distinct interplay patterns. The scan-path was vertical.

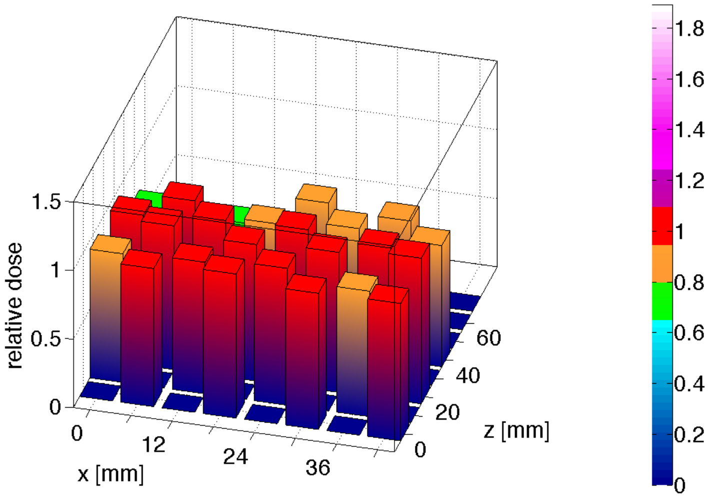

Figure B.6.: Pin point doses of *slice-by-slice re-scanning* ($r = 5$) in the presence of motion of the DeVarPho relative to the standard mode irradiation without motion. The motion causes distinct interplay patterns. The scan-path was vertical.

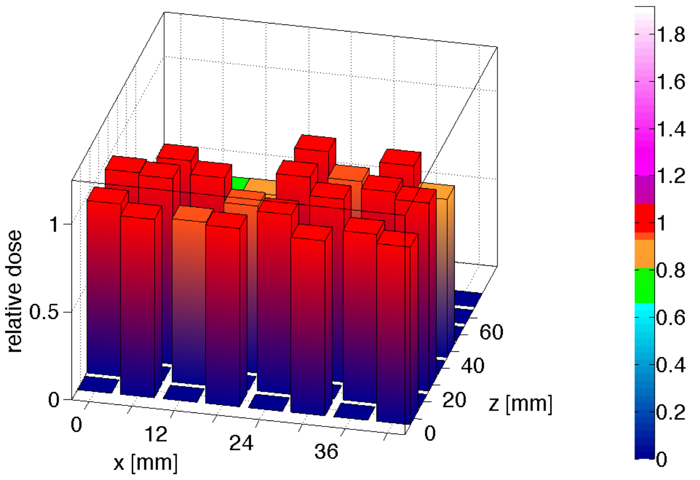

Figure B.7.: Pin point doses of *slice-by-slice re-scanning* ($r = 1$) in the presence of motion of the DeVarPho relative to the standard mode irradiation without motion. The motion causes distinct interplay patterns. The scan-path was horizontal

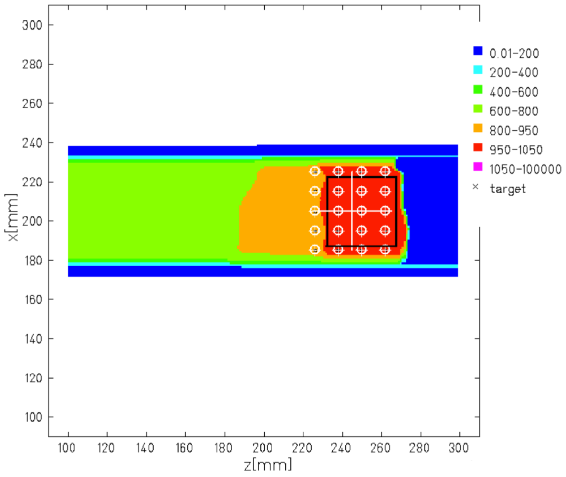

Figure B.8.: The ITV dose distribution of the BreThoPho of the reference phase optimized with the algorithm implemented by Graeff et. al. (Graeff et al., 2012). The white circles represent the pin point chambers.

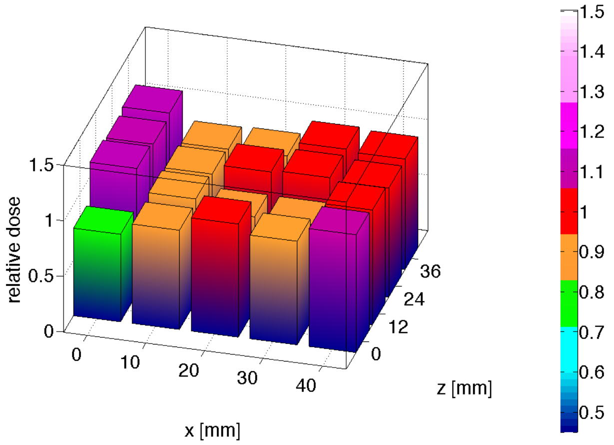

Figure B.9.: Pin point doses of *slice-by-slice re-scanning* ($r = 1$) in the presence of motion of the BreThoPho relative to the standard mode irradiation without motion. The pin points inside the area of 10 mm $\leq x \leq$ 30 mm and 12 mm $\leq y \leq$ 24 mm lie well inside the ITV region without sharp dose gradients. Therefore these pin point are used when quantitative results are reported. The scan-path was horizontal.

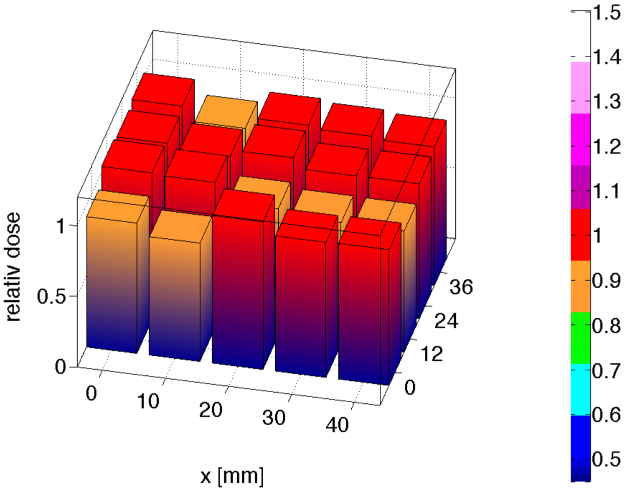

Figure B.10.: Pin point doses of *slice-by-slice re-scanning* ($r = 5$) in the presence of motion of the BreThoPho relative to the standard mode irradiation without motion. The pin points inside the area of 10 mm $\leq x \leq$ 30 mm and 12 mm $\leq y \leq$ 24 mm lie well inside the ITV region without sharp dose gradients. Therefore these pin point are used when quantitative results are reported. The scan-path was horizontal.

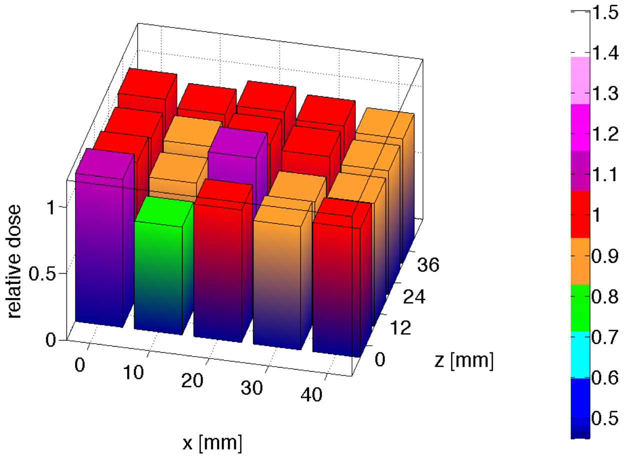

Figure B.11.: Pin point doses of *slice-by-slice re-scanning* ($r = 5$) in the presence of motion of the BreThoPho relative to the standard mode irradiation without motion. The pin points inside the area of 10 mm $\leq x \leq$ 30 mm and 12 mm $\leq y \leq$ 24 mm lie well inside the ITV region without sharp dose gradients. Therefore these pin point are used when quantitative results are reported. The scan-path was vertical.

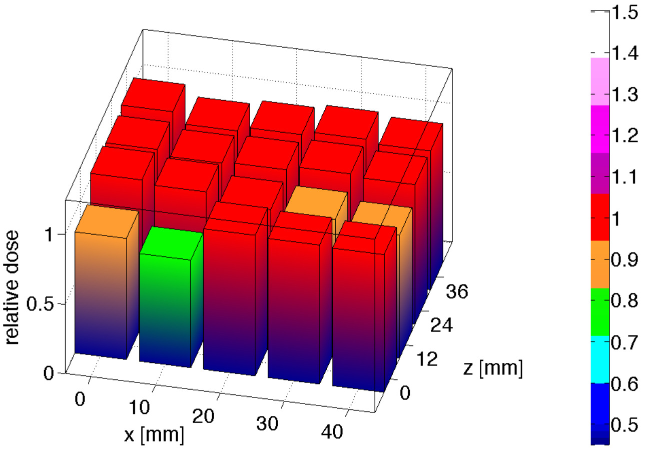

Figure B.12.: Pin point doses of *breath-sampled re-scanning* ($r = 5$) in the presence of motion of the BreThoPho relative to the standard mode irradiation without motion. The pin points inside the area of 10 mm $\leq x \leq$ 30 mm and 12 mm $\leq y \leq$ 24 mm lie well inside the ITV region without sharp dose gradients. Therefore these pin point are used when quantitative results are reported. The scan-path was vertical.

Bibliography

Alpen, E. L. (1998). *Radiation Biophysics*. Academic Press, 2nd edition edition.

Amaldi, U. and Kraft, G. (2008). European Developments in Radiotherapy with Beams of Large Radiobiological Effectiveness. 48(2007):27–41.

Barkas, H. W. (1963). *Nuclear Research Emulsions*. Academic, NewYork, volume 1 edition.

Bathelt, B. (2000). *Filmdosimetrie in der Schwerionen-Tumortherapie: 3-dimensionale Dosisverifikation in gemischten Teilchenstrahlenfeldern*. Dissertation, Universitaet Gesamthochschule Kassel.

Bert, C. and Durante, M. (2011). Motion in radiotherapy: particle therapy. *Physics in Medicine and Biology*, 56(16):R113–44.

Bert, C., Gemmel, A., Chaudhri, N., Luelchtenborg, R., Saito, N., Durante, M., and Rietzel, E. (2008a). Rescanning to mitigate the impact of motion in scanned particle therapy. *GSI Scientific Report*, 1.

Bert, C., Gemmel, A., Saito, N., Chaudhri, N., Schardt, D., Durante, M., Kraft, G., and Rietzel, E. (2010). Dosimetric precision of an ion beam tracking system. *Radiation Oncology (London, England)*, 5:61.

Bert, C., Gemmel, A., Saito, N., and Rietzel, E. (2009). Gated irRadiation with scanned particle beams. *International Journal of Radiation Oncology, Biology, Physics*, 73(4):1270–5.

Bert, C., Grözinger, S. O., and Rietzel, E. (2008b). Quantification of interplay effects of scanned particle beams and moving targets. *Physics in Medicine and Biology*, 53(9):2253–65.

Bert, C., Saito, N., Schmidt, A., Chaudhri, N., Schardt, D., and Rietzel, E. (2007). Target motion tracking with a scanned particle beam. *Medical Physics*, 34(12):4768.

Bethe, H. (1930). Zur Theorie des Durchgangs schneller Korpuskularstrahlen durch Materie. *Annalen der Physik*, 397:325–400.

Bloch, F. (1933a). Bremsvermögen von Atomen mit mehreren Elektronen. *Zeitschrift für Physik A: Hadrons and Nuclei*, 81:363–376.

Bloch, F. (1933b). Zur Bremsung rasch bewegter Teilchen beim Durchgang durch Materie. *Annalen der Physik*, 408:285–320.

Bortfeld, T., Jiang, S. B., and Rietzel, E. (2004). Effects of motion on the total dose distribution. *Seminars in Radiation Oncology*, 14(1):41–51.

Bortfeld, T., Jokivarsi, K., Goitein, M., Kung, J., and Jiang, S. B. (2002). Effects of intra-fraction motion on IMRT dose delivery: statistical analysis and simulation. *Physics in Medicine and Biology*, 47(13):2203–20.

Britton, K. R., Starkschall, G., Tucker, S. L., Pan, T., Nelson, C., Chang, J. Y., Cox, J. D., Mohan, R., and Komaki, R. (2007). Assessment of gross tumor volume regression and motion changes during radiotherapy for non-small-cell lung cancer as measured by four-dimensional computed tomography. *International Journal of Radiation Oncology, Biology, Physics*, 68(4):1036–46.

Brusasco, C., Voss, B., and Schardt, D. (2000). A dosimetry system for fast measurement of 3D depth–dose profiles in charged-particle tumor therapy with scanning techniques. *Nuclear Instruments and Methods in Physics Research Section B: Beam Interactions with Materials and Atoms*, 168:578–592.

Dowdell, S., Grassberger, C., Sharp, G. C., and Paganetti, H. (2013). Interplay effects in proton scanning for lung: a 4d monte carlo study assessing the impact of tumor and beam delivery parameters. *Physics in Medicine and Biology*, 58(12):4137.

Durante, M. and Loeffler, J. S. (2010). Charged particles in Radiation Oncology. *Nature Reviews. Clinical Oncology*, 7(1):37–43.

Durante, M. and Loeffler, J. S. (2013). Charged particle therapy - optimization, challenges and future directions. *Nature Reviews. Clinical Oncology*, 10(7):411–424.

Eckermann, M., Hillbrand, M., Herbst, M., and Rinecker, H. (2011). Scanning proton beam radiotherapy under functional apnea. *Proceedings of the PTCOG 50*.

Eley, J. (2013). *Scanned ion beam therapy for thoracic tumors*. Dissertation, University of Texas.

Elsässer, T. and Scholz, M. (2007). Cluster effects within the local effect model. *Radiation Research*, 167(3):319–29.

Elsässer, T., Weyrather, W. K., Friedrich, T., Durante, M., Iancu, G., Krämer, M., Kragl, G., Brons, S., Winter, M., Weber, K.-J., and Scholz, M. (2010). Quantification of the relative biological effectiveness for ion beam radiotherapy: direct experimental comparison of proton and carbon ion beams and a novel approach for treatment planning. *International Journal of Radiation Oncology, Biology, Physics*, 78(4):1177–83.

Engelsman, M., Rietzel, E., and Kooy, H. M. (2006). Four-dimensional proton treatment planning for lung tumors. *International Journal of Radiation Oncology, Biology, Physics*, 64(5):1589–95.

Evans, P. M. (2008). Anatomical imaging for radiotherapy. *Physics in Medicine and Biology*, 53(12):R151–91.

Fano, U. (1963). Penetration of protons, alpha particles, and mesons. *Annual Review Nuclear Sciene*, 13:1–66.

Ford, E. C., Mageras, G. S., Yorke, E., Rosenzweig, K. E., Wagman, R., and Ling, C. C. (2002). Evaluation of respiratory movement during gated radiotherapy using film and electronic portal imaging. *International Journal of Radiation Oncology, Biology, Physics*, 52(2):522–31.

Fridman, A. and Kennedy, L. (2011). *Plasma Physics and Engineering*. CRC Press.

Friedrich, T., Scholz, U., Elsässer, T., Durante, M., and Scholz, M. (2012). Calculation of the biological effects of ion beams based on the microscopic spatial damage distribution pattern. *International Journal of Radiation Biology*, 88(1-2):103–7.

Furukawa, T., Inaniwa, T., Sato, S., Shirai, T., Mori, S., Takeshita, E., Mizushima, K., Himukai, T., and Noda, K. (2010a). Moving target irradiation with fast rescanning and gating in particle therapy. *Medical Physics*, 37(9):4874.

Furukawa, T., Inaniwa, T., Sato, S., Shirai, T., Takei, Y., Takeshita, E., Mizushima, K., Iwata, Y., Himukai, T., Mori, S., Fukuda, S., Minohara, S., Takada, E., Murakami, T., and Noda, K. (2010b). Performance of the NIRS fast scanning system for heavy-ion radiotherapy. *Medical Physics*, 37(11):5672.

Furukawa, T., Inaniwa, T., Sato, S., Tomitani, T., Minohara, S., Noda, K., and Kanai, T. (2007). Design study of a raster scanning system for moving target irRadiation in heavy-ion radiotherapy. *Medical Physics*, 34(3):1085.

Furukawa, T., Noda, K., Uesugi, T., Naruse, T., and Shibuya, S. (2005). Intensity control in RF-knockout extraction for scanning irRadiation. *Nuclear Instruments and Methods in Physics Research Section B: Beam Interactions with Materials and Atoms*, 240(1-2):32–35.

Gemmel, a., Rietzel, E., Kraft, G., Durante, M., and Bert, C. (2011). Calculation and experimental verification of the RBE-weighted dose for scanned ion beams in the presence of target motion. *Physics in Medicine and Biology*, 56(23):7337–51.

Graeff, C., Durante, M., and Bert, C. (2012). Motion mitigation in intensity modulated particle therapy by internal target volumes covering range changes. *Medical Physics*, 39(10):6004–13.

Graeff, C., Lüchtenborg, R., Eley, J. G., Durante, M., and Bert, C. (2013). A 4d-optimization concept for scanned ion beam therapy. *Radiotherapy and Oncology*, 109(3):419 – 424.

Grözinger, S. O. (2004). *Volume Conformal IrRadiation of Moving Target Volumes with Scanned Ion Beams*. Dissertation, Technical University Darmstadt.

GSI (2013). GSI overview: http://www.gsi.de/en/research/acceleratorfacility.htm.

Haberer, T., Becher, W., Schardt, D., and Kraft, G. (1993). Magnetic scanning system for heavy ion therapy. *Nuclear Instruments and Methods in Physics Research Section A: Accelerators, Spectrometers, Detectors and Associated Equipment*, 330(1-2):296–305.

Hall, E. and Giaccia, A. (2006). *Radiobiology For The Radiologist*. Lippincott Williams & Wilkins.

Hild, S., Durante, M., and Bert, C. (2013). Assessment of Uncertainties in Treatment Planning for Scanned Ion Beam Therapy of Moving Tumors. 85(2):528–535.

Hof, H., Muenter, M., Oetzel, D., Hoess, A., Debus, J., and Herfarth, K. (2007). Stereotactic single-dose radiotherapy (radiosurgery) of early stage nonsmall-cell lung cancer (NSCLC). *Cancer*, 110(1):148–55.

IARC (2013). http://globocan.iarc.fr/factsheet.asp.

ICRU (1993). Prescribing, recording and reporting photon beam therapy. Report 50.

ICRU (1999). Prescribing, recording and reporting photon beam therapy, supplement to ICRU report 50. ICRU report no. 62.

ICRU (2007). Prescribing, recording and reporting proton beam therapy. Report 78.

Ionascu, D., Jiang, S. B., Nishioka, S., Shirato, H., and Berbeco, R. I. (2007). Internal-external correlation investigations of respiratory induced motion of lung tumors. *Medical Physics*, 34(10):3893.

Iwata, H., Murakami, M., Demizu, Y., Miyawaki, D., Terashima, K., Niwa, Y., Mima, M., Akagi, T., Hishikawa, Y., and Shibamoto, Y. (2010). High-dose proton therapy and carbon-ion therapy for stage I nonsmall cell lung cancer. *Cancer*, 116(10):2476–85.

Jiang, S. B., Pope, C., Al Jarrah, K. M., Kung, J. H., Bortfeld, T., and Chen, G. T. Y. (2003). An experimental investigation on intra-fractional organ motion effects in lung IMRT treatments. *Physics in Medicine and Biology*, 48(12):1773–84.

Kaderka, R. (2011). *Out-of-field dose measurements in radiotherapy*. Dissertation, TU Darmstadt.

Kanai, T., Matsufuji, N., Miyamoto, T., Mizoe, J., Kamada, T., Tsuji, H., Kato, H., Baba, M., and Tsujii, H. (2006). Examination of GyE system for HIMAC carbon therapy. *International Journal of Radiation Oncology, Biology, Physics*, 64(2):650–6.

Karger, C. P., Jäkel, O., and Hartmann, G. H. (1999). A system for three-dimensional dosimetric verification of treatment plans in intensity-modulated radiotherapy with heavy ions. *Medical Physics*, 26(10):2125–32.

Karger, C. P., Jäkel, O., Palmans, H., and Kanai, T. (2010). Dosimetry for ion beam radiotherapy. *Physics in Medicine and Biology*, 55(21):R193–234.

Karger, C. P., Peschke, P., Sanchez-Brandelik, R., Scholz, M., and Debus, J. (2006). Radiation tolerance of the rat spinal cord after 6 and 18 fractions of photons and carbon ions: experimental results and clinical implications. *International Journal of Radiation Oncology, Biology, Physics*, 66(5):1488–97.

Keall, P. J., Kini, V. R., Vedam, S. S., and Mohan, R. (2001). Motion adaptive x-ray therapy: a feasibility study. *Physics in Medicine and Biology*, 46(1):1–10.

Keall, P. J., Mageras, G. S., Balter, J. M., Emery, R. S., Forster, K. M., Jiang, S. B., Kapatoes, J. M., Low, D. a., Murphy, M. J., Murray, B. R., Ramsey, C. R., Van Herk, M. B., Vedam, S. S., Wong, J. W., and Yorke, E. (2006). The management of respiratory motion in radiation oncology report of AAPM Task Group 76. *Medical Physics*, 33(10):3874.

Kilby, W., Dooley, J. R., Kuduvalli, G., Sayeh, S., and Maurer, C. R. (2010). The CyberKnife Robotic Radiosurgery System in 2010. *Technology in Cancer Research & Treatment*, 9(5):433–52.

Knopf, A.-C., Hong, T. S., and Lomax, A. (2011). Scanned proton radiotherapy for mobile targets-the effectiveness of re-scanning in the context of different treatment planning approaches and for different motion characteristics. *Physics in Medicine and Biology*, 56(22):7257–71.

Koehler, A., Schneider, R., and Sisterson, J. (1975). Range modulators for protons and heavy ions. *Nuclear Instruments and Methods*, 131(3):437–440.

Koehler, A., Schneider, R., and Sisterson, J. (1977). Flattening of proton dose distributions for large-field radiotherapy. *Medical Physics*, 4(4):297–301.

Korreman, S. S. (2012). Motion in radiotherapy: photon therapy. *Physics in Medicine and Biology*, 57(23):R161–R191.

Kraft, G. (2000). Tumor therapy with heavy charged particles. *Progress in Particle and Nuclear Physics*, 45:S473–S544.

Kraft, S. D., Richter, C., Zeil, K., Baumann, M., Beyreuther, E., Bock, S., Bussmann, M., Cowan, T. E., Dammene, Y., Enghardt, W., Helbig, U., Karsch, L., Kluge, T., Laschinsky, L., Lessmann, E., Metzkes, J., Naumburger, D., Sauerbrey, R., Schürer, M., Sobiella, M., Woithe, J., Schramm, U., and Pawelke, J. (2010). Dose-dependent biological damage of tumour cells by laser-accelerated proton beams. *New Journal of Physics*, 12(8):085003.

Krämer, M. and Durante, M. (2010). Ion beam transport calculations and treatment plans in particle therapy. *The European Physical Journal D*, 60(1):195–202.

Krämer, M., Jäkel, O., Haberer, T., Kraft, G., Schardt, D., and Weber, U. (2000). Treatment planning for heavy-ion radiotherapy: physical beam model and dose optimization. *Physics in Medicine and Biology*, 45(11):3299–317.

Krämer, M. and Scholz, M. (2000). Treatment planning for heavy-ion radiotherapy: calculation and optimization of biologically effective dose. *Physics in Medicine and Biology*, 45(11):3319–30.

Kraus, K. M., Heath, E., and Oelfke, U. (2011). Dosimetric consequences of tumour motion due to respiration for a scanned proton beam. *Physics in Medicine and Biology*, 56(20):6563–81.

Lambert, J., Suchowerska, N., McKenzie, D. R., and Jackson, M. (2005). Intrafractional motion during proton beam scanning. *Physics in Medicine and Biology*, 50(20):4853–62.

Lüchtenborg, R. (2012). *Real-time dose compensation methods for scanned ion beam therapy of moving tumors.* Dissertation, TU Darmstadt.

Leroy, C. and Rancoita, P.-G. (2009). *Principles of Radiation Interaction in Matter and Detection*. World Scientific.

Liu, H., Balter, P., Tutt, T., Choi, B., Zhang, J., Wang, C., Chi, M. Luo, D., Pan, T., Hunjan, S., Starkschall, S., Rosen, I., Prado, K., Liao, Z., Chang, J., Komaki, R., and Dong, L. (2007). Assessing Respiration-Induced Tumor Motion and Internal Target Volume Using Four-Dimensional Computed Tomography for Radiotherapy of Lung Cancer. *International Journal of Radiation Oncology, Biology, Physics*, 68(2):531–540.

Luchtenborg, R., Saito, N., Durante, M., and Bert, C. (2011). Experimental verification of a real-time compensation functionality for dose changes due to target motion in scanned particle therapy. *Medical Physics*, 38(10):5448–58.

Lujan, A., Larsen, E., Balter, J., and Haken, R. T. (1999). A method for incorporating organ motion due to breathing into 3D dose calculations. *Medical Physics*, (26):715–720.

Martens, C., Claeys, I., De Wagter, C., and De Neve, W. (2002). The value of radiographic film for the characterization of intensity-modulated beams. *Physics in Medicine and Biology*, 47(13):2221–34.

MDACC (2013). Homepage the MD Anderson Cancer Center: http://mdanderson.org/patient-and-cancer-information/proton-therapy-center/conditions-we-treat/lung-cancer/index.html.

Mendenhall, N. P., Li, Z., Hoppe, B. S., Marcus, R. B., Mendenhall, W. M., Nichols, R. C., Morris, C. G., Williams, C. R., Costa, J., and Henderson, R. (2012). Early outcomes from three prospective trials of image-guided proton therapy for prostate cancer. *International Journal of Radiation Oncology, Biology, Physics*, 82(1):213–21.

Minohara, S., Kanai, T., Endo, M., and Noda, K.and Kanazawa, M. (2000). Respiratory gated irradiation systems for heavy-ion therapy. *International Journal of Radiation Oncology, Biology, Physics.*, 47(4):1097–1103.

Miyamoto, T., Baba, M., Sugane, T., Nakajima, M., Yashiro, T., Kagei, K., Hirasawa, N., Sugawara, T., Yamamoto, N., Koto, M., Ezawa, H., Kadono, K., Tsujii, H., Mizoe, J.-e., Yoshikawa, K., Kandatsu, S., and Fujisawa, T. (2007). Carbon ion radiotherapy for stage I non-small cell lung cancer using a regimen of four fractions during 1 week. *Journal of thoracic Oncology : official publication of the International Association for the Study of Lung Cancer*, 2(10):916–26.

Miyamoto, T., Yamamoto, N., Nishimura, H., and Koto, M. (2003). Carbon ion radiotherapy for stage I non-small cell lung cancer. *Radiotherapy and Oncology*, 66:127–140.

Mori, S., Furukawa, T., Inaniwa, T., Zenklusen, S., Nakao, M., Shirai, T., and Noda, K. (2013). Systematic evaluation of four-dimensional hybrid depth scanning for carbon-ion lung therapy. *Medical Physics*, 40(3):031720.

Morin, O., Chen, J., and Aubin, M. (2007). Dose calculation using megavoltage cone-beam ct. *Int J Radiat Oncol Biol Phys*, 67:1201–1210.

Muessig, D., Bert, C., Luechtenborg, R., and Gemmel, A. (2012). Bestrahlungsplanung einer Partikelbestrahlung unter Berücksichtigung einer Bewegung eines Zielvolumens. *Patent Application*, DE 10 2012 112 348.9.

Münter, M. W., Wengenroth, M., Fehrenbacher, G., Schardt, D., Nikoghosyan, A., Durante, M., and Debus, J. (2010). Heavy ion radiotherapy during pregnancy. *Fertility and Sterility*, 94(6):2329.e5–7.

Nakamaru, K. (2010). REVIEW OF PARTICLE Physics * Particle Data Group. *Journal of Physics G: Nuclear and Particle Physics*, 37(7A).

Naumann, J. (2011). personal communication.

Newhauser, W. D. and Durante, M. (2011). Assessing the risk of second malignancies after modern radiotherapy. *Nature Reviews. Cancer*, 11(6):438–48.

Pedroni, E., Bacher, R., Blattmann, H., Böhringer, T., Coray, A., Lomax, A., Lin, S., Munkel, G., Scheib, S., Schneider, U., and Torovsky, A. (1995). The 200-MeV proton therapy project at the Paul Scherrer Institute: Conceptual design and practical realization. *Medical Physics*, 22(1):37–53.

Phillips, M. H., Pedroni, E., Blattmann, H., Boehringer, T., Coray, a., and Scheib, S. (1992). Effects of respiratory motion on dose uniformity with a charged particle scanning method. *Physics in Medicine and Biology*, 37(1):223–34.

PTW (2013). http://www.ptw.de/onlinecatalogs.html.

Riboldi, M., Orecchia, R., and Baroni, G. (2012). Real-time tumour tracking in particle therapy: technological developments and future perspectives. *The Lancet Oncology*, 13(9):e383–e391.

Richter, A., Hu, Q., Steglich, D., Baier, K., Wilbert, J., Guckenberger, M., and Flentje, M. (2008). Investigation of the usability of conebeam ct data sets for dose calculation. *Radiation Oncology*, 3(1):42.

Richter, D. (2012). *Treatment planning for tumors with residual motion in scanned ion beam therapy*. Dissertation, Technische Universität Darmstadt.

Richter, D., Saito, N., Chaudhri, N., Härtig, M., Ellerbrock, M., Jäkel, O., Combs, S., Habermehl, D., Herfarth, K., Durante, M., and Bert, C. (2013). 4D patient dose reconstruction for scanned ion beam therapy of moving liver tumors. *International Journal of Radiation Oncology*Biology*Physics*, (submitted).

Rietzel, E. and Bert, C. (2010). Respiratory motion management in particle therapy. *Medical Physics*, 37(2):449.

Rietzel, E., Chen, G. T. Y., Choi, N. C., and Willet, C. G. (2005). Four-dimensional image-based treatment planning: Target volume segmentation and dose calculation in the presence of respiratory motion. *International Journal of Radiation Oncology, Biology, Physics*, 61(5):1535–50.

RKI (2012). *Krebs in Deutschland 2007/2008*. Robert Koch-Institut.

Saito, N., Bert, C., Chaudhri, N., Gemmel, A., Schardt, D., Durante, M., and Rietzel, E. (2009). Speed and accuracy of a beam tracking system for treatment of moving targets with scanned ion beams. *Physics in Medicine and Biology*, 54(16):4849–62.

Schardt, D., Elsässer, T., and Schulz-Ertner, D. (2010). Heavy-ion tumor therapy: Physical and radiobiological benefits. *Reviews of Modern Physics*, 82(1):383–425.

Schardt, D., Rodriguez, J., Voss, B., Heeg, P., and Giesen, U. (2011). Proposal UBIO P11.

Schlegel, W. (2010). If you can't see it, you can miss it: the role of biomedical imaging in radiation oncology. *Radiation Protection Dosimetry*, 139(1-3):321–326.

Schneider, U., Pedroni, E., and Lomax, A. (1996). The calibration of ct hounsfield units for radiotherapy treatment planning. *Physics in Medicine and Biology*, 41:111–124.

Schoemers, C., Feldmeier, E., Haberer, T., Naumann, J., Panse, R., and Peters, A. (2011). Implementation of an intensity feedback-loop for an ion-therapy synchrotron. *Proceedings of IPAC2011*, pages 2851–2853.

Scholz, M. (2003). Effects of ion Radiation in cells and tissue. *Advances in Polymer Science*, 162:95–155.

Scholz, M. and Kraft, G. (1994). Calculation of heavy ion inactivation probabilities based on track structure, x ray sensitivity and target size. *Radiation Protection Dosimetry*, 52:29–33.

Schätti, A., Zakova, M., Meer, D., and Lomax, A. J. (2013). Experimental verification of motion mitigation of discrete proton spot scanning by re-scanning. *Physics in Medicine and Biology*, 58(23):8555.

Schulz-Ertner, D. and Tsujii, H. (2007). Particle Radiation therapy using proton and heavier ion beams. *Journal of clinical Oncology : official Journal of the American Society of Clinical Oncology*, 25(8):953–64.

Seco, J., Robertson, D., Trofimov, A., and Paganetti, H. (2009). Breathing interplay effects during proton beam scanning: simulation and statistical analysis. *Physics in Medicine and Biology*, 54(14):N283–94.

Shackleford, J. a., Kandasamy, N., and Sharp, G. C. (2010). On developing B-spline registration algorithms for multi-core processors. *Physics in Medicine and Biology*, 55(21):6329–51.

Shirato, H., Oita, M., Fujita, K., Watanabe, Y., and Miyasaka, K. (2004). Feasibility of synchronization of real-time tumor-tracking radiotherapy and intensity-modulated radiotherapy from viewpoint of excessive dose from fluoroscopy. *International Journal of Radiation Oncology, Biology, Physics*, 60(1):335–41.

Sonke, J.-J. and Belderbos, J. (2010). Adaptive radiotherapy for lung cancer. *Seminars in Radiation Oncology*, 20(2):94–106.

Spielberger, B., Scholz, M., Krämer, M., and Kraft, G. (2001). Experimental investigations of the response of films to heavy-ion irRadiation. *Physics in Medicine and Biology*, 46(11):2889–97.

Steidl, P. (2011). *Gating for scanned ion beam therapy*. Dissertation, TU Darmstadt.

Steidl, P., Richter, D., Schuy, C., Schubert, E., Haberer, T., Durante, M., and Bert, C. (2012a). A breathing thorax phantom with independently programmable 6D tumour motion for dosimetric measurements in Radiation therapy. *Physics in Medicine and Biology*, 57(8):2235–50.

Steidl, P., Richter, D., Schuy, C., Schubert, E., Haberer, T., Durante, M., and Bert, C. (2012b). A breathing thorax phantom with independently programmable 6D tumour motion for dosimetric measurements in Radiation therapy. *Physics in Medicine and Biology*, 57(8):2235–50.

Tobias, C., Lawrence, J., McCombs, R., Roberts, J., Anger, H., and Huggins, C. (1958). Pituitary IrRadiation with High Energy Proton Beams: a Preliminary Report. *Cancer Research*, 18:121–134.

Tsujii, H. and Kamada, T. (2012). A Review of Update Clinical Results of Carbon Ion Radiotherapy. *Japanese Journal of clinical Oncology*, 42((8)):670–685.

van de Water, S., Kreuger, R., Zenklusen, S., Hug, E., and Lomax, a. J. (2009). Tumour tracking with scanned proton beams: assessing the accuracy and practicalities. *Physics in Medicine and Biology*, 54(21):6549–63.

van Herk, M., Remeijer, P., Rasch, C., and Lebesque, J. V. (2000). The probability of correct target dosage: dose-population histograms for deriving treatment margins in radiotherapy. *International Journal of Radiation Oncology, Biology, Physics*, 47(4):1121–35.

Voss, B., Junk, H., and Stelzer, H. (1998). The monitor system of the therapy project. *GSI-Rep-98-1*, page 187.

Weber, U. and Kraft, G. (1999). Design and construction of a ripple filter for a smoothed depth dose distribution in conformal particle therapy. *Physics in Medicine and Biology*, 44(11):2765–75.

Weichsel, J., Fuchs, T., Lefebvre, E., d'Humières, E., and Oelfke, U. (2008). Spectral features of laser-accelerated protons for radiotherapy applications. *Physics in Medicine and Biology*, 53(16):4383.

WHO (2007). *The World Health Organization's Fight Against Cancer: Strategies That Prevent, Cure and Care.* WHO Press.

Wilson, R. R. (1946). Radiological use of fast protons. *Radiology*, 47(5):487–491.

Woelfelschneider, J. (2011). Fraktionierte Bestrahlung bewegter Tumoren mit gescannten Schwerionen. Diplomarbeit, Technische Hochschule Mittelhessen.

Zenklusen, S. M., Pedroni, E., and Meer, D. (2010). A study on repainting strategies for treating moderately moving targets with proton pencil beam scanning at the new Gantry 2 at PSI. *Physics in Medicine and Biology*, 55(17):5103–21.

Publications related to this work

Scientific reports

Müssig, D., Durante, M., and Bert, C. (2010). Simulation of beam record data for 4D dose calculation. *GSI Scientific Report 2010*, 473.

Müssig, D., Duante, M., and Bert., C. (2011). Rescanning - phase dependence experiments with a moving phantom. *GSI Scientific Report 2011*, 547.

Patent applications

Müssig, D., Gemmel, A„ Lüchtenborg, R., and Bert, C. (2012). Bestrahlungsplanung einer Partikelbestrahlung unter Berücksichtigung einer Bewegung des Zielvolumens *Patent application*, DE 10 2012 112 348.9.

Conference contributions

Müssig, D., Durante, M., and Bert, C. (2010). Bewegungskompensation durch Mehrfachbestrahlung. *DGMP 41. Jahrestagung*, Oral presentation.

Lebenslauf

Persönliche Daten

Name	Dirk Müssig
Geburtstag	30. Juni 1980
Geburtsort	Miltenberg am Main

Ausbildung

seit 05/2009	Mitglied der **Helmholtz Graduate School for Hadron and ion Research (HGS-HIRe)**
seit 05/2009	**TU Darmstadt, GSI Helmholtzzentrum für Schwerionenforschung** Promotion
12/2008	**TU Darmstadt** Diplomabschluss in Physik Titel der Diplomarbeit: Plasmadiagnostik mittels Laser-Thomson-Streuung
04/2002–12/2008	**TU Darmstadt** Physikstudium
08/1998–06/2001	**Gymnasium**, Michelstadt
08/1991–07/1998	**Hermann-Staudinger Gymnasium**, Erlenbach
08/1987–07/1991	**Grundschule**, Mömlingen

Zivildienst

07/2001–04/2002	**Integra GmbH** in Erbach/Odw.

Nebentätigkeiten

08/2007–07/2008	**Goethe Gymnasium** Unterricht im Fach Physik

Danksagungen

An dieser Stelle möchte ich mich bei allen Personen bedanken, die zum Gelingen dieser Arbeit beigetragen haben und meinen Weg während dieser Zeit begleitet haben.

Zunächst danke ich Prof. Marco Durante, der es mir ermöglichte, dieses sehr spannende und auch wichtige Thema in seiner Arbeitsgruppe zu bearbeiten. Seine Bürotür stand jederzeit für offen und es hat stets viel Spaß gemacht mit ihm über die Arbeit zu diskutieren. Prof. Durante ist es gelungen, den tollen Teamgeist der Arbeitsgruppe, welcher unter Prof. Gerhard Kraft entstanden ist, fortleben zu lassen.

Prof. Christoph Bert danke ich nicht nur für die Betreuung dieser Arbeit, sondern auch für das Verständnis und die Hilfsbereitschaft in allen Lebensbereichen. Von den zahlreichen Diskussionen, Hilfestellungen hat die Arbeit entscheidend profitiert. Es ist schon außergewöhnlich, dass ein Betreuer über die Arbeit reden will, obwohl er gerade um kurz vor Mitternacht in der Berliner U-Bahn sitzt!

Der ganzen Gruppe der medizinischen Physik möchte ich für die sehr schöne Zeit, die ich in dieser Arbeitsgruppe verbringen durfte, danken. Natürlich auch allen ehemaligen Mitgliedern. Alexander Gemmel u.a. für seinen Support am HIT. Daniel Richter und Christian Graeff waren eine große Hilfe, wenn es mal wieder Meinungsverschiedenheiten zwischen mir und TRiP4D gab. Viele tolle Diskussionen durfte ich auch mit Thomas Friedrich führen. Ich habe selten jemanden getroffen, der Physik anschaulicher erklären kann. Falls ich bei einem Dosenwerfen einen Stoffgorilla gewinnen sollte, dann werde ich ihn Dir schenken.

Robert Kaderka danke ich, unter anderem, für den Kalender des FC Bayern, welcher noch immer im Büro hängt und rührend an mich erinnert. Matthias Prall danke ich für das Korrekturlesen meiner Arbeit ("What *shall* we do with the drunken sailor"). Sebastian Hild unter anderem dafür, dass er mir geholfen hat mit seinem Tool bunter Bilder zu machen. Jens Wölfelschneider danke ich für viele hilfreiche Diskussionen beim bzgl. der Simulationsumgebung. Außerdem bin ich ihm dankbar, dass er mich beim Fußballspielen zwar einmal ziemlich rabiat von den Beinen geholt, aber dabei nicht schwer verletzt hat. Robert Lüchtenborg für ziemliche viele Dinge, die nicht nur mit der Arbeit zu tun haben. Danke, dass du mich ins Biophysik-Fußballteam aufgenommen hast, obwohl meine Abschlussschwäche im Training inzwischen legendär ist. Ich freue mich schon, Dich aller spätestens am 5. Juli 2014 wieder zu sehen! Vielen Dank auch an Stephan Brons und alle anderen Kollegen des HIT.

Alexander Frank danke ich dafür, dass er mich "überredet"hat, ihn zur Tischtennisweltmeisterschaft in Holland zu begleiten. Das sollten wir wiederholen.

Natürlich möchte ich mich bei meiner Familie, insbesondere bei meinem Opa, für die stetige Unterstützung bedanken. Der allergrößte Dank gilt aber Johanna für die wundervolle Zeit mit ihr. Aber bevor ich lange erzähle für was ich Dir alles dankbar bin - und das wäre jede Menge - versuche ich Dir lieber meine Dankbarkeit so oft wie möglich zu zeigen!

Erklärung zur Dissertation

Hiermit versichere ich, die vorliegende Dissertation ohne Hilfe Dritter nur mit den angegebenen Quellen und Hilfsmitteln angefertigt zu haben. Alle Stellen, die aus Quellen entnommen wurden, sind als solche kenntlich gemacht. Diese Arbeit hat in gleicher oder ähnlicher Form noch keiner Prüfungsbehörde vorgelegen.

Darmstadt, den 16. Dezember 2013

(Dirk Müssig)